

APPLICATION OF LASER TRACKER TECHNOLOGY FOR MEASURING
OPTICAL SURFACES

by

Tom L Zobrist

Copyright © Tom L Zobrist 2009

A Dissertation Submitted to the Faculty of the

COLLEGE OF OPTICAL SCIENCES

In Partial Fulfillment of the Requirements
For the Degree of

DOCTOR OF PHILOSOPHY

In the Graduate College

THE UNIVERSITY OF ARIZONA

2009

THE UNIVERSITY OF ARIZONA
GRADUATE COLLEGE

As members of the Dissertation Committee, we certify that we have read the dissertation prepared by Tom L Zobrist entitled Application of Laser Tracker Technology for measuring optical surfaces and recommend that it be accepted as fulfilling the dissertation requirement for the Degree of Doctor of Philosophy

_____ Date: 11/18/2009
James Burge

_____ Date: 11/18/2009
Jose Sasián

_____ Date: 11/18/2009
Hubert Martin

Final approval and acceptance of this dissertation is contingent upon the candidate's submission of the final copies of the dissertation to the Graduate College.

I hereby certify that I have read this dissertation prepared under my direction and recommend that it be accepted as fulfilling the dissertation requirement.

_____ Date: 12/1/2009
Dissertation Director: James Burge

STATEMENT BY AUTHOR

This dissertation has been submitted in partial fulfillment of requirements for an advanced degree at the University of Arizona and is deposited in the University Library to be made available to borrowers under rules of the Library.

Brief quotations from this dissertation are allowable without special permission, provided that accurate acknowledgment of source is made. Requests for permission for extended quotation from or reproduction of this manuscript in whole or in part may be granted by the copyright holder.

SIGNED: Tom L Zobrist

ACKNOWLEDGEMENTS

I would like to thank my committee for all their hard work and support during my time at the University of Arizona. Jim Burge is incredibly knowledgeable about optical system engineering and optical testing, and is very good about identifying the underlying root of a problem and addressing it. Buddy Marin has been a great boss and mentor during my time working at the Mirror Lab, and the countless hours he spend reading through my dissertation has significantly improved the final version. Jose Sasián has taught me a great deal about optical fabrication and some cool optical testing tricks. Each of them has enhanced my dissertation project and my graduate school experience.

I am thankful for all the help and suggestions on my dissertation from my dissertation writing support group: Stacie Manuel, Ping Zhou, and René Zehnder. I just hope that my suggestions on their dissertations were equally valuable.

There were many people at Steward Observatory and the Mirror Lab that contributed to this project from engineering and design work, to answering technical questions when I cornered them in their offices. I'm thankful for all their hard work, particular thanks to a few individuals who made large contributions. Jeff Hagen wrote all the software and spent countless hours working with me to troubleshoot the bugs and optimize the hardware to get a reliable system that meets the requirements. Paul Maseman spent many late nights helping me (while I had a nasty cold) collect the last of the data I needed to complete the dissertation, and as a reward, he got my cold. Warren Davison designed the SMR pucks and the mechanics for SMR positioning system, while Bill Sisk designed the electronics. Without this system, a Laser tracker Plus measurement would be considerably more tedious.

Marty Valente and his crew at Optical Science's Optical Fabrication and Engineering Facility have been extremely helpful over the years, lending me equipment and allowing me use of their laser trackers and accessories during the various stages of the dissertation. I've learned a lot from my conversations with the opticians and engineers, and value the friendship they have always given me.

My family in Washington State has been very supportive throughout my time in Arizona. I have felt very out of touch with them over the years because of the great distance separating us. The weekly phone call with my parents helped to keep me up to date on the activities of my siblings and allowed me to still feel somewhat connected to their lives. I'm sorry I have not been around as much and hope to see more of you after graduation.

This material is based in part on work supported by the Association of Universities for Research in Astronomy Inc. (AURA) from funds provided by the National Science Foundation under Scientific Program Order No. 10 as issued for support of the Giant Segmented Mirror Telescope for the United States Astronomical Community, in accordance with Proposal No. AST-0443999 submitted by AURA.

DEDICATION

This dissertation is dedicated to Dr. Willard Sperry, Dr. Robert Mitchell, Dr. Roger Yu, and Dr. Walter Kaminski; important professors from my undergraduate that contributed to my love of Physics and interest in Optics. They were always supportive of my education, recognizing my potential early on and encouraging me to continue on to graduate school to pursue a PhD. I am endeared to each of them for their belief in me and the respect they have always shown me.

TABLE OF CONTENTS

LIST OF FIGURES	10
LIST OF TABLES	24
ABSTRACT	28
Chapter 1 INTRODUCTION.....	29
1.1 Motivation.....	30
1.2 Performance Goals.....	33
1.3 Heritage Measuring Optical Surfaces with Laser Trackers.....	34
1.4 Challenges that Motivate System Design.....	39
1.5 Basic Design.....	40
Chapter 2 CHALLENGES THAT INFLUENCE SYSTEM DESIGN AND PERFORMANCE.....	43
2.1 Testing Extreme Geometry.....	43
2.2 Non-reflecting Surface.....	49
2.3 Relative Motion between Test Instrument and Test Surface.....	50
2.4 Air Turbulence in the Measurement Path.....	52
2.5 Systematic Errors Intrinsic to Laser Trackers.....	54
2.6 Effects of Instrumental Drift on the Measurement Data.....	55
Chapter 3 SYSTEM DETAILS	57
3.1 Laser Tracker.....	57
3.1.1 Fundamental Working of a Laser Tracker.....	58
3.1.2 Laser Tracker Selection.....	61
3.1.3 Sphere Mounted Retroreflector Influences.....	66
3.2 External Reference System.....	68
3.2.1 Distance Measuring Interferometer System.....	71
3.2.2 Position Sensing Detector System.....	75
3.2.3 Radiometric Calculations for External Reference System.....	77
3.3 SMR Positioning System.....	79
3.4 SMR Puck.....	81
3.4.1 Teflon Puck.....	82
3.4.2 Air Puck.....	84
3.5 Control Elements.....	87
3.5.1 Electronics.....	88
3.5.2 Torque Motor Control Algorithms.....	90
3.5.3 Software.....	94

Chapter 4 CUSTOM LASER TRACKER CALIBRATION	97
4.1 Radial Calibration	97
4.1.1 Description of Methods	98
4.1.2 Radial Calibration Results	101
4.1.3 Application of Radial Calibration Results	104
4.2 Angular Calibration	104
4.2.1 Description of Methods	105
4.2.2 Angular Calibration Results	107
4.2.3 Application of Angular Calibration Results	122
Chapter 5 CORRELATION BETWEEN LASER TRACKER AND EXTERNAL REFERENCE SYSTEM	123
5.1 Description of Test	125
5.2 Radial Correlation	127
5.2.1 DMI and Radial Laser Tracker Results	128
5.2.2 Spatial Correlation of Distance Measurements	132
5.2.3 Applying DMI Correction	136
5.3 Angular Correlation	137
5.3.1 PSD and Laser Tracker Pointing Results	138
5.3.2 Spatial Correlation of Angle Measurements	143
5.3.3 Applying PSD Correction	148
5.4 Correlation Study Conclusions	150
Chapter 6 DATA COLLECTION AND ANALYSIS	155
6.1 Measurement and Analysis Overview	155
6.2 Data Collection	157
6.3 Data Analysis	163
6.3.1 Description of Data Processing	163
6.3.2 Using Geometry References to Determine the Off-axis Distance and Clocking	165
6.3.3 Comparing Laser Tracker Data with Ideal Surface	168
6.3.4 Applying External Reference Data	169
6.3.4.1 Measuring the Surface Reference Locations	169
6.3.4.2 Calculating Index of Refraction	169
6.3.4.3 DMI Correction	170
6.3.4.4 PSD Correction	172
6.3.5 Applying Custom Calibration Results	172
6.3.6 Outlier Rejection	173
6.3.7 Fitting Zernike Polynomials to Deviation	175
Chapter 7 MEASUREMENT RESULTS AND SYSTEM PERFORMANCE	179

7.1 Large Fold Sphere.....	179
7.2 GMT Segment 1	182
7.3 Analysis of Performance.....	187
7.3.1 Tests of System Accuracy	188
7.3.2 Other Sources of Error.....	195
7.3.3 Performance vs. Goals.....	204
Chapter 8 FINAL COMMENTS.....	211
Appendix A COMPETING TECHNOLOGIES	215
Appendix B HARDWARE TECHNICAL DETAILS AND SPECIFICATIONS	219
B.1 Heterodyne Laser Head.....	219
B.2 Single Beam Interferometer and Retroreflectors	222
B.3 Beam Directing Optics.....	228
B.4 Receivers.....	230
B.5 PC Axis Board	235
B.6 Position Sensing Module	237
B.7 Position Sensing Amplifier.....	239
B.8 Compact FieldPoint for PSD System.....	243
B.9 MicroPC for DMI Monitoring	247
B.10 Electronic Circuit for Temperature Monitoring.....	251
Appendix C LASER TRACKER PLUS MEASUREMENT PROCEDURE.....	255
Appendix D MATLAB DATA ANALYSIS CODE.....	267
D.1 GMT Surface Measurement Analysis Code	267
D.1.1 ltPlusGMT.m	267
D.1.2 CalcIndex.m.....	277
D.1.3 DMICountsToMicrons.m	278
D.1.4 nPtFitxyz.m.....	278
D.1.5 zFit.m.....	282
D.1.6 zFit4.m.....	282
D.1.7 zEval.m.....	283
D.1.8 skim.m	284
D.1.9 meshPlot3.m	284
D.1.10 imagescWithLims.m.....	285
D.1.11 edge2rms.m.....	286
D.1.12 listCoefs.m.....	286
D.1.13 listBothCoefs.m	287
D.1.14 zDisplay.m.....	287
D.2 LFS Surface Measurement Analysis Code	289
D.2.1 ltPlusFoldSphere.m.....	289

D.2.2 lssphere.m	294
D.2.3 nlss11.m	297
D.2.4 gncc2.m	300
D.2.5 fgsphere.m	301
D.3 Radial Calibration Analysis Code	303
D.3.1 RadialCalibration.m	303
D.3.2 ImportFaroSADData.m	309
D.3.3 SphereToCart	310
D.3.4 zDisplay_PZ.m	310
D.3.5 RadialOutlierCorrect.m	311
D.3.6 RadialCalibrationPlot.m	313
D.4 Angular Calibration Analysis Code	314
D.4.1 AngularCalibration.m	314
D.4.2 Slope.m	322
D.4.3 ZernSlopeStandardNorm.m	322
D.4.4 IMCIRCLE.m	328
D.5 Correlation Study Analysis Code	330
Appendix E ORTHOGONAL POLYNOMIALS	337
E.1 Zernike Polynomials	337
E.2 Zernike Slope Polynomials	340
E.3 Zhao Vector Polynomials	342
Appendix F PSD CALIBRATION	345
REFERENCES	351
ILLUSTRATION CREDITS	355

LIST OF FIGURES

Figure 1-1: The image on the left shows the 25 m $f/0.7$ GMT primary mirror, composed of seven 8.4 m diameter segments. The image on the right is a surface plot showing the 14.5 mm of aspheric departure required for each of the off-axis segments [6].	30
Figure 1-2: Laser tracker mounted ~ 2 m above a 0.95 m mirror for <i>in situ</i> testing on the polishing machine. The same arrangement was used for testing the 1.7 m NST mirror [31].	36
Figure 1-3: Laser tracker measurements of the NST mirror surface near the beginning and near the end of loose-abrasive grinding. The plots show the departure from the ideal off-axis paraboloid, in millimeters, with only piston, tip and tilt removed [31].	37
Figure 1-4: Comparison of one of the first optical measurements (two images at left) with laser tracker data taken at the same time (upper right). The difference is shown at lower right. The tracker map is a 6 th -degree Zernike polynomial fit to data such as those shown in Figure 1-3. Focus, coma and astigmatism, which depend strongly on the alignment of the mirror in the optical test, were removed from all three maps. Color bars are labeled in nanometers of surface [31].	38
Figure 1-5: Conceptual drawing of the laser tracker set up for measuring the mirror surface. The laser tracker uses interferometry to measure distance to an SMR. The tracker runs under servo control to follow the SMR as it is scanned across the surface, combining radial distance with the gimbal angles to make a three-dimensional measurement. Effects due to the combined motion of the air, mirror, and tracker are mitigated by separate real-time measurements of distance and lateral motion using a system of four stability references [44].	41
Figure 2-1: The shape measurement of the GMT segments provides several new challenges. The aspheric departure is large and non-axisymmetric, and the long radius of curvature does not allow direct access from within the Mirror Laboratory [6].	44
Figure 2-2: Optical layout for the interferometric test for the off axis GMT mirror segment [6].	45
Figure 2-3: Geometry of the Laser Tracker Plus test setup for measuring GMT mirror segments. The closer the laser tracker is placed to the center of curvature (as $h \rightarrow R$), the closer the measurements are made to normal	

incidence ($\alpha \rightarrow 0$) and the less sensitive the measurements are to surface errors δs due to errors in the angles $\delta\theta$	47
Figure 2-4: Plot showing the sensitivity of the surface measurements to angular errors as a function of laser tracker height above the mirror segment at three radial positions: the center of the mirror, the 70% zone, and the edge of the mirror. If the tracker is at the center of curvature of the mirror (38 m), then it is insensitive to angular errors.	48
Figure 2-5: The external reference system can be used to compensate for relative motion between the test instruments and the mirror surface, by measuring the changes observed by each reference and fitting those changes with rigid body motion [44].	51
Figure 2-6: Plots of the Zernike coefficient fits to the data collected by the distance measuring interferometers of the external reference system showing the tilt changes of the GMT mirror in both axes as the SMR puck is moved across the surface during a typical surface measurement. The puck follows a truncated 16×16 grid of points, oscillating back and forth across the mirror eight times during a single measurement. This oscillation is visible in the tilt components of the Zernike fit of the data. Table E-1 lists the Zernike polynomials used throughout this dissertation.	52
Figure 2-7: The external reference system can be used to compensate for some air effects such as low-order turbulence [44]......	53
Figure 2-8: Laser tracker measurements of NST show systematic, repeatable errors of about $3 \mu\text{m}$ rms. The two plots above are NST measurements at two rotation angles, which agree except for $15 \mu\text{m}$ P-V in 45° component of astigmatism.	54
Figure 2-9: Plot of drift data taken with a $\frac{1}{2}$ " SMR mounted on the surface of a test sphere. Measurements were made at a rate of three data points-per-second, and each was an average of 100 measurements-per-point. The radial value changed over $20 \mu\text{m}$ during the 5 hour measurement run, while the angular values also showed drift.....	55
Figure 3-1: A laser tracker measures the location of an SMR in three dimensions and tracks the relative motion. It can display the measured values in a variety of coordinate systems including spherical (r, θ, ϕ), cylindrical (ρ, θ, z), and Cartesian (x, y, z). Copyright © 2006 FARO Technologies Inc. All Rights Reserved [14].	58
Figure 3-2: Schematic representation of the internal workings of a laser tracker.	59

Figure 3-3: The Faro Xi v2 laser tracker [14].	63
Figure 3-4: Sphere mounted retroreflectors are available from a number of manufactures in three standard sizes: 1 ½ inch, 7/8 inch, and ½ inch.	66
Figure 3-5: The Laser Tracker Plus instrument assembly mounted on the bridge crane at the top of the SOML test tower. The assembly is composed of the laser tracker head and the DMI system's optics, laser head, and remote receivers. Because of the heat generated by the laser head and remote receivers, they are mounted in a separate ventilated compartment from the DMI optics [44].	69
Figure 3-6: Diagram of one of the four surface references that sit at the four compass points around the circumference of the test mirror and are aligned to each of the four DMI laser beams. The majority of the DMI laser light passes straight through the beamsplitter to a retroreflector and back to the interferometer for monitoring the radial fluctuations of the reference beam during mirror testing. The beamsplitter reflects 10% of the DMI laser light to a PSD for monitoring the angular changes of the reference beam. An interference filter is used to pass the laser light to the PSD while blocking ambient room light [44].	70
Figure 3-7: Schematic representation of the light path through each surface reference.	71
Figure 3-8: Schematic representation of the light distribution to each distance measuring interferometer beam. A more detailed drawing of the light path within the single beam interferometers is provided in Figure B-4.	72
Figure 3-9: Plot shows the error that results by not compensating for the deadpath in the distance measuring interferometer measurements. The red curve is the fluctuations measured by the laser tracker during 1 hour of staring. The green and blue curves are measurements from a DMI during the same time period, where the deadpath length was compensated in the green curve, while it was not in the blue curve.	73
Figure 3-10: Diagram of the SMR positioning system at the base of the test tower. The gray disk represents the mirror under test, while the small circle at the intersection of the four strings is the SMR puck [44].	79
Figure 3-11: A close-up of one of the string control mechanisms [44].	80
Figure 3-12: Limit switches constrain the range of string positions so they cannot pull the SMR off the mirror or contact the four surface references at the edge of the mirror. The result is a 12 edged figure that restrict the puck's	

proximity to the edge with the worst limit 8.4 inches and the 12 closest points 3.3 inches.	81
Figure 3-13: Picture of the Teflon puck resting on the surface of the GMT Segment.	82
Figure 3-14: Positioning puck for holding SMR (shown in grey) while measuring, viewed from above and below. Note the inner and outer rings visible in the image on the right, which decouples the SMR (sitting on the inner ring) from the varying tensions in the SMR positioning system strings (attached to the outer ring).....	83
Figure 3-15: The original design for the flexure that connected the inner and outer rings of the Teflon SMR puck is shown on the left.....	84
Figure 3-16: Underside of the air puck showing the three Teflon air pads and the rubber bellows, which lift the puck and the SMR clear of the mirror surface when inflated.	85
Figure 3-17: Once the air is turned off to the air puck, the bellows deflate, allowing the SMR to sit in direct contact with the glass surface.....	86
Figure 3-18: Air puck hose management system that uses a set of counterweights to provide a non-uniform tension in the air hose to prevent it from contacting the surface.....	86
Figure 3-19: Laser Tracker Plus system electrical layout.....	89
Figure 3-20: Layout of the mirror and SMR positioning system during a Laser Tracker Plus measurement. An x - y axis is defined with the origin at the center of the mirror, where (x,y) is the position of the puck on the mirror. The four positioning strings run from the puck through pulleys to the torque and stepper motors. When the air puck is used, there is also an air hose that is connected to the puck.....	91
Figure 3-21: Graphical user interface used to control the Laser Tracker Plus system and monitor the data collection process.	95
Figure 4-1: The systematic tracker errors are calibrated over the scan angles using a small concave spherical surface. The radial line of sight errors are determined by making measurements of the spherical surface with the tracker at its center of curvature [7].....	98
Figure 4-2: Picture of the calibration sphere mounted in position for performing the radial calibration of the laser tracker. The tip, tilt, and piston of the	

- mirror are adjusted by turning the three bolts until the center of curvature of the mirror is aligned to the gimbal point of the laser tracker..... 99
- Figure 4-3: Cross sectional diagram of the adjusters for fine positioning the calibration mirror's CoC to the laser tracker's gimbal. 100
- Figure 4-4: Plot of the raw laser tracker data from a typical radial calibration measurement of the calibration sphere. 102
- Figure 4-5: Surface plots of the Zernike polynomial fit to the residual surface errors from the calibration sphere measured with the laser tracker. The plot on the left is for a typical angular calibration measurement, while the one on the right is the average of all 30 sets [45]. 102
- Figure 4-6: The rms error introduced into each Zernike polynomial due to the radial errors in the laser tracker, excluding the values for piston, tilt, and power, which are due to alignment errors in the test setup. The plot is based on 30 separate measurements of the surface, where the curve represents the mean for each Zernike coefficient and the error bars represent the uncertainty given an average of any 5 of the 30 measurements, where 5 individual measurements averaged together would be representative of a typical set of calibration measurements. The magnitude of the error bar is $\pm \sigma/\sqrt{5}$ [44]. 103
- Figure 4-7: The diagram on the left shows the layout for the angular calibration. The laser tracker at floor measures the fixture location with small angular error compared to the tower tracker. The diagram on the right shows the pattern of multiple scans made to determine the discrepancy between the two trackers, which is used to determine a calibration correction for the angular errors [44]. 106
- Figure 4-8: Specialty fixture designed to hold three 1.5 inch laser tracker balls in direct contact for performing the angular calibration of the laser tracker in the test tower with the aid of another one at floor level. The two outer balls are aimed upward toward the tracker to be calibrated, while the center ball is aimed horizontally toward the tracker at floor level..... 107
- Figure 4-9: Faro laser tracker mounted horizontally in a custom mount built for performing the angular calibration. This laser tracker is locked on to the center SMR in the fixture in the foreground while another laser tracker above in the test tower measures the outer two SMRs in the fixture. The difference in the motion of the fixture is used to determine the angular error of the laser tracker in the tower [45]. 108
- Figure 4-10: The angular calibration measurements were made with four radial scans crossing directly beneath the tower laser tracker to be calibrated. A

0.5 m measurement spacing was selected along each scan for a total of 21 measurements per scan over a 10 m scan diameter, which is approximately the diameter of the circle subtended by the GMT mirror when projected to the floor. The blue arrows in the figure show the direction and relative angular error of the tower laser tracker [45]. 109

Figure 4-11: The four plots above show the difference in angles measured with the laser tracker on the ground and the one in the tower for four different scan lines, where positive values indicate the angular displacement is radially outward. The angles of the scan and the rms error are provided above each plot. The 0° and 90° plots correspond to the Zenith and Azimuth angles of the tower laser tracker. The black curves represent the Zernike slope polynomial fit to the full 2-dimensional data set as a function of radial distance from the center out. The discontinuity is the result of the radial distance changing sign at the center of the scan. 112

Figure 4-12: Radial vector plots of the 16 Zernike slope polynomials used for fitting the angular calibration data. These plots show the projection of the Zernike slope polynomials in the radial direction. 113

Figure 4-13: Vector plot of the radial component of the angular error across the entire measurement area based on the scan measurements presented in Figure 4-11. The area inside the black circle represents the region subtended by GMT. 114

Figure 4-14: The left plot shows the mirror sensitivity for GMT Laser Tracker Plus test as a function of radial displacement from the center of the mirror segment (color scale in microns of surface error per microradian of angular error). The right plot shows the surface error due to angular errors in the laser tracker measurements that can be corrected by applying the angular calibration measurement results (color scale in microns of surface error). The black circle represents the area subtended by the GMT mirror, and the surface error over that region is $0.82 \mu\text{m rms}$. Lateral scale is in meters for both plots..... 115

Figure 4-15: The four plots above represent the residual angular error in the tower laser tracker after applying the correction based on the Zernike slope polynomial fit shown in the plots in Figure 4-11. The residual rms error is provided above each plot. 116

Figure 4-16: The four plots above show the difference in angles measured with the laser tracker on the ground and the one in the tower along each of the four different scan lines for the three different sets of scan measurements, each represented in a different color. The angle of the scan and the rms error are provided above each plot. The 0° and 90° plots correspond to the Zenith and

Azimuth angles of the tower laser tracker. The color curves represent the projection of the Zernike slope polynomial fit to each data set along the scan lines, while the black curve represents the projection of the mean of the three individual polynomial fits as a function of radial distance from the center out. The discontinuity is the result of the radial distance changing sign at the center of the scan. 118

Figure 4-17: The left hand plot shows the laser tracker angular error in the radial direction based on the average of the three sets of scans. The right hand plot shows the expected surface error in the laser tracker measurements due to these angular errors. The black circle represents the area of the test subtended by the GMT mirror. The surface error over the GMT mirror that can be corrected by applying this angular calibration is $0.55 \mu\text{m rms}$ 119

Figure 4-18: The four plots above represent the residual angular error in the tower laser tracker after applying the correction based on the mean value for the Zernike slope polynomial fits listed in Table 4-1 and shown in the plots in Figure 4-16. The residual rms error is provided above each plot, based on the rms of the points for all three scans. 120

Figure 4-19: The left hand plot shows the scan data from one of the angular calibration runs, while the right hand plot shows the projection of the polynomial fit along the scans. The fit looks like a smoothed version of the data because only low-order polynomials are used. The data in the left hand plot shows a large angular error in the tracker measurements running horizontally across the plot (encircled in black), corresponding to an error in the azimuthal encoder or bearing, which is not being properly fit, so this error will not be corrected with the angular calibration. 121

Figure 5-1: Diagram of the test setup used for measuring the correlation between the fluctuations of two of the DMI reference beams for different separations S 126

Figure 5-2: Radial motion measured by the laser tracker, compared to the motion measured by the north and south DMI for the entire data set [45]. 129

Figure 5-3: Relative radial motion measured by the laser tracker, compared to the motion measured by the north and south DMI for the first 300 s of the data set. 129

Figure 5-4: Plots showing a smoothing of the laser tracker data with increased measurement integration time. The table on the right shows the rms of each plot. 130

Figure 5-5: Plots showing a smoothing of the North DMI data with increased measurement integration time. The table on the right shows the rms of each plot.....	131
Figure 5-6: Plots showing a smoothing of the South DMI data with increased measurement integration time. The table on the right shows the rms of each plot.....	131
Figure 5-7: Difference in motions measured by the north and south DMIs.....	132
Figure 5-8: Difference in motions measured by the laser tracker and the North DMI.....	133
Figure 5-9: Correlation between the north and south DMI as a function of spatial separation. So long as the blue curve is below the green curve, the DMIs are measuring more common motion than noise, so the correlation is high.	134
Figure 5-10: Correlation between the north DMI and the laser tracker as a function of spatial separation. Because the blue curve is above the green curve, there is less common motion than DMI noise in the measurements.	135
Figure 5-11: Pictorial representation of the four basis functions that describe motions observed by the distance measuring interferometer system. These basis functions match the four lowest Zernike polynomials, (piston, tilt X, tilt Y, and astigmatism) listed in Table E-1.	137
Figure 5-12: Typical measurements of the dither experienced by the laser tracker in the SOML test tower. Over the course of 1 hour, ~3600 measurements were made with 1 s integration time (left). The right plot shows the first 300 measurements. The fluctuations are almost insignificant at less than 0.5 μ rad rms [45].....	139
Figure 5-13: PSD measurements of the dither in the north reference beam. The plot on the left shows the pointing results at 1 s intervals for the entire data set (nearly 1 hour long) measured at the edge of the mirror. Each color represents a consecutive 300 s long block of time. The plot on the right shows just the first 300 s of the data set.	140
Figure 5-14: PSD measurements the dither in the south reference beam. The plot on the left shows the pointing results at 1 s intervals for the entire data set (nearly 1 hour long) measured at the edge of the mirror. Each color represents a consecutive 300 s long block of time. The plot on the right shows just the first 300 s of the data set.	141

Figure 5-15: Plots showing a smoothing of the laser tracker data with increased measurement integration time. The table on the right shows the rms of each plot.....	141
Figure 5-16: Plots showing a smoothing of the north PSD data with increased measurement integration time. The table on the right shows the rms of each plot.....	142
Figure 5-17: Plots showing a smoothing of the south PSD data with increased measurement integration time. The table on the right shows the rms of each plot.....	142
Figure 5-18: Difference in motions measured by the north and south PSDs. Much of the high frequency noise remains after the subtraction, showing poor correlation for the PSD measurements.	143
Figure 5-19: Difference in motions measured by the laser tracker and the north PSD. The plot still show a lot of the high frequency noise, showing that there is poor correlation for the high frequency component of the measurements.	144
Figure 5-20: Correlation between the north and south PSDs for motion in the north-south direction, as a function of spatial separation. Where the blue curve is below the green curve, the PSDs are measuring more common motion than noise.....	145
Figure 5-21: Correlation between the north and south PSDs for motion in the east-west direction, as a function of spatial separation. Where the blue curve is below the green curve, the PSDs are measuring more common motion than noise.....	145
Figure 5-22: Correlation between the north PSD and the laser tracker in the north-south direction for different spatial separations. Because the blue curve is above the green curve, there is less common motion than PSD noise in the measurements, so the correlation is low.....	147
Figure 5-23: Correlation between the north PSD and the laser tracker in the east-west direction for different spatial separations. Because the blue curve is above the green curve, there is less common motion than PSD noise in the measurements, so the correlation is low.....	147
Figure 5-24: Pictorial representation of the basis functions that describe the motion measured by the PSD system. These functions are labeled by the corresponding Zhao polynomials, which are discussed in Section E.3.....	149

- Figure 5-25: Vector plots of the eight low-order Zhao polynomials that are the closest match to the eight PSD basis functions shown pictorially in Figure 5-24 above. 149
- Figure 6-1: The portion of the master control GUI that is used to connect the Laser Tracker Plus control software to the laser tracker. 157
- Figure 6-2: The portion of the master control GUI that is used to set up the SMR positioner and Laser Tracker Plus system for a surface measurement. 158
- Figure 6-3: Image of the edge of the GMT mirror segment showing one of the surface references and the fixture used to hold an SMR for measuring the locations of the clocking marks around the circumference of the mirror [45]. 159
- Figure 6-4: View through the eyepiece of the geometry reference of one of the four scribe marks on the edge of GMT. A reticle in the eyepiece is used to align the geometry reference to the scribe mark on the mirror. 160
- Figure 6-5: Image of the Tracker XY Display showing the location of the SMR puck on the surface of the mirror (black dot), as well as the locations of points to be measured (magenta dots) and those already measured (blue dots)... 162
- Figure 6-6: The GMT Monitor Log provides a visual reference of all the system activity during a measurement run. Any errors that occur during a measurement will be displayed here for the operator to see and respond to. 162
- Figure 6-7: Plots showing the amount of the piston, tip, tilt, and astigmatism measured by the distance measuring interferometer reference system during measurement set gmt1 090630 3 mod.xls. Almost all the motion can be described as rigid-body motion. 171
- Figure 6-8: Plots showing residual piston and tilt error remaining after the transformation of the data to the geometry references. Several outlying points are visible in both plots. In the right-hand plot, the coarse outlier correction has removed several outlying points. 174
- Figure 6-9: The plot on the left shows the data from Figure 6-8 after the plane has been fit and removed. The remaining outlying point is prominent in the plot, and is now easily removed by the fine outlier correction without risk of removing any valid data from the surface measurement. The plot on the right shows the residual surface error in the data after removing the last outlier. 175
- Figure 6-10: The left-hand plot shows a contour plot representation of the measurement data from gmt1 090630 3 mod.xls, while the right-hand plot show the Zernike polynomial fit to the measurement data. 177

- Figure 6-11: Plots showing the data from gmt1 090630 3 mod.xls with power removed [45]..... 178
- Figure 7-1: Testing of the 3.75 m spherical mirror with the Laser Tracker Plus system. One of the references is visible in the foreground, with two of the three other visible in the background. An optician positions the SMR mounted at the end of a wooden wand for the next measurement [44]. 180
- Figure 7-2: Measurements of a 3.75 m spherical mirror surface with laser tracker only on the left, and the corrected plot after applying the data from the external reference system. The plots show the departure from the best-fit sphere [44]. 181
- Figure 7-3: The plot on the left shows the first GMT measurement with a 600 μm P-V error in the surface figure, primarily power. The plot on the right shows a residual error, primarily spherical aberration and astigmatism, of 180 μm P-V after removing power. 183
- Figure 7-4: Figure of the GMT mirror at the end of loose-abrasive grinding [45]..... 185
- Figure 7-5: Figure of the GMT mirror taken on October 29, 2009 to guide the figuring during polishing. 185
- Figure 7-6: Comparison of Laser Tracker Plus measurements made on October 29, 2009 with fringes obtained by the GMT principal test during the same time period. 186
- Figure 7-7: GMT mirror set up under the SOML test tower for a surface measurement with the Laser Tracker Plus system [45]. 187
- Figure 7-8: Results of two consecutive GMT measurements made with the Laser Tracker Plus system with the mirror rotated 90° between measurements. Both measurements are shown in the standard mirror orientation, with the parent axis toward the negative x direction. Power, which is a rotationally symmetric aberration, has been removed to emphasize the comparison of the non-symmetric aberrations. 190
- Figure 7-9: The left hand plots show the average of the 0° rotation measurements, the center plots show the average of the 90° rotation measurements, and the right hand plots shows the differences. The top row of plots is without applying the angular calibration correction. The center row is for the case when only the calibration coefficients from Table 4-1 with a mean greater than the standard deviation are used. The bottom row of plots is when all the coefficients are used. The right hand plots show that error between the two orientations is reduced more by using all of the angular calibration

coefficients. Piston, tilt and all rotationally symmetric aberrations have been removed from the plots.....	192
Figure 7-10: Alternating ridges and valleys in the data similar to a washboard due to excessive torque motor forces tilting the puck as it scans back and forth across the mirror. The left plot show a side view of the ridges, which are on the order of 150 μm P-V.....	196
Figure 7-11: Plots showing streaks in the data caused by dust contaminants on the mirror surface during testing. It appears that particles stuck to the SMR and prevented direct contact with the mirror surface for several consecutive measurement positions.....	197
Figure 7-12: Two consecutive measurements of GMT using the Laser Tracker Plus system, where the left hand plot was measuring with the laser tracker in absolute distance mode, while the right hand plot was measured in interferometric mode.	198
Figure 7-13: Example of a discontinuity in a surface measurement caused by the laser tracker loosing lock on the SMR and performing an ADM reset to reacquire the distance.	199
Figure 7-14: Two consecutive sets of measurements of GMT. The set on the left still has the seals inflated, while they were deflated before measuring the set on the right. A change of over 6 μm rms power was measured.	200
Figure 7-15: Temperature measurements of the GMT mirror showing a 0.4 K thermal gradient between the front and back faces of the mirror and a 0.5 K variation across the back plate. Values represent difference from ambient, in K.	201
Figure 7-16: Plots of the GMT mirror segment with significantly different amounts of power due to changes in the thermal gradients across the mirror. The measurement on the left was taken shortly after washing the front surface and had a measured thermal gradient of ~ 1 K front to back. The measurement on the right was taken after the mirror was allowed to passively equilibrate overnight, reducing the thermal gradient to 0.4 K, which changed the power by 31 μm	202
Figure 7-17: The underside of the GMT mirror cell, with the hoses from the “suckulators” that are used to actively ventilate the mirror cell.....	203
Figure 7-18: Errors in the GMT axial support forces measured by loadcells in the mirror cell.	204

Figure 8-1 : Laser Rail system manufactured by API for verifying that laser tracking systems meet their performance requirements as specified in the ASME B89 standard.[2]	214
Figure B-1 : Agilent 5517B laser head dimensions [1]. Image used with permission from Agilent Technologies, Inc.	221
Figure B-2 : Agilent 10705A single beam interferometer (left) and Agilent 10704A retroreflector (right) [1]. Image used with permission from Agilent Technologies, Inc.....	223
Figure B-3 : Agilent 10705A single beam interferometer dimensions [1]. Image used with permission from Agilent Technologies, Inc.....	223
Figure B-4 : Single beam interferometer reference and measurement laser beam paths [1]. Image used with permission from Agilent Technologies, Inc.....	225
Figure B-5 : Agilent 10704A retroreflector dimensions [1]. Image used with permission from Agilent Technologies, Inc.	228
Figure B-6 : Dimensions of the Agilent 10701A 50% beam splitter (left) and Agilent 10707A beam bender (right) [1]. Image used with permission from Agilent Technologies, Inc.....	229
Figure B-7 : Dimensions of the Agilent 10780F remote receiver with 2 meter fiber optic and remote sensor [1]. Image used with permission from Agilent Technologies, Inc.....	231
Figure B-8 : Optical misalignment resulting in lateral displacement of the measurement beam with respect to the reference beam at recombination results in signal loss.....	233
Figure B-9 : Agilent 10885A PC axis board used to process the signals from the DMI used in the Laser Tracker Plus system.....	235
Figure B-10 : On-Trak Photonics PSM 2-10 position sensing module dimensions [33].....	238
Figure B-11 : Images of the front and rear panels of the On-Trak Photonics OT-301 versatile position sensing amplifier, dimensionally identical to the OT-301 S504 high gain position sensing amplifier used for the Laser Tracker Plus system.	240
Figure B-12 : National Instruments cFP-1804 Ethernet/serial interface for Compact FieldPoint, which has slots for four modules for inputting or	

outputting digital or analog signals, for interfacing remote instruments with a compute via Ethernet or serial port connection.	244
Figure B-13 : The TS-7300 single board computer MicroPC used for diagnostic monitoring of the Laser Tracker Plus system instrument cluster atop the bridge crane.	248
Figure B-14 : Schematic of the thermocouple amplification circuit used to monitor changes in the temperature in and around the Distance Measuring Interferometer laser head, receiver electronics, and optics. The circuit produces a nominal gain of 5001, which for the type T thermocouples used, results in a temperature constant of 200 mV/°C.	252
Figure B-15 : Pinout for the Linear Technology LT1013 dual precision op amp used in the thermocouple amplification circuit shown in Figure B-14	253
Figure E-1 : Relations between the \bar{s} and \bar{t} polynomials. The Laplacian vectors are the overlap between \bar{s} and \bar{t} sets. The dashed circles and associated solid arrows illustrate the local behaviors of the vectors in different sets.	344
Figure F-1 : Bench top setup for calibrating a Position Sensing Detector. The PSD is mounted on a two-axis stage with electronic indicators to measure displacements at the micron level, while a laser spot is incident on the detector face. The change in voltage is compared to the change in position to determine the detector's linearity and calibration coefficients.	346
Figure F-2 : PSD interface frontend developed in LABVIEW by Gallagher [15].	347
Figure F-3 : Resulting plots from the bench top calibration showing the linearity the PSD. From the slope of the lines, the calibration coefficients relating output voltage and displacement can be determined.	348

LIST OF TABLES

Table 1-1: A summary of the various optical tests for the 8.4-m GMT primary mirror segments to guide the fabrication and verify the final surface figure so that each segment meets the required performance goals [7].	31
Table 1-2: Requirements and goals for the Laser Tracker Plus system based on the fabrication requirements for manufacturing the GMT segments [44].	33
Table 2-1: Geometric parameters for a Laser Tracker Plus measurement of GMT.	48
Table 2-2: Stages of Optical Fabrication.	49
Table 3-1: Comparison of laser tracker models from each of the three major laser tracker manufactures. Performance values are as specified by the manufacturers.	62
Table 3-2: Results of the head-to-head test performed to compare the API Tracker 3 with the Faro Xi v2 laser tracker.	65
Table 3-3: Performance of the SMR used for Laser Tracker Plus measurements, as measured by the manufacture and reported in the provided certificate of calibration.	67
Table 3-4: Relative beam length of the four DMI references compared to the laser tracker beam length at various positions along the GMT mirror surface.	74
Table 3-5: List of components and quantities required for the DMI system used in the Laser Tracker Plus system.	75
Table 3-6: List of the component and quantities required for the PSD system used in the Laser Tracker Plus system.	76
Table 3-7: Radiometric calculations of the performance of the external reference system when a 10% beamsplitter is used in the surface reference. The upper portion of the table shows the transmittance through the light path from the laser to the input fiber of the DMI system and the resultant minimum optical power. This is compared to the minimum optical power required by the receiver. The lower portion of the table shows the minimum optical power transmitted through the system from the laser to the input of the PSD, and the resulting maximum potential voltage after amplification.	78
Table 4-1: List of Zernike slope polynomial coefficients from the individual fits to each of the three sets of laser tracker angular calibration measurements.	

The mean and standard deviation for each coefficient is also listed. The polynomials are defined in Table E-2.	117
Table 5-1: Expressions for the total perturbation and variance for two separate sensors and their difference.	124
Table 6-1: List of fit coefficients for the Zernike polynomials through 6 th degree for the data set gmt1 090630 3 mod.xls.	176
Table 7-1: List of values measured for the GMT mirror over the year long loose-abrasive grinding phase of fabrication. The table shows steady improvement in the mirrors figure, guided exclusively by Laser Tracker Plus measurements. Values for aberrations are rms surface. Values for astigmatism, coma, and trefoil are RSS of the two components. SA and SA2 are the first two spherical aberrations. The units are microns rms.	184
Table 7-2: Worst case comparison of GMT figure measurements made with the Laser Tracker Plus system when the mirror is rotated 90° between measurements. Fits and the subtractions are done in mirror coordinates.	191
Table 7-3: Comparison of GMT figure measurements made with the Laser Tracker Plus system with the mirror rotated 90° between measurements and the angular calibration correction applied.	193
Table 7-4: Laser Tracker Plus system accuracy.	207
Table 7-5: Expected errors in the fit of low-order Zernike polynomials to a GMT surface measurement due to the errors listed in Table 7-4 for individual Laser Tracker Plus measurements. These values meet the system design specifications listed in Table 1-2.	209
Table A-1: A comparison of competing technologies with similar accuracy and range to the Laser Tracker Plus system.	218
Table B-1: Agilent 5517B laser head specifications [1].	220
Table B-2: Agilent 10705A single beam interferometer technical specifications [1].	227
Table B-3: Agilent 10704A retroreflector technical specifications [1].	227
Table B-4: Technical specifications for the Agilent 10701A 50% beam splitter and the Agilent 10707A beam bender [1].	230
Table B-5: Technical specifications for Excel Precision model 1031F remote receiver [13].	232

Table B-6 : Technical specifications for the On-Trak Photonics PSM 2-10 position sensing module [33].....	238
Table B-7 : On-Trak Photonics OT-301 S504 high gain position sensing amplifier specifications [33].....	241
Table B-8 : Pinout for the 9 pin D connector used by On-Trak Photonics for connecting their PSD modules to their amplifiers.....	243
Table B-9 : OT-301 series PSD amplifier internal switch settings for use with a PSM 2-10 duo-lateral position sensing module.....	243
Table B-10 : National Instruments cFP-1804 Compact FieldPoint Ethernet/serial interface specifications.....	245
Table B-11 : National Instruments cFP-AI-118 analog input module specifications.....	246
Table B-12 : National Instruments cFP-AI-110 analog input module specifications.....	247
Table B-13 : Technologic Systems TS-7300 single board computer specifications...	249
Table B-14 : List of the input sources, expected nominal signal voltage, and voltage ranges used with each channel of the TS-9700 analog-to-digital converter used with the MicroPC. Channel 7 was set to monitor the supply voltage by setting jumper PJ5, the thermocouple voltages were input through the 10-pin header, and the DMI receiver voltages were input through the terminal block. The appropriate set of pin numbers is noted for each channel...	250
Table B-15 : Linear Technology LT1013 dual precision op amp specifications at 25°C, $V^+ = +5$ VDC, and $V^- = 0$ V [22].....	253
Table E-1 : List of the first 66 functions for the RMS Zernike polynomials up through 10 th degree. The coefficient for each function is listed in the form $Z_{n,m}$ where n is the degree of the polynomial, and m describes the rotational dependence. If $m > 0$, the function has an $m\phi$ cosine-dependence, if $m < 0$, the function has an $m\phi$ sine-dependence, and if $m = 0$, the function is rotationally symmetric.....	338
Table E-2 : List of the first 36 functions for the Zernike slope polynomials up through 6 th degree. The coefficient $\vec{\nabla}Z_{n,m}$ is the gradient of the Standard Zernike polynomial $Z_{n,m}$, where n is the order of the polynomial, and m describes the rotational dependence. These coefficients are normalized to ± 1 at the edge.....	340

Table E-3 : Analytic expression for the first 10 functions for both the \vec{S} and the \vec{T} polynomial sets, expressed in terms of the Zernike polynomials listed in Table E-1	343
Table F-1 : List of nominal clocking angle of the PSDs for each surface reference...	349

ABSTRACT

The pages of this dissertation detail the development of an advanced metrology instrument for measuring large optical surfaces. The system is designed to accurately guide the fabrication of the Giant Magellan Telescope and future telescopes through loose-abrasive grinding. The instrument couples a commercial laser tracker with an advanced calibration technique and a set of external references to mitigate a number of error sources. The system is also required to work as a verification test for the GMT principal optical interferometric test of the polished mirror segment to corroborate the measurements in several low-order aberrations. A set of system performance goals were developed to ensure that the system will achieve these purposes. The design, analysis, calibration results, and measurement performance of the Laser Tracker Plus system are presented in this dissertation.

Chapter 1

INTRODUCTION

The fabrication of extremely large telescopes holds many new challenges as the ever increasing size requires fast, segmented optics. The challenge in manufacturing stems from the difficulty in measuring the surface of these highly aspheric, off-axis mirror segments during all stages of fabrication [6]. Conventional techniques using large optical generators allow the surface to be generated within a few microns of the desired shape. However, maintaining that shape throughout loose-abrasive grinding and polishing is a challenge due to the difficulty of measuring rough ground surfaces.

This dissertation details the development of an advanced metrology instrument designed to accurately guide the fabrication of large telescope mirror segments during loose-abrasive grinding. The instrument, referred to as the Laser Tracker Plus system throughout, uses a commercial laser tracker, which is a portable coordinate measurement machine that measures the location of a target that contacts the mirror surface and is moved to multiple positions. The laser tracker is coupled with an advanced calibration technique and a set of external references to mitigate a number of error sources [7, 44].

The Laser Tracker Plus system builds on previous experience of using laser trackers for measuring optical surfaces, covered in Section 1.3. The system is further expected to corroborate the optical interferometric test of the polished mirror, in several low-order aberrations. The design, analysis, calibration, and measured performance of the Laser Tracker Plus system will be presented in this dissertation.

1.1 Motivation

This system was designed specifically to guide the loose-abrasive grinding of the Giant Magellan Telescope (GMT) primary mirror segments [7]. The GMT design uses seven 8.4 m mirror segments arranged in a close pack structure that produces an $f/0.7$ ellipsoidal parent mirror with an effective aperture of about 25 m [24]. The central segment is on-axis, while the surrounding six segments are all off-axis. Each of the six identical off-axis segments has a 38 m radius of curvature, and 14.5 mm of peak to valley (P-V) aspheric departure [9]. Figure 1-1 shows a computer image depicting GMT, along with a surface plot showing the shape of the aspheric departure for each of the six off-axis mirror segments.

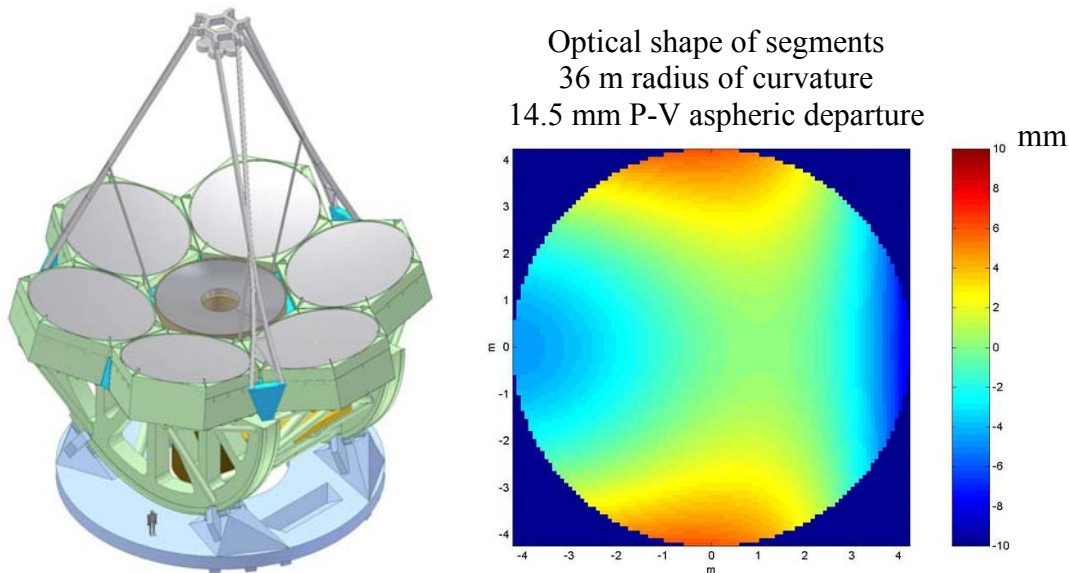


Figure 1-1: The image on the left shows the 25 m $f/0.7$ GMT primary mirror, composed of seven 8.4 m diameter segments. The image on the right is a surface plot showing the 14.5 mm of aspheric departure required for each of the off-axis segments [6].

Accurate testing of the GMT primary mirror is critical to the project. To ensure that the correct optical figure is fabricated, a set of measurement systems with overlapping capabilities has been produced, assuring that the GMT primary mirror segments meet their performance goals and the production schedule [7]. A summary of the different tests is given below in Table 1-1. The suite of tests is designed so each stage of the fabrication is guided by at least one of the tests, and all of the tests together provide a redundant set of verification measurements over all spatial frequencies.

Table 1-1: A summary of the various optical tests for the 8.4-m GMT primary mirror segments to guide the fabrication and verify the final surface figure so that each segment meets the required performance goals [7].

Optical Test	Function	Purpose	Performance
<u>Principal test</u> [9] Interferometry using fold spheres plus a Computer Generated Hologram (CGH)	Measure entire surface to ~2 cm spatial resolution	Guide polishing, qualify finished surface	Low order: correctable with <25 N rms actuator force Higher order: <30 nm rms surface irregularity
<u>Scanning pentaprism measurements</u> [38]	Measure surface errors corresponding to lowest bending modes	Redundant test for low order shape, including Radius of Curvature	Lowest order modes: correctable with <20 N rms actuator force
<u>Laser Tracker Plus</u> [44]	Measure surface with ~50 cm spatial resolution	Guide coarse figuring Redundant test of shape	~1 μm rms 0.25 μm rms goal
<u>Shear test</u> [37] using principal interferometric test	Shift mirror to allow separation of test errors from mirror features	Redundant test of high order figure errors	< 20 nm rms

One traditional method for testing a rough ground aspheric surface is to use an infrared interferometer and a set of null lenses positioned at the center of curvature of the test surface [6, 16]. However, it was decided that infrared interferometry would be impractical for testing the GMT segments. This is discussed further in Section 2.1.

In lieu of using an infrared interferometry system to guide the loose-abrasive grinding phase of the GMT fabrication, it was decided that a laser tracker based system would be used instead. The system is required to measure the low-order aberrations accurately enough that once the segment surface is polished out, the interference fringes can be resolved by the principal optical test. Furthermore, the deviation from the nominal figure must be within capture range of polishing. This would require the surface figure to have a minimum measurement accuracy of about $2\ \mu\text{m}$ rms over the entire surface of the segment. The performance goals for the system are discussed in Section **1.2**.

Because the GMT primary is composed of segments with two different shapes (one on-axis and six off-axis segments), the system needs to work for measuring both types with minimal hardware changes. This is not an issue for a laser tracker, which is fairly insensitive to the geometry of the surface it is measuring. This insensitivity allows the Laser Tracker Plus to measure future mirror surfaces, such as the Large Synoptic Survey Telescope primary and tertiary mirrors [10], in addition to both types of GMT segments.

An additional design goal for the system was to provide corroboration of the principal optical test in its measurements of the low-order aberrations (up through trefoil). This is necessary because the complexity of the principal optical test can produce significant alignment aberrations (particularly defocus, coma, and astigmatism) if the mirror segment and all the individual components of the test are not optimally positioned [30].

1.2 Performance Goals

The design of the Laser Tracker Plus system was driven by a set of performance requirements and goals, which are outlined in Table 1-2. It is difficult to project the ultimate accuracy of the system, so a set of minimum requirements, goals, and ambitious

Table 1-2: Requirements and goals for the Laser Tracker Plus system based on the fabrication requirements for manufacturing the GMT segments [44].

Top-level requirement	Implied requirements
Minimum requirements	
<ol style="list-style-type: none"> 1. Guide figuring to within capture range of principal optical test. 2. Reduce geometry errors (RoC, off-axis distance, clocking) to levels that can be corrected by polishing (~10 μm P-V surface). 	<ol style="list-style-type: none"> 1. Net accuracy of 2 μm rms for first 10-15 Zernike polynomials. 2. Measure distance from tracker to segment to 0.6 mm. <ul style="list-style-type: none"> • equivalent to 1 μm rms defocus 3. Measure physical references at edge of segment to 1 mm. <ul style="list-style-type: none"> • limits focus and astigmatism to ~1 μm rms
Goals	
<ol style="list-style-type: none"> 1. Verify that focus and astigmatism are small enough to be corrected within the 30 N rms force budget for active correction. 2. Determine radius of curvature to 0.5 mm. 3. Determine off-axis distance to 2 mm and clocking angle to 50 arcseconds. 	<ol style="list-style-type: none"> 1. Measure astigmatism accurate to 1 μm rms surface <ul style="list-style-type: none"> • correctable with 12 N rms force 2. Measure defocus accurate to 0.5 μm rms. <ul style="list-style-type: none"> • equivalent to 0.3 mm radius error • correctable with 17 N rms force 3. Measure distance from tracker to segment to 0.3 mm. 4. Measure physical references at edge of segment accurate to 0.5 mm. <ul style="list-style-type: none"> • equivalent to 25 arcseconds clocking
Ambitious goals	
<ol style="list-style-type: none"> 1. Verify that focus, astigmatism and coma are small enough to be corrected within ~half of the 30 N rms force budget. 2. Determine radius of curvature to 0.3 mm. 3. Determine off-axis distance to 1 mm and clocking angle to 50 arcseconds. 	<ol style="list-style-type: none"> 1. Measure astigmatism accurate to 0.5 μm rms surface <ul style="list-style-type: none"> • corresponds to 1 mm change in off-axis distance • correctable with 6 N rms force 2. Measure coma accurate to 0.14 μm rms surface <ul style="list-style-type: none"> • correctable with 20 N rms force 3. Measure defocus accurate to 0.3 μm rms. <ul style="list-style-type: none"> • equivalent to 0.2 mm radius error • corresponds to 0.4 mm change in off-axis distance • correctable with 10 N rms force 4. Measure distance from tracker to segment to 0.2 mm. 5. Measure physical references at edge of segment accurate to 0.5 mm. <ul style="list-style-type: none"> • Equivalent to 25 arcseconds clocking, leaving room for astigmatism that looks like clocking.

goals were established. The requirements and goals are related to the manufacturing specifications for the GMT segments [6]. The segment specifications include tight tolerances on radius of curvature, off-axis distance, and clocking angle, each of which corresponds to a particular low-order aberration or combination of aberrations. For example, an error in off-axis distance is equivalent to a combination of power, astigmatism, and coma in the surface [32]. The segment specification also allows limited amounts of low-order aberrations like astigmatism that can be corrected at the telescope with the active mirror support and realignment of the segment.

1.3 Heritage Measuring Optical Surfaces with Laser Trackers

A laser tracker is a portable coordinate measuring machine. It measures line-of-sight distance and the two angles between the instrument head and a movable target. As the target is moved, the laser tracker uses a feedback system to track the target's motion. To measure a surface, the target is moved across the surface under test and the laser tracker profiles the shape. Laser trackers work almost equally well for measuring any surface geometry, but they do have an optimum orientation that will maximize their accuracy when testing concave optical surfaces. This is because a laser tracker has excellent accuracy and resolution for the line-of-sight distance, as measured with its internal distance measuring interferometer, but the angular measurements are less precise. To minimize its sensitivity to angles, a tracker would ideally be mounted at the center of curvature of the optic it is testing.

The concept of measuring optical surfaces with a laser tracker was pioneered by others at Steward Observatory, but this dissertation builds on that heritage. The first rigorous test of the concept involved the measurement of a 1.8 m spherical mirror with a 10 m radius of curvature. Three different commercial laser trackers were used. All three trackers showed the surface to be accurate to less than 2 μm rms from a perfect sphere when measured from the center of curvature. This shows the trackers were accurate to better than 2 μm rms in this favorable geometry [31]. Further testing with the trackers located within 3 m of the mirror surface showed that their accuracy was not significantly degraded when measuring from this less favorable geometry.

As part of the development for making the GMT segments, a 1.7 m off-axis prototype mirror (approximately a 1/5 scale model of the GMT segment) was made. This mirror is the primary mirror of the New Solar Telescope (NST) at Big Bear Solar Observatory [11]. It was polished with a 30 cm stressed-lap polishing tool similar to the 1.2 m lap that is being used for the GMT segment. It was measured using some of the same techniques used for GMT, including a hybrid reflective-diffractive null corrector (a prototype for the GMT principal test) to compensate for the aspheric departure and allow a full-aperture interferometric measurement.

During testing, the NST mirror remained on the polishing turntable, while the tracker was mounted about 2 m above the mirror on a bridge that was locked in place for each measurement. This arrangement is shown in Figure 1-2 for a different mirror. It was observed, by rotating the mirror to different orientations, that the tracker has systematic errors that appeared as astigmatism in the mirror surface. This may have been related to

the fact that the recommended calibration measurements could not be performed with the tracker mounted over the mirror, due to space constraints. To mitigate this error, two measurements were routinely made, with the mirror rotated 90° between them. This allowed the astigmatism to be characterized and averaged out of the surface measurement data.

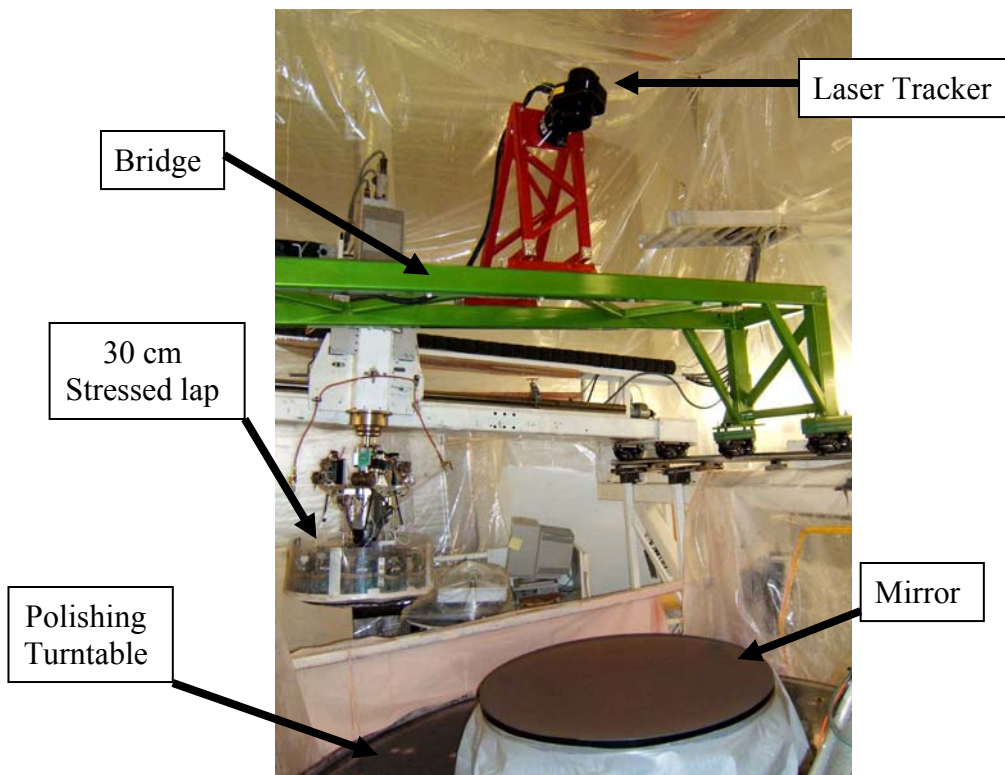


Figure 1-2: Laser tracker mounted ~ 2 m above a 0.95 m mirror for *in situ* testing on the polishing machine. The same arrangement was used for testing the 1.7 m NST mirror [31].

The tracker measurements were used to guide the mirror fabrication from an initial measured error of $14 \mu\text{m}$ rms surface at the beginning of loose-abrasive grinding to a measured error of $0.9 \mu\text{m}$ rms ($0.6 \mu\text{m}$ rms with focus removed) by the start of polishing [31]. Figure 1-3 shows tracker data taken near the beginning and near the end

of loose-abrasive grinding. The astigmatism in the early measurement was repeatable and was gradually reduced through figuring. All measurements include some power, which was treated as a real error to be corrected by figuring. By the end of loose-abrasive grinding, non-repeatable noise contributed 1-2 μm rms to the measured errors. This noise was reduced in the polynomial fits that guided the figuring.

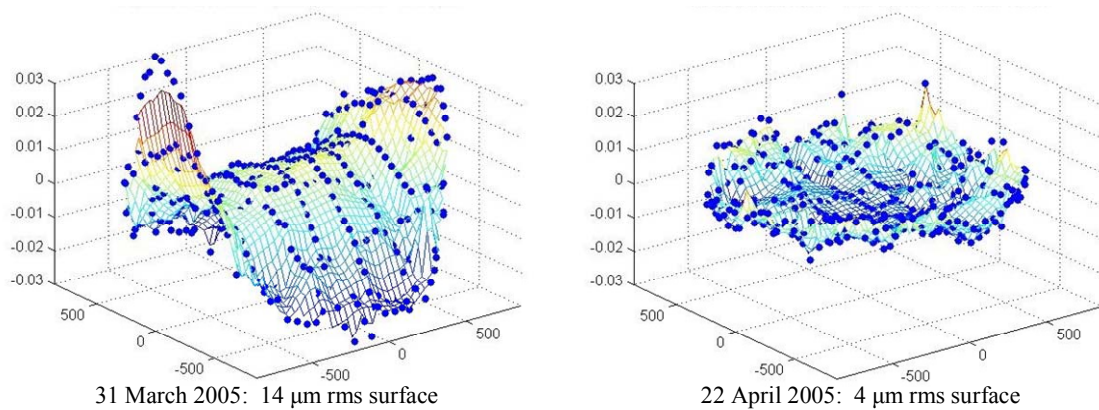


Figure 1-3: Laser tracker measurements of the NST mirror surface near the beginning and near the end of loose-abrasive grinding. The plots show the departure from the ideal off-axis paraboloid, in millimeters, with only piston, tip and tilt removed [31].

The purpose of the tracker measurements was to guide the figuring to an accuracy that would allow optical testing. The first optical measurement easily resolved fringes at 633 nm, and had good agreement to the tracker measurement, as shown in Figure 1-4. This result shows the accuracy of the mirror surface after figuring solely on the basis of laser tracker measurements. Focus, astigmatism and coma were strongly affected by the alignment of the mirror in the optical test. With these aberrations removed, the difference between the optical measurement and the polynomial fit to the tracker measurement was 0.5 μm rms surface [31].

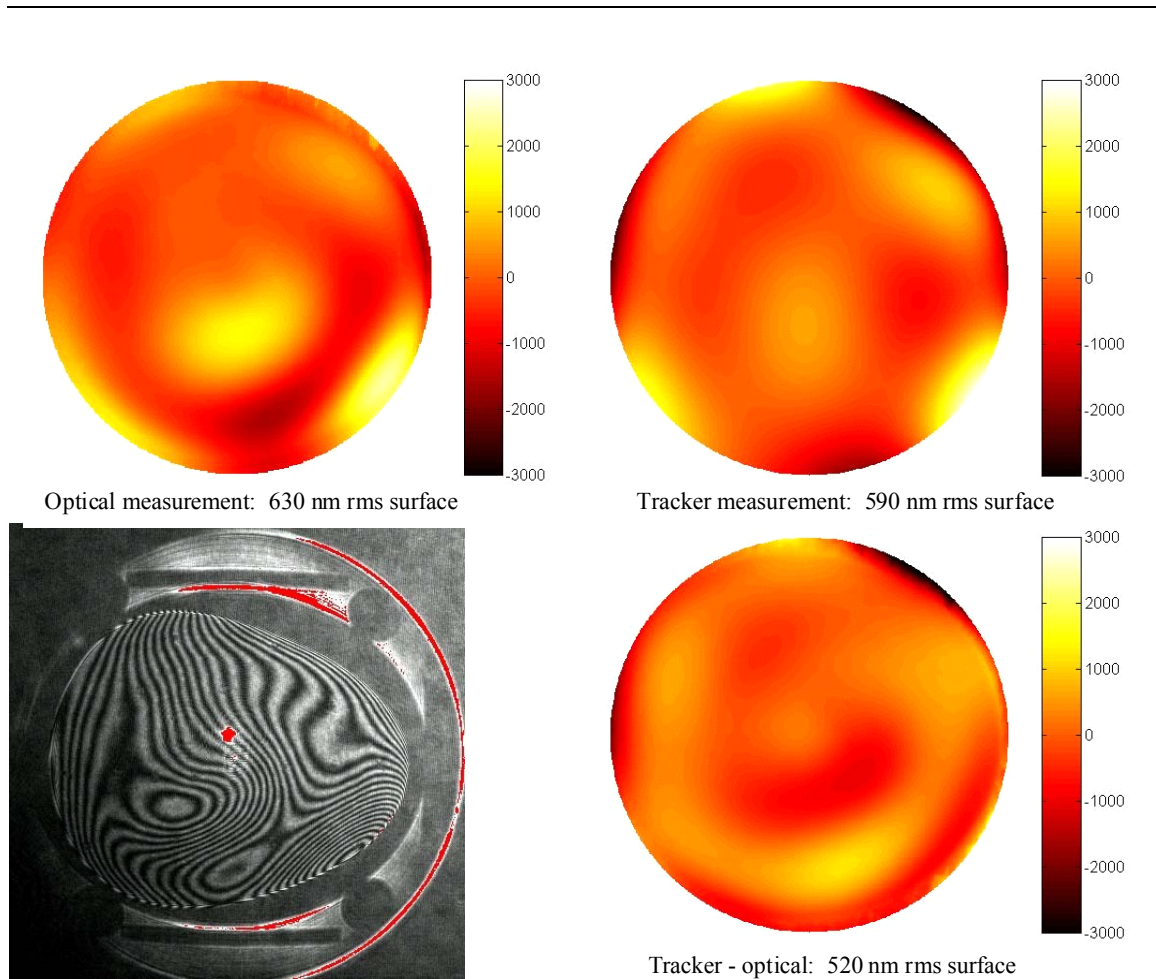


Figure 1-4: Comparison of one of the first optical measurements (two images at left) with laser tracker data taken at the same time (upper right). The difference is shown at lower right. The tracker map is a 6th-degree Zernike polynomial fit to data such as those shown in Figure 1-3. Focus, coma and astigmatism, which depend strongly on the alignment of the mirror in the optical test, were removed from all three maps. Color bars are labeled in nanometers of surface [31].

Unlike the laser tracker measurements of GMT, the laser tracker measurements of NST had a less favorable testing geometry, the target SMR (sphere mounted reflector) had to be positioned by hand, there were no real-time references to correct for rigid-body motions and index fluctuations, nor was a custom calibration of the laser tracker

performed. These improvements were incorporated into the Laser Tracker Plus system for measuring the GMT segment.

1.4 Challenges that Motivate System Design

To achieve the system's operation and performance goals, a number of challenges must be addressed in the design. These challenges include:

- Testing extreme geometry – The testing for GMT requires new methods and hardware due to the off-axis nature of the segment, the very large aspheric departure, and the long radius of curvature [6].
- Non-reflecting surface – Because the system will primarily be used to guide the loose-abrasive grinding phase of fabrication, the surface will be rough ground. Traditional measurement techniques that utilize light incident on specular surfaces will not work since too much of the light will be scattered by the rough surface [26].
- Relative motion – If either the test instrument or the optic under test moves during the measurement, then errors can couple into the surface measurement [12,36].
- Air turbulence – Pockets of warm or cold air moving around within the testing environment can introduce errors into the surface measurements [3].
- Intrinsic systematic errors – Laser trackers have inherent errors which limit their performance and accuracy. A portion of these errors (due to imperfections in system components such as the bearing and encoders or misalignment of the

steering optics and gimbals) are systematic and repeatable. The accuracy can be improved if the repeatable portion of these errors are characterized and backed out using an advanced calibration technique [31,43].

- Instrumental drift –Properties of a measuring instrument may change over time [23].

Chapter 2 provides a detailed discussion of each of these major challenges, including the techniques used to mitigate the errors each produces.

1.5 Basic Design

Multiple measurement technologies were considered and rejected during the initial design phase of this project. A discussion of those technologies follows in Appendix A. Figure 1-5 shows a conceptual drawing of the final system. It combines three measurement subsystems and a fourth positioning system to accurately measure the surface of the mirror during fabrication. The three measurement subsystems are a commercial laser tracker system, along with four distance measuring interferometers (DMI) and four position sensing detectors (PSD), which together form the external reference system that compensates for rigid-body motion and large-scale variations in refractive index. The fourth system is the SMR positioning system, which moves the sphere-mounted retroreflector (SMR) between measurement locations across the surface of the mirror under test. The system is described in greater detail in Chapter 3.

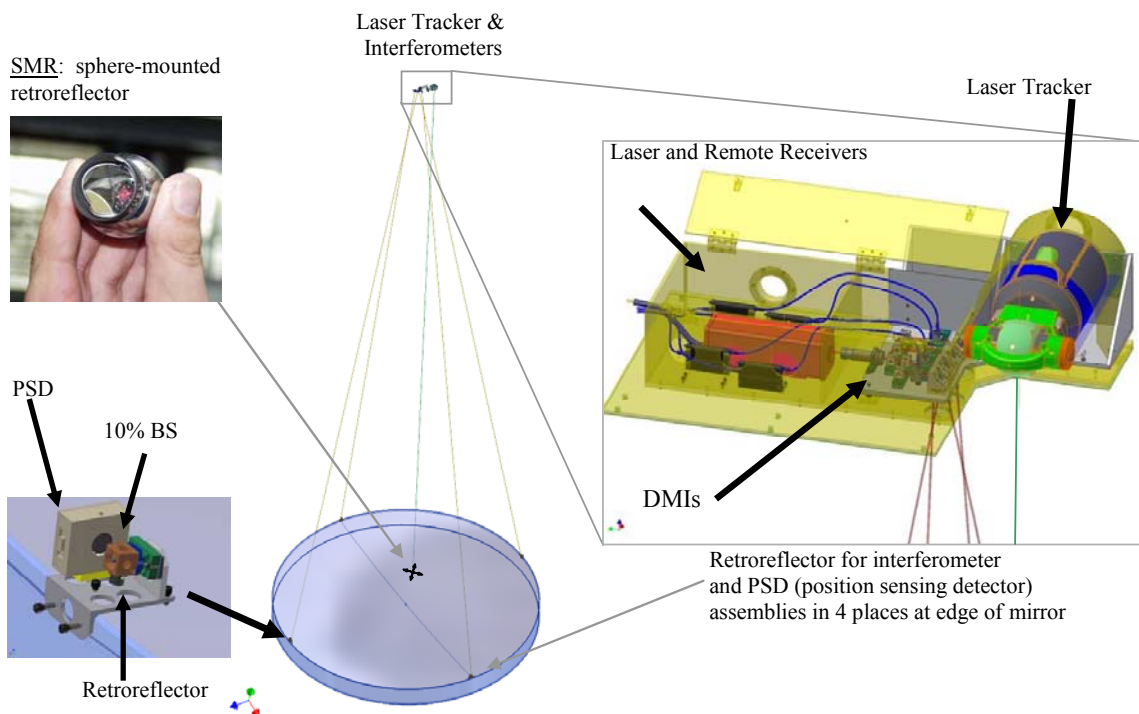


Figure 1-5: Conceptual drawing of the laser tracker set up for measuring the mirror surface. The laser tracker uses interferometry to measure distance to an SMR. The tracker runs under servo control to follow the SMR as it is scanned across the surface, combining radial distance with the gimbal angles to make a three-dimensional measurement. Effects due to the combined motion of the air, mirror, and tracker are mitigated by separate real-time measurements of distance and lateral motion using a system of four stability references [44].

Chapter 4 discusses the details and results of an advanced calibration technique used to improve the laser tracker's measurement accuracy. Chapter 5 discusses the correlation measurements that were performed in the Mirror Lab test tower for determining the nature of the seeing due to air turbulence and other effects. The results from this study provided insight on how best to apply the data from the external reference system for improving the accuracy of the measurements. Chapter 6 discusses the analysis of the data, while Chapter 7 presents some of the measurement results for different

mirrors, along with a comparison of the obtained measurement results to the original performance goals for the system. This dissertation concludes in Chapter **8** with a few closing comments about the study.

Chapter 2

CHALLENGES THAT INFLUENCE SYSTEM DESIGN AND PERFORMANCE

To achieve the operation and performance goals for this system, a number of challenges must be addressed. These challenges are outlined below, along with the system design parameters that were influenced to mitigate their effects.

2.1 Testing Extreme Geometry

Because GMT is the largest and fastest telescope mirror ever attempted, it has an extreme geometry that makes the testing very challenging. New methods and hardware are developed because of the off-axis nature of the segment, the very large aspheric departure, and the long radius of curvature (RoC). The fabrication of GMT could not rely on the Steward Observatory Mirror Laboratory's heritage of building the Large Binocular Telescope (LBT), the world's largest telescope to date, for LBT's on-axis primaries have 1/10 the aspheric departure and about half the RoC of GMT [6]. A rotationally symmetric null system cannot be used as in the past, a single computer generated hologram (CGH) cannot be used because the magnitude of the aspheric departure is so great, and RoC is so great that the center of curvature is beyond the top of the test tower. These issues are shown pictorially in Figure 2-1.

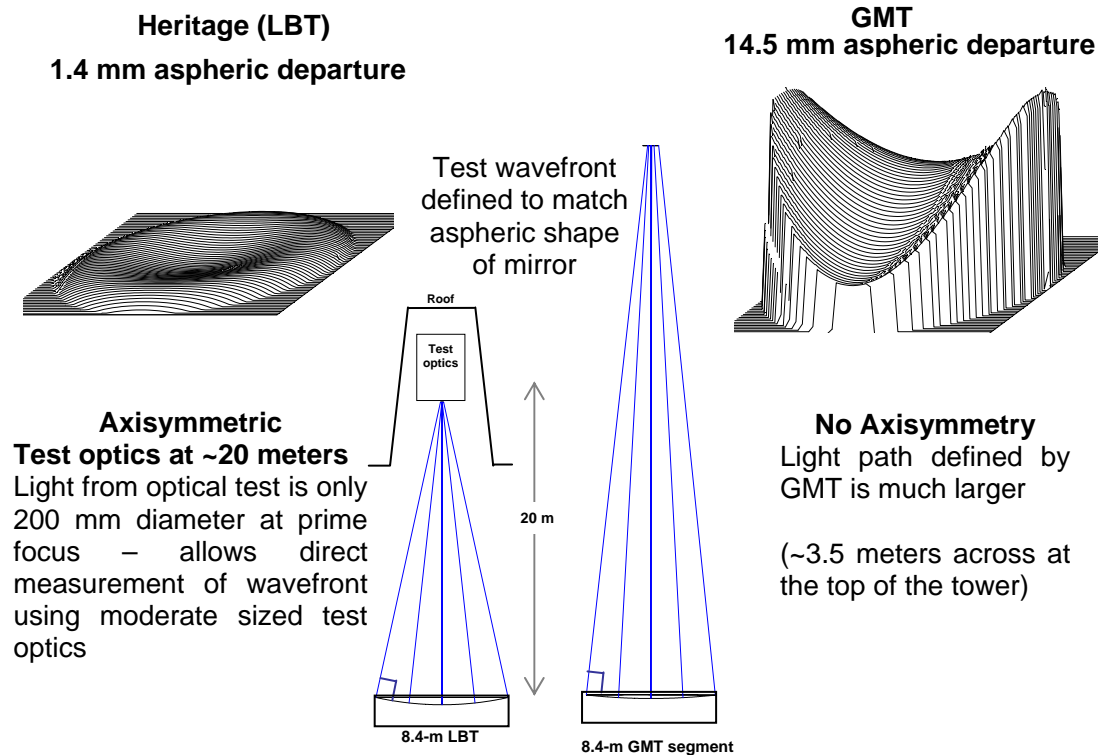


Figure 2-1: The shape measurement of the GMT segments provides several new challenges. The aspheric departure is large and non-axisymmetric, and the long radius of curvature does not allow direct access from within the Mirror Laboratory [6].

To test the GMT segments interferometrically, a hybrid reflective/diffractive null system was developed. This interferometric null test is called the GMT principal test, and it builds on the experience gained fabricating the New Solar Telescope (NST) primary mirror. The optical layout of the GMT principal test is shown in Figure 2-2. Two spherical mirrors fold the optical path to keep it within the confines of the Mirror Laboratory, while also compensating for much of the aspheric departure. A CGH provides the remaining high-order correction required to null the segment wavefront. The null requires alignments tolerances of $\sim 10 \mu\text{m}$ between the CGH and the small fold sphere, and $\sim 100 \mu\text{m}$ between the two fold spheres. The large fold sphere is an active

3.75 m diameter mirror, and its shape must be monitored by an interferometer at its center of curvature (CoC), so that it can be actively corrected by actuators to maintain its nominal shape. As is apparent from Figure 2-2, the principal test is very complicated, and may prove difficult to keep aligned. Furthermore, it can only be used to measure the shape of a polished mirror with less than $\sim 1 \mu\text{m}$ rms irregularity, so it cannot be used to guide the loose-abrasive grinding. For this reason, some other test instrument must be used, something that will work with GMT's extreme geometry.

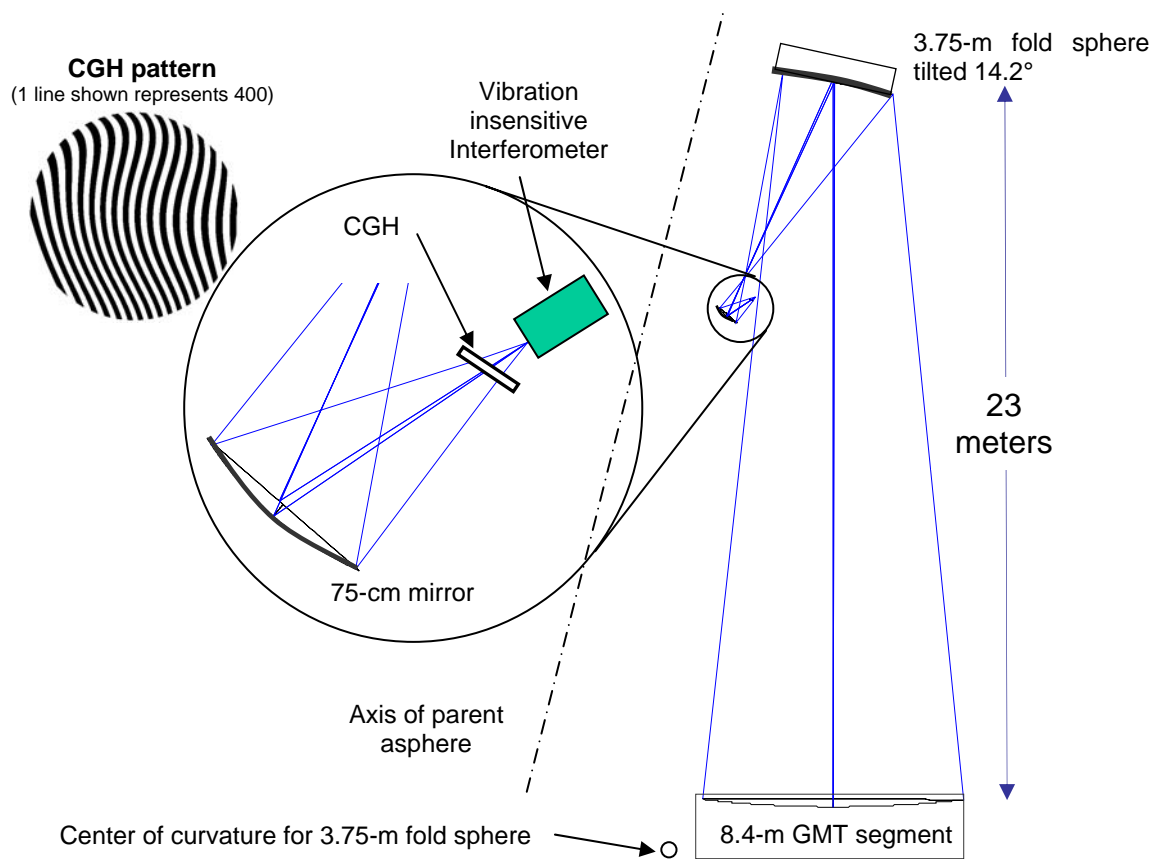


Figure 2-2: Optical layout for the interferometric test for the off axis GMT mirror segment [6].

A laser tracker measures almost equally well for any surface geometry, making it a good choice for profiling the GMT surface. To take advantage of the optimum orientation that maximizes the laser tracker's accuracy by minimizing its sensitivity to angles, the tracker should be mounted at the CoC of the optic it is testing. For the case of GMT, this point is not easily accessible due to its long RoC, so the laser tracker is located as high above the GMT mirror segment as possible, about 1 m below the large fold sphere shown in Figure 2-2. The geometry for this system is shown in Figure 2-3. The angle α describes the deviation of the line of sight from the surface normal, while $\delta\theta$ is the angular error in the laser tracker's measurement of the pointing angle θ . The resulting surface error due to the pointing error is

$$\delta s = r \sin \alpha \delta \theta, \quad (2.1)$$

where r is the radial distance measured by the laser tracker. For a spherical mirror, α can be calculated from

$$\sin \alpha = \frac{R-h}{R} \sin \theta = \frac{R-h}{R} \frac{x}{r}, \quad (2.2)$$

where R is the RoC of the mirror, h is the height of the laser tracker above the mirror, and x is the lateral displacement of the SMR from the mirror center.

Using this, the sensitivity of the surface measurements to angular error in the line of sight of the tracker is

$$\frac{ds}{d\theta} = \frac{R-h}{R} r \sin \theta = \frac{R-h}{R} x. \quad (2.3)$$

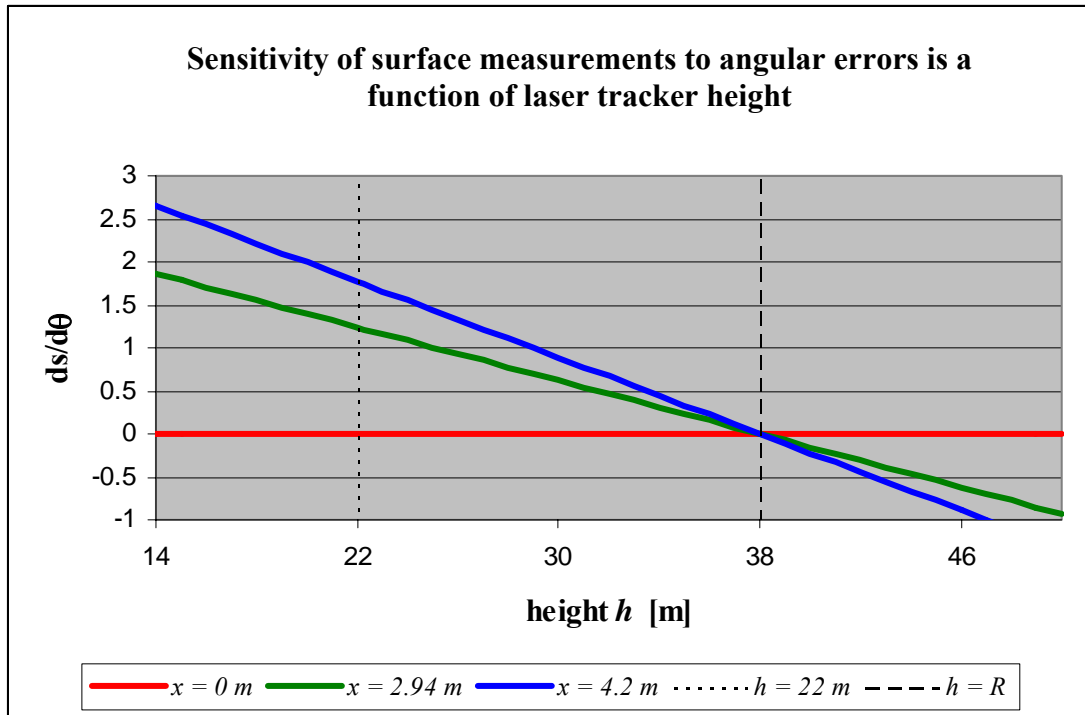


Figure 2-4: Plot showing the sensitivity of the surface measurements to angular errors as a function of laser tracker height above the mirror segment at three radial positions: the center of the mirror, the 70% zone, and the edge of the mirror. If the tracker is at the center of curvature of the mirror (38 m), then it is insensitive to angular errors.

Table 2-1: Geometric parameters for a Laser Tracker Plus measurement of GMT.

Geometric Parameters	For GMT
Height of tracker above mirror (h)	22.3 m
ROC of mirror (R)	38 m
Diameter of mirror (D)	8.4 m
Maximum tracker scan angle (θ_{max})	10.7°
Tracker scan angle at 70% zone (θ_{ave})	7.5°
Maximum deviation of line of sight from surface normal (α_{max})	4.4°
Average deviation of line of sight from surface normal at 70% zone (α_{ave})	3.1°
Maximum sensitivity to angle ($ds/d\theta$)	1.7 $\mu\text{m}/\mu\text{rad}$
Average sensitivity to angle ($ds/d\theta$)	1.2 $\mu\text{m}/\mu\text{rad}$

2.2 Non-reflecting Surface

During manufacturing, a mirror undergoes several distinct fabrication steps. These steps are outlined in Table 2-2. During loose abrasive grinding, the mirror surface will be rough, similar to frosted glass. This roughness causes incident light to be scattered in all directions, preventing most of it from reflecting back to the source. For this reason, visible light interferometers cannot be used during this stage to guide the fabrication.

Table 2-2: Stages of Optical Fabrication.

Stage	Process	Final Surface Figure	Final Surface Roughness
Generation	Diamond Cutting Wheel	~10 $\mu\text{m rms}$	~100 $\mu\text{m rms}$
Loose Abrasive Grinding	Coarse: Silicon carbide grit Sizes 200-50 μm Ceramic lap	~10 $\mu\text{m rms}$	~10 $\mu\text{m rms}$
	Fine: Aluminum oxide grit Sizes 40-5 μm Ceramic lap	~1 $\mu\text{m rms}$	~1 $\mu\text{m rms}$
Polishing	Cerium oxide or rouge polishing compound Sizes 5-1 μm Pitch lap	~100 nm rms	~1 nm rms

The traditional method for guiding the loose abrasive stage of fabrication is performed with an infrared interferometer, which is less sensitive to scattering caused by the rough surfaces. The total integrated scatter for a reflective surface is

$$I_{scat} = (4\pi R_q/\lambda)^2. \quad (2.4)$$

Because the wavelength λ of an infrared interferometer is about 17 times longer than that of a standard visible interferometer, it can work with a 17-times-larger RMS surface roughness R_q .

The technique for using an infrared interferometer was initially considered, but due to the large aspheric departures and long radius of curvature discussed in Section 2.1, it was determined impractical. It would be impractical to null the wavefront adequately without a CGH, and the use of such a CGH in the infrared would require significant development for at least two reasons:

1. The corrected wavefront is very sensitive to wavelength, which is uncertain at a significant level in a 10.6 μm CO₂ laser [30].
2. The CGH would have to be etched into a germanium or zinc-selenide substrate, which is uncommon and would require significant research and development.

A laser tracker, on the other hand, is a good choice of instruments for guiding the loose abrasive grinding stage of fabrication, because it is insensitive to surface roughness, allowing it to be used on rough ground or polished surfaces alike.

2.3 Relative Motion between Test Instrument and Test Surface

One major limitation with using a laser tracker for measuring the surface is that the entire surface cannot be measured at the same time the way an interferometer does. Relative motion of the testing instruments and the optic under test will couple errors into the surface measurement when point-by-point measurements are performed. The

introduced errors will be impossible to back out after the fact unless the relative motion is known for every point. The Laser Tracker Plus system incorporates a system of external references, which are continuously monitored to determine the changes in the relative locations of the mirror and laser tracker. These changes are then used to back out the relative motion component from the laser tracker measurements of the mirror surface by assuming the changes are due to rigid body motions of the mirror. This is illustrated in Figure 2-5.

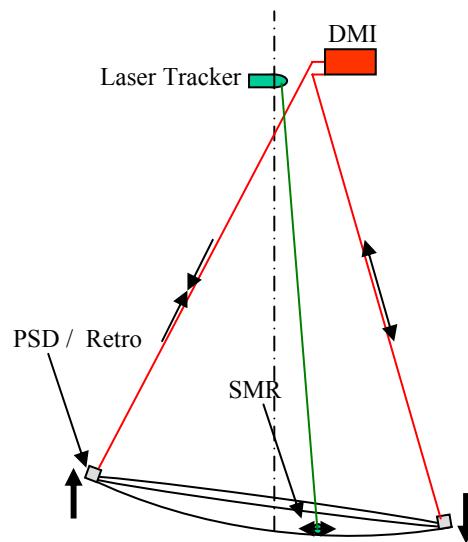


Figure 2-5: The external reference system can be used to compensate for relative motion between the test instruments and the mirror surface, by measuring the changes observed by each reference and fitting those changes with rigid body motion [44].

Examination of the information collected by the DMIs during a typical measurement indicates that one of the largest error contributions that must be corrected from the laser tracker data is due to the weight of the SMR puck (discussed in Section 3.2.3) deflecting the mirror as it moves about the surface. This is visible in the tilt plots in Figure 2-6. The effect this has in the laser tracker data if left uncorrected is to

give the appearance that the mirror surface is flatter at the edge (having a longer RoC) than in reality, resulting in an error in the measured power of the mirror

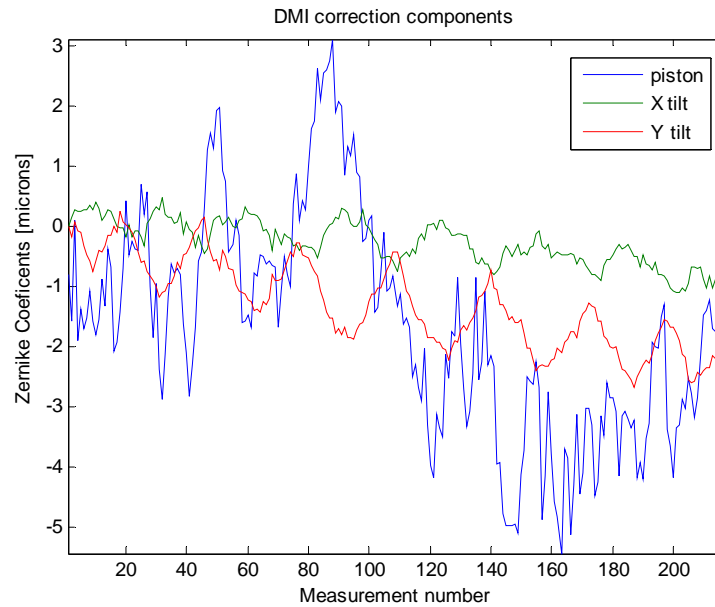


Figure 2-6: Plots of the Zernike coefficient fits to the data collected by the distance measuring interferometers of the external reference system showing the tilt changes of the GMT mirror in both axes as the SMR puck is moved across the surface during a typical surface measurement. The puck follows a truncated 16×16 grid of points, oscillating back and forth across the mirror eight times during a single measurement. This oscillation is visible in the tilt components of the Zernike fit of the data. Table E-1 lists the Zernike polynomials used throughout this dissertation.

2.4 Air Turbulence in the Measurement Path

Air turbulence is another effect that can introduce errors into the surface measurements. Air turbulence is caused by pockets of warm or cold air that are moving around within the testing environment. These air pockets have a slightly different index of refraction from the surrounding air, which results primarily in pointing errors and, to a lesser extent, errors in the optical path measurement, as illustrated in Figure 2-7.

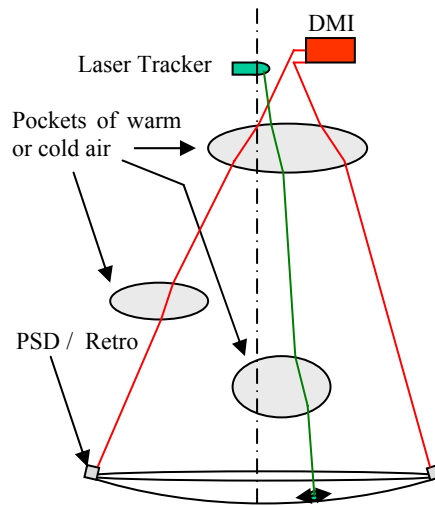


Figure 2-7: The external reference system can be used to compensate for some air effects such as low-order turbulence [44].

The effects of air turbulence can be separated into two categories: low-order and high-order effects. Low-order air turbulence will affect the measurements much the same way that relative motion does, so the external reference system should compensate for it in much the same way that relative motion is compensated. The high-order air turbulence is caused by small scale variations across the testing environment that are not correlated. This will tend to introduce a noise component to the measured values for the laser tracker and each of the external reference arms. By averaging multiple measurements at each of the ~200 positions, measured over time scales longer than that of the air turbulence, the errors introduced by this noise can be reduced to an acceptable level. Analysis and early testing indicated that a measurement integration time on the order of 10 s provides a reasonable amount of noise averaging, while still allowing the entire mirror surface to be measured in about an hour. This subject is discussed further in Chapter 5.

2.5 Systematic Errors Intrinsic to Laser Trackers

Previous surface measurements with a laser tracker showed a strong agreement between the laser tracker and interferometric measurements of the NST primary mirror (discussed in Section 1.3) providing confidence that the proposed method will work for GMT. Measurements made of the NST mirror also showed a component of astigmatism in the surface measurements which did not rotate with the mirror, shown in Figure 2-8. It was decided that this was an error intrinsic to the laser tracker, and that a specialized calibration was needed to identify the magnitude of similar intrinsic errors and back them out of the data.

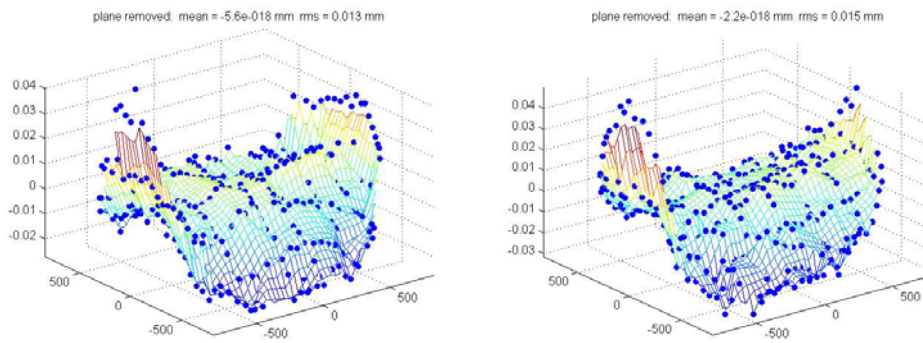


Figure 2-8: Laser tracker measurements of NST show systematic, repeatable errors of about $3\ \mu\text{m}$ rms. The two plots above are NST measurements at two rotation angles, which agree except for $15\ \mu\text{m}$ P-V in 45° component of astigmatism.

A laser tracker's accuracy can be improved by the combination of calibration for systematic errors and averaging for noise. A thorough discussion of the calibration procedure is covered in Chapter 4, which includes two separate techniques for calibrating the radial errors and the angular errors.

2.6 Effects of Instrumental Drift on the Measurement Data

Drift is caused by continual or incremental change over time of numerous physical parameters of the system. Drift is present in all measurements at some level. The plots in Figure 2-9 show an instrumental drift of $10\ \mu\text{m}$ over 5 hours from a Leica LTD 600 laser tracker measured in the laboratory.

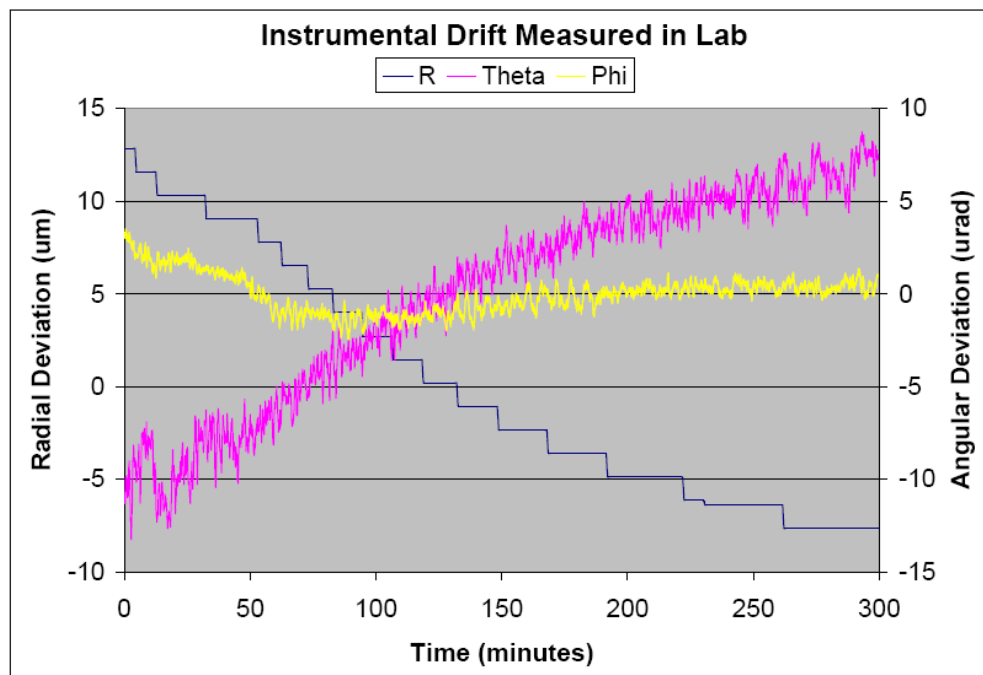


Figure 2-9: Plot of drift data taken with a $\frac{1}{2}$ " SMR mounted on the surface of a test sphere. Measurements were made at a rate of three data points-per-second, and each was an average of 100 measurements-per-point. The radial value changed over $20\ \mu\text{m}$ during the 5 hour measurement run, while the angular values also showed drift.

Sources of drift may include:

- Changes in temperature, humidity or barometric pressure in the testing area resulting in a refractive index change of the air.
- Temperature changes causing a length change of the test tower or instruments.
- A settling of the mirror support system in the mirror cell.

- A change of the lasing wavelength of either the laser in the laser tracker or the distance measuring interferometer.

The external reference system will correct much of the systematic drift. Some of the remaining drift may be identified and then removed from the measurement data by examining its variations with time.

Chapter 3

SYSTEM DETAILS

The Laser Tracker Plus system is composed of several subsystems. These include the laser tracker itself, the external reference system, the SMR Positioning system and the SMR puck, along with the control elements such as software and data acquisition electronics. The mechanics and electronics for the SMR Positioning system and SMR pucks were designed by other engineers at Steward Observatory, but I developed the control algorithms and adjusted the mechanics to get the system to operate reliably. Another Steward engineer wrote all the control software based on software requirements, user interface specifications, and control algorithms I provided. The details of these subsystems are described in this chapter.

3.1 Laser Tracker

Laser trackers have been around for many years, with their main application in the automotive and aerospace industries. Most applications for commercial laser trackers require accuracy of around 25 μm ; however, an accuracy of 1 μm rms is needed to meet the performance goals discussed in Section 1.2. This is possible because the measurement of relative distance is intrinsically accurate to better than 1 μm . To achieve it in practice, a survey of available commercial laser trackers was first performed to evaluate and pick the laser tracker with the best base performance. Next, an advanced

calibration technique was performed to identify any intrinsic errors in the laser tracker, to characterize the repeatable portion of the errors, and to provide a software correction to improve the final measurement accuracy. Finally, the laser tracker is coupled with an external reference system to compensate for errors introduced by rigid-body motion and large-scale variations in refractive index of the air.

3.1.1 Fundamental Working of a Laser Tracker

A laser tracker is a portable coordinate measuring machine that works by measuring the distance and two angles between a sphere mounted retroreflector (SMR) and the laser tracker head (see Figure 3-1). A distance measuring interferometer (DMI) calculates the radial distance r , while a pair of motorized steering mirrors with encoders measures the two orthogonal angles θ and ϕ . From these three measurements, the SMR's

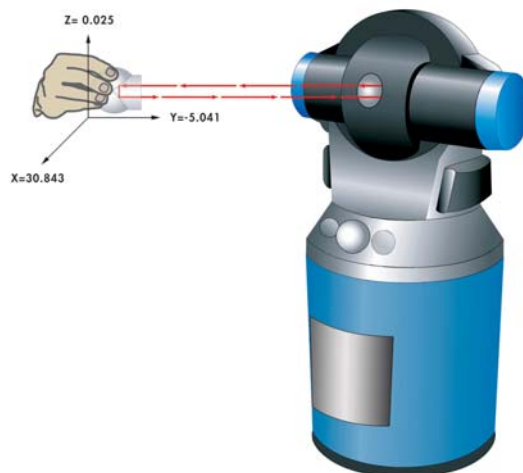


Figure 3-1: A laser tracker measures the location of an SMR in three dimensions and tracks the relative motion. It can display the measured values in a variety of coordinate systems including spherical (r , θ , ϕ), cylindrical (ρ , θ , z), and Cartesian (x , y , z). Copyright © 2006 FARO Technologies Inc. All Rights Reserved [14].

location is determined in the laser tracker's spherical polar coordinate system. A feedback system within the laser tracker automatically rotates the steering mirrors to track the SMR as it moves between measurement locations. The internal components of a laser tracker are illustrated in Figure 3-2.

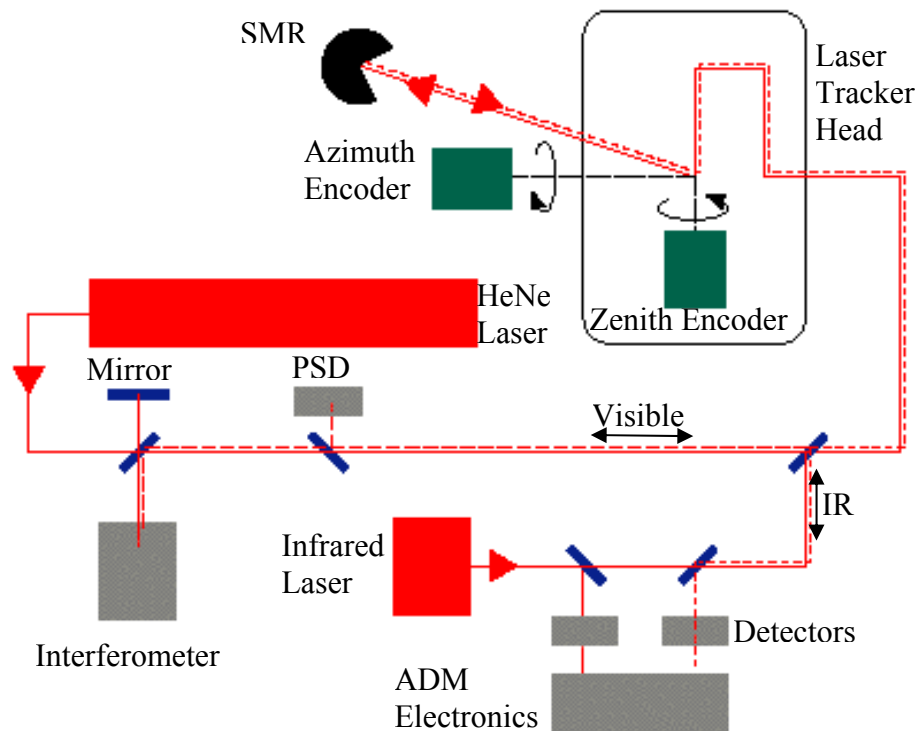


Figure 3-2: Schematic representation of the internal workings of a laser tracker.

The laser tracker measures the radial distance r one of two ways: Absolute Distance Mode (ADM), or relative distance mode – typically referred to as Interferometric Mode (IFM). In ADM, the laser tracker uses a modulated infrared laser to calculate the radial distance r between the laser tracker head and the SMR by using time-of-flight measurements. This method is less accurate than IFM, but does not require a known starting point to calculate the radial distance. With IFM, the laser tracker uses

its internal displacement measuring interferometer (DMI) to calculate the distance that the SMR moves from a known location to its current location by counting interference fringes [4]. DMIs are accurate to about 1 nm or 1 ppb [36]. While this method tends to be more accurate, the SMR must be moved from the known location – for instance the “home nest” – to the measurement point without breaking the beam. If the laser beam between the laser tracker and the SMR is “broken”, then the SMR will have to be re-homed to reestablish the radial distance. This is the main limitation with using IFM: it can only be done if one SMR is moved from point to point as opposed to measuring multiple fixed SMRs.

Because a laser beam is used to calculate the radial distance r between the laser tracker and the SMR, the refractive index of the air n through which the laser beam is propagating must be accurately known, as well as the wavelength of the laser light λ . Changes in either λ or n that are not correctly accounted for will result in an error in the radial measurement Δr . The drift in the laser wavelength $\Delta\lambda$ ($\sim 0.001\text{ppm}/24$ hours) is considered small enough to be negligible, so it is not automatically compensated by the laser tracker. The index of the air n is a function of temperature, humidity and barometric pressure in the measurement environment, so the laser tracker has a built in weather station to measure these values and calculate the index n , using the procedure described in Section **6.3.4.2**.

Gradients across the measurement environment can result in both radial and angular measurement error. An extreme example of this is a $1^\circ\text{C}/\text{m}$ gradient, where a temperature change of 1°C will result in a 1 ppm change in the refractive index of air. This gradient will result in a 1 ppm/m radial error and a $1\ \mu\text{rad}/\text{m}$ angular error.

A laser tracker's ability to measure angles is less accurate than its ability to measure the radial distance. The angular accuracy is limited by the tracker's intrinsic measurement accuracy (encoders and internal position sensing detector) and by refraction of the beam due to temperature variations and air turbulence in the measurement environment. The turbulence causes small changes in the refractive index n , resulting in small errors in the measured radial distance r but significant deviations in the laser beam direction. The three dimensional accuracy of measuring the position of the SMR is typically limited by these angular errors. Averaging multiple measurements will mitigate the effect of high-order air turbulence, while the intent of the external reference system is to mitigate the low-order errors. To better understand how these errors couple to the laser tracker measurements, a correlation study was performed, which is discussed in Chapter 5. Repeatable errors in the measurement of angles are reduced by a custom calibration, described in Chapter 4.

3.1.2 Laser Tracker Selection

There are three major manufactures of laser trackers: Automated Precision Inc. (API) [2], Faro Technologies Inc. [14], and Leica Geosystems (owned by Hexagon Metrology) [27]. Each laser tracker model has its strengths and limitations depending upon the desired application. A concise comparison of popular laser tracker models from each company is provided in Table 3-1.

Table 3-1: Comparison of laser tracker models from each of the three major laser tracker manufactures. Performance values are as specified by the manufacturers.

	API Tracker 3 [2]	Faro Xi v2 [14]	Leica LTD 640 [27]
<u>Physical Parameters</u>			
Tracker Head Height	14 inches	21.75 inches	34.5 Inches
Tracker Head Weight	19 lbs	48 lbs	75.2 lbs
<u>Measurement Envelope</u>			
Azimuth	640° ($\pm 320^\circ$)	540° ($\pm 270^\circ$)	470° ($\pm 235^\circ$)
Elevation	+ 80° - 60°	+75° - 50°	$\pm 45^\circ$
Distance (radial)	> 60 meters	0-35 meters	0-40 meters
<u>3D Accuracy</u>			
Accuracy of a Coordinate	$\pm 5 \mu\text{m/m}$	$18.1 \mu\text{m} + 3.0 \mu\text{m/m}$	$\pm 10 \mu\text{m/m}$
<u>DMI (Interferometer) Performance</u>			
Accuracy of DMI	$1 \mu\text{m/m}$	$1.8 \mu\text{m} + 0.4 \mu\text{m/m}$	$\pm 10 \mu\text{m} \pm 0.5 \mu\text{m/m}$
Distance repeatability	$\pm 2.5 \mu\text{m/m}$	$\pm 1 \mu\text{m}$	$\pm 2 \mu\text{m}$
Resolution	$1 \mu\text{m}$	$0.158 \mu\text{m}$	$1.26 \mu\text{m}$
<u>ADM Performance</u>			
Accuracy of ADM	$\pm 15 \mu\text{m}$ or $1.5 \mu\text{m/m}$, (whichever is greater)	$\pm 9.8 \mu\text{m} + 0.4 \mu\text{m/m}$	$\pm 25 \mu\text{m}$ ($\pm 0.1\text{mm}$ @45° elevation)
Distance repeatability	$\pm 25 \mu\text{m}$	$\pm 1 \mu\text{m} + 1 \mu\text{m/m}$	$\pm 12 \mu\text{m}$
Resolution	$1 \mu\text{m}$	$0.5 \mu\text{m}$	$1 \mu\text{m}$
<u>Angular Performance</u>			
Resolution	0.07 arcsec	0.02 arcsec	0.14 arcsec
Repeatability	$2.5 \mu\text{m/m}$	$2 \mu\text{m} + 2 \mu\text{m/m}$	$7.5 \mu\text{m} + 4 \mu\text{m/m}$
Accuracy (Static)	$5 \mu\text{m/m}$	$18 \mu\text{m} + 3 \mu\text{m/m}$	$15 \mu\text{m} + 6 \mu\text{m/m}$

Each manufacturer produces laser tracker models that are capable of measuring in both IFM and ADM modes, while Faro and API additionally produce ADM only models and Leica produces an IFM only model. API produces the smallest and lightest model trackers, but they require firm mounting to maintain their performance due to sensitivity to the vibrations and torque of their own internal motors. The Leica trackers, on the other hand, are the largest and heaviest, but are insensitive to small vibrations, allowing them to free-stand and be easily moved between measurement positions. The Leica laser trackers have the coarsest measurement resolution ($1.3 \mu\text{m}$ in IFM and 0.14 arcsec in

angle), while Faro trackers have the finest measurement resolution (0.16 μm in IFM and 0.02 arcsec in angle). Faro trackers have the shortest advertised measurement range (0-35 meters), while the API tracker has the longest advertised range (>60 meters). API trackers tend to be the lowest priced, while Faro trackers tend to be the most expensive. All of the trackers are designed to measure with accuracies better than 25 μm in ADM. If accurate measurements on the order of 1 μm are desired, special attention must be made to the geometry of the test setup and the limitations of the trackers [8].

After extensive testing and comparison of the various laser tracker options, the Faro Tracker Xi (shown in Figure 3-3) was selected for a number of reasons. These reasons include finer angular and distance resolution, superior measurement repeatability and accuracy, less calibration complexity, and better expected reliability.



Figure 3-3: The Faro Xi v2 laser tracker [14].

To achieve the measurement goals of sub-micron surface measurement accuracy, the selected laser tracker would need to have sub-micron measurement resolution. This eliminated the Leica laser tracker because the best distance measuring resolution available at the time was 1.26 μm . For this reason, the choice of laser tracker was limited to either a Faro or an API, both of which have sub-micron distance resolution.

A head-to-head test was performed to compare the API Tracker 3 with the Faro Xi v2 laser tracker. Eight targets ($\frac{1}{2}$ inch SMRs) were measured over a volume spanning a horizontal separation of about 12 m and a vertical separation of about 6 m, which is comparable to the volume involved for the alignment measurements of the GMT principal test. For some tests, the set of eight targets were measured from the tracker at two locations, separated by 10 m. The two sets of target coordinates were compared after a best-fit coordinate transformation was performed. This comparison was made for three different measurement modes: absolute distance mode, using both single-face and two-face measurements, and interferometer mode in single-face. In the two-face measurements, the target is measured in the standard (frontsight) method, and again in backsight method with the azimuth rotated 180° and zenith taken to its supplement, and the results are averaged. In other tests, measurements in two different modes were compared, with the tracker at a single location. Table 3-2 lists results of several comparison measurements between the Faro and API laser trackers. In order to evaluate the effects of air turbulence, measurements were made with the lab air handling system on (most results in Table 3-2) and off (labeled AH off in Table 3-2).

Table 3-2: Results of the head-to-head test performed to compare the API Tracker 3 with the Faro Xi v2 laser tracker.

comparison	rms displacement (3D, in mm)	
	Faro	API
IFM v ADM 1-face	0.036	1.1
IFM v ADM 2-face	0.088	1.1
ADM 1-face v ADM 2-face	0.095	0.040
2 tracker locations in IFM	0.096	could not measure
2 tracker locations in ADM 1-face	0.074	0.056
2 tracker locations in ADM 2-face	0.040	0.036
2 locations in ADM 1-face, AH off	0.11	0.10
2 locations in ADM 2-face, AH off	0.040	0.080

The first API tracker we evaluated was unreliable and the tests were not meaningful. A second round of tests was made with another API tracker, operated by a company representative. These are the results listed in Table 3-2. The second API tracker and the Faro tracker had similar accuracy in most cases. The other cases, including IFM measurements, the API tracker gave mysteriously large errors. In still other cases the API tracker failed to measure at all. The general conclusion from these tests was that the better reliability of the Faro tracker outweighs any difference in accuracy.

3.1.3 Sphere Mounted Retroreflector Influences

An SMR is a stainless steel tooling ball that has been bored out and a retroreflecting mirror assembly installed such that the mirror vertex is coincident with the ball's center. SMRs, shown in Figure 3-4, are available from a number of manufactures in three standard sizes: 1 ½ inch, ¾ inch, and ½ inch. SMRs are precision made: they are highly spherical for accuracy, have a grade 25 finish so they are smooth, and made out of 440C stainless steel so that they are both magnetic and corrosion resistant. The centering error of the retroreflector affects the laser tracker measurement accuracy, and for this reason, the SMRs are available in higher grades of centering for higher cost. Typical grades of centering accuracy are ± 0.0005 inch ($\pm 12.5 \mu\text{m}$), ± 0.00025 inch ($\pm 6.4 \mu\text{m}$), and ± 0.0001 inch ($\pm 2.5 \mu\text{m}$). This centering error is broken down between X-Y runout radius error (lateral offset of the mirror vertex to the ball's center) and depth error (vertical offset of the mirror vertex to the ball's center).



Figure 3-4: Sphere mounted retroreflectors are available from a number of manufactures in three standard sizes: 1 ½ inch, ¾ inch, and ½ inch.

Each SMR is measured at the factory and shipped with a certificate of calibration which lists the individual measured values and the specification for each performance parameter. The specification of the SMR that is used for Laser Tracker Plus measurements is listed in Table 3-3. Errors in the ball diameter are compensated for in software. There is no reported runout error in the mirror centering, so rotational orientation of the SMR about the line of sight does not need to be maintained during a measurement. Since the SMR's retroreflector is pointed roughly normal to the surface at all times, the depth error couples to the line-of-sight deviation α across the mirror, listed in Table 2-1, to result in a maximum error at the edge of 0.14 μm P-V, with an average error of 0.1 μm P-V across the mirror. This error is not very large, but it is systematic across the mirror, such that it looks like power and will result in an error in the measurement of RoC.

Table 3-3: Performance of the SMR used for Laser Tracker Plus measurements, as measured by the manufacture and reported in the provided certificate of calibration.

CERTIFICATE OF CALIBRATION			
Date of calibration:	9/22/2007		
Size of SMR:	1.5 inch		
Manufacturer:	Faro Technologies		
Serial number:	7369B		
PERFORMANCE	VALUE	UNIT	FROM/TO SPEC.
Ball diameter for 1.5 inch SMR	1.50010	inch	1.49990/1.50010
SMR X-Y runout radius	0.00000	inch	0.00000/0.00050
SMR depth error for 1.5 inch SMR	0.00007	inch	-0.00050/0.00050

3.2 External Reference System

The purpose of the external reference system is to correct for changes that affect the measurement accuracy over the time period it takes to measure the entire mirror surface. The external reference system is used to correct for drift in the measurement environment, dimensional changes of the test tower, and sagging of the mirror supports. It turns out that a significant error that couples into the laser tracker measurements is a slight tilting of the mirror in its cell (visible in Figure 2-4) caused by the weight of the SMR and puck being moved to different positions across the surface of the mirror. This effect giving the appearance of negative power because the edge of the mirror tilts down as the puck approaches it, causing the edge to appear artificially lower. Each of these effects if left uncorrected will limit the accuracy of the surface measurements.

Because a laser tracker measures both radial distance and angles, the external reference system is designed to compensate for both types of errors. A set of four distance measuring interferometers monitor radial fluctuation between the Laser Tracker Plus instrument assembly mounted in the SOML test tower (see Figure 3-5), and the surface reference (see Figure 3-6) mounted on the mirror segment being tested. Each surface reference is aligned to one of the four DMI laser beams, so that the laser light retroreflects back to the interferometer.

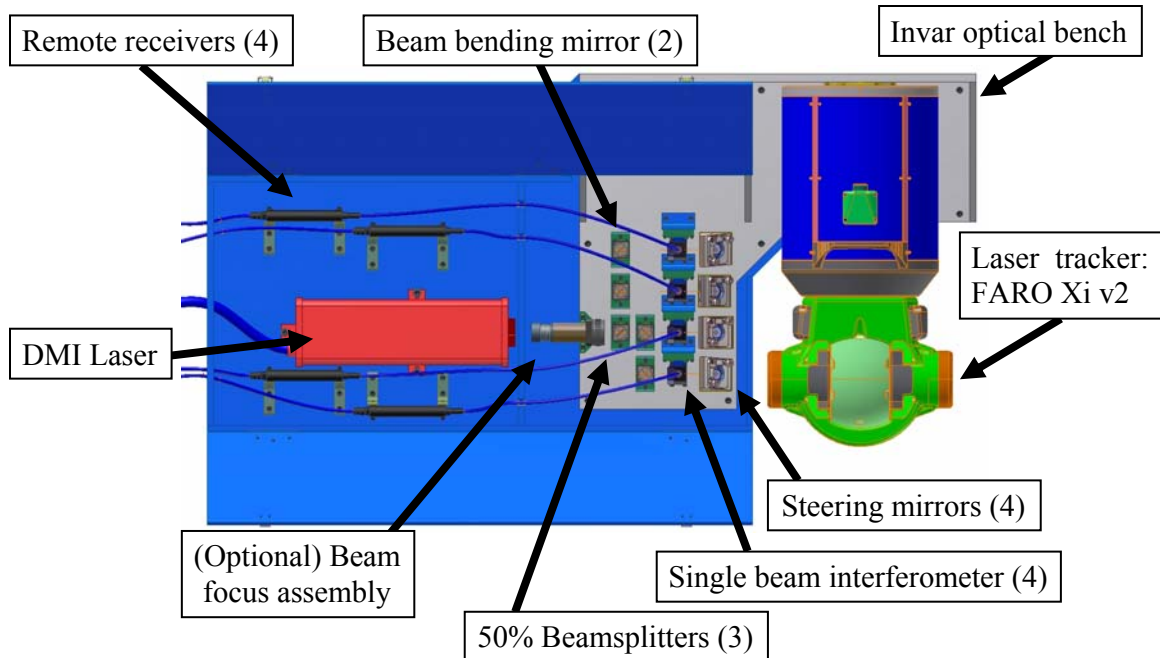


Figure 3-5: The Laser Tracker Plus instrument assembly mounted on the bridge crane at the top of the SOML test tower. The assembly is composed of the laser tracker head and the DMI system's optics, laser head, and remote receivers. Because of the heat generated by the laser head and remote receivers, they are mounted in a separate ventilated compartment from the DMI optics [44].

Each surface reference contains a retroreflector, a beamsplitter, and a position sensing detector (PSD), show schematically in Figure 3-7. The retroreflector is required to complete the DMI's measurement beam, which is used for monitoring the radial changes in each of the reference beams. The beamsplitter diverts 10% of the laser light through an interference filter to the PSD, which is used for monitoring the angular changes of the reference beams. The filter allows the laser light to pass through while blocking the ambient room light to improve the accuracy of the PSD measurements. The PSDs actually measure the lateral motion of the reference beam, but combined with the radial distance, the angular motion can be calculated.

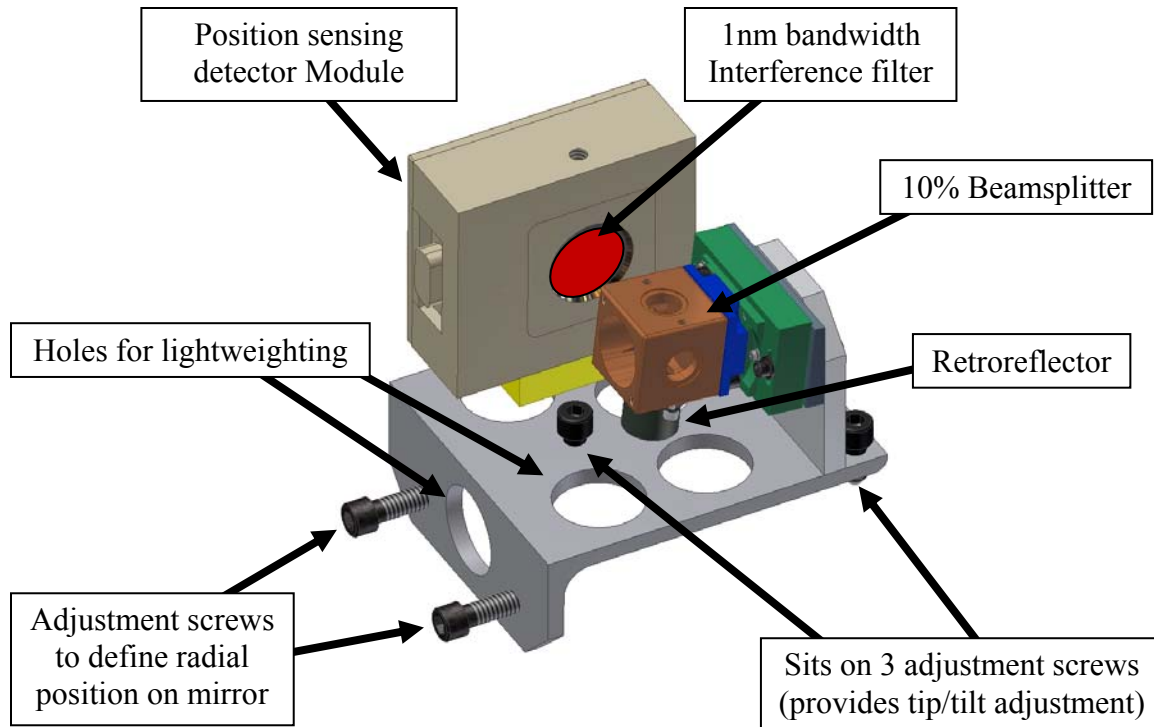


Figure 3-6: Diagram of one of the four surface references that sit at the four compass points around the circumference of the test mirror and are aligned to each of the four DMI laser beams. The majority of the DMI laser light passes straight through the beamsplitter to a retroreflector and back to the interferometer for monitoring the radial fluctuations of the reference beam during mirror testing. The beamsplitter reflects 10% of the DMI laser light to a PSD for monitoring the angular changes of the reference beam. An interference filter is used to pass the laser light to the PSD while blocking ambient room light [44].

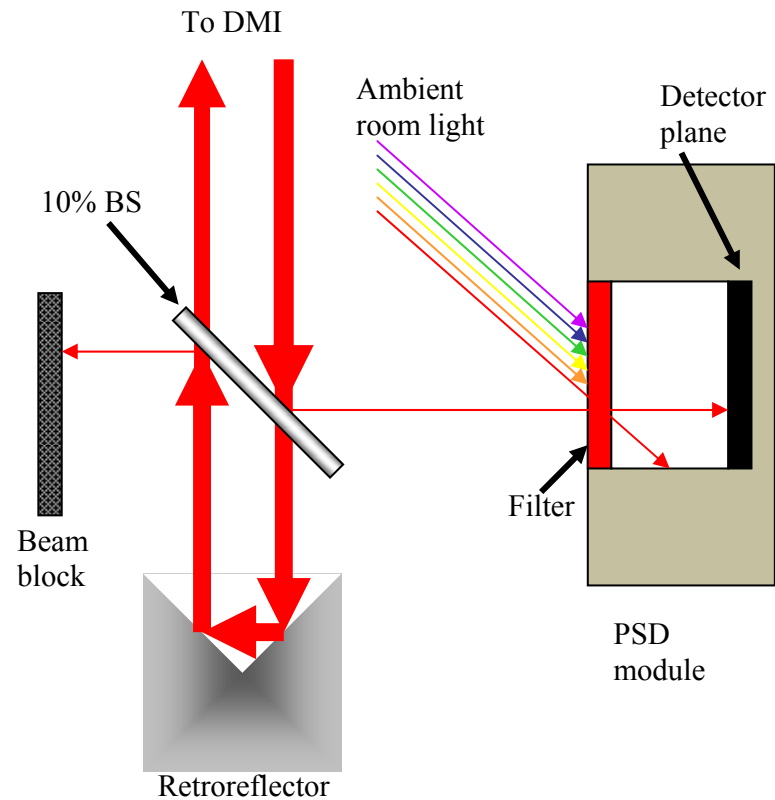


Figure 3-7: Schematic representation of the light path through each surface reference.

3.2.1 Distance Measuring Interferometer System

The DMI system has four separate measurement beams, each with a dedicated single beam interferometer, all powered by a single heterodyne laser head. A series of beam splitters and steering mirrors distribute the laser light through each of the interferometers, then down to the retroreflectors at the surface of the mirror segment under test, shown schematically in Figure 3-8. The light from each interferometer measurement beam is retroreflected back to the interferometer where it interferes with the reference beam at the receiver, allowing the displacement of the retroreflector to be

measured. The DMI system provides information about changes in the measuring environment that may affect the laser tracker's radial measurement accuracy.

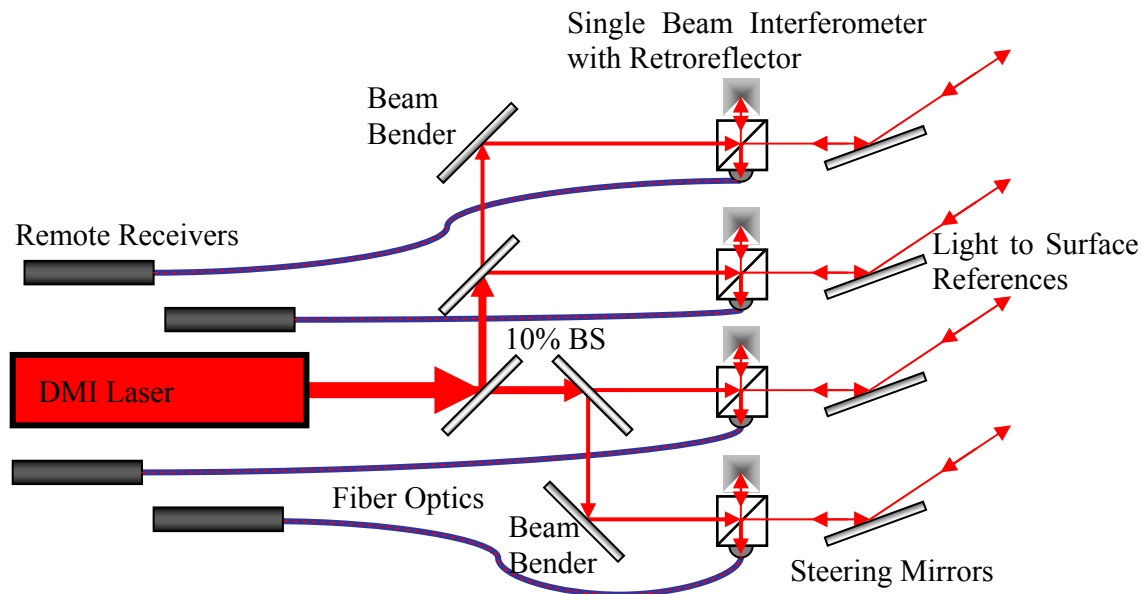


Figure 3-8: Schematic representation of the light distribution to each distance measuring interferometer beam. A more detailed drawing of the light path within the single beam interferometers is provided in Figure B-4.

A DMI generates optical fringes when relative movement occurs between the measurement optics of the system. Each fringe generated represents displacement by one-half of the laser's wavelength in air λ . For the laser used in the Laser Tracker Plus system, $\lambda_0 = 0.63299137$ microns is the vacuum wavelength, which is related to the wavelength in air by $\lambda = \lambda_0/n$, where n is the index of refraction of the air. The resolution of the DMI system used in the Laser Tracker Plus system is electronically extended beyond $\lambda/2$ to $\lambda/64$. Each count in the digital output represents a displacement $\Delta s = \lambda/64$. In a reading of C counts, the displacement is

$$\Delta s = C \frac{\lambda}{64} = C \frac{\lambda_0}{64n}. \quad (3.1)$$

The DMIs in the external reference system have a deadpath distance of over 22 m. The deadpath distance is the difference in the optical path lengths of the reference and measurement arms of the system when the measurement is initiated. A change in refractive index causes an apparent displacement due to the large deadpath. The measured displacement must be compensated for the change in the index. This compensation is based on measurements of air temperature, barometric pressure, and relative humidity. The deadpath distance is approximated to be the radial distance measured by the laser tracker to the surface reference. Measuring the deadpath distance to an accuracy of 1% reduces the displacement error by a factor of 100, which is adequate.

Figure 3-9 shows the displacement error that results from not compensating for the index change. The error of $4\ \mu\text{m}$ over the 22 m deadpath is the result of an index change $\Delta n = 1.8 \times 10^{-7}$, corresponding to a temperature change of $\Delta T = 0.19\ \text{K}$

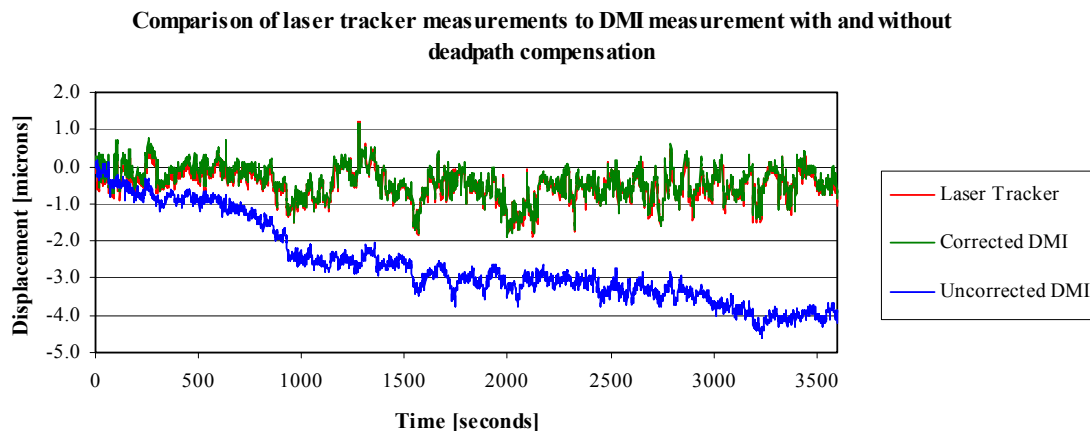


Figure 3-9: Plot shows the error that results by not compensating for the deadpath in the distance measuring interferometer measurements. The red curve is the fluctuations measured by the laser tracker during 1 hour of staring. The green and blue curves are measurements from a DMI during the same time period, where the deadpath length was compensated in the green curve, while it was not in the blue curve.

The Laser Tracker Plus system is designed to exploit this error and use it to compensate for error in the laser tracker measurements. The assumption being that the laser tracker has a similar length deadpath, and therefore suffers the same errors that the DMIs do as a result of thermal gradients and changing environmental conditions. Table 3-4 list the relative lengths of the deadpaths for the four DMI beams and the length of the laser tracker beam at various positions across the GMT mirror surface. The expression that gives the true displacement change in the DMI readings is

$$\Delta s = C \frac{\lambda_0}{64n} + \left(\frac{n_0}{n} - 1 \right) D, \quad (3.2)$$

where D is the deadpath distance measured in microns and n_0 is the initial index of refraction of the air at the start of the measurement run.

Table 3-4: Relative beam length of the four DMI references compared to the laser tracker beam length at various positions along the GMT mirror surface.

Interferometer beam lengths					Laser tracker distances		
North	South	East	West	Average	Vertex	Edge	70% Zone
22.342 m	22.321 m	22.380 m	22.399 m	22.361 m	22.294 m	22.457 m	22.374 m

The information collected from the DMIs is then used to improve the laser tracker surface measurement data of the mirror segment, as described in Section 6.3.4.3. Table 3-5 lists the individual components that make up the DMI system, while the technical details of the individual components of the DMI system are provided in Appendix B.

Table 3-5: List of components and quantities required for the DMI system used in the Laser Tracker Plus system.

Vendor	Description	P/N	Quantity
Agilent Technologies	5517B laser Head opt. H10	5517B	1
	Laser power supply	10884A	1
	Laser head cable 20 meters	10881C	1
	single beam interferometer	10705A	4
	50% beam splitter	10701A	3
	1 inch cell mount	10710A	11
	Fiber optic pickup adapter	10705A-080	4
	Receiver cable 20m	10880C	4
	Single laser-axis board ISA	10885A	4
	4 board interconnect cable	10885A-004	1
	10885A Manual	10885A-0B2	1
	Retroreflector	10704A	4
Zygo Corporation	7025 10% beam splitter	6191-0138-09	4
Excel Precision Inc.	Receiver w/ 2 meter fiber	1031F	4
Thor Labs	1 inch aluminum mirror	PF10-03-G01	4
	90° cage block mirror mount	KCB1	4

3.2.2 Position Sensing Detector System

A PSD is a lateral effect silicon photodiode that provides an analog output directly proportional to the position of the centroid of a light spot on the detector's active area, allowing simultaneous monitoring of light intensity and position. Four duolateral (two-dimensional) type PSDs were used with the Laser Tracker Plus system. The output signal of this type of PSD is two ± 10 V analog signals indicating the location of the laser beam centroid along each axis of the detector face, and a 0-6 V analog signal indicating the light intensity. The advantage of using a PSD over a discrete element device (such as a CCD) is that PSD have superior position linearity, greater analog resolution, faster

response time, and simpler operating circuits. A disadvantage is that all light incident on the detector contributes to the centroid calculation, including ghost reflections and stray light [33].

The PSD system consists of four Position Sensing Modules, each connected to a Position Sensing Amplifier via a standard serial (50 foot long, male-male DB9) patch cord. Each of the four DMI laser beams (reference beams) ends at a surface reference mounted at one of the four compass points around the circumference of the mirror under test. Each one of these surface references contains a PSD module (see Figure 3-6) that monitors the lateral motion of its reference beam. A portion of the light from the DMI reference beam is diverted to the PSD by a Zygo 7025 10% beamsplitter. The angular motion of the beam can be calculated from the lateral motion measured by its PSD and its distance. These measurements can provide information about changes in the measuring environment that may affect the angular measurement accuracy of the laser tracker, as discussed in Section 6.3.6. Table 3-6 lists the individual components that make up the PSD system. Appendix B contains the technical details of the individual components.

Table 3-6: List of the component and quantities required for the PSD system used in the Laser Tracker Plus system.

Vendor	Description	P/N	Quantity
On-Track Photonics	10mm × 10mm duolateral PSD	PSM2-10	4
	High Sensitivity Position Sensing Amplifier	OT-301 S504	4
National Instruments	Compact FieldPoint Ethernet Interface	cFP-1805	1
	8-Channel, 16-Bit Analog Input Module	cFP-AI-118	1
	4-Channel, 16-Bit Analog Input Module	cFP-AI-110	1
	Compact FieldPoint Connector Block	cFP-CB-1	2
Melles Griot	633nm interference filter	03 FIL 006	4
Server Supply, Inc.	50ft Male-Male DB9 serial extension cable	PCM-2120-50	4

3.2.3 Radiometric Calculations for External Reference System

Radiometric analysis of the system ensured that the selected Agilent laser would have enough power for the reference system. The results are presented in Table 3-7 below. The Agilent laser head had a measured optical output power of 631 μW when it was purchased. This value was then used to investigate the system performance if a 10% beamsplitter diverted laser light from the DMIs to the PSDs.

The calculation in the upper portion of the table tracks the power from the laser through the optical system to determine the minimum input power at the receiver's fiber optic input. The minimum transmittance through each component is listed, along with the appropriate Agilent or Zygo part number where applicable, to determine the power loss through the system. Below this is listed the receiver sensitivity, which is the minimum power required for the receiver to operate. The Excel Precision Model 1031F receiver requires at least 2.2 μW of power to operate, while the expected minimum power through the system is 27 μW when using a 10% beamsplitter. This provides a safety factor of 12 and allows for degradation of the laser and optics over time.

The calculations in the lower portion of the table show the optical power from the laser light that reaches the PSD. Again, the transmittance is shown for each of the components in the optical system to determine the minimum optical power at the PSD. This power is then converted to current to determine the minimum current that will reach the amplifier. To achieve reliable performance from the PSD system, a voltage signal $>1\text{ V}$ is required after amplification; for this reason, the maximum amplifier gain from the On-Trak Photonics OT-301 S504 high gain position sensing amplifier is used in the

calculations. With the gain set at maximum, the resulting voltage achievable is 27 V, demonstrating the amplifier has more than enough gain to meet the requirements.

Table 3-7: Radiometric calculations of the performance of the external reference system when a 10% beamsplitter is used in the surface reference. The upper portion of the table shows the transmittance through the light path from the laser to the input fiber of the DMI system and the resultant minimum optical power. This is compared to the minimum optical power required by the receiver. The lower portion of the table shows the minimum optical power transmitted through the system from the laser to the input of the PSD, and the resulting maximum potential voltage after amplification.

System Components	Optical Power [μ W]	Transmittance (minimum)	Model Number (Agilent unless specified)
DMI OPTICAL CHARACTERISTICS			
Laser	631		5517B
50% BS1		39%	10701A
50% BS2		39%	10701A
Interferometer		59%	10705A
Fold Mirror		90%	
10% BS		82%	Zygo 7025
Retroreflector		86%	10704A
10% BS		82%	Zygo 7025
Fold Mirror		90%	
Power at Fiber Input	26.5		
Minimum Required Power	2.2		
PSD OPTICAL CHARACTERISTICS			
Laser	631		5517B
50% BS1		39%	10701A
50% BS2		39%	10701A
Interferometer		39%	10705A
QWP		99%	
Fold Mirror		90%	
10% BS		8%	Zygo 7025
Filter		50%	
Optical Power at PSD Input	1.33		
PSD ELECTRICAL CHARACTERISTICS			
PSD Sensitivity	0.40 A/W		PSM2-10
PSD Output to Amplifier	0.53 μ A		
Maximum Amplifier Gain	5×10 V/A		
Maximum Amplifier Output	27 V		OT 301 S504
Minimum Required Output	1 V		

3.3 SMR Positioning System

This system, designed by Warren Davison of Steward Observatory, moves an SMR safely across the surface of the mirror via computer control, allowing mirrors up to 8.4 m diameter to be measured without people being on the mirror or its support platform, minimizing changing loads that would cause rigid-body motion. A typical Laser Tracker Plus system measurement consists of a uniform distribution of about 200 samples across the surface of an 8.4 m mirror with about 0.5 m sampling interval.

The 1.5 inch SMR is carried by a puck described in more detail in Section 3.4. The puck is attached to four strings that control its position, as shown in Figure 3-10. The length and tension of each string is controlled by a motorized winch via computer controlled motors. Two stepper motors control the position of the puck on the surface, while two torque motors adjust the string tension via a complex algorithm that reels in the slack and pays out more string as required.

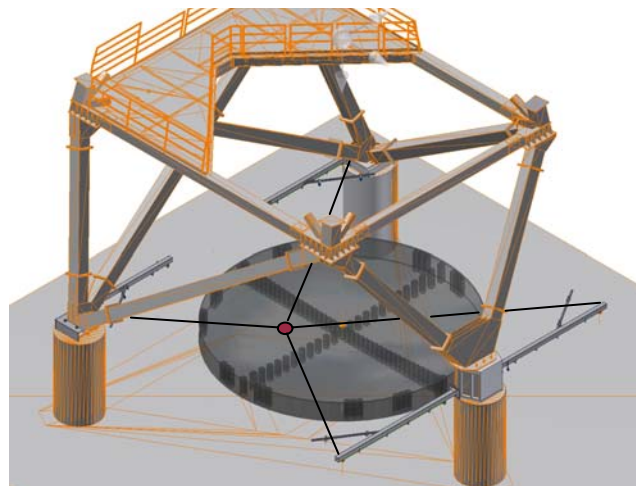


Figure 3-10: Diagram of the SMR positioning system at the base of the test tower. The gray disk represents the mirror under test, while the small circle at the intersection of the four strings is the SMR puck [44].

The winches and associated pulleys that control the string lengths are mounted on steel beams about 3 m above floor level (slightly above the mirror surface) where they can be left permanently without interfering with traffic in the lab (shown in Figure 3-11). Limit switches constrain the range of string positions so they cannot pull the SMR off the mirror or contact the four surface references at the edge of the mirror. The result is a 12 sided figure, as shown in green in Figure 3-12, that restricts the puck's proximity to the edge of the mirror to greater than 200 mm in numerous locations, making sampling near the edge of the mirror difficult.

The SMR follows a pattern programmed into the control computer, pausing at each sample point long enough for the laser tracker and external reference system to make measurements before moving on to the next point. Each measurement position is controlled to an accuracy of a few centimeters. The precise sample locations do not matter because the position is measured by the laser tracker.

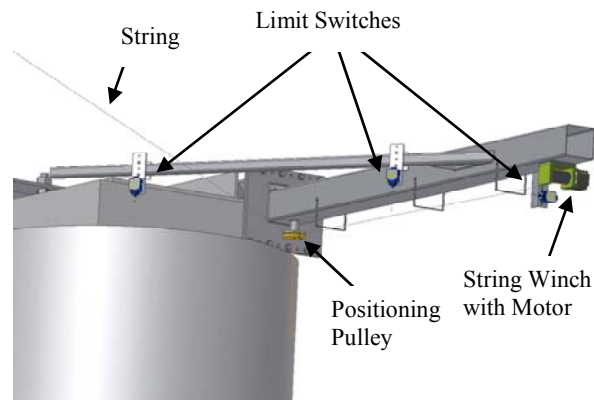


Figure 3-11: A close-up of one of the string control mechanisms [44].

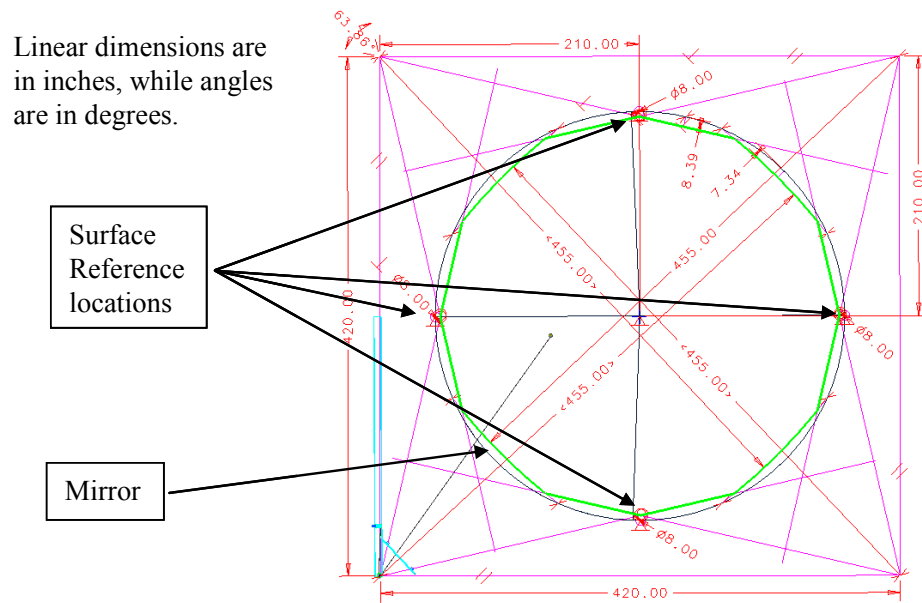


Figure 3-12: Limit switches constrain the range of string positions so they cannot pull the SMR off the mirror or contact the four surface references at the edge of the mirror. The result is a 12 edged figure that restrict the puck's proximity to the edge with the worst limit 8.4 inches and the 12 closest points 3.3 inches.

3.4 SMR Puck

A 1.5 inch SMR, composed of a retroreflecting mirror assembly mounted inside a 1.5 inch stainless steel tooling ball, is used with the SMR Positioning system. Because dragging the steel SMR across the mirror's rough ground surfaces would destroy the accuracy of the SMR and could damage the glass, a puck is used to transport the SMR and provide mutual protection to both the SMR and the glass surface. Two different types of pucks have been developed for the different stages of fabrication:

- A puck made of Teflon and rubber for testing during generation and the early parts of loose abrasive grinding.

- An air puck for testing during the later stages of loose abrasive grinding and for testing a polished surface.

The details of these two different pucks are described in this section.

3.4.1 Teflon Puck

The initial version of the SMR puck uses a durable form of Teflon called Rulon[®] that can slide across the glass surface without significant wear (Figure 3-13). In this version, the SMR is separated from the glass by a thin layer of Teflon, which maintains its thickness (minimal wear against the rough surface) to a small fraction of a micron during the course of a measurement. This version is used to measure the ground surface because it is less sensitive to the tooling marks and roughness of the surface, but it poses a risk of producing scratches if slid across a polished surface.



Figure 3-13: Picture of the Teflon puck resting on the surface of the GMT Segment.

Because the GMT segment is aspheric, the RoC changes significantly across the surface, causing the gap between the SMR and the surface to vary. To minimize the

height errors in the measurements due to this effect, the SMR sits on a smaller inner ring of Teflon (34 mm in diameter), which is sized to limit the error due to the non-constant RoC to less than $0.2\ \mu\text{m}$ across the entire surface. The small size of the inner ring would make the puck susceptible to tipping over, so the puck contains a larger outer ring that provides additional stability and mass. The rings are visible in the images in Figure 3-14.

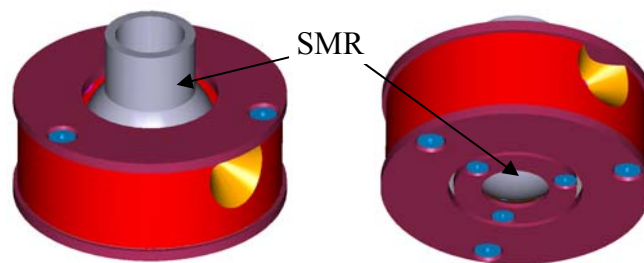


Figure 3-14: Positioning puck for holding SMR (shown in grey) while measuring, viewed from above and below. Note the inner and outer rings visible in the image on the right, which decouples the SMR (sitting on the inner ring) from the varying tensions in the SMR positioning system strings (attached to the outer ring).

The strings from the SMR positioning system attach to the outer ring, where the additional mass minimizes the risk of excessive string tension lifting the puck from the mirror surface, affecting the measurement and potentially damaging the mirror. The inner and outer rings are connected by a flexure that provides the inner ring with enough motion to decouple it from the outer ring so that it will sit flush to the surface to minimize measurement errors. The original flexure design was too stiff to provide adequate decoupling of the inner and outer rings, allowing the string tension to affect the SMR placement on the mirror surface. It allowed for around $100\ \mu\text{m}$ of motion between the inner and outer rings of the puck, but this proved to be inadequate. I modified the design by cutting slits in the flexure to allow more range of motion between the two rings,

allowing the inner ring to sit flush on the mirror surface even if the outer ring was not. The modified flexure can accommodate more than 1 mm of misalignment between the inner and outer rings, making the puck less sensitive to the torque motor settings, which cause the outer ring of the puck to tilt or lift if the string tensions are too high. The modification improved the performance of the puck and eliminated numerous sources of error in the data, decreasing the urgency of switching to the pneumatic puck. The original and modified flexure designs are shown in Figure 3-15.

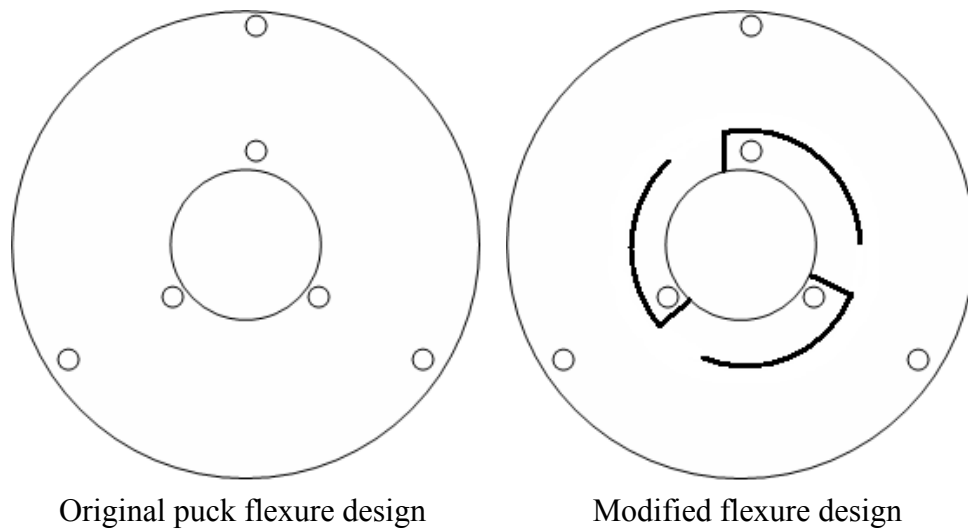


Figure 3-15: The original design for the flexure that connected the inner and outer rings of the Teflon SMR puck is shown on the left.

3.4.2 Air Puck

Tests of the Teflon puck slid across a polished surface showed a risk of scratches if the surface was not absolutely clean. For this reason, a new puck was developed, with three small flexible rubber air bearings, that is used when measuring polished surfaces.

The rubber air bearings have a built-in bellows so that they expand when pressurized, lifting the puck from the surface. Teflon pads (60 mm in diameter) were added to keep the rubber from sticking to the polished glass, and to prevent the puck from getting caught in the 50 mm drain hole at the center of the GMT mirror segment. The underside of the air puck is shown in Figure 3-16.



Figure 3-16: Underside of the air puck showing the three Teflon air pads and the rubber bellows, which lift the puck and the SMR clear of the mirror surface when inflated.

This puck also has the advantage that the SMR rests directly on the glass surface while the tracker data is recorded, as shown in Figure 3-17. Air pressure is applied to lift the puck and SMR a millimeter above the surface while the air bearings remain nearly in contact with the glass. The puck slides to the next position on a cushion of air, and then slowly lowers the SMR to the surface as the air bleeds out.

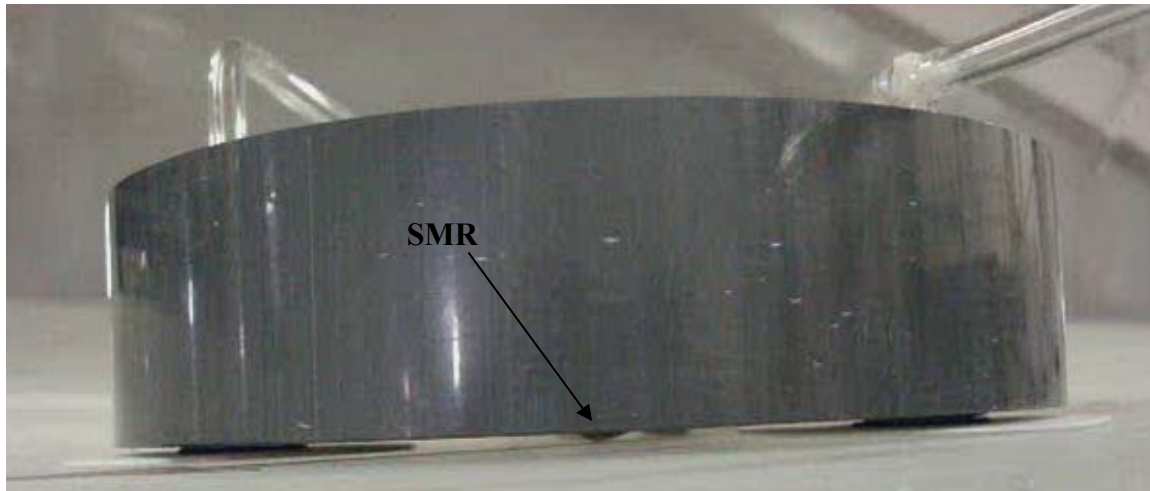


Figure 3-17: Once the air is turned off to the air puck, the bellows deflate, allowing the SMR to sit in direct contact with the glass surface.

One major disadvantage of the air puck over the Teflon puck is that an air line needs to be run to the puck as it moves across the surface. The hose needs to spool out and reel in as the air puck moves across the mirror, without touching the surface to minimize the risk of scratches. To achieve this, a separate hose management system was required, shown in Figure 3-18.

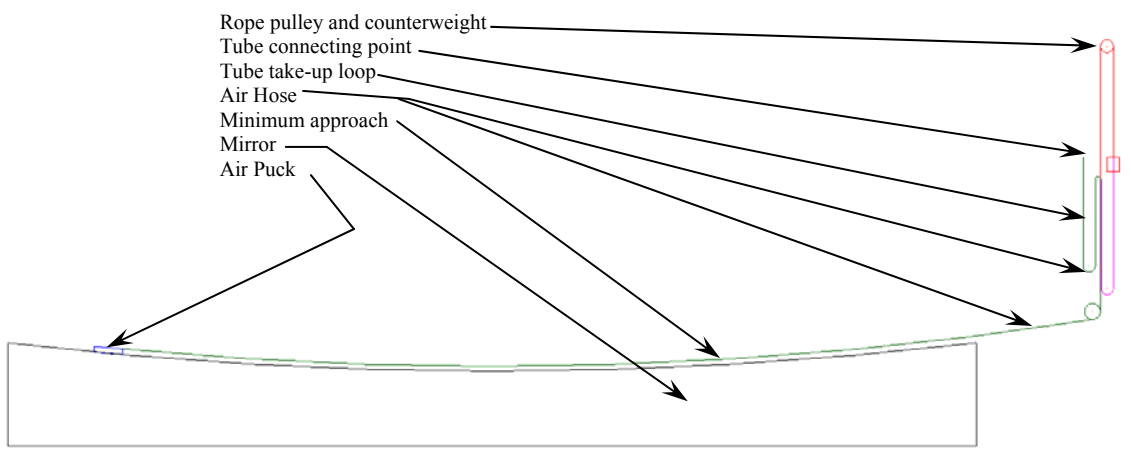


Figure 3-18: Air puck hose management system that uses a set of counterweights to provide a non-uniform tension in the air hose to prevent it from contacting the surface.

The desire is that the hose will pull with only a minimum amount of tension so it will not lift the puck from the surface or pull it away from the desired measurement location. The reality is that, in order to keep the hose from dragging across the mirror surface, the tension in the hose must be higher than desired, causing it to pull considerably against the puck. There is also a strong hysteresis component to the tension on the hose, which can affect system performance differently depending on the direction that the puck is being scanned. Both of these effects were ultimately compensated for in software, but they made the development of a stable torque motor control algorithm for the air puck more difficult than the original algorithm developed for the Teflon puck.

3.5 Control Elements

To get the different subsystems to work together as a complete system, control elements are required to tie together and allow communication between the individual subsystems. Electronic components and computer processors collect and transmit the electronic signals from the individual measurement systems to the master control console, where all the data are combined. Custom software written to control each element of the system provides prompts to synchronize data collection and queue each process at the appropriate time. This section describes the electronic and computer infrastructure that ties all the system subcomponents of the Laser Tracker Plus system together, along with the control software used to operate it.

3.5.1 Electronics

The Laser Tracker Plus system electronics are distributed between three locations: atop the bridge crane, in the interstitial space of the tower, and at floor level. The laser tracker head and the DMI optics, laser, and receivers are all mounted in a compartment on the bridge crane, where they can be moved into position for a Laser Tracker Plus surface measurement, but can be moved out of the way for a principal test measurement. The instrument cluster on the bridge crane also contains a MicroPC that provides diagnostic information to the operator console, including DMI receiver intensities that provides information on the stability and alignment of the DMI reference beams, thermocouple readings that provide information about the temperature changes around the DMI laser and optics, and an electronic signal to indicate the bridge crane is in the proper position for testing. (There is also a blue light on the bridge crane that illuminates when the crane is in the proper position to provide a visual indication as well.)

To minimize the heat load and mass on the bridge crane, much of the required tower electronics were positioned in the interstitial space between the inner environmentally controlled portion of the test tower, where the measurements occur, and the outer shell surrounding the tower. It is a good place to mount support electronics and computer because it is close enough to the test instruments to conveniently run cables, and has its own dedicated air handling system to exhaust the heat load without affecting the temperature in the measurement area. The laser tracker controller and the computer, interferometer measurement boards, and power supplies for the DMIs are located in the interstitial space.

The remainder of the Laser Tracker Plus components are located at the base of the test tower (at floor level), adjacent to the mirror. These components include the master control computer (operator's workstation), the PSD electronics, and the SMR positioning system electronics. An Ethernet network connects the instruments in the test tower with those at floor level. Figure 3-19 shows the electrical layout of the different electronic components that make up the Laser Tracker Plus system.

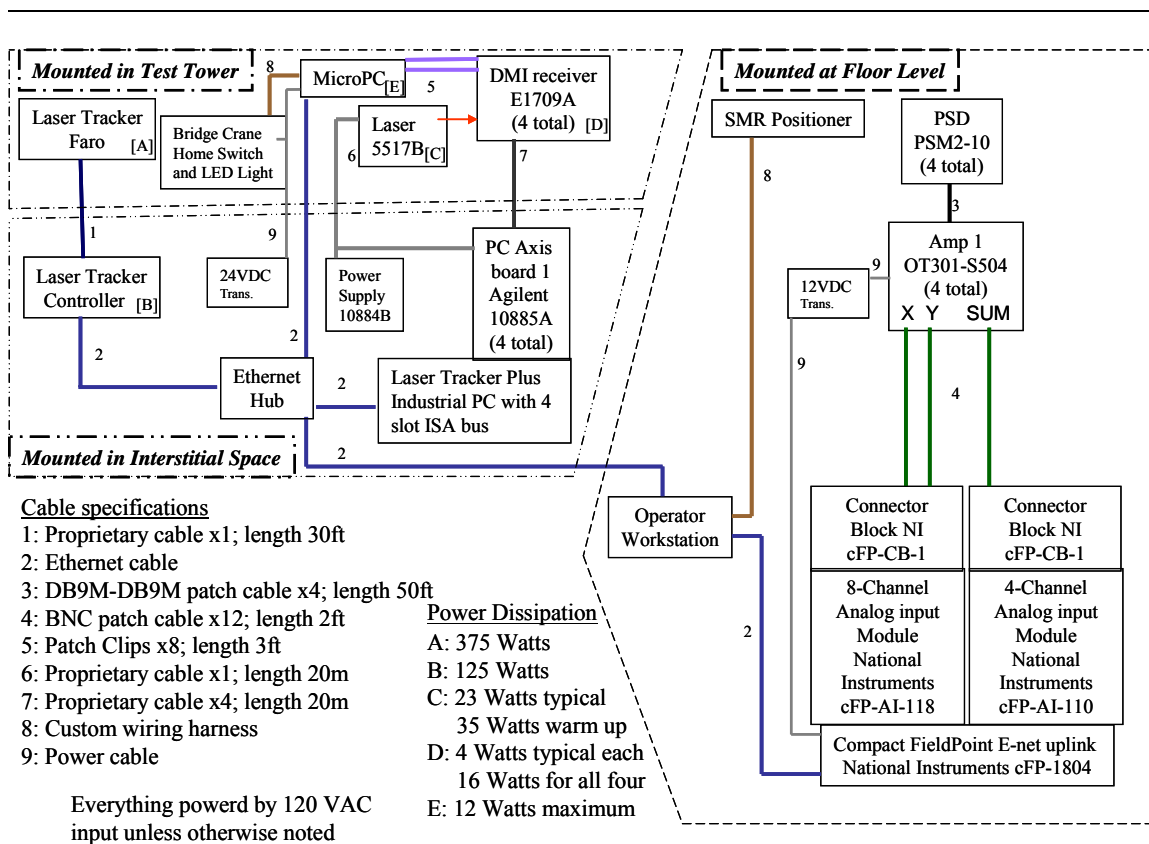


Figure 3-19: Laser Tracker Plus system electrical layout.

Appendix B contains some additional details of the electronic components used, including:

1. The MicroPC system used with the DMI electronics,
2. The amplification circuit used with the thermocouples, and

3. The Compact FieldPoint electronics used with the PSDs.

The details of the SMR positioning electronics are not covered, for that system was designed by another engineer and is beyond the scope of this dissertation; however, the development of the control algorithms for controlling the torque motors is covered in the next section.

3.5.2 Torque Motor Control Algorithms

The SMR positioning system is set up with two stepper motors on the west side of the mirror measurement area, and two torque motors on the east side, as shown in Figure 3-20. The string from each motor attaches to the SMR puck after passing through a pulley mounted in the corners of a square region that is $B = 10.668$ m on a side, with the mirror positioned in the center. Fundamentally, the stepper motors are used to determine the position for the SMR puck, while the torque motors are supposed to maintain tension on the strings. Reality is far more complicated than this.

The amount of force each torque motor must exert on the puck varies drastically depending on where the puck is on the mirror. If the torque is set too high on the west side of the mirror, the puck will be lifted off surface. If the torque value is too low on the east side of the mirror, the torque motors will not be able to pull the puck up the sloped surface to the edge of the mirror. If the puck is on the north or south half of the mirror and one torque motor is pulling too hard compared to the other, one of the stepper motor strings will go slack, preventing the puck from reaching the desired location. For instance, with the puck on the north half of the mirror, if the north torque motor is not

pulling hard enough compared to the south torque motor, the south stepper motor string will go slack, but if it is pulling too hard compared to the south torque motor, the north stepper motor string will go slack. Trying to get the two torque motors balanced to get good puck positioning performance across the entire mirror was one of the more challenging portions of the project.

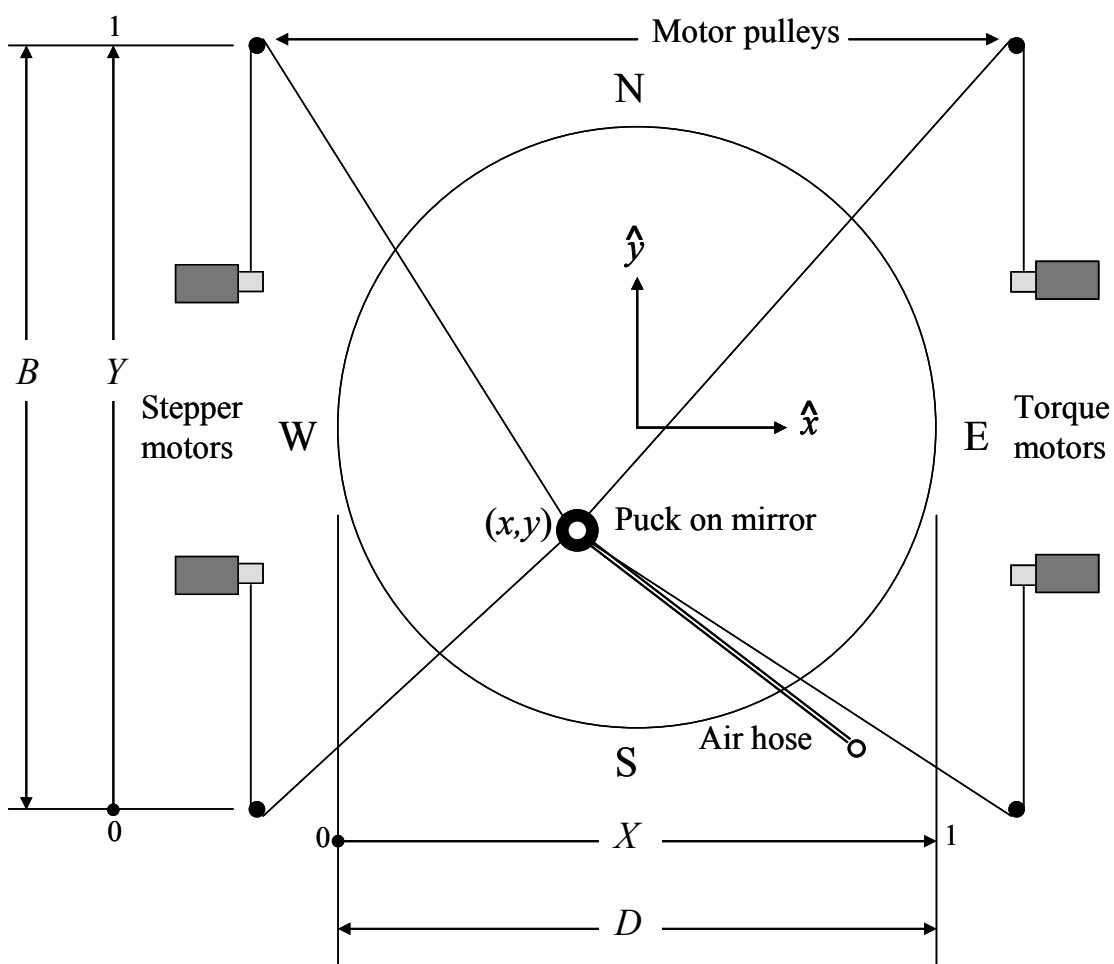


Figure 3-20: Layout of the mirror and SMR positioning system during a Laser Tracker Plus measurement. An x - y axis is defined with the origin at the center of the mirror, where (x,y) is the position of the puck on the mirror. The four positioning strings run from the puck through pulleys to the torque and stepper motors. When the air puck is used, there is also an air hose that is connected to the puck.

Because there are two different SMR pucks used, two different torque algorithms needed to be developed. The original algorithm developed for use with the Teflon puck was symmetric across the east-west axis of the mirror. The torque required for the two torque motors is a function of X , the normalized position of the puck on the mirror in the east-west direction, where $X = 0$ at the west edge of the mirror and $X = 1$ at the east edge. X is defined as

$$X = \frac{x + \frac{1}{2}D}{D}, \quad (3.3)$$

where x is the puck's position on the mirror in the east-west direction and $D = 8.4$ m is the diameter of the mirror. A torque coefficient in the x direction is defined as

$$T_x = [2 + 5X + 3X^4] \text{ in}\cdot\text{lb}, \quad (3.4)$$

where the form and coefficients were found empirically to give good results. The ratio of the torque between the two motors is a function of the puck's normalized position in the north-south direction Y , where $Y = 0$ at the south edge of the area enclosed between the motor pulleys and $Y = 1$ at the North edge of the measurement area. Y is defined as

$$Y = \frac{y + \frac{1}{2}B}{B}, \quad (3.5)$$

where y is the puck's position on the mirror in the north-south direction and $B = 10.668$ m is the distance between the motor pulleys enclosing the measurement area.

The torque algorithm for the individual torque motors is given by

$$T_N = \frac{27}{64}T_x + \frac{5}{4}T_x(1 - Y)^4 \quad (3.6)$$

for the north torque motor, and

$$T_S = \frac{27}{64} T_x + \frac{5}{4} T_x Y^4 \quad (3.7)$$

for the south torque motor. Again, the form and coefficients were determined empirically.

The torque algorithm is complicated further for the air puck due to the force applied to the puck from the air hose. The extra force being applied by the air hose required that the torque coefficient T_x needed to be increased by 2 in·lb, such that

$$T_x = 4 + 5X + 3X^4 \text{ in·lb.} \quad (3.8)$$

Because the air hose is mounted on the south side of the mirror, the east-west symmetry is now broken. Due to the air hose's proximity to the pulley for the south torque motor, the assumption was made that the air hose and the south torque motor would generally be pulling on the puck in the same direction, and that the north torque motor must balance their combined force. This assumption works fairly well over most of the mirror surface, so the algorithm that determines the torque to the south torque motor was modified to

$$T_S = \frac{27}{64} T_x + \frac{5}{4} T_x (1 - Y)^4 - T_A + T_H, \quad (3.9)$$

where $T_A = 2 \text{ in·lb}$ is the equivalent torque due to the air hose and $T_H = \pm 0.2 \text{ in·lb}$ accounts for the hysteresis in the air hose management system. T_H is positive when the north stepper motor is retracting (pulling more air hose out of the air hose management system) and is negative when the north stepper motor is paying out string (the air hose is retracting). The torque algorithm for the north torque motor is unchanged from that shown in Equation 3.6.

3.5.3 Software

The control software was all written by Jeff Hagen of Steward Observatory. It was written in C, built on a LINUX operating system. The control software simultaneously reads the outputs from the three major measurement systems (the laser tracker, the DMIs, and the PSDs), the weather monitors (the laser tracker's weather station and the thermocouple electronics monitors), and the diagnostic monitors (the DMI intensities, the PSD intensities, and the bridge crane home position monitor), while it monitors and controls the SMR positioning system. The software is run from the master control computer at the base of the SOML test tower. Another computer at the top of the test tower contains the four DMI single laser-axis boards and is connected directly to the Faro laser tracker, allowing it to trigger the measurement cycle and collect simultaneous measurements from the laser tracker and the external references, after which it signals the master control computer the measurement is complete. The software then controls the SMR positioner to move the puck to the next measurement location.

Faro Technologies provided a user's development suite that contained numerous JAVA scripts that allowed the Faro laser tracker and its weather station to be operated with software written for LINUX, while the National Instruments Compact FieldPoint ethernet interface that digitized the analog output from the PSD system was read from LINUX via a MODBUS interface, requiring the control software to interface with both of these protocols. Hagen wrote the drivers that read the output from the Agilent Technologies DMIs, the drivers that controlled the positioning motors of the SMR positioning system, and the drivers that read the analog and digital ports on the MicroPC

that monitored the DMI beam intensity (used to indicate alignment), the thermocouple circuit output (used to monitor temperature fluctuations around the DMI laser head and optics), and the bridge crane home position (used to indicate that the system is in the correct position for testing a mirror segment).

The software is controlled with a graphical user interface (GUI), shown in Figure 3-21. The upper right portion of the GUI provides the controls for the laser tracker along with a readout of its current status. The lower right portion provides the motors controls of the SMR Positioning system and a readout of the current status.

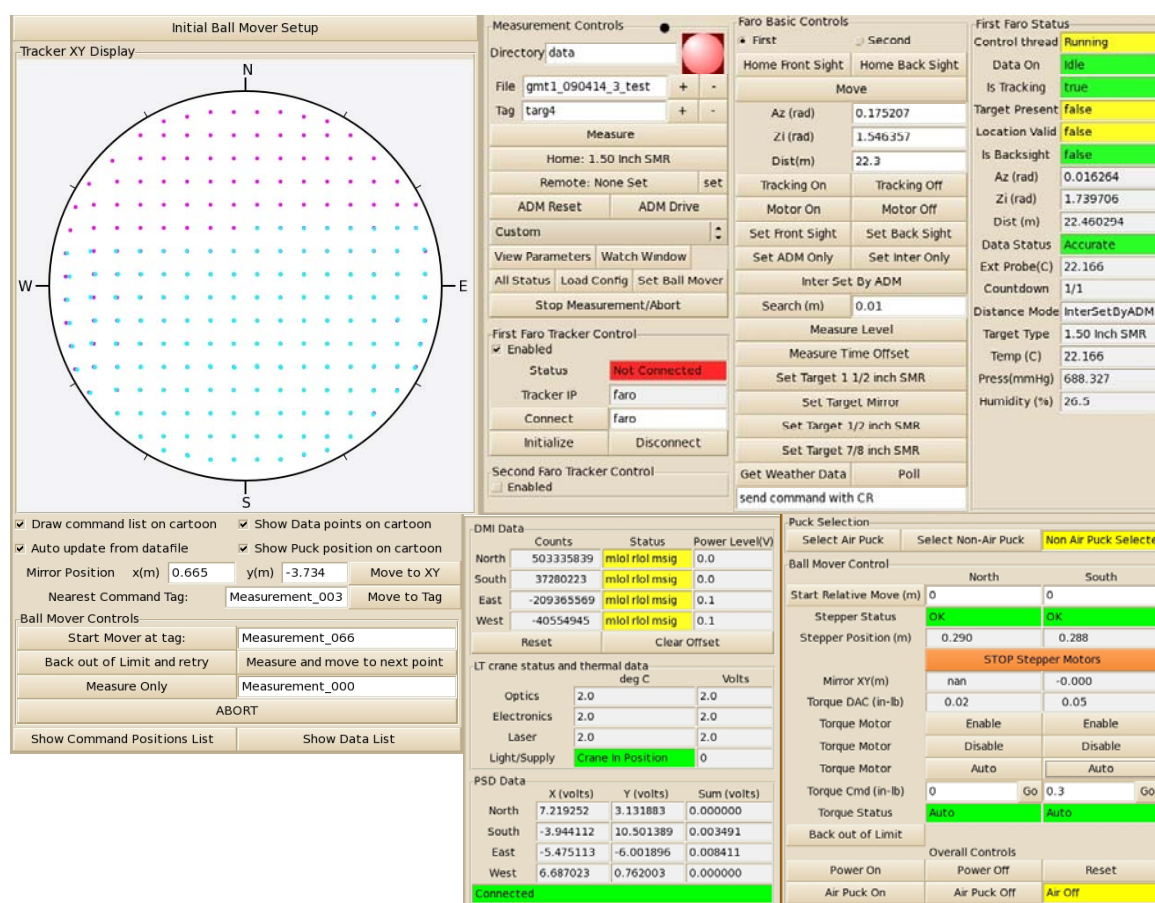


Figure 3-21: Graphical user interface used to control the Laser Tracker Plus system and monitor the data collection process.

Lower center contains the readouts from all four DMIs and PSDs, the readout for the temperature measurements of the DMI laser and optics, as well as the readout for the bridge crane home switch status. The upper center contains the controls to select the parameters for a measurement run, while the left side contains the display of output from the measurement run. Data collection using this software is discussed in Section **6.2**.

Chapter 4

CUSTOM LASER TRACKER CALIBRATION

To improve the accuracy of the commercial laser tracker, a set of custom calibrations to measure repeatable intrinsic errors in the laser tracker were devised. There are both radial and angular calibrations which determine the repeatable errors in the laser tracker's measurement of radius as a function of angle, as well as angle as a function of angle. There are numerous publications about characterizing laser trackers to identify intrinsic errors [35,43] and calibration techniques that use precision coordinate measuring machines [34], air bearings[16], and linear rails[28] to evaluate laser tracker performance. The Laser Tracker Plus calibration uses a different approach that calibrates for sub-micron accuracy only over the subtended angular region used to measure an 8.4 m mirror.

4.1 Radial Calibration

A custom radial calibration was devised to characterize any intrinsic errors in the laser tracker's measurement of radius as a function of angle. Some major geometric sources for this type of errors include misalignments of the gimbal axes and offset of the steering mirror's center [43]. The method described characterizes the total radial error over the region of interest so that it can be backed out of the measurement if necessary.

4.1.1 Description of Methods

A small concave reference sphere is used to calibrate the laser tracker's measurement of radial displacement. This is accomplished by measuring the surface of the mirror from its center of curvature, as shown in Figure 4-1. Because the radial distance is constant for all angles, the measurement is insensitive to angular errors, allowing a determination of the repeatable portion of the radial error.

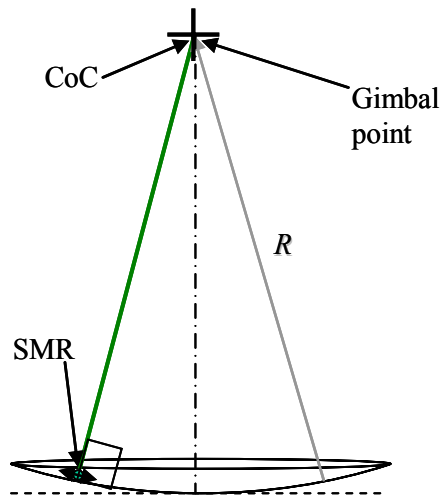


Figure 4-1: The systematic tracker errors are calibrated over the scan angles using a small concave spherical surface. The radial line of sight errors are determined by making measurements of the spherical surface with the tracker at its center of curvature [7].

A 150 mm diameter $f/1.6$ spherical mirror was selected, covering a solid angle larger than the $f/2.6$ cone that an 8.4 m mirror subtends from the tracker. The size of the mirror allows it to be installed *in situ* to calibrate of the laser tracker while it is mounted in the tower. The calibration mirror mounts in a cell suspended in an Invar plate which bolts directly beneath the laser tracker head. Figure 4-2 shows a picture of the Invar plate holding the calibrations sphere mounted in position beneath the laser tracker for performing the radial calibration.

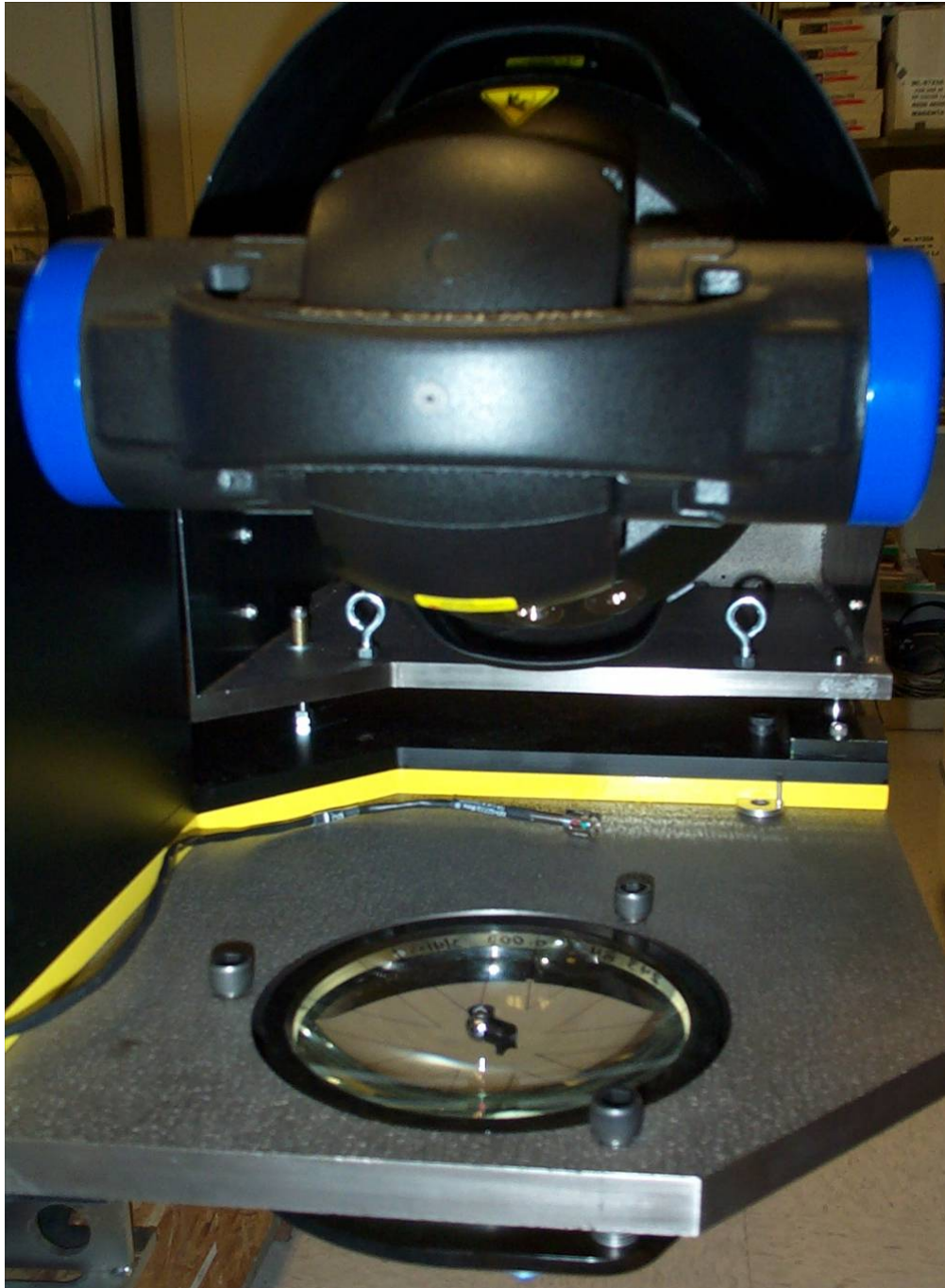


Figure 4-2: Picture of the calibration sphere mounted in position for performing the radial calibration of the laser tracker. The tip, tilt, and piston of the mirror are adjusted by turning the three bolts until the center of curvature of the mirror is aligned to the gimbal point of the laser tracker.

The mechanics were designed to maintain sub-micron alignment of the calibration mirror to the laser tracker while the surface is being measured with a 0.5 inch SMR. Figure 4-3 shows a cross section diagram of the adjusters used to fine position the mirror's CoC to the laser tracker's gimbal.

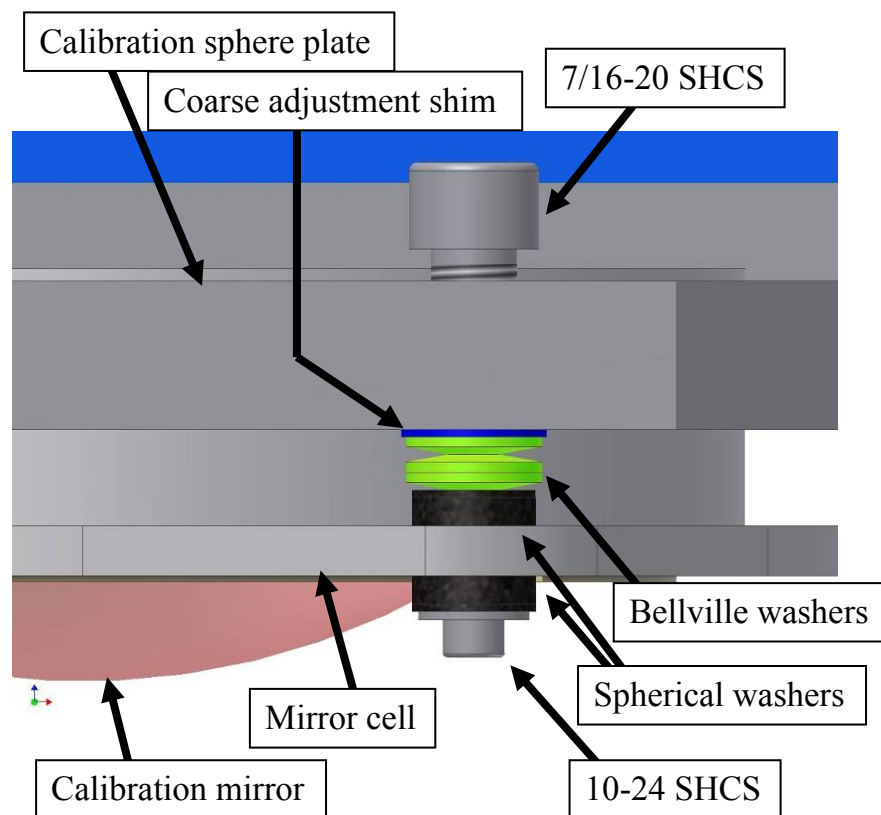


Figure 4-3: Cross sectional diagram of the adjusters for fine positioning the calibration mirror's CoC to the laser tracker's gimbal.

The three adjustable mounting points that secure the calibration mirror cell to the Invar mounting plate bolted beneath the laser tracker allow fine adjustment of the relative tilt and separation between the mirror and the laser tracker. The fine adjustment is accomplished using a differential thread arrangement for the three sets of bolts, where 7/16-20 bolts are center tapped for a 10-24 bolt, resulting in $0.6\ \mu\text{m}$ of motion for each

degree of rotation of the 7/16 bolt. Bellville washers are used to provide enough compliance to adjust the mirror's position, while maintaining enough preload to prevent the mirror from moving appreciably while the surface was being measured. The thickness of the Invar plate was chosen to provide enough stiffness that it will deflect less than $0.1 \mu\text{m}$ as the 0.5 inch SMR is being moved across the surface of the calibration mirror.

4.1.2 Radial Calibration Results

Thirty separate measurements of the calibration mirror were made. A typical set of measurements is shown in Figure 4-4. A least-squares fit of the data to time was used to remove any linear drift, following which the nominal spherical shape of the calibration sphere was subtracted from the data. An aperture defined by the angle subtended by the GMT mirror as seen by the laser tracker was used to normalize the radial component of the data. Any points lying beyond this aperture were deleted. Because radial errors couple directly into surface errors, the best way to evaluate the radial errors is to fit Zernike polynomials to them; therefore, each set of measurements was fit by the first 45 Zernike polynomials (through 8th degree). Appendix E contains a discussion of the Zernike polynomials used throughout this dissertation, which are normalized so that their rms is unity. Figure 4-5 shows a surface plot of the Zernike polynomial fit to the data plotted in Figure 4-4 on the left, and the surface plot for the average Zernike polynomial fit for all 30 data sets on the right.

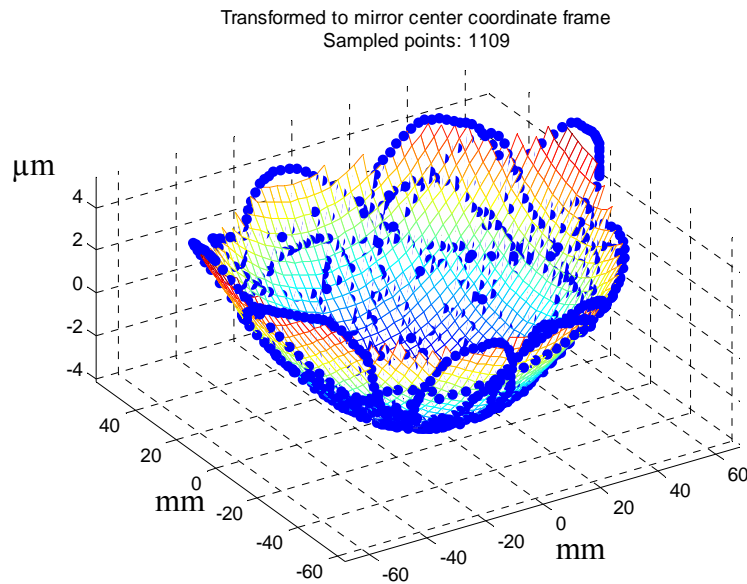


Figure 4-4: Plot of the raw laser tracker data from a typical radial calibration measurement of the calibration sphere.

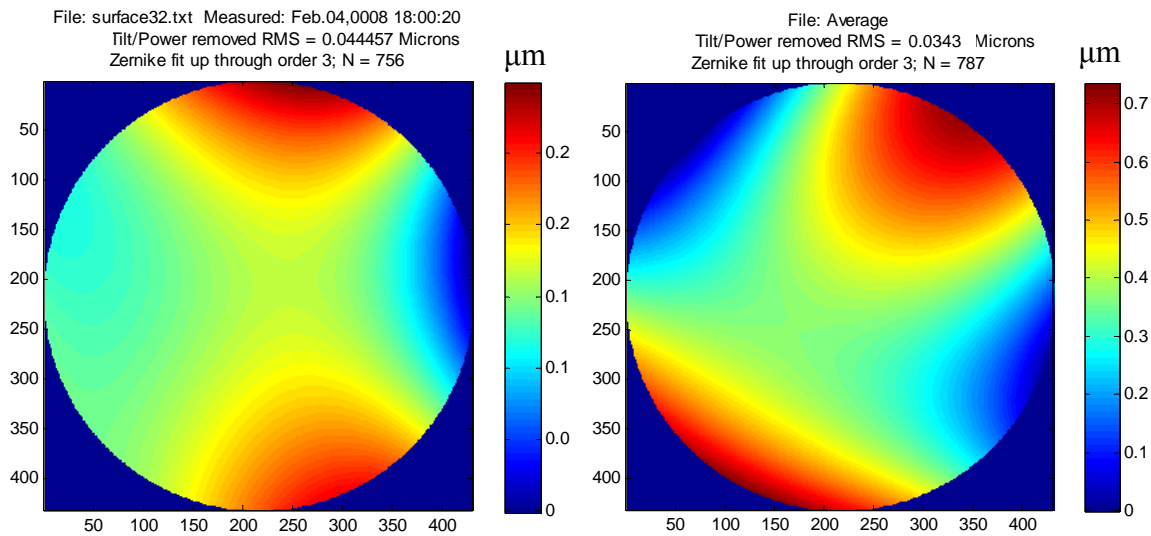


Figure 4-5: Surface plots of the Zernike polynomial fit to the residual surface errors from the calibration sphere measured with the laser tracker. The plot on the left is for a typical angular calibration measurement, while the one on the right is the average of all 30 sets [45].

The mean and standard deviation σ of each Zernike coefficient were calculated for each of the 30 separate measurements, and used to generate the plot in Figure 4-6. The curve represents the mean for each Zernike coefficient and the error bars represent the uncertainty given an average of any 5 of the 30 measurements, where 5 measurements averaged together would represent a typical radial calibration run. The tilt and power aberrations were due to a small displacement of the mirror's CoC to the laser tracker's gimbal point, so they were neglected. This left the 0° astigmatism term as the largest error term at $0.03 \mu\text{m}$.

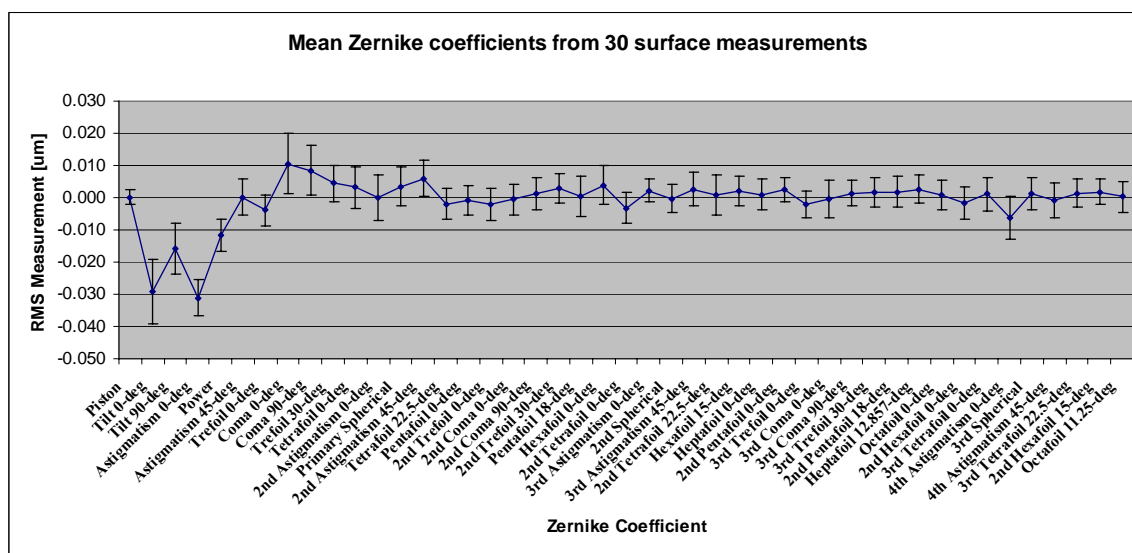


Figure 4-6: The rms error introduced into each Zernike polynomial due to the radial errors in the laser tracker, excluding the values for piston, tilt, and power, which are due to alignment errors in the test setup. The plot is based on 30 separate measurements of the surface, where the curve represents the mean for each Zernike coefficient and the error bars represent the uncertainty given an average of any 5 of the 30 measurements, where 5 individual measurements averaged together would be representative of a typical set of calibration measurements. The magnitude of the error bar is $\pm \sigma/\sqrt{5}$ [44].

4.1.3 Application of Radial Calibration Results

The ambitious goals specified in Table 1-2 for the measurement accuracy of astigmatism is 0.5 μm rms surface, for coma is 0.14 μm , and for defocus is 0.3 μm . Each one of these radial aberration errors was measured to be less than 1/10 of the goal values. Therefore it was determined that no correction for radial errors was required at this time; however, it would be prudent to re-perform this test each time the laser tracker returns from its factory recalibration and cleaning to insure that the radial aberration errors are still reasonably small.

If the errors had been larger, or this technique was applied to another instrument with larger radial errors, then the radial correction would be applied as follows. The correction is expressed as a polynomial fit to the calibration data. The correction can be applied to measured surface data by subtracting the polynomial fit from the surface data directly. Alternatively, the correction can be applied by subtracting the fit from a polynomial fit to the surface data (simply subtracting the polynomial coefficients). In either case, the coordinates of the surface data and those of the calibration data must be normalized consistently.

4.2 Angular Calibration

When a laser tracker makes a measurement, it measures the radial distance using a displacement measuring interferometer (DMI) and the two angular components through the combination of angular encoders and a position sensing detector (PSD). The radial measurement is significantly more accurate than the angular measurement; therefore the

3D accuracy of a laser tracker measurement is limited by the accuracy of the angular component of the measurement. The purpose of the angular calibration is to improve the angular accuracy of one laser tracker by performing a custom calibration with the use of a second laser tracker. It would also be possible to use a stand-alone DMI in lieu of a second laser tracker.

4.2.1 Description of Methods

The laser tracker to be calibrated is mounted nadir pointing (looking straight down) in the test tower, while the second laser tracker is mounted at floor level, looking horizontally along a straight line which passes through the point directly below the first laser tracker, as illustrated by Figure 4-7. The test only measures errors in the radial direction along the mirror surface from polar angle errors. Errors in the transverse direction do not couple into surface errors for the geometry with the laser tracker mounted above the mirror. A constellation of reference points is located in view of both laser trackers so that the locations of both trackers can be determine in a common coordinate frame to make the data processing easier.

The tracker in the tower measures horizontal displacement of an SMR primarily with its angular encoders, while the floor-mounted tracker measures the same displacement much more accurately with its DMI. An SMR has a narrow angle of acceptance, so a fixture has been designed that holds three 1.5 inch SMRs in direct contact along a straight line (see Figure 4-8). The two outer balls are aimed upward toward the tracker to be calibrated, while the center ball is aimed horizontally toward the

tracker at floor level. The location of the center ball is halfway between the two outer balls. The purpose of this is to eliminate sensitivity to offset errors from rotation of the fixture.

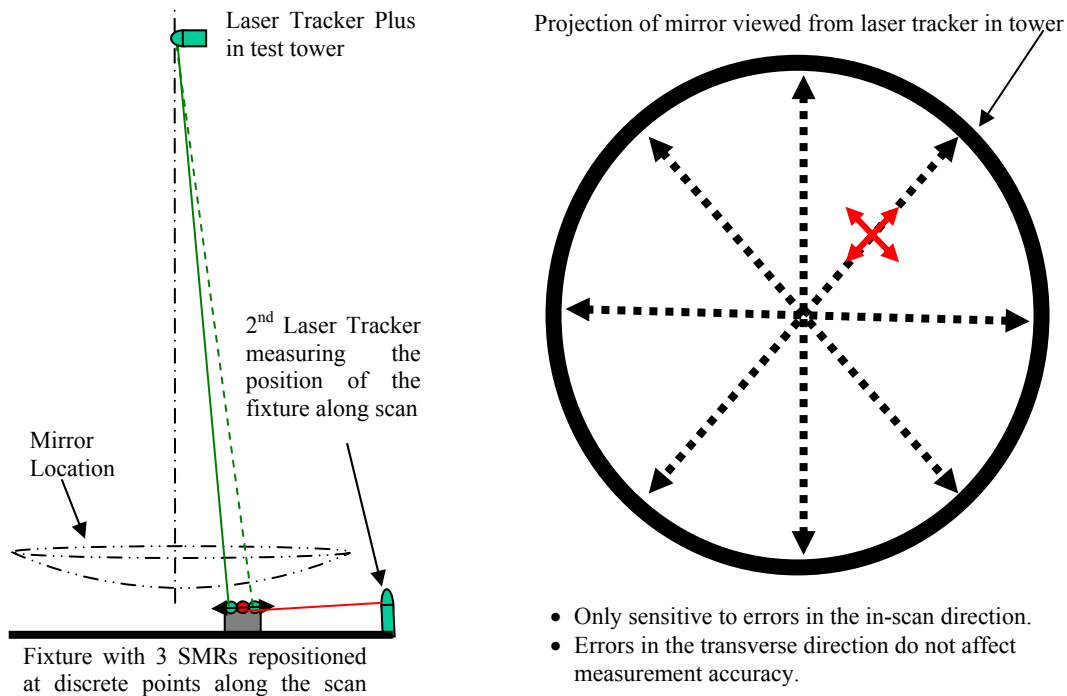


Figure 4-7: The diagram on the left shows the layout for the angular calibration. The laser tracker at floor measures the fixture location with small angular error compared to the tower tracker. The diagram on the right shows the pattern of multiple scans made to determine the discrepancy between the two trackers, which is used to determine a calibration correction for the angular errors [44].

The fixture is moved along the direct line-of-sight of the tracker at the floor, allowing its position to be determined using the higher accuracy measuring capability of the DMI. The laser tracker in the tower uses ADM to determine the location of the two outer tracker balls as the fixture is moved through different angles from its perspective. The difference in the position of the fixture measured by the two laser trackers is used to determine the angular error in the upper tracker.

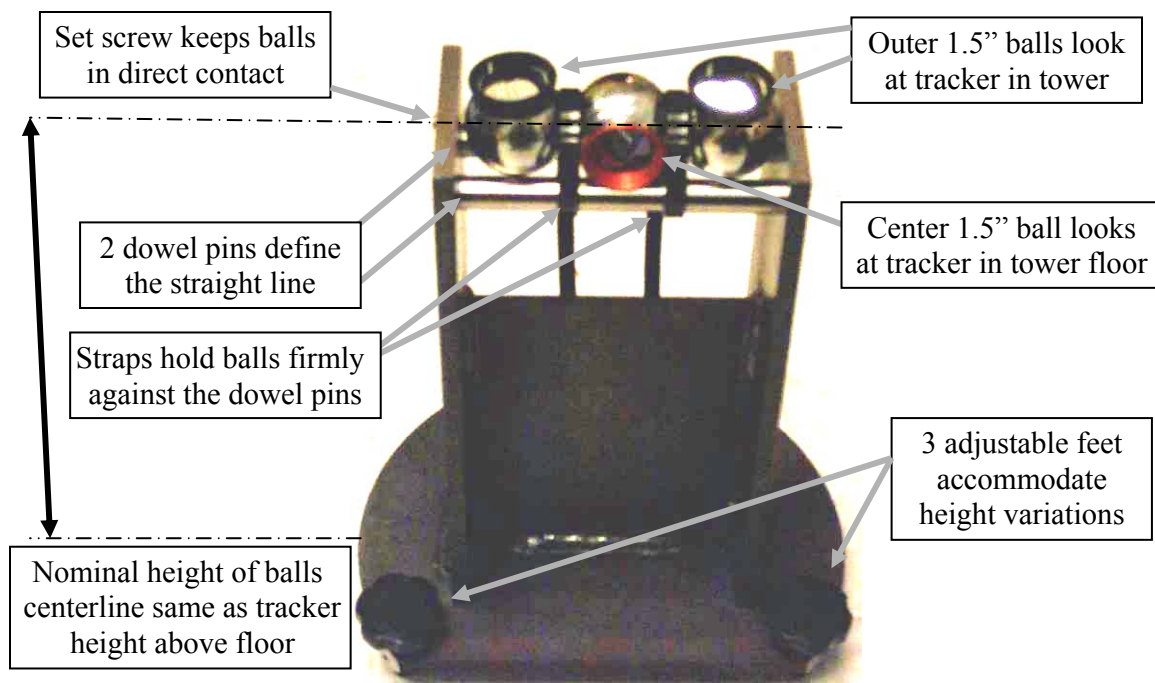


Figure 4-8: Specialty fixture designed to hold three 1.5 inch laser tracker balls in direct contact for performing the angular calibration of the laser tracker in the test tower with the aid of another one at floor level. The two outer balls are aimed upward toward the tracker to be calibrated, while the center ball is aimed horizontally toward the tracker at floor level.

4.2.2 Angular Calibration Results

To perform the angular calibration, the laser tracker at floor level was mounted horizontally in a custom mount shown in Figure 4-9. Four scan lines were marked on the floor, two of them aligned to the rotation angles of the laser tracker in the tower, while the other two are the 45° lines in between. All four scans cross at the point directly beneath the laser tracker in the tower, where the error is defined to be zero. A 0.5 m measurement spacing was selected along each scan for a total of 21 measurements per

scan over a 10 m scan diameter, which is approximately the diameter of the circle subtended by the GMT mirror when projected to the floor, shown in Figure 4-10.

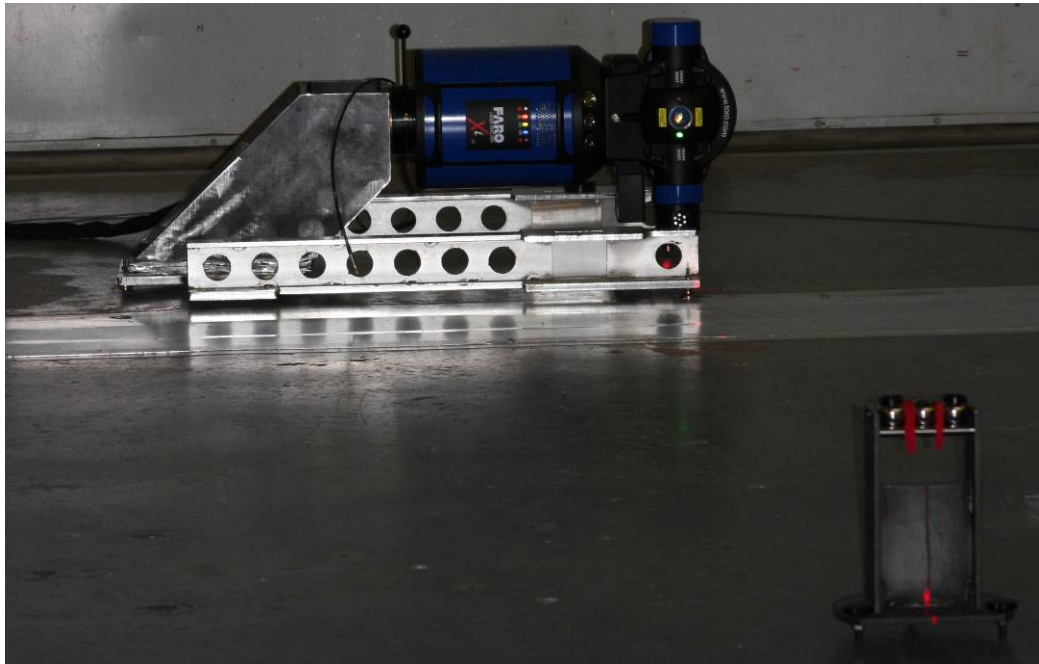


Figure 4-9: Faro laser tracker mounted horizontally in a custom mount built for performing the angular calibration. This laser tracker is locked on to the center SMR in the fixture in the foreground while another laser tracker above in the test tower measures the outer two SMRs in the fixture. The difference in the motion of the fixture is used to determine the angular error of the laser tracker in the tower [45].

For each scan, the floor laser tracker was set up so its line of sight is aligned to one of these scan lines along the floor. Six tracker ball nests were laid out into a measurement constellation around the measurement envelope at the base of the tower (4 nests on the floor of the test tower, and two on the West column of the test tower). The reference points are measured by both trackers and a fit is performed to co-align the floor laser tracker into the tower laser tracker's coordinate frame for each scan. The tower tracker measures the location of the first of the six nests in ADM, and measures the subsequent five in IFM, while the floor tracker measures all six nests in IFM. Without

breaking the beam to the floor tracker, the SMR is placed into the center position in the three-ball fixture, which is positioned at one end of the first line on the floor. With the center ball aimed at the tracker on the floor, and the outer two balls pointed upward to the laser tracker in the tower, the system is now set up to begin the measurement scan.

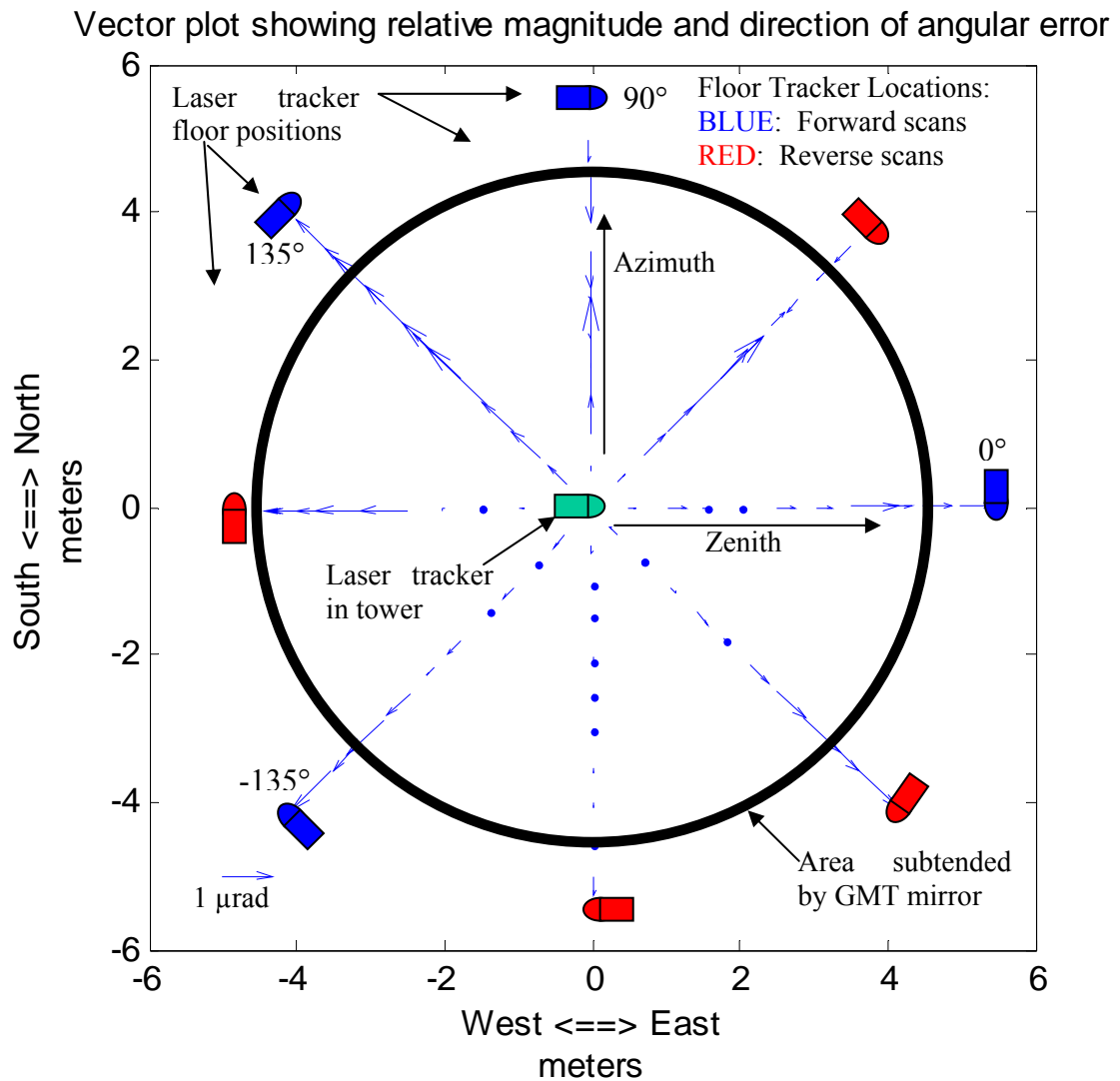


Figure 4-10: The angular calibration measurements were made with four radial scans crossing directly beneath the tower laser tracker to be calibrated. A 0.5 m measurement spacing was selected along each scan for a total of 21 measurements per scan over a 10 m scan diameter, which is approximately the diameter of the circle subtended by the GMT mirror when projected to the floor. The blue arrows in the figure show the direction and relative angular error of the tower laser tracker [45].

At each measurement position, the laser tracker at floor level measured the location of the center ball in IFM, while the tower tracker measured the location of one of the two outer balls (say the left ball) in ADM. Ideally, both trackers make the measurements simultaneously with the same measurement parameters (say a 25 measurement average). The tower tracker now moves its laser beam to the other tracker ball (right ball) and locates it with ADM. Two more sets of simultaneous measurements are made by each laser tracker, such that two measurements of 25 averages are made of both the center ball and the right ball. The tower tracker now moves its laser beam back to the left ball and measures it with ADM. A final set of 25 averaged measurements is made simultaneously by both laser trackers. The four sets of measurements made by each laser tracker are then averaged together, and the measurement difference between the two trackers for the in-scan distance is computed, which is converted into an angular error for the tower tracker. The assumption is that the laser tracker at the floor measuring in IFM with its DMI has much better accuracy than the tracker in the tower, so any discrepancy between the two sets of measurements is an angular error in the tower tracker. This angular error is then recorded for the laser tracker angle that corresponds to that position along the scan. The fixture is then moved along the line to the next location while both laser trackers are tracking the fixture's motion.

Each scan was measured with a down and back measuring technique, in which the integer meter valued points (-5, -4, ..., 0, 1, ..., 5 m) were measured scanning in one direction, and the half-meter valued points (4.5, 3.5, ..., 0.5, -0.5, ..., -4.5 m) were measured on the return scan. Because the data were time-stamped and the two halves of

the scan were spatially overlapped, a linear drift with time could be backed out of the measurements.

Three complete sets of angular calibration scans were made, two in the “forward” direction and one in the “reverse” direction, as illustrated in Figure 4-10. The same positions on the floor were measured in the same order for both the forward and reverse scans, the only difference is that the floor tracker was moved to the other side of the scan area in an effort to detect any errors in the measurements that can be attributed to the floor tracker. The forward and reverse scans agree, supporting the assumption that all the errors measured in the angular calibration were due to angle measurements in the tower tracker that was being calibrated.

Figure 4-11 shows the results of the four individual scans for one of the forward sets of calibration data, with each measurement point represented as a blue dot, where positive values indicate the angular displacement is radially outward. The four scans were processed using a variation on the scanning pentaprism technique detailed by Su in his dissertation [39] and applied to measurements made of the New Solar Telescope primary mirror [38]. It was decided that Zernike slope polynomials (listed in Table E-2) are the appropriate choice for fitting the angular calibration data, because an error in the measured value of the angle is equivalent to a mapping error, or distortion in the “image” of the mirror, and Zernike slope polynomials are commonly used to correct for distortion in measurement interferograms taken with complex null systems [41]. The additional benefit of using Zernike slope polynomials is that they are reduced from regular standard Zernike polynomials by one power of r . To determine what the surface errors are from the angular errors, the fit of the Zernike slope polynomial to the angular errors is

multiplied by the mirror sensitivity (computed using Equation 2.3), which is proportional to r . The result is a set of basis functions for the surface error that have the same form as standard Zernike polynomials, with some differences in the normalization.

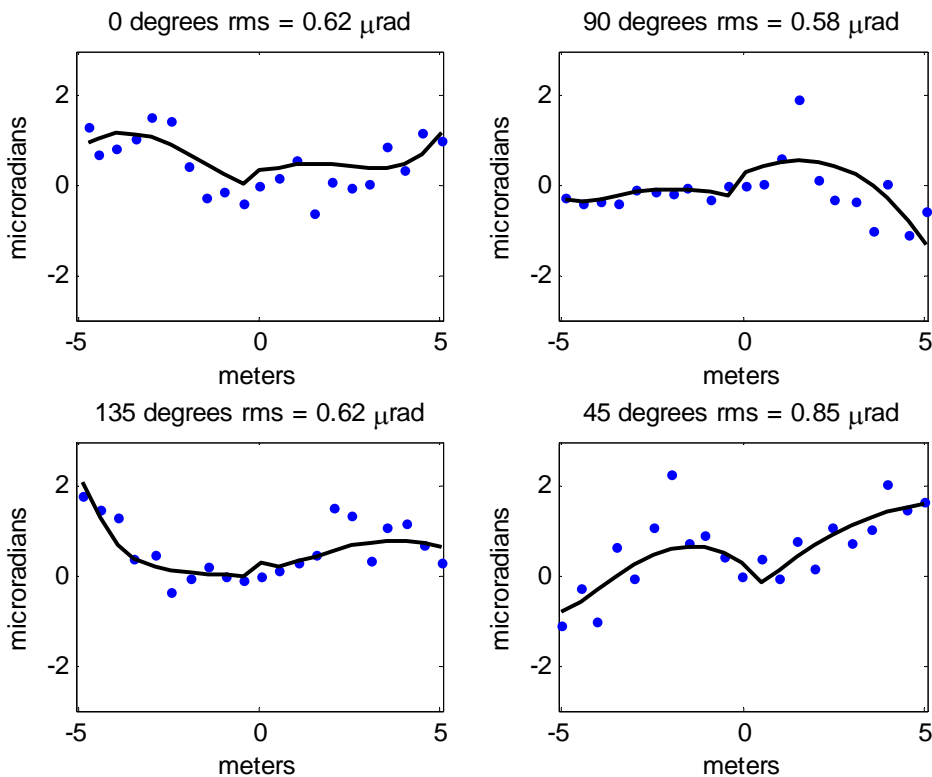


Figure 4-11: The four plots above show the difference in angles measured with the laser tracker on the ground and the one in the tower for four different scan lines, where positive values indicate the angular displacement is radially outward. The angles of the scan and the rms error are provided above each plot. The 0° and 90° plots correspond to the Zenith and Azimuth angles of the tower laser tracker. The black curves represent the Zernike slope polynomial fit to the full 2-dimensional data set as a function of radial distance from the center out. The discontinuity is the result of the radial distance changing sign at the center of the scan.

Because the derivatives of the Zernike polynomials are gradients, the Zernike slope polynomials are vector polynomials, and must be projected into the direction of the scans to determine the radial component (a 2-D scalar function). The number of polynomials that could be used in the fit was limited by the angular resolution of the data

because there were only four radial scans. Figure 4-12 shows the radial projection of the 16 Zernike slope polynomials used to fit the angular calibration data.

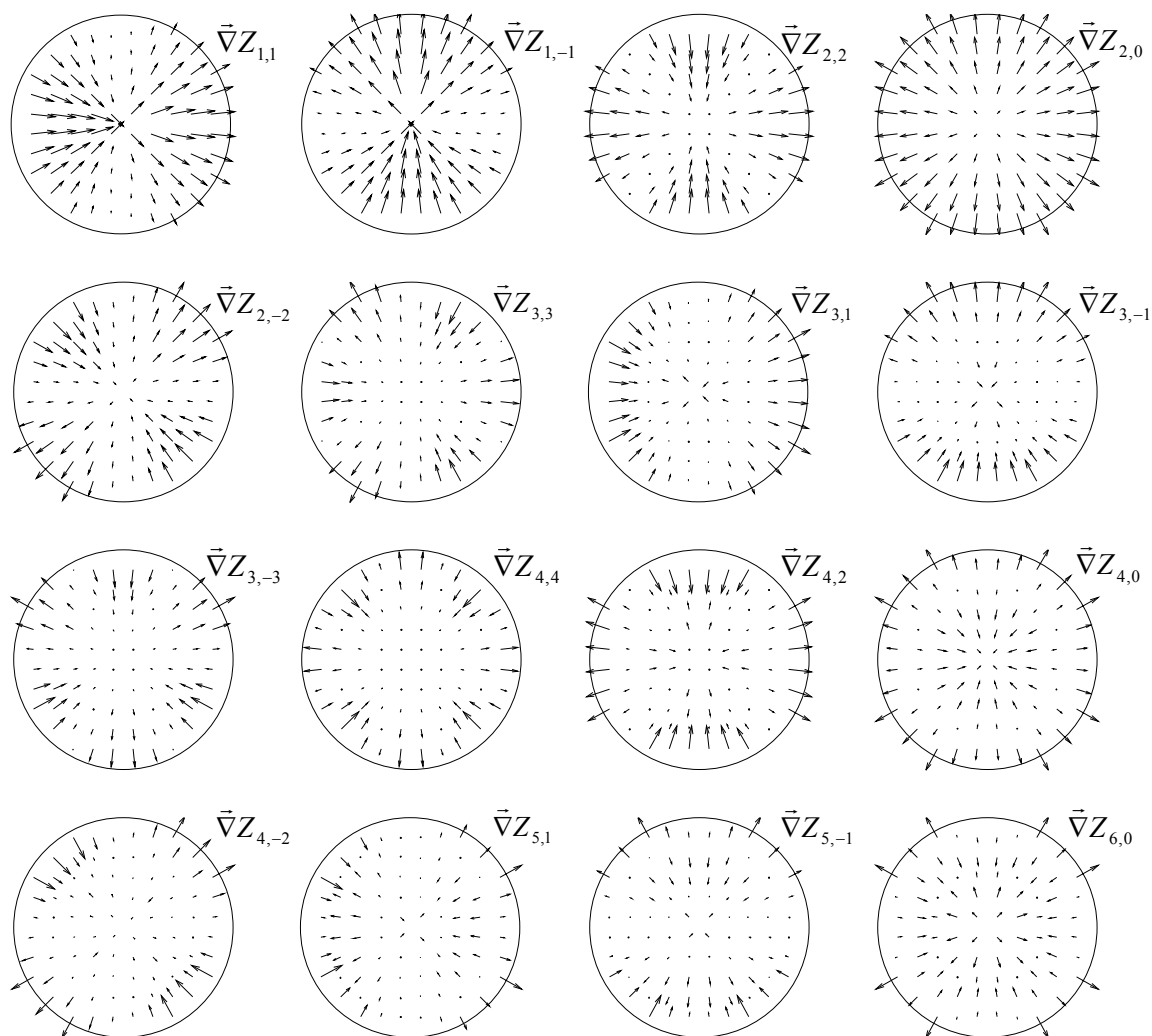


Figure 4-12: Radial vector plots of the 16 Zernike slope polynomials used for fitting the angular calibration data. These plots show the projection of the Zernike slope polynomials in the radial direction.

The Zernike slope polynomials were simultaneously fit to all four sets of scan data. Each scan contains an arbitrary offset, which was adjusted to give zero error at the common center of the scans. A sensitivity matrix was calculated, consisting of the radial

components of the Zernike slope polynomials at the measurement points along each scan. Radial positions of the measurement points were normalized by the semi-diameter of the measurement area (5 m in this case). The matrices from all four scans were then combined and fit to the measured data. The result was a set of polynomial coefficients which formed a single 2-dimensional error surface that best fit the data, shown as a vector plot in Figure 4-13. The black lines in each of the four scan line plots in Figure 4-11 represent that error surface evaluated along each scan angle.

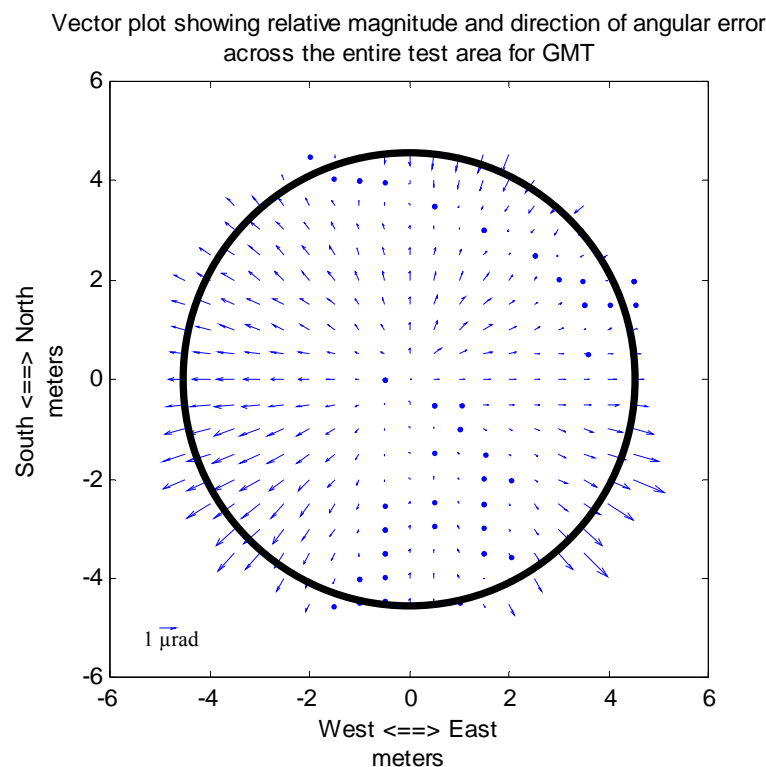


Figure 4-13: Vector plot of the radial component of the angular error across the entire measurement area based on the scan measurements presented in Figure 4-11. The area inside the black circle represents the region subtended by GMT.

The scan data are fit by evaluating each scan across the diameter as two radial scans from center out (0 at the center and +5 m at the edge) in opposite directions (angles

differing by 180°). The cusp formed at the center of the black fit line is because the first derivative of the radial projections of the Zernike slope polynomials is discontinuous at the center because the radial distance changing sign at the center of the scan. This discontinuity at the center is not an issue, because the mirror sensitivity is zero at the center, as seen by the left plot in Figure 4-14, so it goes away. The right plot is generated by multiplying the mirror sensitivity with the fit to the angular errors (Figure 4-13), which shows the expected surface error due to laser tracker angular errors that can be corrected.

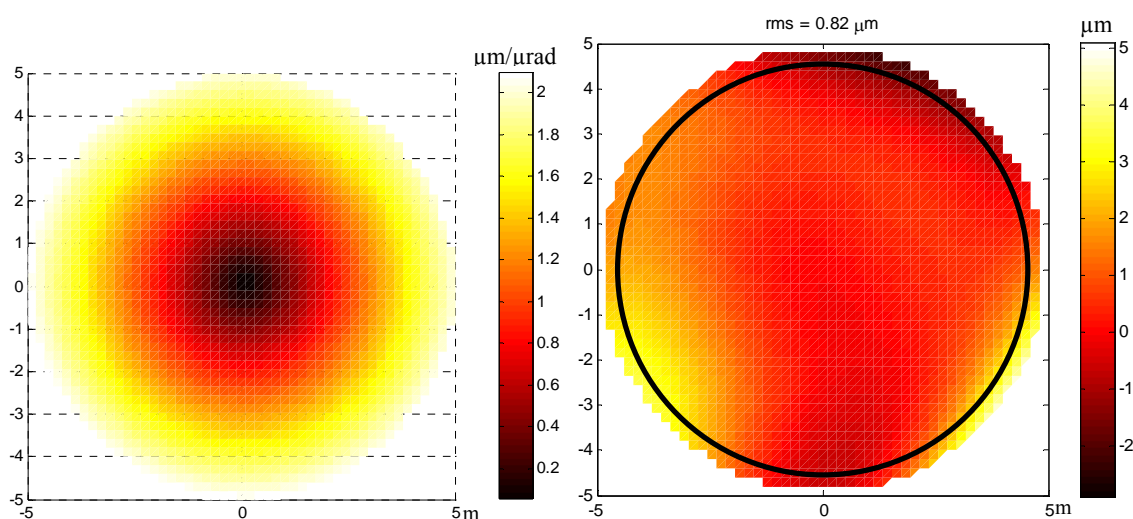


Figure 4-14: The left plot shows the mirror sensitivity for GMT Laser Tracker Plus test as a function of radial displacement from the center of the mirror segment (color scale in microns of surface error per microradian of angular error). The right plot shows the surface error due to angular errors in the laser tracker measurements that can be corrected by applying the angular calibration measurement results (color scale in microns of surface error). The black circle represents the area subtended by the GMT mirror, and the surface error over that region is $0.82 \mu\text{m}$ rms. Lateral scale is in meters for both plots.

The angular error surface computed from the Zernike slope polynomial fit to the data shown in Figure 4-11 is quite small, less than $1 \mu\text{rad}$ rms, but it appears to be statistically significant and worth correcting. Figure 4-15 shows the residuals from the

four angular scans for the first forward scan set after correcting for the angular error surface based on the polynomial fit. The residual error for each plot has been reduced to about $0.5 \mu\text{rad}$ rms, which is consistent with laser tracker noise measurements taken in the test tower. This residual $0.5 \mu\text{rad}$ error results in about $0.6 \mu\text{m}$ rms surface error.

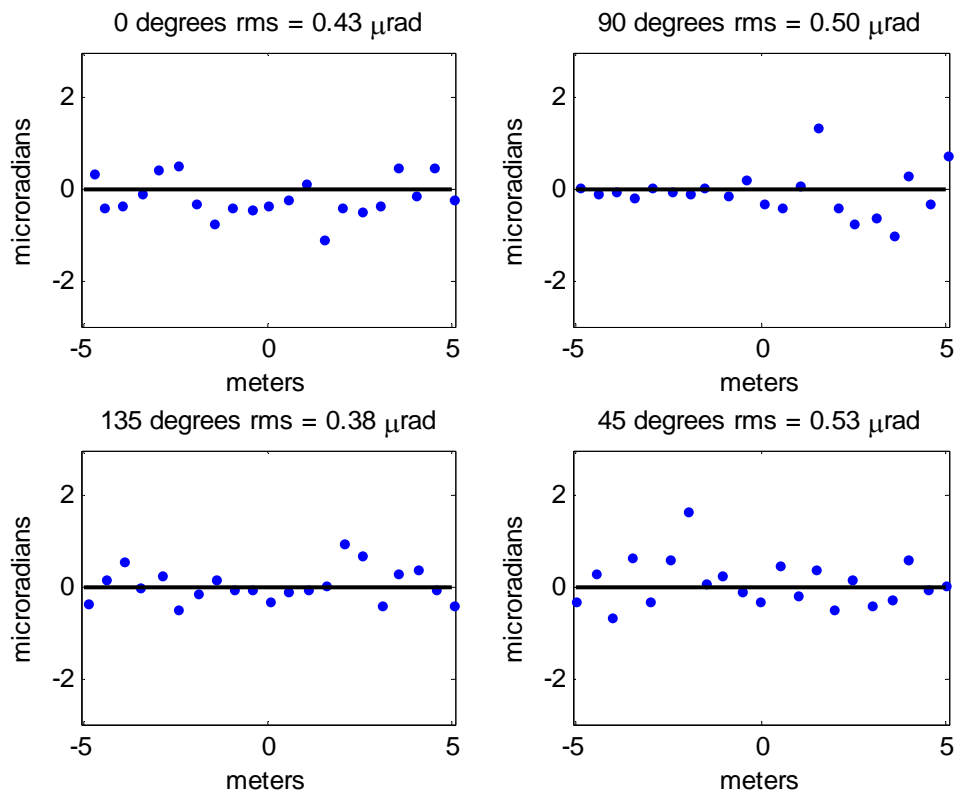


Figure 4-15: The four plots above represent the residual angular error in the tower laser tracker after applying the correction based on the Zernike slope polynomial fit shown in the plots in Figure 4-11. The residual rms error is provided above each plot.

All three sets of scans (the two forward sets and one reverse set) were evaluated in this way, and the values of the coefficients from the Zernike slope polynomial fit are listed in Table 4-1, along with their mean and standard deviations. The scan data from all three sets of scans are presented in Figure 4-16. The blue data are the forward scan plots

shown previously, while the green data are the second forward scan, and the red data are the reverse scan data. The color curves represent the projection of the polynomial fits to each data set along the scan lines, while the black curve represents the projection of the mean of the three polynomial fits. The rms value reported for each scan is based on the root-mean-square of the points for all three sets along each scan angle.

Table 4-1: List of Zernike slope polynomial coefficients from the individual fits to each of the three sets of laser tracker angular calibration measurements. The mean and standard deviation for each coefficient is also listed. The polynomials are defined in Table E-2.

Zernike Slope Term	Coefficients (μrad)				
	Set 1 (F)	Set 2 (F)	Set 3 (R)	Mean	St Dev
$\bar{\nabla}Z_{n,m}$					
$\bar{\nabla}Z_{1,1}$	-0.15	-0.03	-0.09	-0.09	0.06
$\bar{\nabla}Z_{1,-1}$	0.15	0.31	0.12	0.19	0.10
$\bar{\nabla}Z_{2,2}$	0.57	0.14	0.48	0.40	0.23
$\bar{\nabla}Z_{2,0}$	0.75	0.52	0.95	0.74	0.22
$\bar{\nabla}Z_{2,-2}$	0.16	-0.49	-0.48	-0.27	0.37
$\bar{\nabla}Z_{3,3}$	0.21	-0.05	0.43	0.20	0.24
$\bar{\nabla}Z_{3,1}$	-0.66	-0.12	-0.02	-0.27	0.34
$\bar{\nabla}Z_{3,-1}$	-0.80	-0.60	-0.68	-0.69	0.10
$\bar{\nabla}Z_{3,-3}$	-0.47	0.53	0.10	0.05	0.50
$\bar{\nabla}Z_{4,4}$	-0.40	0.04	-0.59	-0.32	0.32
$\bar{\nabla}Z_{4,2}$	0.31	0.11	-0.05	0.12	0.18
$\bar{\nabla}Z_{4,0}$	-0.44	-0.72	-0.65	-0.60	0.15
$\bar{\nabla}Z_{4,-2}$	-0.71	0.15	0.02	-0.18	0.46
$\bar{\nabla}Z_{5,1}$	0.75	-0.03	-0.16	0.18	0.49
$\bar{\nabla}Z_{5,-1}$	-0.29	-0.16	0.08	-0.13	0.19
$\bar{\nabla}Z_{6,0}$	0.24	0.45	0.44	0.37	0.12

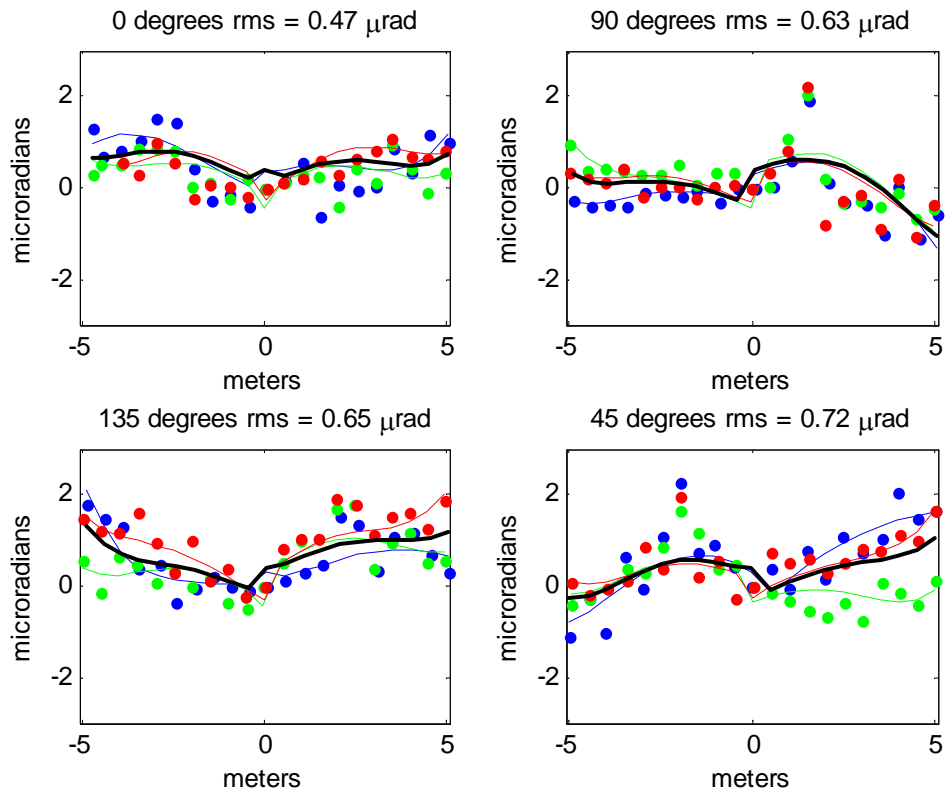


Figure 4-16: The four plots above show the difference in angles measured with the laser tracker on the ground and the one in the tower along each of the four different scan lines for the three different sets of scan measurements, each represented in a different color. The angle of the scan and the rms error are provided above each plot. The 0° and 90° plots correspond to the Zenith and Azimuth angles of the tower laser tracker. The color curves represent the projection of the Zernike slope polynomial fit to each data set along the scan lines, while the black curve represents the projection of the mean of the three individual polynomial fits as a function of radial distance from the center out. The discontinuity is the result of the radial distance changing sign at the center of the scan.

The left hand plot in Figure 4-17 shows the mean for the three polynomial fits listed in Table 4-1. It is displayed as a 2-dimensional vector plot, where only the radial component of the angular errors is displayed. Again, this is because only the radial component of the angular errors contributes to surface errors through the relationship expressed in Equation 2.3. The right hand plot show the resulting surface error expected

due to the angular errors defined by the left hand plot. The black circle represents the area subtended by GMT, and the total surface error across GMT that could be removed by applying this angular correction is $0.55 \mu\text{m}$ rms.

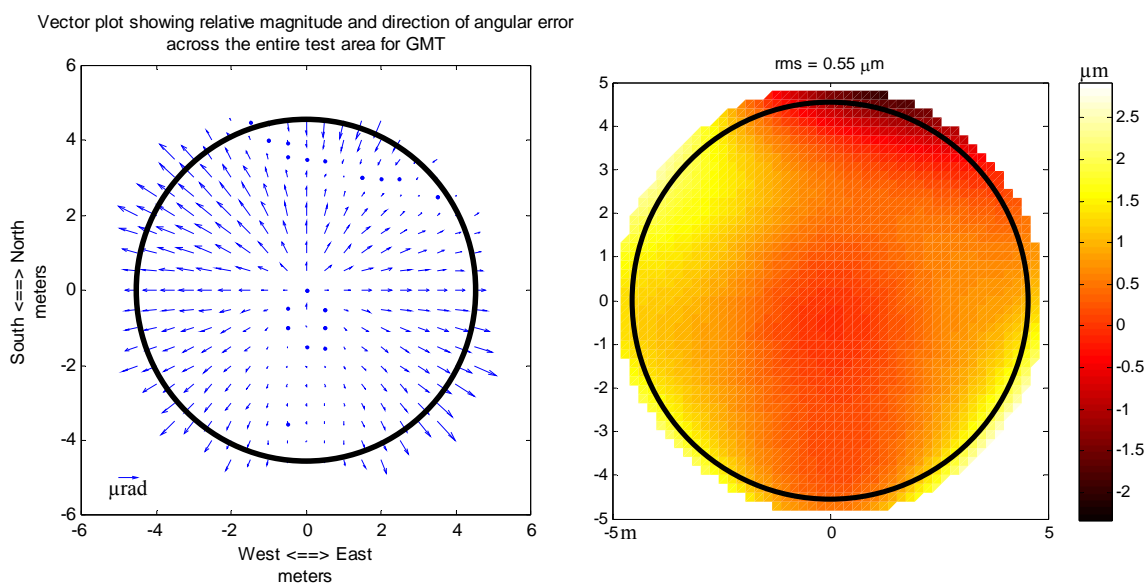


Figure 4-17: The left hand plot shows the laser tracker angular error in the radial direction based on the average of the three sets of scans. The right hand plot shows the expected surface error in the laser tracker measurements due to these angular errors. The black circle represents the area of the test subtended by the GMT mirror. The surface error over the GMT mirror that can be corrected by applying this angular calibration is $0.55 \mu\text{m}$ rms.

By using the mean of the three fits, the total correction is less than using an individual fit for a specific data set, but the mean of the three sets is less susceptible to noise in the individual angular calibration measurements. For this reason, the mean of the three polynomial fits is used to correct the Laser Tracker Plus measurements. Figure 4-18 shows the residual errors in the angular calibration scan data when the mean polynomial fit is subtracted from the individual sets of scan data. The residual rms for this case is not as low as it was for the residuals from an individual set of scan data, as

shown in Figure 4-15, in part because the fit is not as good over all three data sets, resulting in a smaller magnitude for the correction.

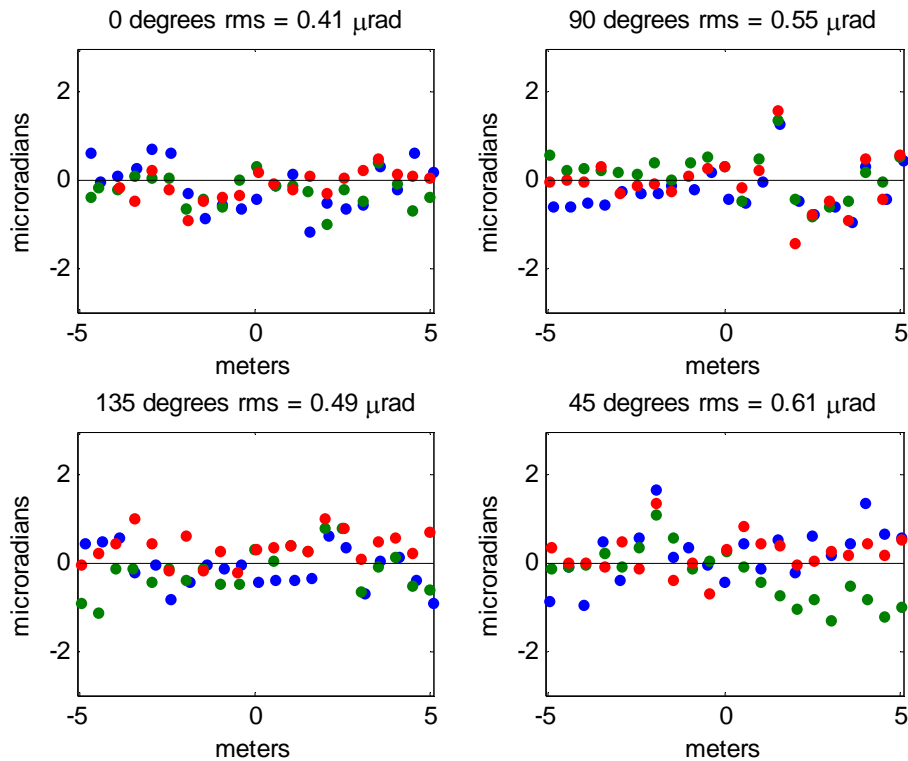


Figure 4-18: The four plots above represent the residual angular error in the tower laser tracker after applying the correction based on the mean value for the Zernike slope polynomial fits listed in Table 4-1 and shown in the plots in Figure 4-16. The residual rms error is provided above each plot, based on the rms of the points for all three scans.

The polynomial fit of the data is imperfect, because it does not adequately fit all the real angular tracker errors measured. Errors that are not fit will not be corrected, leaving some residual real angular errors, as shown in Figure 4-19. The left hand plot shows the four scan lines from one of the angular calibration runs appropriately laid out across the measurement area, where the magnitude of the error between the scans has been interpolated. The right hand plot shows the projection of the polynomial fit along

each scan, with the area between the scans interpolated. The fit looks like a smoothed version of the data because only low-order polynomials are used. The data in the left hand plot shows a large angular error in the tracker measurements running horizontally across the plot (encircled in black), corresponding to an error in the azimuthal encoder or bearing, which is not being properly fit, so this error will not be corrected with the angular calibration. Higher order polynomials would be required to better fit that error. Probably a better choice would be to rotate the laser tracker head to move that bad region out of the area used during mirror testing and hope that another bad spot does not rotate in from the other side. If this option is chosen, then the angular and radial calibrations will need to be performed again, to ensure that no other major errors are present, and to determine the calibration corrections required.

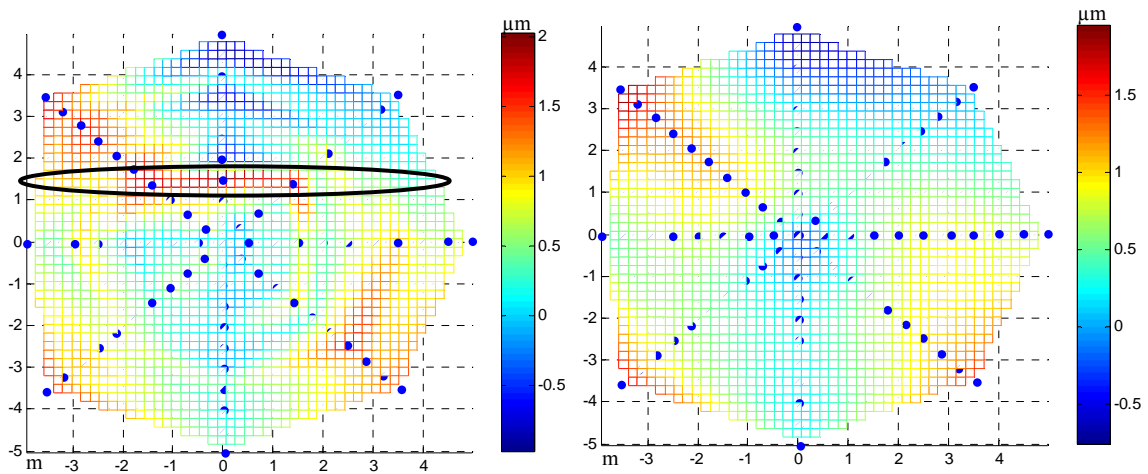


Figure 4-19: The left hand plot shows the scan data from one of the angular calibration runs, while the right hand plot shows the projection of the polynomial fit along the scans. The fit looks like a smoothed version of the data because only low-order polynomials are used. The data in the left hand plot shows a large angular error in the tracker measurements running horizontally across the plot (encircled in black), corresponding to an error in the azimuthal encoder or bearing, which is not being properly fit, so this error will not be corrected with the angular calibration.

4.2.3 Application of Angular Calibration Results

To apply the angular calibration results to a set of surface measurement data, a sensitivity matrix for the Zernike slope polynomials listed in Table 4-1 must first be generated. This is similar to the sensitivity matrix used to fit the polynomials in Section 4.2.2, except that the polynomials are evaluated at the surface measurement points instead of the points of the calibration scans. Again, the coordinates of the surface data and those of the calibration data must be normalized consistently.

Next, the mean coefficients listed in Table 4-1 are multiplied by the sensitivity matrix to determine the expected angular error at each of these measurement locations. Equation 2.1 is then used to determine the surface error δs by combining the angular error $\delta\theta$ with the local radial slope α at each measurement location. Equation 2.2 can be used to calculate values for α at each measurement location by approximating GMT as a sphere, or a more rigorous calculation can be performed to determine the actual values of α across the GMT surface. Finally, the surface error δs calculated for each point is subtracted from the measured surface errors values for those points to complete the angular calibration offset.

Chapter 5

CORRELATION BETWEEN LASER TRACKER AND EXTERNAL REFERENCE SYSTEM

When a laser tracker makes a measurement, it measures the radial distance using a displacement measuring interferometer (DMI) and the two angular components through the combination of angular encoders and a Position Sensing Detector (PSD). The largest source of measurement uncertainty comes from effects due to measuring through the air. Index variations in the air, due to temperature gradients and pockets of warmer and cooler air moving around the measurement environment, cause fluctuations in the perceived radial distance, as well as lensing effects that cause lateral motion of the laser beam. Both of these effects introduce small errors into the measurement, limiting the accuracy. Likewise, drift and motion of the mirror with respect to the test instruments in the tower will also introduce errors in the measurements that need to be corrected.

The Laser Tracker Plus system has a set of external references to mitigate these effects. To understand how best to apply the reference information to the measurement data, a study was performed to determine whether there is sufficient correlation between spatially separated sensors to allow one sensor to correct for perturbations (relative motion and index variations) of another sensor. A criterion is needed for deciding whether making the correction will improve the measurement by rejecting the correlated perturbation, or worsen it by adding noise from the reference. This can be thought of in the following way. For two given sensors, A and B , which could be two DMIs or one DMI and one laser tracker, the perturbation each sensor measures can be thought of as a

component common to both sensors, Z_{cor} , plus the non-common perturbation that is noise, N . Table 5-1 shows the equations of total perturbation and variance for both sensors A and B alone, and their difference.

Table 5-1: Expressions for the total perturbation and variance for two separate sensors and their difference.

SENSOR	TOTAL PERTURBATION	VARIANCE
A alone	$Z_A = Z_{cor} + N_A$	$\sigma_A^2 = \sigma_{Cor}^2 + \sigma_{N_A}^2$
B alone	$Z_B = Z_{cor} + N_B$	$\sigma_B^2 = \sigma_{Cor}^2 + \sigma_{N_B}^2$
$A - B$	$Z_{A-B} = N_A - N_B$	$\sigma_{A-B}^2 = \sigma_{N_A}^2 + \sigma_{N_B}^2$

If the values from just one sensor are used, say sensor A , then the variance due to the perturbation is $\sigma_A^2 = \sigma_{Cor}^2 + \sigma_{N_A}^2$; similarly for sensor B . If the difference is taken between the two sensors, then the variance due to the perturbation is $\sigma_{A-B}^2 = \sigma_{N_A}^2 + \sigma_{N_B}^2$. The idea is to minimize the variance due to the perturbation by using sensor B as a reference to correct for perturbations seen by sensor A , but only when $\sigma_{A-B} < \sigma_A$, i.e. if $\sigma_{N_B} < \sigma_{Cor}$.

The base measurement is the laser tracker (LT). For line-of-sight displacements, the reference is a set of DMIs; for lateral displacements, it is a set of PSDs. If the correlation is good enough in the real measurement situation, i.e. if $\sigma_{LT-ref} < \sigma_{LT}$, then a better estimate of the mirror surface is obtained by using the references to correct for perturbations in the laser tracker measurements. σ_{LT} represents the rms perturbation in the laser tracker measurement at one position, and includes contributions from relative motion, index variations, and instrumental noise. Likewise, σ_{ref} includes relative motion

(highly correlated with the laser tracker), index variations (somewhat correlated depending on separation and air conditions), and instrumental noise (uncorrelated) in the reference measurements.

5.1 Description of Test

The idea for the test is to evaluate the effects measured by two of the four surface references, and the laser tracker, when the surface references and the SMR are mounted on the floor of the Steward Observatory Mirror Laboratory (SOML) test tower. The floor of the test tower is very rigid, so the perturbation in the measurements should be primarily index variations and instrumental noise. Data were measured for an extended period of time with a 1 s measurement interval, which was decided to be a reasonable time interval for each measurement point and allows the individual measurement points to be averaged to evaluate the effect of integration time. At the same time the references are collecting data, the laser tracker is also measuring the position of a fixed SMR located beside one of the surface references. These measurements are repeated for several different spatial separations by moving two of the surface references and the SMR closer together. The air handling system was running throughout the entire test, which took about four hours to complete.

The data are used to evaluate perturbations in the individual measurements and correlation between the different measurement systems as a function of spatial separation. The comparisons between the laser tracker and the references are the most important in this study, because they simulate use of the references in the Laser Tracker Plus system.

Results comparing two identical references are also presented, because this is a better way to examine the spatial correlation of environmental perturbations, in particular index variations.

This study was conducted using the Laser Tracker Plus system installed in the SOML test tower. The setup is shown in Figure 5-1. The surface references were initially positioned on blocks on the floor so that they were nominally along the same lines of sight that they would be on if they were positioned around the edges of an 8.4 m mirror. A nest with a laser tracker SMR was placed atop the same block that the north surface reference was mounted on. The east and west surface references remained stationary throughout the measurements, while the north and south surface references and the SMR were moved in 1 m steps toward the center of the measurement area (equivalent to the center of the mirror).

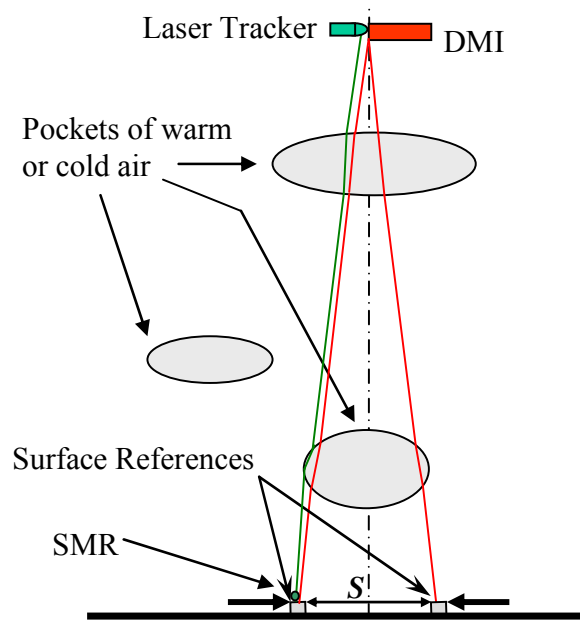


Figure 5-1: Diagram of the test setup used for measuring the correlation between the fluctuations of two of the DMI reference beams for different separations S .

Each time the north and south surface references were moved, the north and south steering mirrors, mounted up with the other DMI optics, were adjusted to point at the new measurement locations, and the references were realigned to the DMI beams. A HeNe laser, pointing due south aligned to the azimuth encoder axis of the laser tracker, was used to maintain the relative clocking angles of the PSD references. A pentaprism was used to divert the laser light 90° to reflect off flat mirrors mounted on the sides of the PSDs on both the north and south surface references. For each measurement location, the north and south surface references were aligned to their DMI beams in tip, tilt, and lateral position, and aligned in clocking to cause the HeNe alignment laser beam to retroreflect off the flat mirror and back through the pentaprism to the laser head. The laser tracker's SMR moved with the north surface reference to each new measurement location.

At each measurement location, all of the references and the laser tracker simultaneously measured at their maximum rate over an extended period of time, and the results were averaged into 1 s intervals. For most cases, measurements were made for 5 minutes. For the case of the two measurement positions closest together (loosely referred to as the center of the mirror) and farthest apart (referred to as the edge of the mirror), a set of 1 hour long measurements were made.

5.2 Radial Correlation

Because radial errors couple directly into surface measurement errors, the radial correction is critical for improving the surface measurement accuracy. The results from the DMI system are routinely applied to the laser tracker data to improve the accuracy of

the data with good results. The following sections present the results of the radial portion of the correlation study, with special emphasis on the measurements that were made at the edge of the mirror because this is the location of the references in normal operation.

5.2.1 DMI and Radial Laser Tracker Results

The data measured for the position when the two references were spaced the furthest apart is shown in Figure 5-2. The plots shows variations measured by the two DMIs compared to the variations measured by the laser tracker for the same time period. The general shapes of all three plots agree well and show real drift of about 4 μm , but the DMIs have more noise. The laser tracker has lower noise in part because it measures 20 times faster than the DMIs, so it is capable of measuring 20 times more data per second, so it should have about $\frac{1}{\sqrt{20}} \approx 0.22$ times less noise than the DMIs from this alone.

Figure 5-3 shows the relative motion of the same DMIs and laser tracker over just the first 5 minutes of the data set. The relative magnitude and shape of the noise for the DMIs versus the laser tracker is clearer to see.

The 4 μm drift is probably due to thermal expansion of the tower. It represents a temperature change of about 0.02 K. The 1 hour duration is representative of a single scan of the 8.4 m segment, typically about 40 minutes.

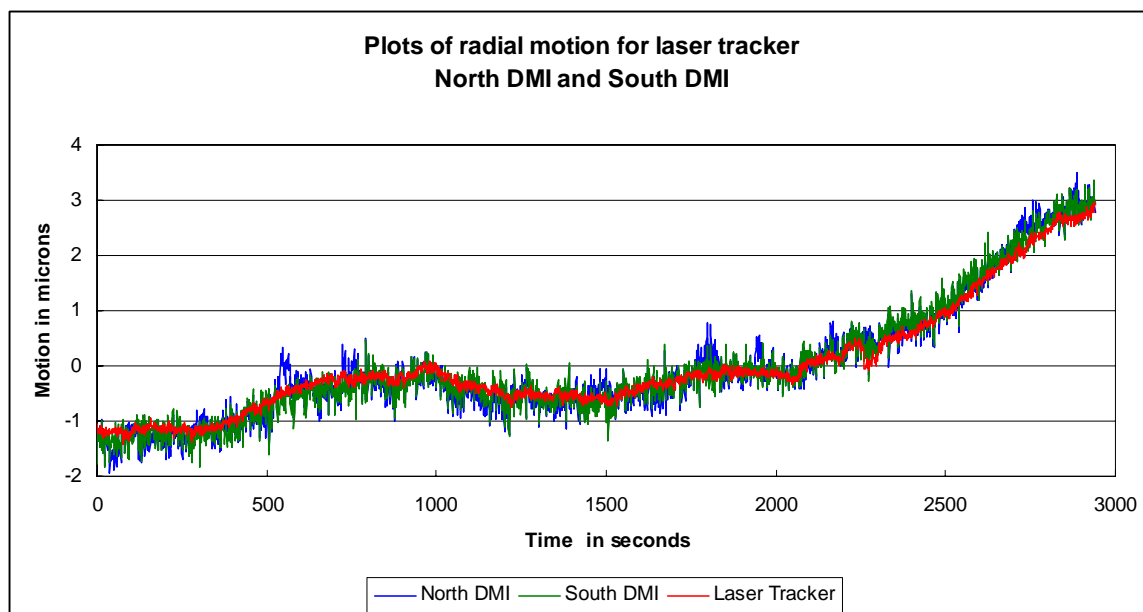


Figure 5-2: Radial motion measured by the laser tracker, compared to the motion measured by the north and south DMI for the entire data set [45].

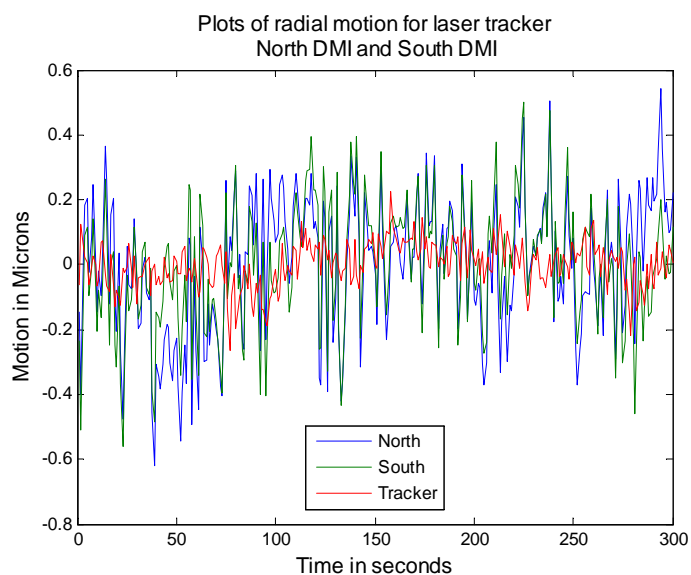


Figure 5-3: Relative radial motion measured by the laser tracker, compared to the motion measured by the north and south DMI for the first 300 s of the data set.

The noise in both the laser tracker and the DMIs can be reduced by averaging over longer time intervals. Figure 5-4 shows plots of the laser tracker motions for four different integration times: 1, 2, 5, and 10 s. The plots are generated by averaging consecutive sets of 1 s measurements. A table of the rms values for each integration time is provided on the right. A similar set of plots and tables of rms values for each time interval are provided in Figure 5-5 and Figure 5-6 for the north and the south DMI readings.

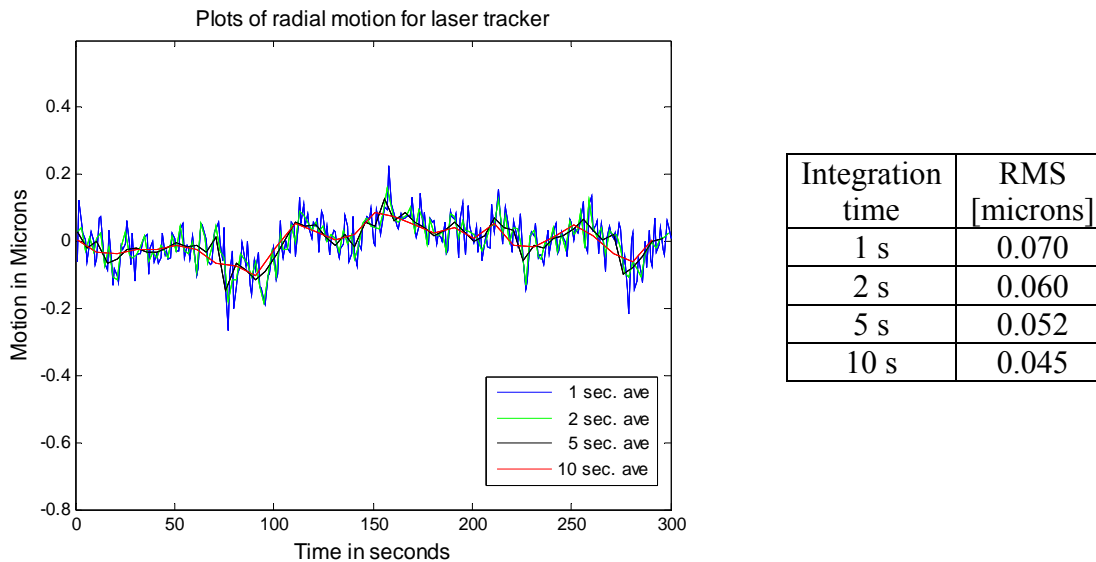


Figure 5-4: Plots showing a smoothing of the laser tracker data with increased measurement integration time. The table on the right shows the rms of each plot.

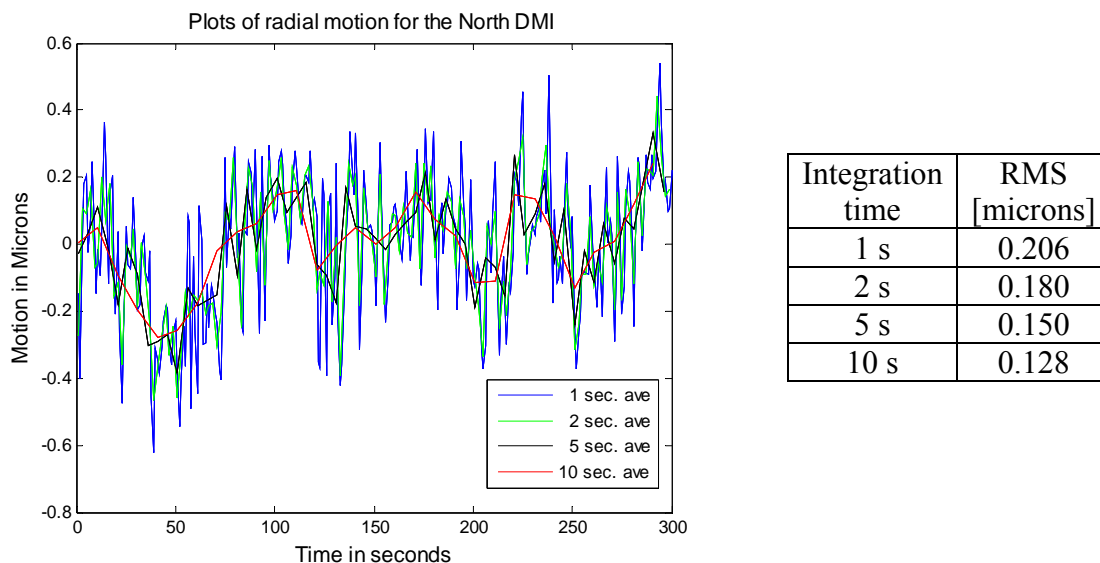


Figure 5-5: Plots showing a smoothing of the North DMI data with increased measurement integration time. The table on the right shows the rms of each plot.

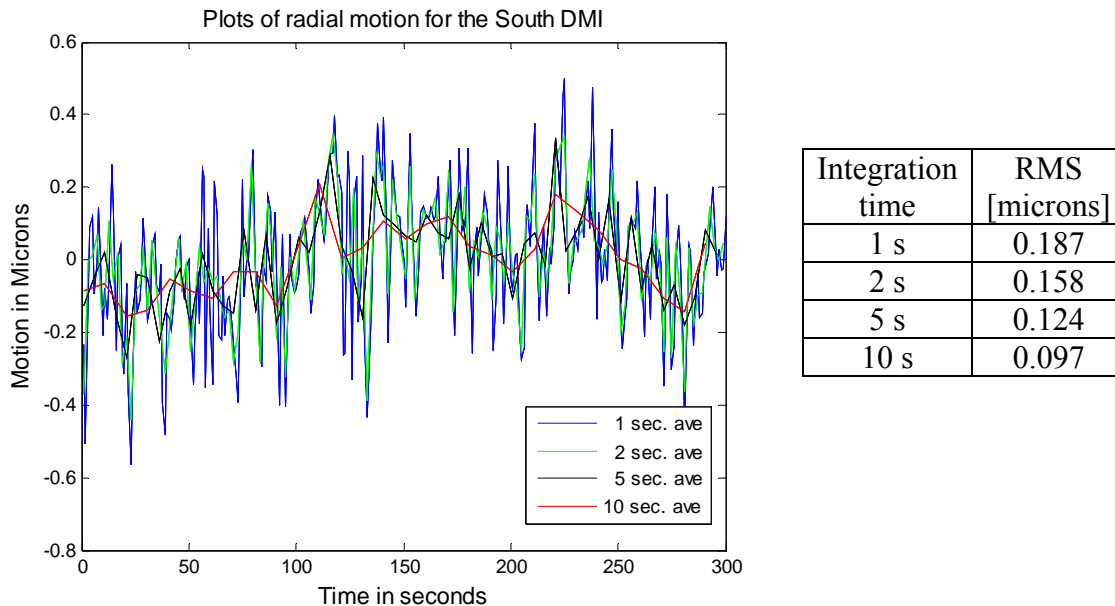


Figure 5-6: Plots showing a smoothing of the South DMI data with increased measurement integration time. The table on the right shows the rms of each plot.

5.2.2 Spatial Correlation of Distance Measurements

The spatial correlation of the distance measurements can be determined by taking the difference between two DMI readings as a function of the separation of the surface references. Figure 5-7 shows the difference as a function of time for the north and south DMIs, separated by 9.3 m (which projects to 8.4 m at the height of the mirror). This indicates that the high frequency component of the DMI data is correlated spatially, or that it contains instrumental effects that are common to both DMI references. There is less correlation between the two DMIs at lower frequencies, < 0.1 Hz. There is some correlation even at low frequencies, because the rms difference is about the same as the rms of either DMI alone, as opposed to being $\sqrt{2}$ larger as it would if the motion were uncorrelated.

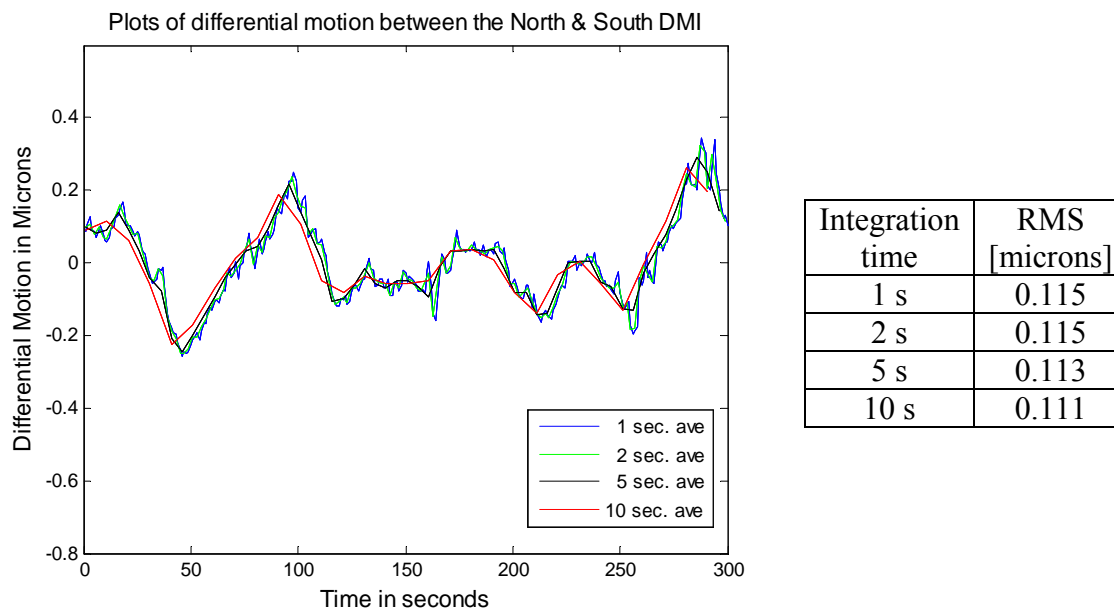


Figure 5-7: Difference in motions measured by the north and south DMIs.

There is no similar high-frequency correlation between a DMI and the laser tracker. Figure 5-8 shows the difference as a function of time for the north DMI and the laser tracker, separated by 0.2 m. Most of the high-frequency differential motion is due to the DMI, which has much more high-frequency structure than the laser tracker.

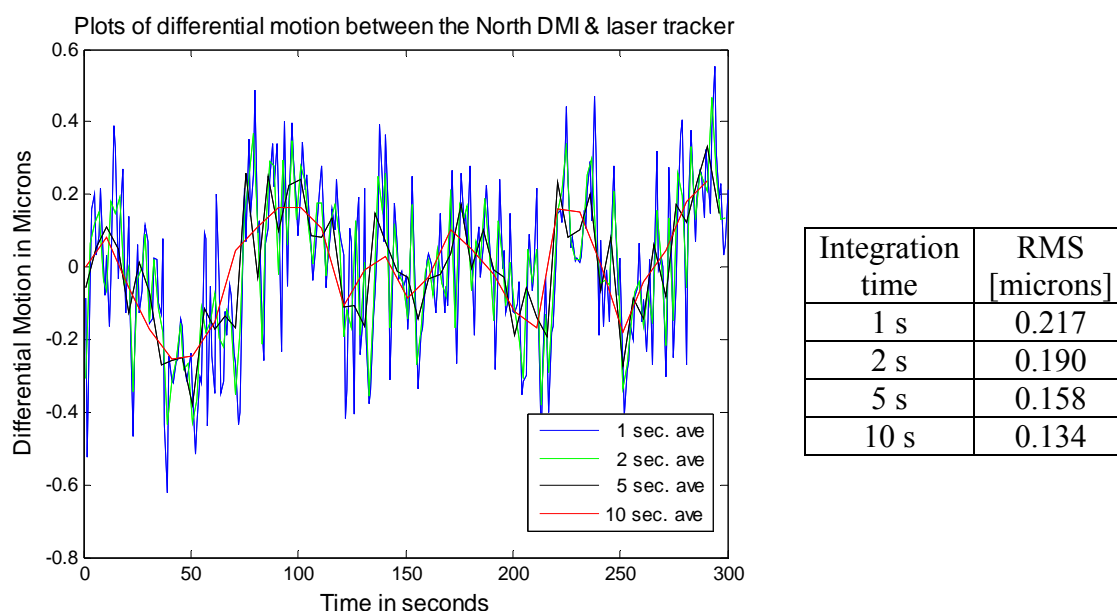


Figure 5-8: Difference in motions measured by the laser tracker and the North DMI.

The expectation is that the correlation between the different measurement systems will be highest for small separations, and will decrease as the spatial separation increases. For the two DMIs, this appears to be the case, as shown in the plot in Figure 5-9. To generate the plot, a 300 s long set of the measurement data was extracted for each measurement location. The rms difference between the two DMIs and the rms of a single DMI are shown as a function of separation.

In Figure 5-9, the upper plot shows the real magnitude of the motion, while the lower plot is normalized by the rms of the single DMI, to account for variations in the

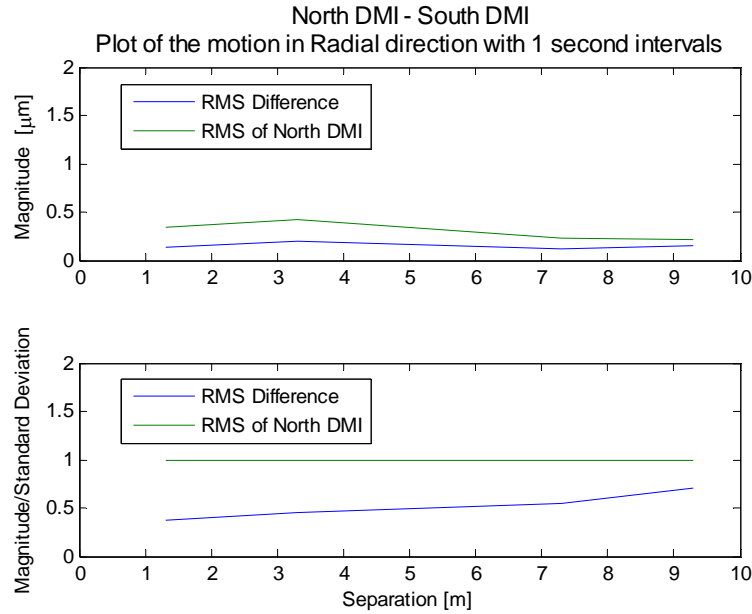


Figure 5-9: Correlation between the north and south DMI as a function of spatial separation. So long as the blue curve is below the green curve, the DMIs are measuring more common motion than noise, so the correlation is high.

conditions among different data sets. The green curves are σ_A , the standard deviation of the north DMI, as a function of its position (distance from the south DMI). The blue curves are σ_{A-B} , the rms difference between the north and south DMIs, as a function of separation. In both cases, the mean displacement is subtracted. So long as $\sigma_{A-B} < \sigma_A$, then $\sigma_{Cor} > \sigma_N$, so the two instruments are measuring more common motion than noise. Therefore, the error in the measurement is reduced by subtracting the two readings.

Figure 5-10 contains a similar set of plots showing the correlation between the laser tracker and the north DMI. This time, σ_{LT} is the standard deviation of the laser tracker, which is used to generate the green curves, while the blue curves are σ_{LT-DMI} , the rms difference between the north DMI and the laser tracker. The standard deviation of

the laser tracker is used to normalize the quantities in the lower plots. The rms difference is greater than the rms tracker reading for all separations ($\sigma_{LT-DMI} > \sigma_{LT}$), indicating $\sigma_{Cor} < \sigma_{N_{DMI}}$, so there is more DMI noise than correlated motion. In this case, applying the DMI correction by subtracting the DMI value from the laser tracker value would couple more noise into the data than common motion it would remove.

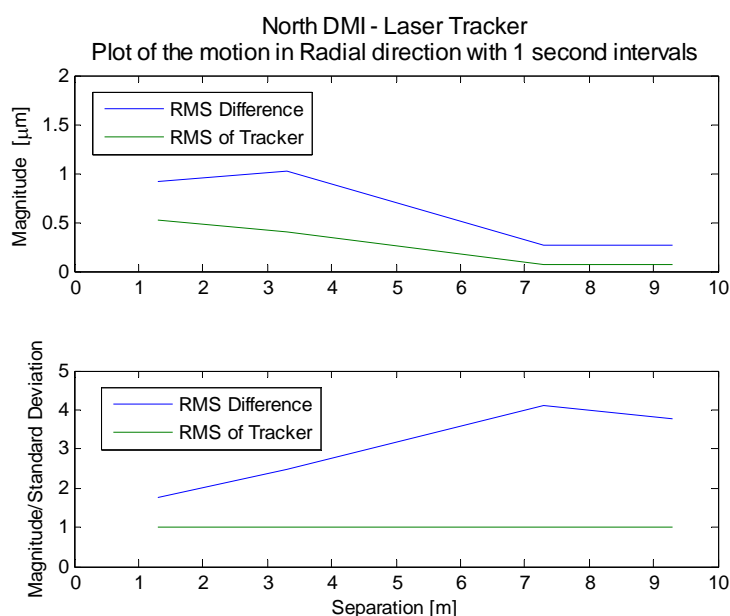


Figure 5-10: Correlation between the north DMI and the laser tracker as a function of spatial separation. Because the blue curve is above the green curve, there is less common motion than DMI noise in the measurements.

Note that the upper plot shows the opposite of the trend expected for spatial correlation. When the quantities are normalized to correct for variations in measurement conditions (such as air turbulence), the expected reduction in correlation with separation returns.

Because these correlation measurements were done on the floor, which is very stiff, the actual relative motion is very small, so the measurements are dominated by

partially correlated index variations and uncorrelated instrumental noise. For a real measurement on the mirror surface, the mirror mount is not as stiff, so there is more common motion from the mirror tipping on its mount, as seen in Figure 2-6. In that case, the common motion is greater than the noise, so performing the DMI correction gives a net decrease in the measurement error. For this reason, the DMIs are important components for improving the Laser Tracker Plus measurement accuracy. Figure 5-2 also shows that drift in the tower dimensions causes significant correlated motion over a period of 1 hour, though it is not significant in the 5 minute durations used for Figure 5-9 and Figure 5-10. The sources of correlated motion dominate the DMI noise in a real surface measurement, so it is clearly beneficial to apply the correction.

5.2.3 Applying DMI Correction

The four DMI measurements can be described by four basis functions, three describing the planar motions of the mirror surface (piston, tip, and tilt), and a fourth non-planar term (astigmatism) that indicates the deviation of the measurements from a plane. These basis functions are represented pictorially in Figure 5-11. The basis functions match the first four Zernike polynomials listed in Table E-1. With the DMI values reported in microns to match the laser tracker data, a fit of the first four Zernike polynomials is made to the four DMI displacements. The piston, tip, and tilt terms are interpreted as rigid-body motion of the segment. Motion of the Laser Tracker Plus instrument platform, and linear variations in refractive index, have the same signature as motion of the segment, and they can be compensated using the same formula. The

contribution of this motion is then evaluated at the location of the tracker measurement, and an offset is applied to the tracker measurement at that location.

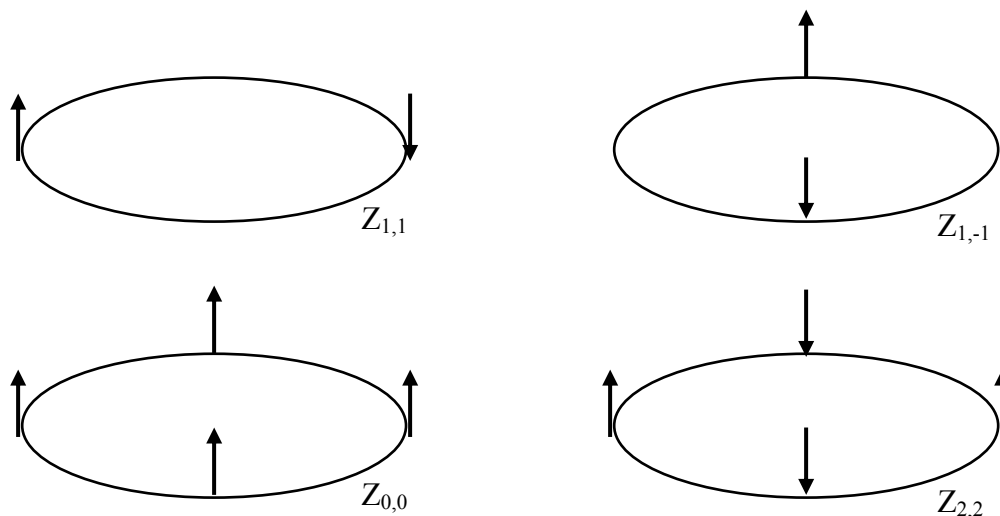


Figure 5-11: Pictorial representation of the four basis functions that describe motions observed by the distance measuring interferometer system. These basis functions match the four lowest Zernike polynomials, (piston, tilt X, tilt Y, and astigmatism) listed in Table E-1.

5.3 Angular Correlation

The PSD system is used for making angular corrections to the laser tracker surface measurements. The angular errors $\delta\theta$ produce a mapping error that indirectly couples into surface measurement errors δs . The magnitude of this coupling is a function of the angle of incidence α at the measurement point; as expressed in Equation 2.1. It was initially believed (based on laser tracker angular noise measurements made years earlier in the old test tower with a different laser tracker) that these angular errors would limit the accuracy of the Laser Tracker Plus system if they were not corrected. For this

reason, the PSD references were added to the Laser Tracker Plus system design. The results measured during this correlation study indicate that the laser tracker pointing is considerably less noisy than the earlier measurements indicated, and it is therefore unnecessary to make any corrections using the PSD results. The following sections present the results of the angular portion of the correlation study, again with special emphasis on the measurements that were made at the edge of the mirror because this is the locations of the references in normal operation.

5.3.1 PSD and Laser Tracker Pointing Results

The first step in evaluating the angular correlation is to look at the magnitude of the dither measured by the laser tracker and the PSDs when staring in the test tower. This gives an indication of the pointing stability for the different instruments. The laser tracker results are shown in Figure 5-12 for the case when the references and laser tracker beam were located at the region on the floor that approximated the edge of the mirror. Measurements were made for nearly an hour, with each point integrated for 1 s. The results for the entire data set are shown in the plot on the left, while the plot on the right shows just the first 300 s of data. The resulting surface errors are almost insignificant with noise fluctuations less than 0.5 μrad rms. This results in an average surface error of about 0.55 μm rms.

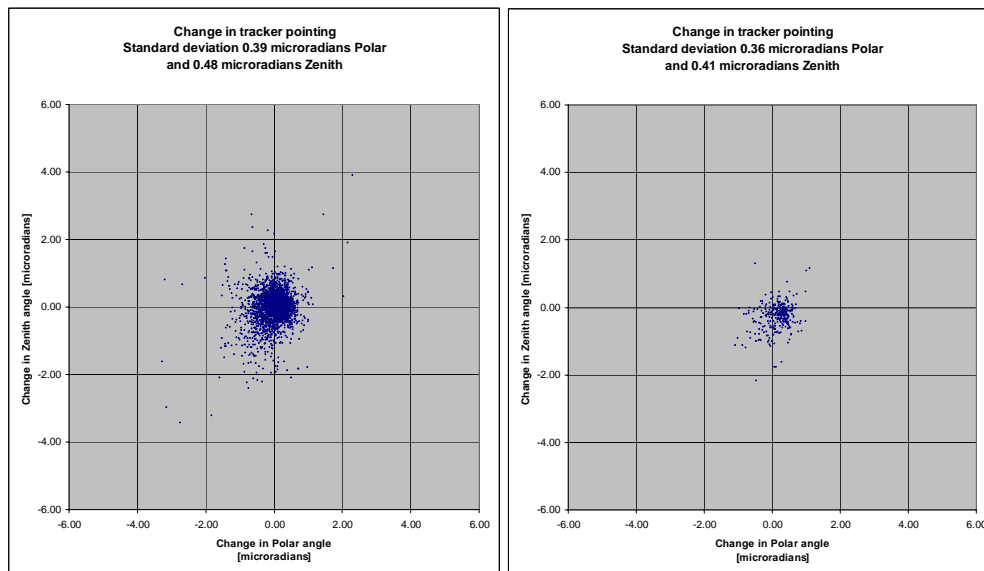


Figure 5-12: Typical measurements of the dither experienced by the laser tracker in the SOML test tower. Over the course of 1 hour, ~ 3600 measurements were made with 1 s integration time (left). The right plot shows the first 300 measurements. The fluctuations are almost insignificant at less than $0.5 \mu\text{rad rms}$ [45].

The measurements of the fluctuations in the PSDs' readings were not nearly as good as those of the laser tracker. Like the DMIs, the PSD measurements are noisier than the laser tracker measurements, which may be a result of the much slower data collection rate. The results for the north PSD are shown in Figure 5-13, while those for the south PSD are shown in Figure 5-14. The lateral displacements measured by the PSDs have been converted to angles at the Laser Tracker Plus instrument platform. The left-hand plots in both figures show the dither in the reference beam measured by each PSD over the entire hour-long data set. Each point represents a 1 s long averaged measurement of the reference beam location. The different colors represent consecutive 300 s long blocks of time. The uniform distribution of the colors in each plot indicates there was little long-

term drift affecting the measurements of either PSD. The right-hand plots show just the first 300 s of the same data sets.

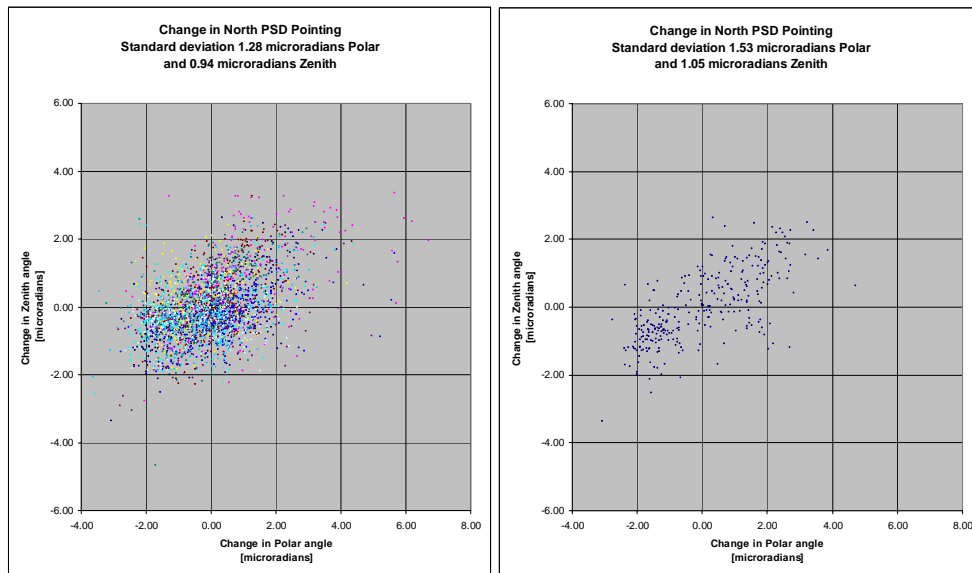


Figure 5-13: PSD measurements of the dither in the north reference beam. The plot on the left shows the pointing results at 1 s intervals for the entire data set (nearly 1 hour long) measured at the edge of the mirror. Each color represents a consecutive 300 s long block of time. The plot on the right shows just the first 300 s of the data set.

The plots shown in Figure 5-12 through Figure 5-14 can each be represented as two orthogonal time-series plots, shown in Figures 5-15 through 5-17. Similar to the radial time-series plots, each of the angular time-series plots contain four curves with different integration times: 1, 2, 5, and 10 s. A table of the rms values for each integration time is provided to the right of each plot, showing that by integrating over longer periods of time, the noise in both the laser tracker and the PSDs measurements is reduced. Each of the plots was generated by averaging consecutive sets of 1 s integration time measurements to determine the mean value for each integration time.

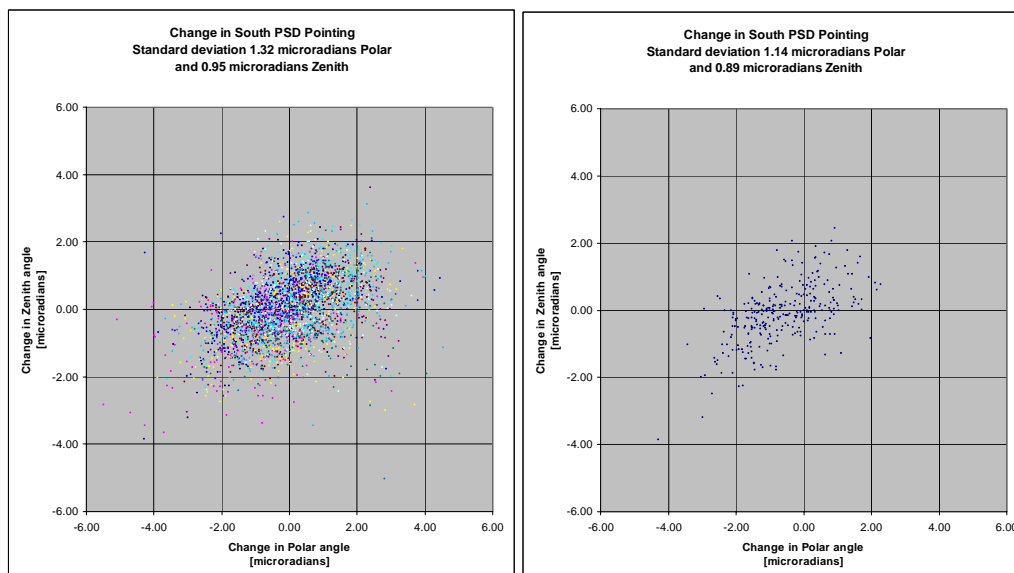
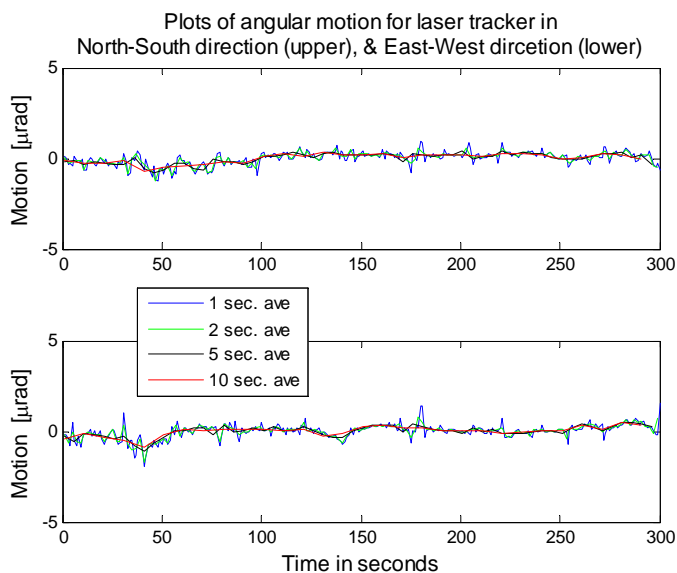


Figure 5-14: PSD measurements the dither in the south reference beam. The plot on the left shows the pointing results at 1 s intervals for the entire data set (nearly 1 hour long) measured at the edge of the mirror. Each color represents a consecutive 300 s long block of time. The plot on the right shows just the first 300 s of the data set.



Integration Time	RMS [μrad]
North-South direction	
1 s	0.36
2 s	0.33
5 s	0.29
10 s	0.26
East-West direction	
1 s	0.41
2 s	0.35
5 s	0.31
10 s	0.28

Figure 5-15: Plots showing a smoothing of the laser tracker data with increased measurement integration time. The table on the right shows the rms of each plot.

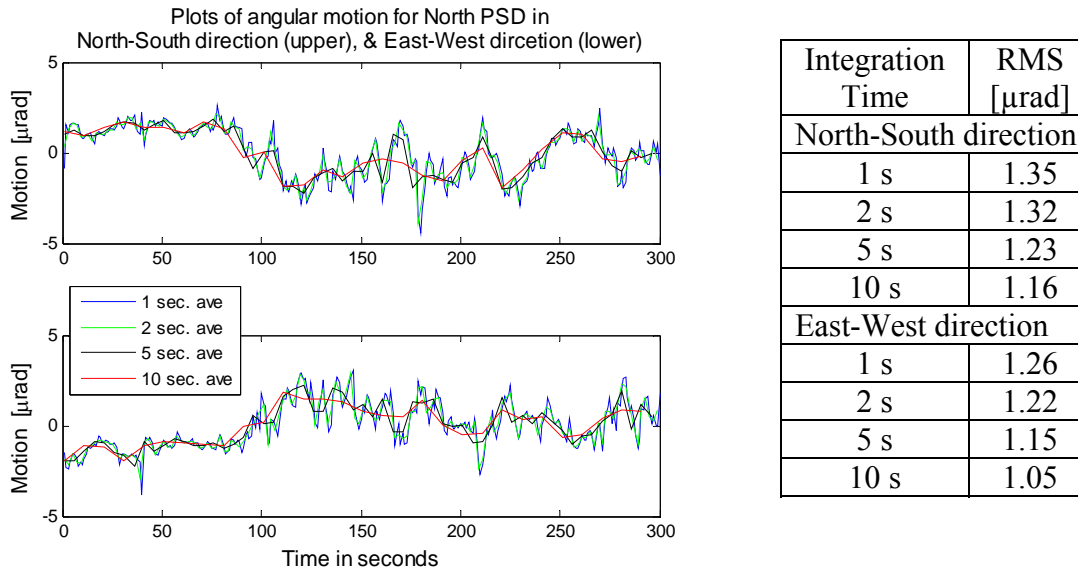


Figure 5-16: Plots showing a smoothing of the north PSD data with increased measurement integration time. The table on the right shows the rms of each plot.

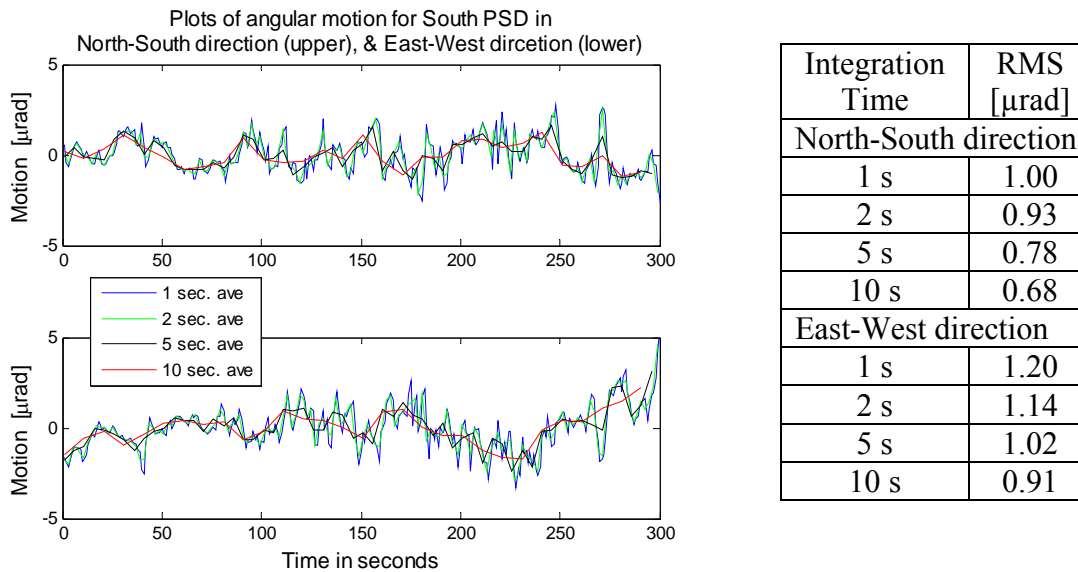


Figure 5-17: Plots showing a smoothing of the south PSD data with increased measurement integration time. The table on the right shows the rms of each plot.

5.3.2 Spatial Correlation of Angle Measurements

Unlike the radial correlation results that were discussed in Section 5.2.2, the PSDs are not as well correlated as the DMIs. Figure 5-18 shows that when the difference is taken between the motions of the north and south PSDs, much of the high-frequency fluctuations remain and the rms is worse. Figure 5-19 shows the difference in the motions measured by the laser tracker and the north PSD, showing the majority of the high-frequency measurement fluctuations remain and the rms is worse for each curve. This indicates poor correlation between the two instruments.

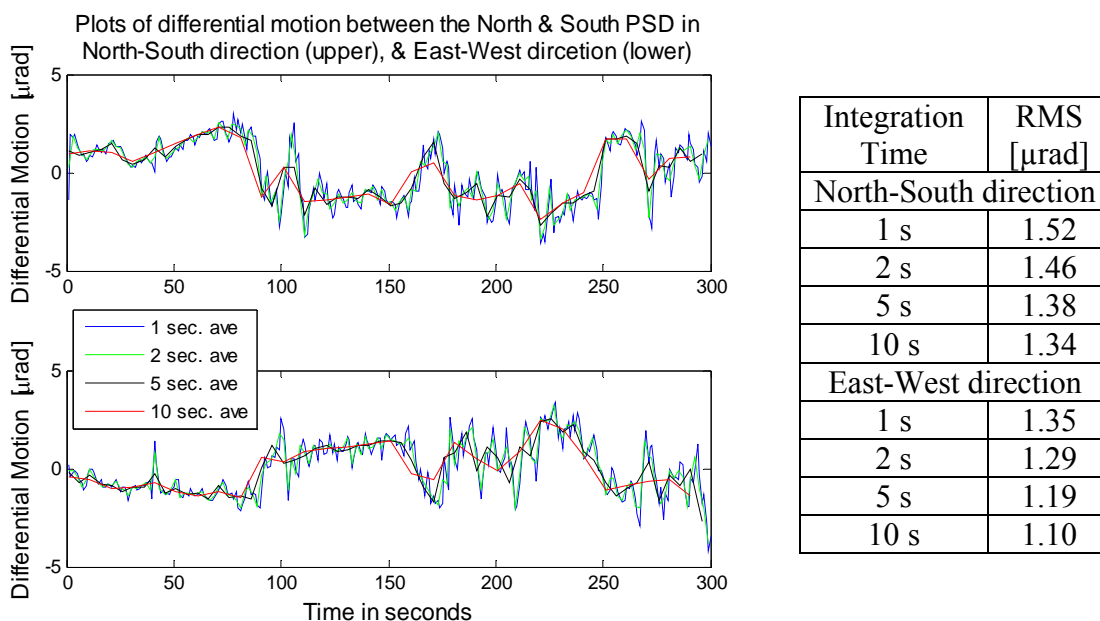


Figure 5-18: Difference in motions measured by the north and south PSDs. Much of the high frequency noise remains after the subtraction, showing poor correlation for the PSD measurements.

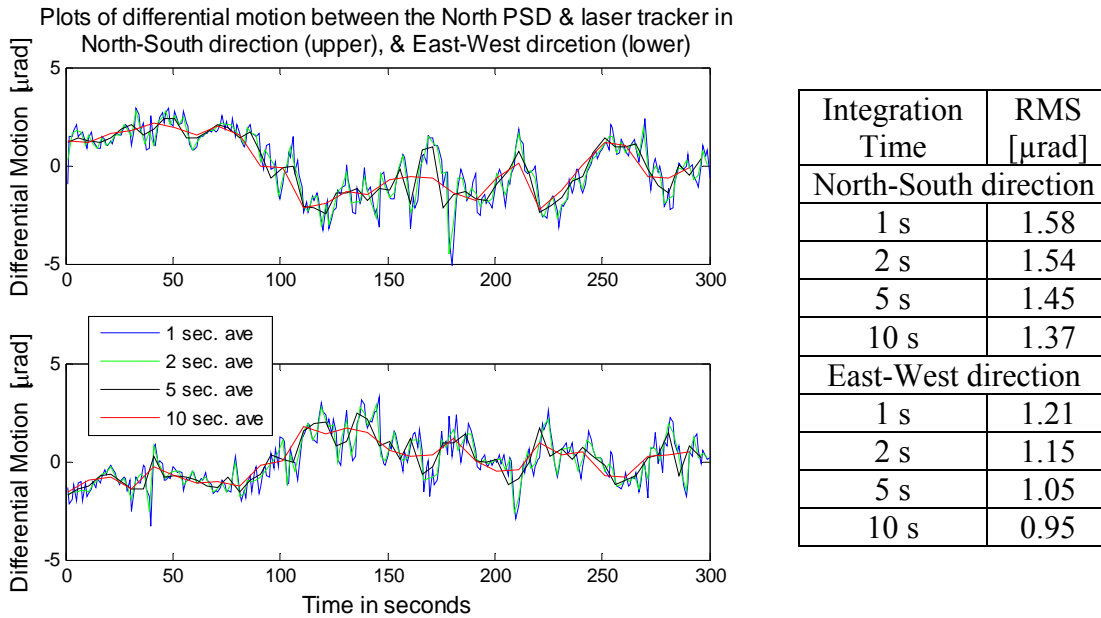


Figure 5-19: Difference in motions measured by the laser tracker and the north PSD. The plot still show a lot of the high frequency noise, showing that there is poor correlation for the high frequency component of the measurements.

Again, the expectation is that the angular correlation between the different measurement systems will be higher when they are close together, and will decrease with increased spatial separation. The plots in Figure 5-20 show the spatial correlation between the north and south PSDs in the north-south direction, while Figure 5-21 is for the east-west direction. The two sets of plots generally show the expected trend of decreased correlation with increased spatial separation. The green curve in the upper plot is σ_A , the rms lateral motion measured by the north PSD and converted to an angular deviation at the Laser Tracker Plus instrument platform. Each data set contains 300 samples at 1 s intervals. The blue curve is σ_{A-B} , the rms difference between the north and south PSD readings in each direction over the 300 s long measurement for each spatial separation position. In all cases, the mean is subtracted.

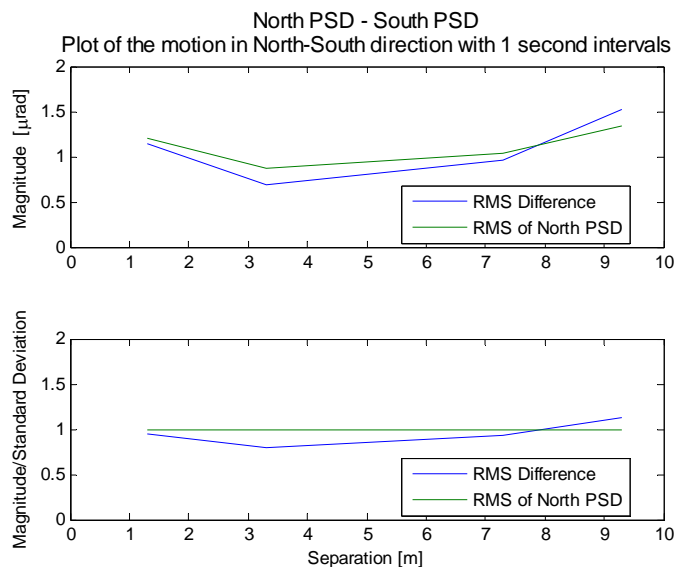


Figure 5-20: Correlation between the north and south PSDs for motion in the north-south direction, as a function of spatial separation. Where the blue curve is below the green curve, the PSDs are measuring more common motion than noise.

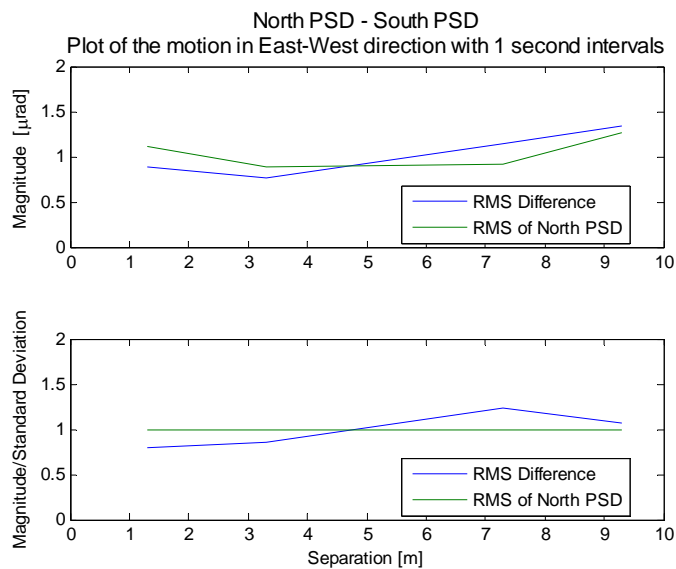


Figure 5-21: Correlation between the north and south PSDs for motion in the east-west direction, as a function of spatial separation. Where the blue curve is below the green curve, the PSDs are measuring more common motion than noise.

The upper plot in each figure shows the real magnitude of the motion, while the lower plot is normalized by the standard deviation to account for variation in the conditions among different data sets. So long as the rms difference in motions measured along a particular axis of the PSDs is less than the standard deviation of an individual PSD ($\sigma_{A-B} < \sigma_A$), then the two PSDs are measuring a common motion that is larger than the noise ($\sigma_{Cor} > \sigma_N$). The plots show that there is good correlation between the PSDs for separations $S < 8$ m in the north-south direction and $S < 5$ m in the east-west direction. Beyond that point, $\sigma_{Cor} < \sigma_{NB}$, so the correlation is poor between PSDs sitting on opposite edges of the mirror.

Figures 5-22 and 5-23 show a similar set of plots comparing the correlation between the laser tracker and the north PSD along each axis. This time, the green plots are σ_{LT} , the standard deviation of the laser tracker in each axis, while the blue plots are σ_{LT-PSD} , the rms difference between the north PSD and the laser tracker in a particular direction. The standard deviation of the laser tracker is used to normalize the quantities in the lower plot. The blue plot is well above the green plot for all separations ($\sigma_{LT-PSD} > \sigma_{LT}$), indicating that $\sigma_{Cor} < \sigma_{N_{PSD}}$, so there is poor correlation and the PSDs should not be used to correct the laser tracker angles.

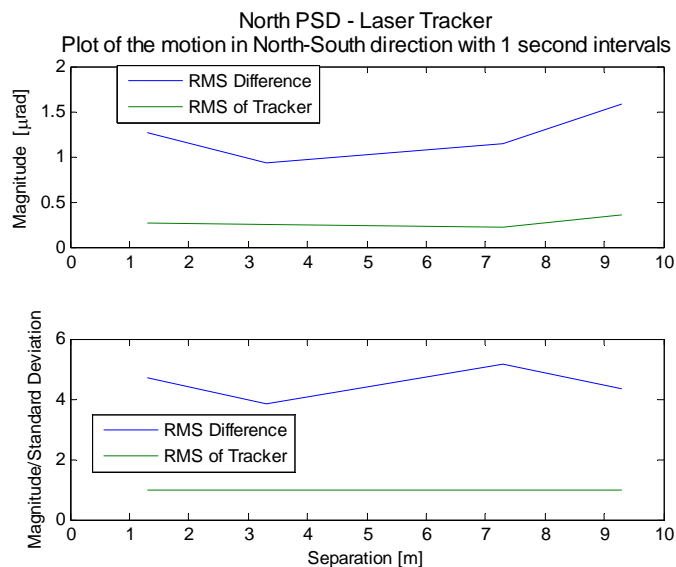


Figure 5-22: Correlation between the north PSD and the laser tracker in the north-south direction for different spatial separations. Because the blue curve is above the green curve, there is less common motion than PSD noise in the measurements, so the correlation is low.

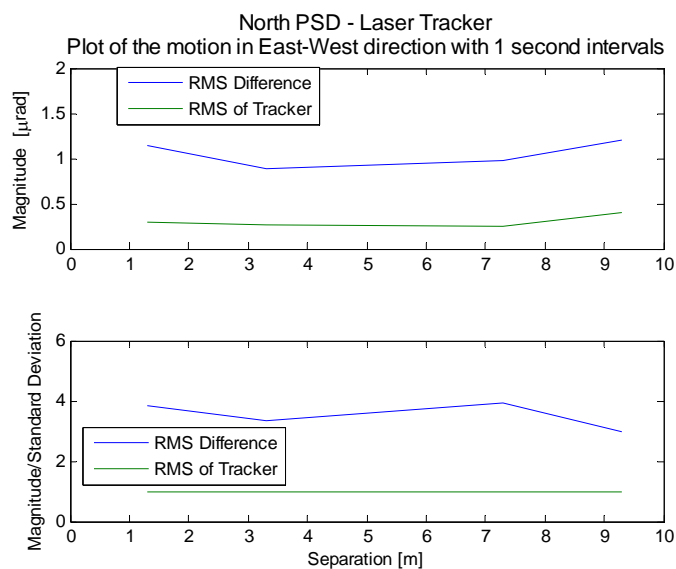


Figure 5-23: Correlation between the north PSD and the laser tracker in the east-west direction for different spatial separations. Because the blue curve is above the green curve, there is less common motion than PSD noise in the measurements, so the correlation is low.

5.3.3 Applying PSD Correction

The angular correlation study gives two important conclusions. First, the laser tracker angle measurements have so little noise due to index variations and instrumental effects that there is no need to apply a PSD correction. Second, applying a PSD correction would make the measurements worse because the added errors from noise and instrumental effects exceed any reduction of correlated motion. However, in different measurement conditions, it might be beneficial to apply a PSD correction, so a description of the process is included in this section for completeness. It is important to keep in mind that there must be good correlation to apply the correction; otherwise the measurements could be made worse by coupling in additional errors.

A PSD measures lateral motion of the reference beam. In order to apply a correction to the laser tracker's angle measurements, the PSD displacements are converted to equivalent angular shifts at the Laser Tracker Plus instrument platform. The details of this conversion are discussed in Appendix F.

The PSDs measure angular displacements at four points, which need to be interpolated at the position of the SMR. This can be done by fitting polynomials to the PSD displacements. Zhao developed a set of vector polynomials that optimally describe mapping errors [41,42]. The PSD displacements can be used to measure the lowest order Zhao polynomials, which are discussed in Appendix E. To do this, a set of basis functions must first be determined to describe the motions measured by the PSDs. Because there are four PSDs, each measuring two axes of motion, then eight basis functions are required to completely describe the motions measured by the PSDs. These

basis functions are expressed pictorially in Figure 5-24. These functions are similar to several low-order Zhao polynomials, which are shown as vector plots in Figure 5-25.

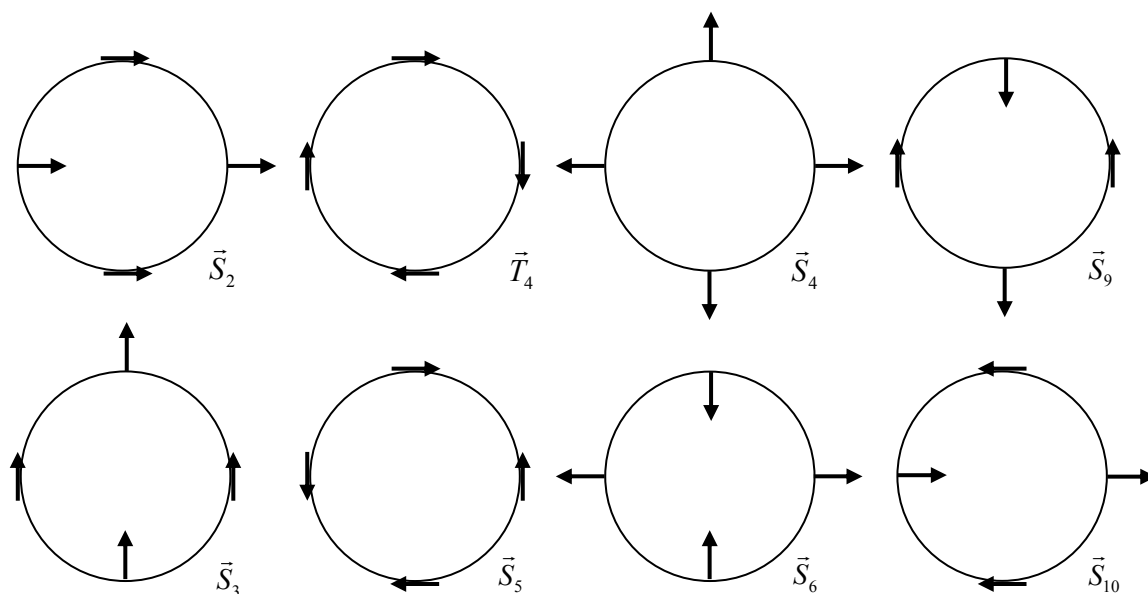


Figure 5-24: Pictorial representation of the basis functions that describe the motion measured by the PSD system. These functions are labeled by the corresponding Zhao polynomials, which are discussed in Section E.3.

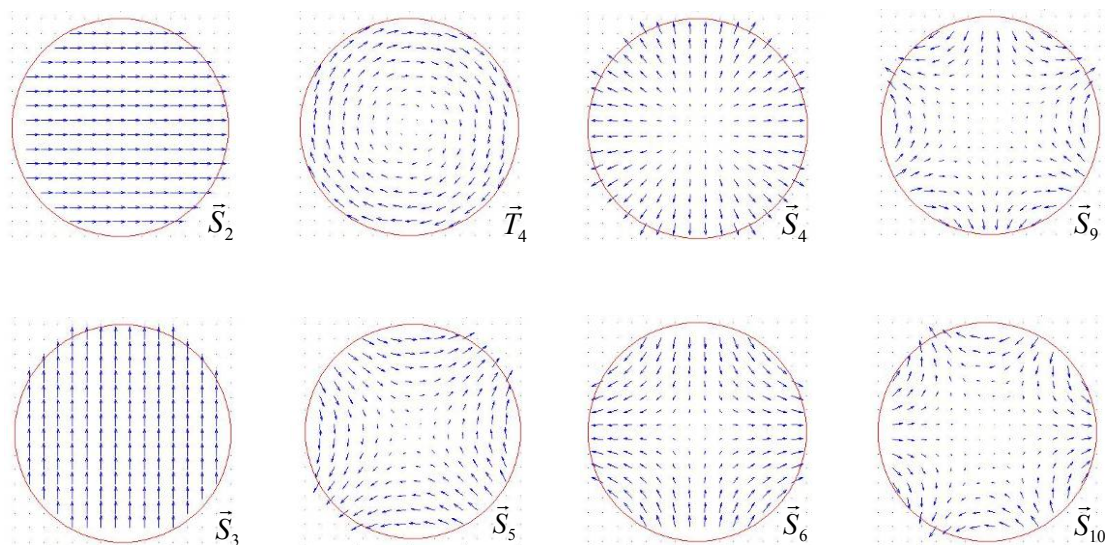


Figure 5-25: Vector plots of the eight low-order Zhao polynomials that are the closest match to the eight PSD basis functions shown pictorially in Figure 5-24 above.

The two basis function on the far right of Figure 5-24 most closely match the \vec{S}_9 and \vec{S}_{10} Zhao polynomials, however it is more likely that a fit of the data to distortion mode this high will be driven more by noise rather than real motion. Including all eight modes in the fit would likely include a lot of noise, so only the four lowest mode are included ($\vec{S}_2, \vec{S}_3, \vec{S}_4, \& \vec{T}_4$). These remaining Zhao polynomials are evaluated at the PSD positions to give their influence functions, which together form an 4×8 interaction matrix that is used to solve for the polynomial coefficients that fit a given set of PSD measurements. The polynomials are then evaluated at the position of the SMR for the simultaneous laser tracker measurement. The result is the angular error, which is subtracted from the laser tracker measurements. This correction is made before the laser tracker measurements are compared to the ideal mirror surface.

In the geometry of the GMT measurements, only the radial displacements cause a significant surface error, but there is no harm in applying the correction in both radial and tangential directions. The two angles measured by the laser tracker do not correspond to the radial and tangential angles on the mirror, so correcting only the radial angles does not simplify the process.

5.4 Correlation Study Conclusions

When the correlation study was conceived, it was decided that the measurements would be made to compare the correlation between two identical sensors: two of the surface references. An important conclusion from the study is that the measurements

from the DMIs and PSDs are noisier than the laser tracker measurements. In retrospect, it is too bad that two laser trackers were not available at the time of this study. This would have given a better measurement of environmental perturbations, but the combination of a laser tracker and a DMI or PSD is more relevant to the optimum use of external references in the Laser Tracker Plus system.

The specifics of why the DMIs and PSDs are noisier than the laser tracker are not clear, but it is most likely the combination of larger instrumental noise and their lower sampling rate. For the distance measurements, it makes sense that the number of samples averaged is the main factor, because the measurements from the two instruments are fundamentally identical. This is not true for the angle measurements. The effect of index variations is the same, but the instrumental noise characteristics for both sensors may be very different.

For the DMIs, the manual states that the error sources can be broken down into three categories: intrinsic instrumentation errors, environmental errors, and installation errors. Because the references were stationary for this study, the installation errors are effectively zero, leaving just the instrumental noise and the environmental effects. The instrumental errors break down into wavelength stability, electronic error, and optical nonlinearity for a combined contribution of $\sim\pm 0.06 \mu\text{m}$. Figure 5-5 and Figure 5-6 show DMI perturbations on the order of $\pm 0.2 \mu\text{m}$, so the index variations appear to dominate over instrumental noise.

An integrating sphere was used to measure the instrumental noise for the PSDs. The integrating sphere provided a stable, uniform intensity light source that fully illuminated the PSD detector, eliminating potential pointing errors that could have

resulted by using a laser beam as a source. The detector was positioned at the output of the integrating sphere, to minimize environmental effects. By using a stable source, the instrumental noise for the PSD system can be determined from the measured fluctuations, which are the result of noise in the detector or readout electronic. Despite the efforts to stabilize the source, a drift of ~ 15 mV was recorded. It is unclear if this was instrumental or setup related. This drift would correspond to an angular change of ~ 0.29 μrad at a distance of 25 m, which is approximately the distance from the Laser Tracker Plus electronics in the tower to the floor where the majority of the correlation measurements were made. Making the assumption that the drift is due to mechanical instability in the setup, a linear fit with time was made to the PSD data and removed. The residual PSD perturbation is about 1.8 mV rms, which corresponds to an angular error at 25 m of 0.032 μrad . This is considerably smaller than the fluctuations measured during the study, indicating that environmental effects probably cause most of the measured fluctuations in the tower. The PSDs are limited by their sampling rate, where 34 measurements per second is typical compared to 1000 samples per second for the laser tracker. Assuming random perturbations, the PSD outputs should be about six times noisier than the laser tracker based on their sampling rates. In fact the PSD is only about three times noisier, indicating that if the hardware that digitizes the PSD analog signal were replaced with a digitizer that could sample at 1000 Hz, the PSDs might have less noise than the laser tracker, making a PSD correction possible.

Another important difference between the distance measurements and angle measurements is that the distance measurements on the mirror are known to be affected by rigid-body motion, which is 100% correlated, i.e. the plane fit to the four DMIs,

evaluated at the SMR location, is perfectly correlated with the real motions measured by the laser tracker (ignoring the errors in measuring the motion). The angle measurements on the mirror may not be affected much by relative motion. They could be if the Laser Tracker Plus instrument platform in the tower were to tilt, but the laser tracker scatter plot in Figure 5-12 indicates there is very little motion due to that. Therefore, there is no reason to think the angular measurements on the mirror have any more correlation than those on the floor. Since the angle correlation failed the test on the floor, it is safe to assume it would fail on the mirror.

More insight can be gained into possible correlations when the surface references are on the mirror by examining the PSD motions recorded in GMT surface measurement data set gmt1 090630 3 mod.xls. There is a drift component in the PSD measurements of about 0.55 μrad P-V, and the standard deviation of the PSD measurements is 1.13 μrad . If the assumption is made that the drift is correlated with the laser tracker, then $\sigma_{Cor} \approx 0.2 \mu\text{rad}$ rms, while $\sigma_{N_{ref}} = 1.13 \mu\text{rad}$ rms. Assuming the noise in the laser tracker measurements is still $\sigma_{N_{LT}} = 0.5 \mu\text{rad}$ rms, then the error made by not correcting for the correlated motion with the PSD is

$$\sigma_{LT}^2 = \sigma_{Cor}^2 + \sigma_{N_{LT}}^2 = (0.2 \mu\text{rad})^2 + (0.5 \mu\text{rad})^2 = (0.54 \mu\text{rad})^2.$$

This 0.54 μrad rms error in angle would cause a 0.65 μm rms error in the GMT surface.

If the PSD correction were to be made, than the resulting error would become

$$\sigma_{LT-ref}^2 = \sigma_{N_{LT}}^2 + \sigma_{N_{ref}}^2 = (0.5 \mu\text{rad})^2 + (1.13 \mu\text{rad})^2 = (1.24 \mu\text{rad})^2,$$

which would cause a 1.49 μm rms error in the GMT surface. Based on these assumptions for a real surface measurement, $\sigma_{LT-ref} > \sigma_{N_{LT}}$, so performing the PSD correction adds

more noise to the laser tracker measurement than the amount of correlated motion removed, thus decreasing the accuracy.

For the distance measurement, however, Figure 5-2 shows $\sim 4 \mu\text{m}$ P-V of correlated motion between the DMIs and the laser tracker for these tests on the floor, while Figure 2-6 shows $\sim 2 \mu\text{m}$ P-V of correlated motion due to the tilt of the mirror from the weight of the puck. The net effect is about $1 \mu\text{m}$ rms of correlated motion. The error made by not correcting for the correlated motion with the DMIs is

$$\sigma_{LT}^2 = \sigma_{Cor}^2 + \sigma_{N_{LT}}^2 = (1 \mu\text{m})^2 + (0.07 \mu\text{m})^2 = (1 \mu\text{m})^2,$$

where $\sigma_{N_{LT}}$ comes from the values listed in Figure 5-4. The error after performing the DMI correction is

$$\sigma_{LT-ref}^2 = \sigma_{N_{LT}}^2 + \sigma_{N_{ref}}^2 = (0.07 \mu\text{m})^2 + (0.2 \mu\text{m})^2 = (0.21 \mu\text{m})^2,$$

from the DMI perturbations listed in Figure 5-5 and Figure 5-6. This shows that during a real surface measurement, $\sigma_{LT-ref} < \sigma_{N_{LT}}$, so performing the DMI correction improves the measurement accuracy by removing the real relative motion. Values here are for 1 s integration time. Figure 5-4 to Figure 5-6 show that the error could be reduced to about $0.15 \mu\text{m}$ rms with a 10 s integration time.

Chapter 6

DATA COLLECTION AND ANALYSIS

This chapter starts by providing an overview of the data collection and analysis process. Following this, the details of using the Laser Tracker Plus control software are discussed, explaining the process of making a surface measurement. The analysis of those surface measurements using the MATLAB scripts provided in Appendix D is then explained.

6.1 Measurement and Analysis Overview

The purpose of the measurement is to compare the actual surface of the mirror with the ideal off-axis, near-parabolic surface. The geometric parameters – radius of curvature, off-axis distance, and clocking – are fixed. No fitting is performed to determine the best-fit off-axis surface with varying off-axis distance or radius of curvature. All departures from the ideal surface are treated as errors to be corrected by figuring. Variation of the geometric parameters is only allowed toward the end of the fabrication process, when the figuring is guided by optical measurements, not at the early stages when the laser tracker measurements guide the process.

The laser tracker measurement consists of a number of samples (typically between 200 – 250) on the surface, four geometry reference points that are used to define the off-axis distance and clocking, and the locations of the four surface references that are

used to improve the accuracy of the laser tracker measurements by compensating in part for drift and relative motion between the segment and the laser tracker. The geometry reference points are near the edge of the segment, at known clocking angles and known distances from both the surface and the outer edge. The segment prescription defines the positions of these references with respect to the optical axis of the parent. Because the four geometry references are measured together with the surface points, the positions of the surface points with respect to the parent axis can be determined.

The surface data are collected by moving the SMR puck to predesignated positions across the mirror surface using the SMR positioning system. At each of these locations, the puck comes to rest and the laser tracker and DMIs take simultaneous measurements as fast as they can, and average them over a specific integration time, then the SMR moves on to another position. When an integration time of 1 s is used, it takes about 15 s for the Laser Tracker Plus system to measure then move to the next measurement positions, so the entire surface measurement takes ~1 hour.

Following the measurements, the data are processed to determine the deviation of the actual surface from the ideal surface. The surface points and the reference points are measured initially in the laser tracker's coordinate system. In order to compare the surface data with the ideal surface, all the data are transformed to a parent coordinate system whose origin is at the parent vertex and whose z -axis is the parent axis. The transformation is determined by a least-squares fit to the four geometry reference points, using their measured tracker coordinates and their known parent coordinates. The same transformation is then applied to both the surface data and the surface reference points.

With the surface points transformed to parent coordinates, they can be compared with the ideal surface after applying a compensation for the radius of the SMR. The distance of each point from the surface is then calculated, giving the surface error at each point. These surface errors are displayed in segment coordinates and polynomials are fit to them. The polynomial fit is then used to guide the next grinding run to correct the surface figure errors.

6.2 Data Collection

Appendix C contains a step-by-step procedure for measuring a mirror surface with the Laser Tracker Plus system, which is overviewed here. The first step is to connect the software to the laser tracker. This is done by pressing the **Connect** on the GUI interface (shown in Figure 6-1). If the **Status** box changes to read **Not Initialized**, then press the **Initialize** button. The **Status** box will change to read **Initializing**. This will take a couple of minutes for the laser tracker to finish its encoder count, at the end of which the **Status** box will read **Initialized**. At this point, the laser tracker is ready.

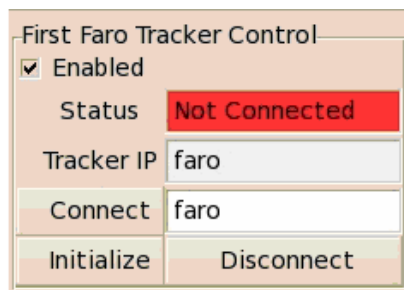


Figure 6-1: The portion of the master control GUI that is used to connect the Laser Tracker Plus control software to the laser tracker.

The system then needs to be set up to initialize the SMR positioner and measure the locations of the references. This is done by pressing the Initial Ball Mover Setup button to open the setup display (shown in Figure 6-2). The filename that the data will be saved to is selected. The Measure and Set Ball Mover Encoders button is pressed to make a single laser tracker measurement to determine the SMR puck location. This is used to initialize the SMR positioner torque motor encoders and provide the starting point to the position control program.

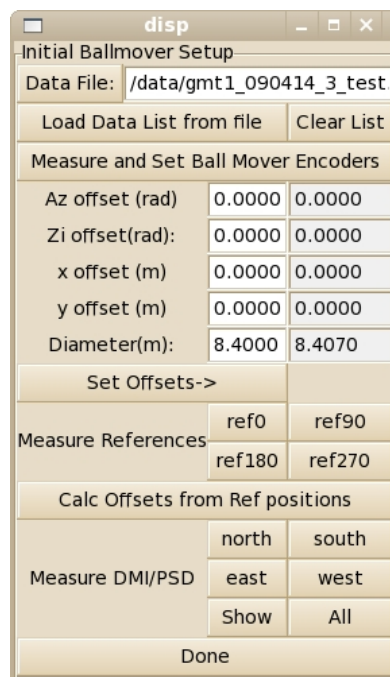


Figure 6-2: The portion of the master control GUI that is used to set up the SMR positioner and Laser Tracker Plus system for a surface measurement.

Following this, the four geometry references around the perimeter of the mirror segment are measured to determine its position and orientation with respect to the laser tracker and SMR positioning system center. A custom fixture was designed to hold an SMR at a fixed distance from the edge of the mirror and in direct contact with the optical

surface, shown in Figure 6-3. The entire fixture is made of plastic to minimize risk of damaging the mirror. The body of the fixture sits against the mirror face on three plastic balls, while two more define its position against the edge of the mirror. It has a hole in the center where the SMR sits, and an eyepiece with a reticle that is used to align the fixture to the center of the clocking scribe mark, shown in Figure 6-4. It is preferable that all four references are measured without breaking the laser tracker beam for highest accuracy. If the laser tracker beam is broken while measuring the four geometry references, the measurements must be restarted. However, if the beam is broken after measuring the references but before starting the surface measurements, the surface measurements can still be made, because any error that results in remeasuring the radial distance from the tracker to the SMR will couple into piston, which is neglected.



Figure 6-3: Image of the edge of the GMT mirror segment showing one of the surface references and the fixture used to hold an SMR for measuring the locations of the clocking marks around the circumference of the mirror [45].

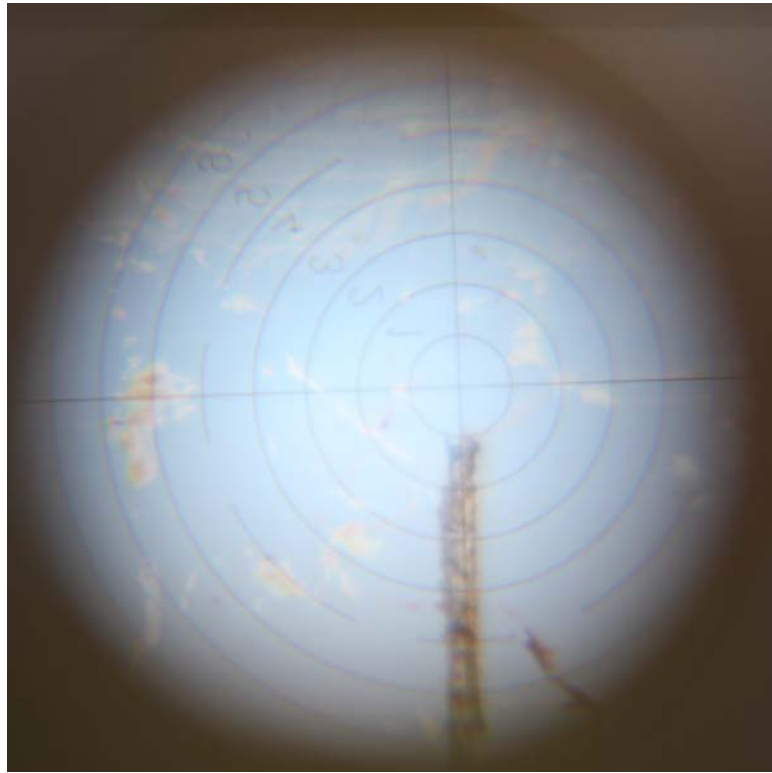


Figure 6-4: View through the eyepiece of the geometry reference of one of the four scribe marks on the edge of GMT. A reticle in the eyepiece is used to align the geometry reference to the scribe mark on the mirror.

Finally, the locations of the surface references are measured. Because the surface references have a built-in retroreflector for use with the DMIs, the laser tracker can typically get a return from it to measure the location of the surface reference. Occasionally, the laser tracker cannot get a lock on the retroreflector, so an SMR needs to be set at the opening of the beamsplitter to get the two angles, while 50 mm needs to be added to the radius measurement to account for the separation between the center of the SMR and the DMI retroreflector. If multiple measurements are made each time, the surface reference locations typically only need to be measured once, and then copied into subsequent measurement sets.

With all the reference positions measured, the **Calc Offsets from Ref** position button is pressed to determine **x** and **y offsets** values, which are used to determine the displacement of the segment's center from the SMR positioner nominal center so that the commanded points can be shifted to the mirror's actual position. The **Measure and Set Ball Mover Encoders** button is pressed again to set the encoder values to account for the offsets. The setup is now complete, so the **Done** button is pressed to close the window.

The user then selects a set of predetermined measurement locations for the SMR positioner to move the puck to, and starts the data collection subroutine. The SMR puck is moved to the first measurement location and a set of measurements is made simultaneously from the laser tracker, the weather station, the DMIs, and the PSDs. When complete, the SMR positioning system moves the SMR puck to the next measurement location and the process continues. As the measurements are made, the operator's display shows (in the **Tracker XY Display** in Figure 6-5) the current position of the SMR as a black dot, along with the locations of all the preselected measurement positions as magenta dots, and the positions where measurements have already been made as blue dots.

If an error occurs during a measurement run (such as the SMR positioner tripping a limit switch), a tone is sounded and an error message is displayed in the **GMT Monitor Log** window (shown in Figure 6-6) to alert the operator of the nature of the error so it can be corrected. Once all the measurement locations have been measured, a tone is made to signal the measurement run's completion. The data analysis of the measurements is discussed in the next section.

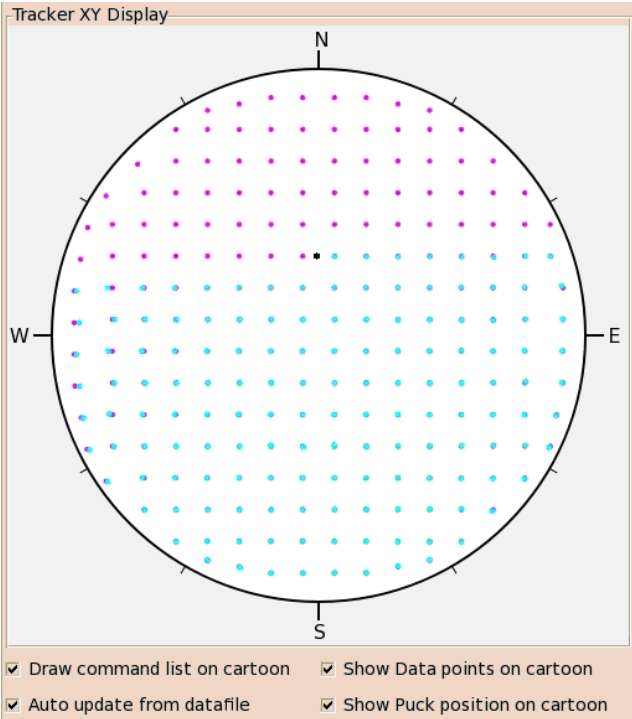


Figure 6-5: Image of the Tracker XY Display showing the location of the SMR puck on the surface of the mirror (black dot), as well as the locations of points to be measured (magenta dots) and those already measured (blue dots).



Figure 6-6: The GMT Monitor Log provides a visual reference of all the system activity during a measurement run. Any errors that occur during a measurement will be displayed here for the operator to see and respond to.

6.3 Data Analysis

At the time of writing this dissertation, the data analysis of the surface measurements made with the Laser Tracker Plus system is performed off-line using MATLAB. It is expected that the data analysis will eventually be incorporated into the control software to allow real-time analysis of the data. The MATLAB scripts used to process the data are included in Appendix D. This section discusses the steps that are used to process the data, incorporated in those MATLAB scripts.

6.3.1 Description of Data Processing

Each measurement run with the Laser Tracker Plus system should be saved as a separate file by the operator, as described in the operating procedure listed in Appendix C. The file names should indicate what mirror is being tested, the date of the test, which measurement of that day, and additional information about the test at the discretion of the operator. An example file name is `gmt1_090630_3.csv` that indicates the mirror under test is the first segment of the Giant Magellan Telescope, measured on June 30, 2009, and that this is the third measurement of it that day. Each of these files is saved as a comma separated value (.csv), and contains all the measurements made by the system, including the geometry reference points, the surface reference locations, the surface measurement points, the DMI reference data, encoder calibration points, and any other measurements the operator initiates.

These .csv files must first be opened in EXCEL, to delete all non-desired measurement points. These include the encoder calibration points and may include

others depending on specifics of the individual measurement runs. The data need to be organized such that the geometry references are the first four points in the file, in the order 0, 90, 180, and 270 degrees. The next four points in the file need to be the locations of the surface reference in the order North, South, East, and West. The remaining points are the surface measurement data and corresponding DMI reference data. Next the file is saved as an EXCEL file (.xls). The current convention is to change the file name so that all the underscores are replaced by spaces, and the subscript mod is added to indicate the data file has been modified. The new filename for the example above becomes gmt1 090630 3 mod.xls. The measurement file must be saved in the appropriate folder so that the data processing program can find the file when run. For the MATLAB script listed in Appendix D, the data file are saved in folder: C:\Documents and Settings\slap\My Documents\GMT\Data\Segment1.

To begin the data analysis in MATLAB, the function `ltPlusGmt.m` must be run in the command window to process the desired file. This is a function that Buddy Martin originally wrote, and I modified. This is done with a command similar to `ltPlusGmt('gmt1 090630 3 mod.xls',90,90,-90,0,0,-22.3,1,6,-30,30,200,30)`. The quantity in single quotes is the data file, the first six numbers are the initial guess at the coordinate transformation required to transform all data to a segment-based coordinate system (discussed further in Section 6.3.2). The next argument is set to 1 to apply external reference correction and 0 otherwise (discussed in Section 6.3.4). The next argument indicates the degree of the polynomial fit (discussed in Section 6.3.7), where 6 indicates a fit to Zernike polynomials up through 6th degree – the first 28 polynomials listed in Table E-1. The next two arguments define the z-scale for the surface plots that

are generated so that multiple data sets can be compared on the same scale. The last two arguments are the coarse and fine outlier cutoff values, where points with surface errors greater than these values will be eliminated at different steps in the processing (discussed in Section 6.3.7).

MATLAB uses the command `xlsread` to access the desired measurement file and extract required data to be processed. Each data point contains: the laser tracker's polar coordinates for the surface point; the DMI and PSD readings from the external reference system; the temperature, pressure, and relative humidity measurements from the weather station; and the timestamp encoding the date and time the measurement was made.

6.3.2 Using Geometry References to Determine the Off-axis Distance and Clocking

A set of geometry reference marks are scribed around the circumference of the mirror at the 0, 90, 180, and 270 degree locations. The 0° point is the point farthest from the parent axis, and the angles increase counter-clockwise around the mirror. Using four geometry references provides some redundancy, giving a least-squares solution and an indication of any significant error in any of the four points. Typical residual errors after the best-fit transformation are about 0.2 mm, consistent with the uncertainty in placing the ball on the mirror. This is adequate to define the segment's off-axis distance and clocking angle, but not to define the piston, tip and tilt of the surface at the micron level. These three parameters are determined from the surface data, and are ignored up to values on the order of 100 μm . Any larger deviations in piston, tip, and tilt would indicate a problem with the measurement.

The locations of these marks are measured during the initial setup performed before the surface measurements are started. The coordinates of these four SMR positions are known in a coordinate system centered on the mechanical center of the mirror. The laser tracker measures in spherical polar coordinates with the tracker head at the origin. The measured points are first converted from polar to Cartesian coordinates. Next, the locations of the geometry references measured with the laser tracker are used to find the transformation from the tracker's coordinate system to the parent coordinate system. The analysis program does this coordinate transformation in two steps. The first step goes from tracker coordinates to a segment coordinate system with the origin at the center of the segment surface, z -axis perpendicular to the segment's flat rear surface, and x -axis directed away from the parent axis. This is done because the compensation based on the external DMI references is done most naturally in segment coordinates, as are polynomial fits and display of data, while the calculations of surface errors is done most naturally in parent coordinates. The first transformation is done by finding the best-fit transformation from the measured tracker coordinates of the four geometry references to the known segment coordinates. The second step goes from the segment coordinate system to the parent coordinate system, a fixed transformation defined by the segment prescription.

The MATLAB function `nPtFitxyz.m`, provided in Section **D.1.4**, is used to determine the coordinate transformation that minimizes the sum squared distance between the measured geometry references and their known positions in the segment coordinate system. It requires an initial guess of the transformation from tracker coordinates to segment coordinates. The transformation is defined by 3 rotations

followed by 3 translations. These values are input into the parameters required by ItPlusGmt. For the example above, the values 90,90,-90,0,0,-22.3 are used. There are many conventions in use for the 3 rotations. The *xyz*-convention from Goldstein was used, where the rotations are (in order) about the original *z*-axis, about the new *y*-axis, and about the new *x*-axis [18]. For the Laser Tracker Plus system in the Mirror Lab, the tracker's *z*-axis points east and its *x*-axis points down. When the segment is in its standard orientation, with its *x*-axis pointing west, the rotations of the coordinate axes are approximately:

$$R_z = 90^\circ,$$

$$R_y = 90^\circ,$$

$$R_x = -90^\circ.$$

(For different orientations of the segment, only R_y varies with the clocking orientation of the GMT segment.) The three translation values (0, 0, -22.3 m) correspond to the separation between the laser tracker and the mirror center in *x*, *y*, and *z*, where the numbers in the example indicate that the mirror and the laser tracker are aligned in *x* and *y*, but the mirror is 22.3 m below the laser tracker. Note that the rotations and translations are applied to the coordinate axes, not to the segment. Since the initial coordinate system is defined by the tracker, the transformation to segment coordinates can be thought of as transforming the tracker to the center of the segment, with its *x*-axis pointing away from the parent axis.

6.3.3 Comparing Laser Tracker Data with Ideal Surface

The coordinate transformation determined from the fit of the geometry references is used to transform all the surface measurements into the parent coordinate system. An ideal surface is calculated based on the mirror's correct radius of curvature, off-axis distance, and clocking angle. In the parent coordinates it is

$$z = \frac{r^2}{R + \sqrt{R^2 - (k + 1)r^2}}, \quad (6.1)$$

where $R = 36$ m is the RoC, $k = -0.9983$ is the conic constant, and r is the radial distance from the GMT parent axis, which has an off-axis distance of $r = 8.71$ m to the mechanical center of the segment. The x and y positions of each point are used to determine r and calculate z at each position.

A compensation for the radius r_b of the SMR is made by projecting each measured point a distance r_b in the direction perpendicular to the ideal surface. This compensation is made using the MATLAB script `radiusComp`. The departure of each point from the ideal surface is then determined by subtracting the ideal z from the measured z and taking the projection normal to the mirror surface. The departure from the ideal surface contains piston, tip, and tilt due to imperfect knowledge of the positions of the geometry references. These are removed from the surface errors.

6.3.4 Applying External Reference Data

If desired, the measurements from the External Reference system can be used to improve the measurement accuracy of the surface measurements by setting the eighth argument in the `ltPlusGmt` input to a 1.

6.3.4.1 Measuring the Surface Reference Locations

As part of the standard setup for a Laser Tracker Plus measurement, the locations of the surface references are measured with the laser tracker. The surface reference locations are combined with the DMI displacement values to determine the relative motion of the mirror, or apparent motion due to index variations, which is then used to compensate the laser tracker measurements.

6.3.4.2 Calculating Index of Refraction

Because the Laser Tracker Plus system uses lasers to measure distances through the air, an accurate knowledge of the index of refraction is required to convert from laser wavelength fringes to physical distance. The laser tracker has a built-in weather station that it uses to automatically compute the index of refraction to calculate the radial distance. The same correction is applied to the DMI reference data. Assuming a standard and homogeneous air composition, a 1 ppm change in the index of refraction will result from any one of the following conditions:

- a 1°C change in air temperature,

- a 2.5 mm of mercury change in air pressure,
- an 80% change in relative humidity.

The temperature, pressure, and relative humidity are measured by the weather station and recorded for each measurement point in the data file. These values are then used to calculate the index of refraction of the air at the time each measurement was made. The modified Edlen equations outlined in the appendix of Estler's paper are applied in the MATLAB script `CalcIndex.m`, which is provided in Section **D.1.2** [12]. The constants Estler recommends were used with the exception of the CO₂ concentration which was set at 450ppm because that is the value used by the Faro laser tracker used for calculating index of refraction.

6.3.4.3 DMI Correction

The output from the DMI system is in counts, which is converted to microns to match the radial measurements from the laser tracker using the MATLAB function `DMICountsToMicrons.m`, provided in Section **D.1.3**. The measured DMI displacements are assumed to be due to axial motion, so the projection in the vertical direction is used to determine the relative motion. Next, a fit of the projected displacements to rigid-body motions is performed for each measurement position. The four displacements can be described by four basis functions, three describing the planar motions of the mirror surface (piston, tip, and tilt), and a fourth non-planar term (astigmatism) that indicates the deviation of the measurements from a plane. These basis functions match the first four Zernike polynomials listed in Table **E-1**.

The MATLAB script `zFit4.m`, which is a specialized version of the more general function `zFit.m`, fits the first four Zernike polynomials to the axial displacements and reports the coefficients, which are displayed graphically for the entire measurement set in Figure 6-7. At present, the DMIs are only used to correct the laser tracker data for apparent rigid-body motion. The piston, tip, and tilt coefficients for each measurement point are used to correct the z coordinate of the surface point measured by the laser tracker. The assumption that the errors can be described by rigid-body motion is very good, as can be seen by the extremely small magnitude of the astigmatism term in Figure 6-7.

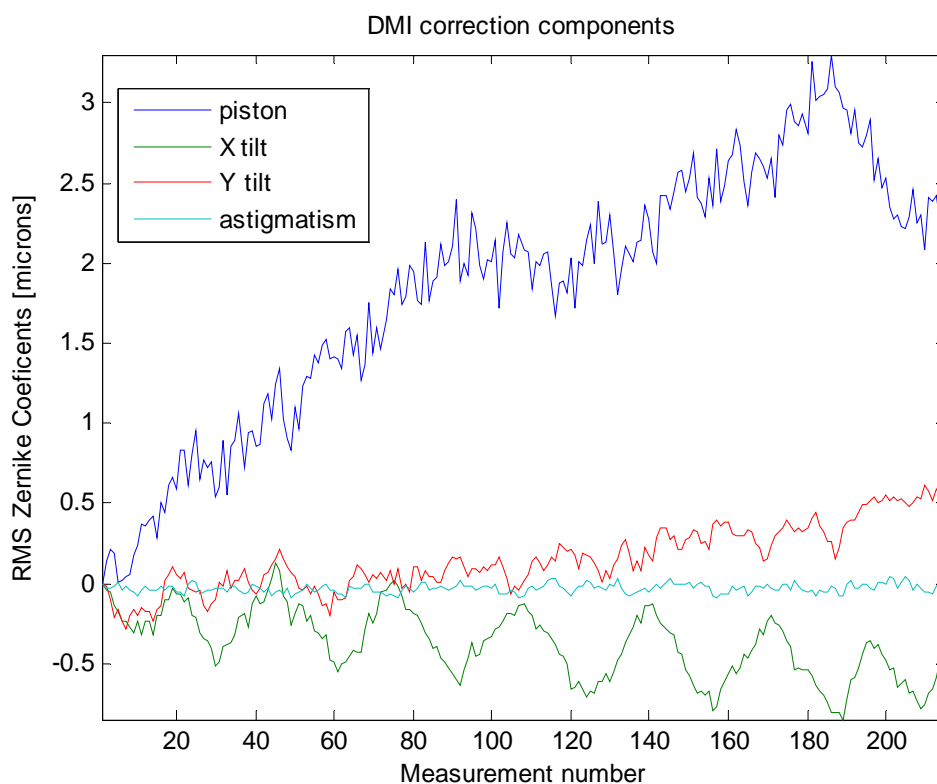


Figure 6-7: Plots showing the amount of the piston, tip, tilt, and astigmatism measured by the distance measuring interferometer reference system during measurement set `gmt1 090630 3 mod.xls`. Almost all the motion can be described as rigid-body motion.

6.3.4.4 PSD Correction

At the time of writing this dissertation, it was decided that the angular accuracy of the laser tracker was good enough that there was no need to make a PSD correction, and that applying the correction would simply add noise. For this reason, data analysis does not actually include a PSD correction. In case it becomes necessary to start applying the PSD correction at some point in the future, the description of how to apply the correction is discussed in Section 5.3.3.

6.3.5 Applying Custom Calibration Results

The results of the custom calibration discussed in Chapter 4 indicate that the radial errors are small enough that they can be neglected. If they were large enough to require correction, then the Zernike coefficients that were measured and are shown graphically in Figure 4-6 would be multiplied by the sensitivity matrix generated in Section 6.3.7, and the results subtracted from the radial coordinate measured for each surface point.

The angular calibration results would be applied in much the same way that that the PSD correction would be applied. A sensitivity matrix would be generated giving the influence of each Zernike Slope polynomial at each surface data point. This sensitivity matrix is then multiplied by the coefficients listed in Table 4-1 to determine the angular error at each measurement position. The angular error is subtracted from the measured angular coordinates.

6.3.6 Outlier Rejection

During the course of a measurement run, an occasional measurement point will have considerably more error than the rest. This error is often attributed to dust or other contaminants on the mirror surface, or the SMR positioner pulling up on the puck too much. If these outlying points are left in the data set when fit to polynomials, they can bias the fit too much, resulting in poor or inconsistent fit results. For this reason, a two-step outlier rejection process is included in the data analysis, using the MATLAB function `skim.m` listed in Section **D.1.8**.

Because the fit to the nominal geometry reference positions is imperfect, some residual piston and tilt remain. This is visible in left-hand plot in Figure **6-8**, which shows the surface data for measurement `gmt1_090630_3_mod.xls` following the transformation to segment coordinates and the DMI corrections. To remove this residual error, a fit of a plane to the data is required, which will then be subtracted from the data. However, several outlying points are visible in the data, and these points will affect the fit made to the data. The first step is to perform a coarse outlier removal, where points beyond a certain threshold (in this case $>200\ \mu\text{m}$) are rejected before the initial planar fit to the data is implemented. The data after applying the coarse threshold are shown in the right-hand plot in Figure **6-8**. These plots are generated using the MATLAB function `meshPlot3.m` listed in Section **D.1.9**.

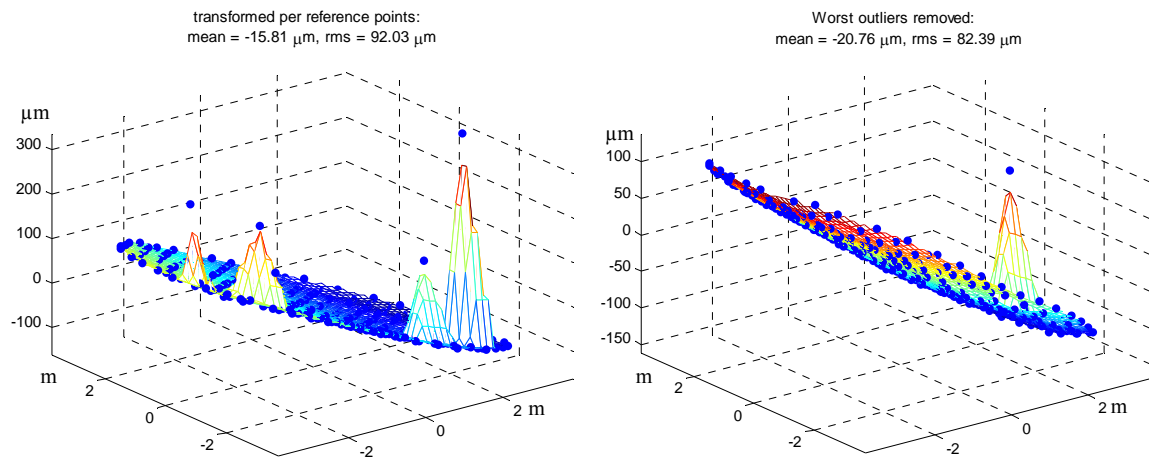


Figure 6-8: Plots showing residual piston and tilt error remaining after the transformation of the data to the geometry references. Several outlying points are visible in both plots. In the right-hand plot, the coarse outlier correction has removed several outlying points.

The coarse outlier correction has removed several of the outlying points, but one still remains. This one could not be removed without clipping valid data points from the set. It will have to be removed after fitting and removing a plane. After the coarse outlier correction has removed all of the outlying points possible, the plane is fit and removed from the data. Figure 6-9 shows the result on the left-hand side. The remaining outlying point is prominent in the plot and can easily be removed by the fine outlier correction. The fine threshold is set to a value where any remaining outlying points can be removed without clipping valid data. In this example, the fine threshold was arbitrarily set for 30 μm , but any value between say 20 – 150 μm would be sufficient to strip off the last remaining outlier. After removing the last outlying point, the details of the surface errors are clearly visible.

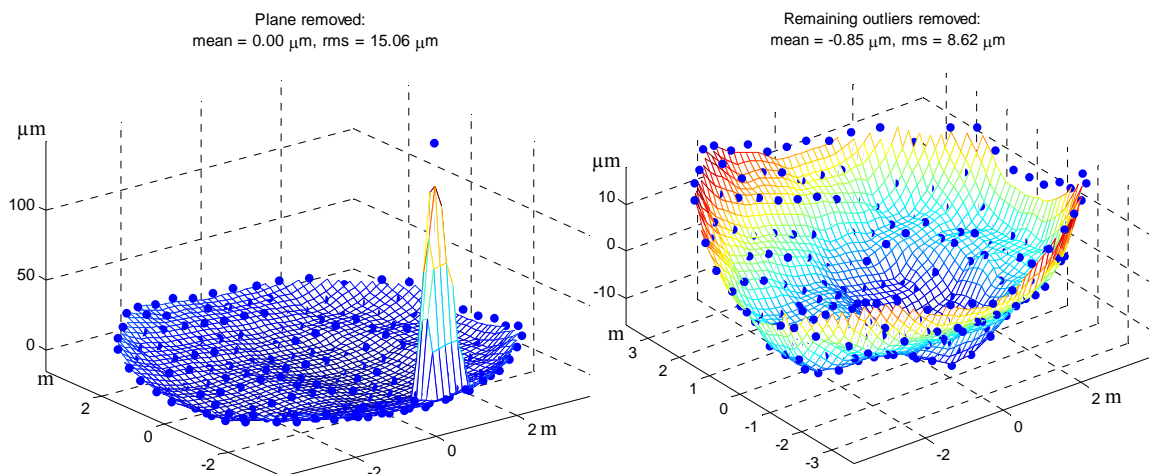


Figure 6-9: The plot on the left shows the data from Figure 6-8 after the plane has been fit and removed. The remaining outlying point is prominent in the plot, and is now easily removed by the fine outlier correction without risk of removing any valid data from the surface measurement. The plot on the right shows the residual surface error in the data after removing the last outlier.

6.3.7 Fitting Zernike Polynomials to Deviation

After the data have been processed to remove any outlying points and the plane, Zernike polynomials are fit to the data. The Zernike fit is used to represent the surface errors for removal during fabrication. The MATLAB function `zFit.m` is used to fit polynomials up through the degree desired (in this case 6). The function `zFit.m` calls another function `zEval.m`, which creates a sensitivity matrix giving the influence of each Zernike polynomial at the positions of the surface data. The least-squares fit gives the coefficients of polynomials normalized to ± 1 at the edge of the segment. The coefficients are converted to coefficients of polynomials normalized to an rms of 1 (the Zernike polynomials listed in Table E-1) with the MATLAB script `edge2rms.m`. Both of the sets of coefficients are saved in an EXCEL file of the same name as the data with the suffix `Fit`

added. For the case of the example, the file gmt1 090630 3 mod Fit.xls is generated,

where the values are listed in Table 6-1.

Table 6-1: List of fit coefficients for the Zernike polynomials through 6th degree for the data set gmt1 090630 3 mod.xls.

$Z_{n,m}$	Microns at edge	Microns rms	Aberration
$Z_{0,0}$	-0.23	-0.23	Piston
$Z_{1,1}$	-0.64	-0.32	Tilt 0°
$Z_{1,-1}$	1.96	0.98	Tilt 90°
$Z_{2,2}$	-3.14	-1.28	Astigmatism 0°
$Z_{2,0}$	13.70	7.91	Power
$Z_{2,-2}$	-4.38	-1.79	Astigmatism 45°
$Z_{3,3}$	2.29	0.81	Trefoil 0°
$Z_{3,1}$	1.47	0.52	Coma 0°
$Z_{3,-1}$	-2.93	-1.04	Coma 90°
$Z_{3,-3}$	-0.08	-0.03	Trefoil 30°
$Z_{4,4}$	-2.48	-0.78	Tetrafoil 0°
$Z_{4,2}$	3.38	1.07	2 nd Astigmatism 0°
$Z_{4,0}$	3.36	1.50	Primary Spherical
$Z_{4,-2}$	-0.18	-0.06	2 nd Astigmatism 45°
$Z_{4,-4}$	0.27	0.08	Tetrafoil 22.5°
$Z_{5,5}$	0.59	0.17	Pentafoil 0°
$Z_{5,3}$	-2.24	-0.65	2 nd Trefoil 0°
$Z_{5,1}$	-2.29	-0.66	2 nd Coma 0°
$Z_{5,-1}$	0.07	0.02	2 nd Coma 90°
$Z_{5,-3}$	-0.23	-0.07	2 nd Trefoil 30°
$Z_{5,-5}$	0.77	0.22	Pentafoil 18°
$Z_{6,6}$	0.76	0.20	Hexafoil 0°
$Z_{6,4}$	-1.36	-0.36	2 nd Tetrafoil 0°
$Z_{6,2}$	4.04	1.08	3 rd Astigmatism 0°
$Z_{6,0}$	2.62	0.99	2 nd Spherical
$Z_{6,-2}$	0.03	0.01	3 rd Astigmatism 45°
$Z_{6,-4}$	-0.28	-0.07	2 nd Tetrafoil 22.5°
$Z_{6,-6}$	0.21	0.06	Hexafoil 15°

From these coefficients, a plot of the surface described by the fit can be generated using the MATLAB function `zDisplay.m`. Figure 6-10 shows the fit to the surface data in the right-hand plot, while the left-hand plot shows the actual data displayed as a contour plot using the MATLAB function `imagescWithLims.m`. Note that the fit is smooth and continuous. The low-order fit has adequate spatial resolution to guide the figuring during loose-abrasive grinding.

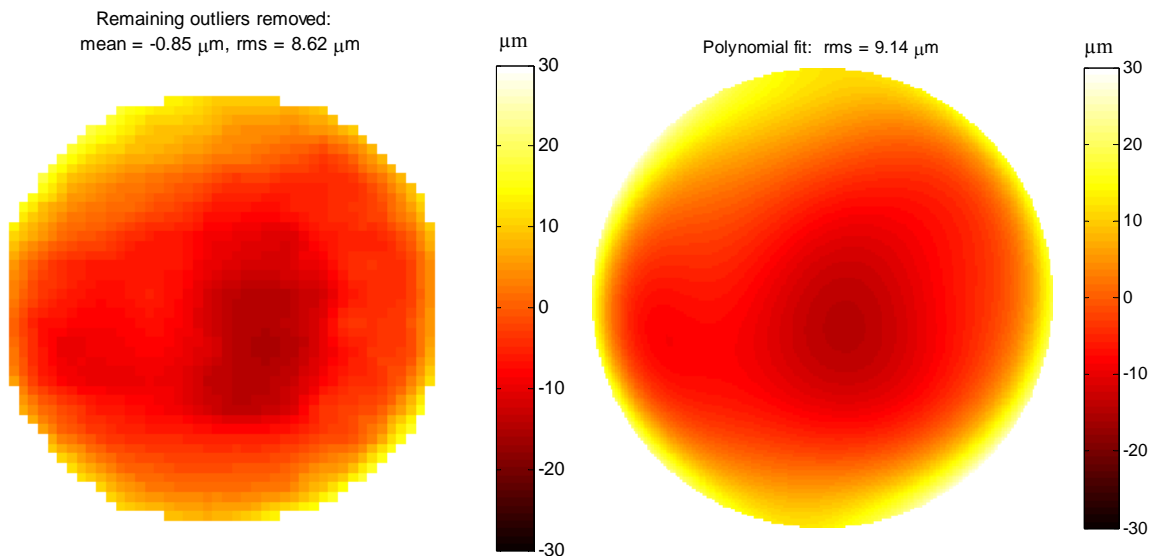


Figure 6-10: The left-hand plot shows a contour plot representation of the measurement data from `gmt1 090630 3 mod.xls`, while the right-hand plot show the Zernike polynomial fit to the measurement data.

The Laser Tracker Plus system is sensitive to power, so it measures errors in the radius of curvature (RoC) of the mirror. The right-hand plot in Figure 6-9 shows 7.9 μm rms of power, equivalent to 4.8 mm in the RoC, while the fabrication tolerance for the RoC is ± 1.0 mm and the measurement tolerance is ± 0.5 mm. The RoC of the GMT segment is very sensitive to thermal gradients between the front and back faces of the mirror. A 1°C gradient will produce 35 μm rms of power in measurement [17]. If the

mirror is not in good equilibrium when the surface measurements are made, the power error can dominate the figure error, as it does in Figure 6-9. For this reason, the data analysis software also produces plots of the figure error with power subtracted so that the other figure errors are apparent. Figure 6-11 shows the surface error with power subtracted off, represented as a mesh plot on the left and a contour plot on the right.

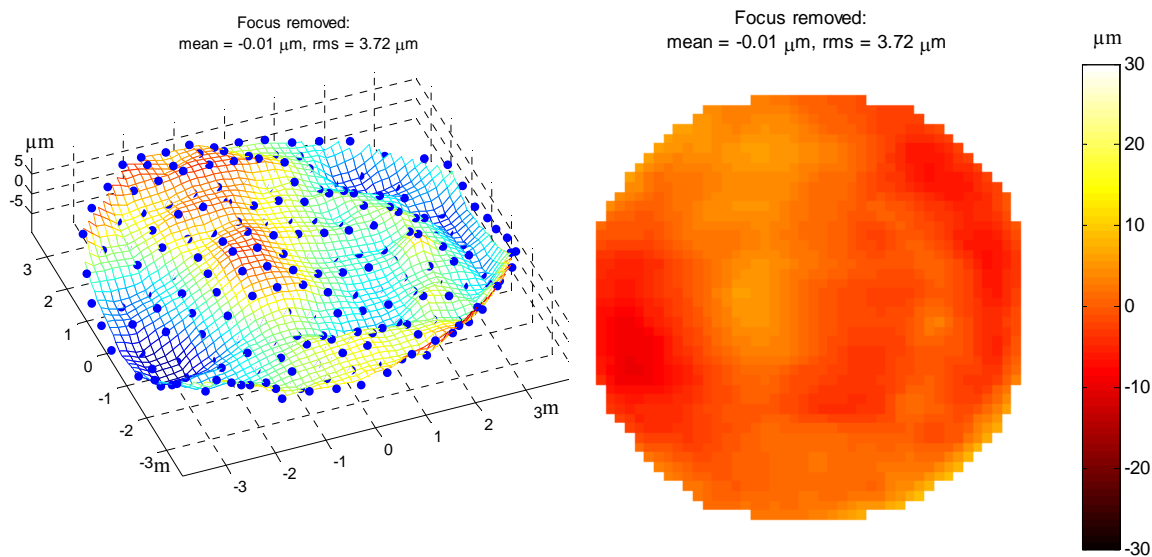


Figure 6-11: Plots showing the data from gmt1_090630_3_mod.xls with power removed [45].

Chapter 7

MEASUREMENT RESULTS AND SYSTEM PERFORMANCE

The Laser Tracker Plus system has two intended functions, to guide the loose-abrasive grinding phase of GMT and future mirrors, and to act as a verification test for the GMT principal test. Presented in this chapter are measurement results from GMT and the large fold sphere (LFS, part of the GMT principal test), which demonstrate the Laser Tracker Plus system's performance.

7.1 Large Fold Sphere

At the time of this writing, the GMT principal test has not been able to resolve fringes across the entire GMT segment, so no direct quantitative comparison can be made between optical interferometric data and the Laser Tracker Plus system measurement results to evaluate the accuracy of the system as a verification instrument. However, measurements of the LFS were made with the system after the mirror's completion, and the results from those measurements provide evidence that the ultimate accuracy of the Laser tracker Plus system will meet its design requirements.

The large fold sphere is a 3.75 m spherical mirror with a 25.5 m radius of curvature. This mirror, shown in Figure 7-1, is part of the null corrector for the principal optical test of the GMT segment [9]. The mirror was mounted at the base of the 28 m test tower and the Laser Tracker Plus system was in its standard position near the top of the

tower, about 22 m above the mirror. At the time of this measurement the SMR positioning system was not installed. Instead, the SMR was attached to a wooden wand and moved manually from position to position across the mirror surface. This required that a person climb onto the mirror's mounting platform to reach the wand and move the SMR. This caused up to 20 μm of rigid-body motion of the mirror (as indicated by the reference DMIs) but it was largely elastic. For the results presented here, the SMR positioner climbed on the platform to reposition the SMR for each sample and climbed off before the data were recorded. Over a period of about 1.5 hours, 93 locations across the mirror were measured with the laser tracker, DMIs, and PSDs. Each measurement was an average with an integration time of 10 s.



Figure 7-1: Testing of the 3.75 m spherical mirror with the Laser Tracker Plus system. One of the references is visible in the foreground, with two of the three other visible in the background. An optician positions the SMR mounted at the end of a wooden wand for the next measurement [44].

The laser tracker data were processed by fitting a spherical surface. The DMI correction was applied to the laser tracker measurements. A plane was fit to the 4 DMI displacements (projected to the vertical direction) for each sample and evaluated at the lateral position of the SMR (as measured by the laser tracker). The DMIs' deviation from a plane was not used as part of the correction of laser tracker data because it was essentially zero, driven completely by noise. Figure 7-2 shows the deviation from the best-fit sphere, before and after applying corrections based on the reference DMIs. The rms deviation is $1.4\ \mu\text{m}$ rms with no DMI correction and $0.38\ \mu\text{m}$ rms after the DMI correction. An optical interferometer measurement was made at about the same time as the Laser Tracker Plus measurement. The optical data show that the mirror surface has about $50\ \text{nm}$ rms astigmatism (which will be corrected in operation, along with other low-order aberrations, by the adjustable support) and $40\ \text{nm}$ rms in other figure error. The $0.38\ \mu\text{m}$ rms deviation of the corrected tracker data reflects the accuracy of the Laser Tracker Plus system in this favorable geometry (almost normal incidence).

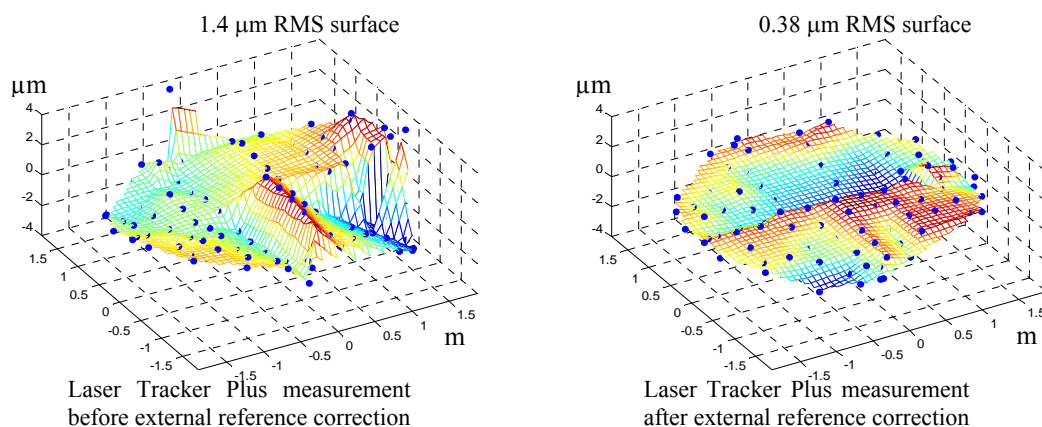


Figure 7-2: Measurements of a 3.75 m spherical mirror surface with laser tracker only on the left, and the corrected plot after applying the data from the external reference system. The plots show the departure from the best-fit sphere [44].

7.2 GMT Segment 1

The off-axis shape of the GMT mirror was generated with a diamond cutting wheel on the Large Optical Generator (LOG) prior to loose-abrasive grinding. In January of 2007, the generation of the mirror had finished based on profile measurements with an LVDT contact probe, and laser tracker measurements with the tracker sitting on the surface of the segment and the SMR held a fixed distance above the surface. These measurements were inconsistent at the level of 300 μm P-V, but, indicated that the mirror was generated to the correct shape to within that accuracy. At that point, the LOG was retooled for loose-abrasive grinding: the generating head was removed, and the stressed lap was installed. Loose-abrasive grinding was initially started in March of 2008, but was delayed due to several issues and did not begin again in earnest until late June.

The first GMT measurements using the Laser tracker Plus system were made on July 11, 2008. It was the first measurement using the SMR positioning system, which was still very crude, requiring command line entries to move each stepper motor without any feedback controls. For ease of measurement, two sets of linear scans were made across the mirror's diameter by using only one stepper motor and the opposite torque motor at a time, while disabling the other two. Following this, a trial and error technique was used to reposition the SMR to numerous positions within each quadrant of the mirror to fill in the surface data. The data from that first measurement of GMT are shown in Figure 7-3.

The previous measurement of GMT using other measuring systems indicated that the mirror surface was correct to 300 μm P-V, but the Laser Tracker Plus measurement

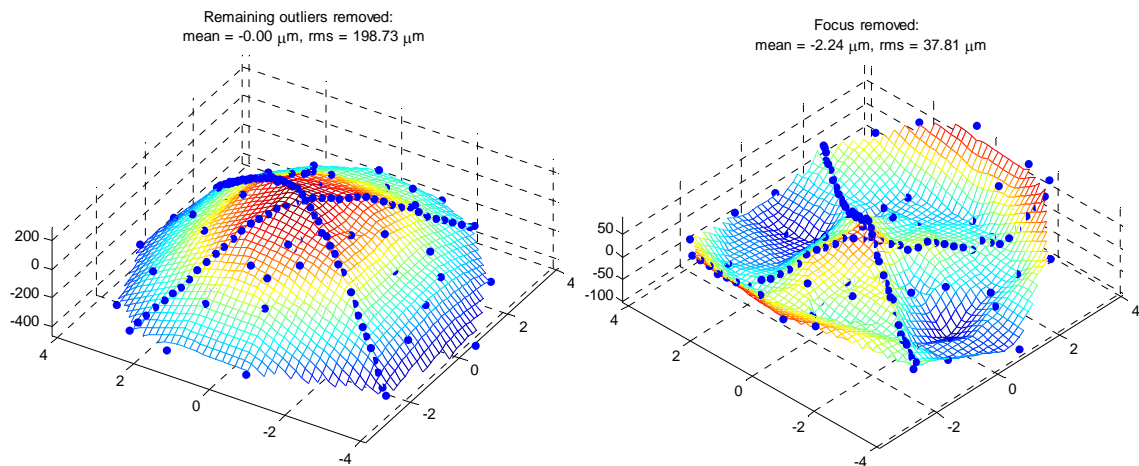


Figure 7-3: The plot on the left shows the first GMT measurement with a 600 μm P-V error in the surface figure, primarily power. The plot on the right shows a residual error, primarily spherical aberration and astigmatism, of 180 μm P-V after removing power.

showed an error of 600 μm P-V power. This is equivalent to a radius of curvature (RoC) error of about 100 mm. The radius error was ultimately determined to be the result of incorrect parameters used in the analysis of the previous measurements, but it points out a useful aspect of the Laser Tracker Plus system. Many techniques used to measure large optics are blind to RoC errors, but the Laser Tracker Plus system is nearly as sensitive to power as it is to other aberrations, making it invaluable given the tight RoC tolerance of the GMT mirrors. It has however been difficult to accurately control the RoC of GMT during fabrication due to a large sensitivity of radius to temperature gradients across the mirror. This is discussed further in Section 7.3.2.

Since that first measurement, the loose-abrasive grinding of the GMT segment has been guided exclusively by the Laser Tracker Plus system. Steady improvement has been made to the mirror's figure during the last year. Table 7-1 shows the improvements in the mirror's P-V and rms errors, as well as the magnitude of several key aberrations. A

close inspection of the numbers in Table 7-1 shows a time period in early 2009 where very little improvement was made in the mirror figure. There was considerable amount of down-time on the mirror's production this time, due to construction work in the Mirror Lab required for the installation of components for the principal test and the scanning pentaprism test, as well as other activities.

Table 7-1: List of values measured for the GMT mirror over the year long loose-abrasive grinding phase of fabrication. The table shows steady improvement in the mirrors figure, guided exclusively by Laser Tracker Plus measurements. Values for aberrations are rms surface. Values for astigmatism, coma, and trefoil are RSS of the two components. SA and SA2 are the first two spherical aberrations. The units are microns rms.

Date	P-V	RMS	Power	Astig.	Trefoil	Coma	SA	SA2
Jul-08	813.3	198.7	-175.2	29.9	6.7	3.8	23.4	-3.3
Aug-08	619.5	158.8	-143.3	29.5	10.8	4.6	14.9	7.3
Sep-08	588.8	132.2	-110.0	17.0	28.7	11.4	18.8	0.6
Oct-08	240.7	55.8	-34.4	32.9	1.4	7.6	12.4	21.6
Nov-08	235.6	33.8	14.2	30.4	2.6	10.5	8.1	11.0
Dec-08	208.6	32.8	6.1	33.8	2.9	8.8	7.0	4.6
Jan-09	215.0	34.9	13.1	33.4	2.3	7.6	4.3	-0.9
Feb-09	202.5	34.0	4.8	32.2	3.4	8.2	7.4	-4.3
Mar-09	124.3	24.7	-18.7	16.8	1.2	2.4	1.9	-1.6
Apr-09	38.8	5.5	2.1	4.6	0.7	1.5	2.6	0.3
May-09	38.1	7.4	7.6	1.3	0.5	1.4	1.7	0.9
Jun-09	42.2	8.6	8.3	2.4	0.8	1.2	1.5	0.8

The June 2009 measurements in Table 7-1 were taken at the completion of loose-abrasive grinding. Plots of the surface figure are provided in Figure 7-4. Polishing started on GMT in July, but progress has been slow. Figure 7-5 shows the figure of the mirror as of October 29, 2009. At present, only the outer meter of the mirror had been polished out while the center is still gray. Several attempts to measure the mirror's figure with the principal test have been made, but the interferometric fringes obtained are too poor to numerically unwrap the phase. The Laser Tracker Plus system has continued to

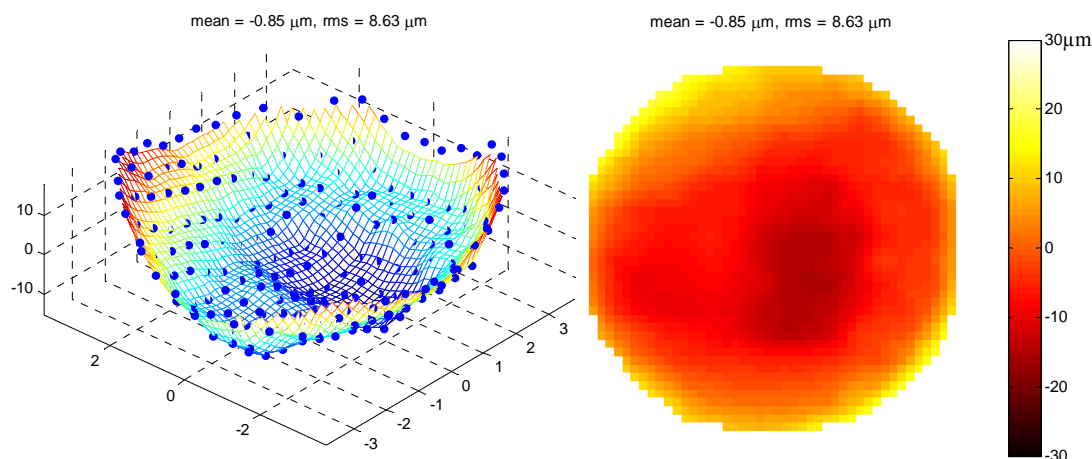


Figure 7-4: Figure of the GMT mirror at the end of loose-abrasive grinding [45].

be useful for guiding the figuring of the mirror while it gets polished out. Figure 7-6 shows a comparison of the mirror's surface measured with the Laser Tracker Plus system with the optical fringes obtained with GMT principal test. The large slopes due to the high edge and other figure errors in the GMT segment result in fringe density higher than the interferometer can resolve, causing gaps in the fringe data and preventing the phase from being numerically unwrapped to determine the true shape of the mirror surface.

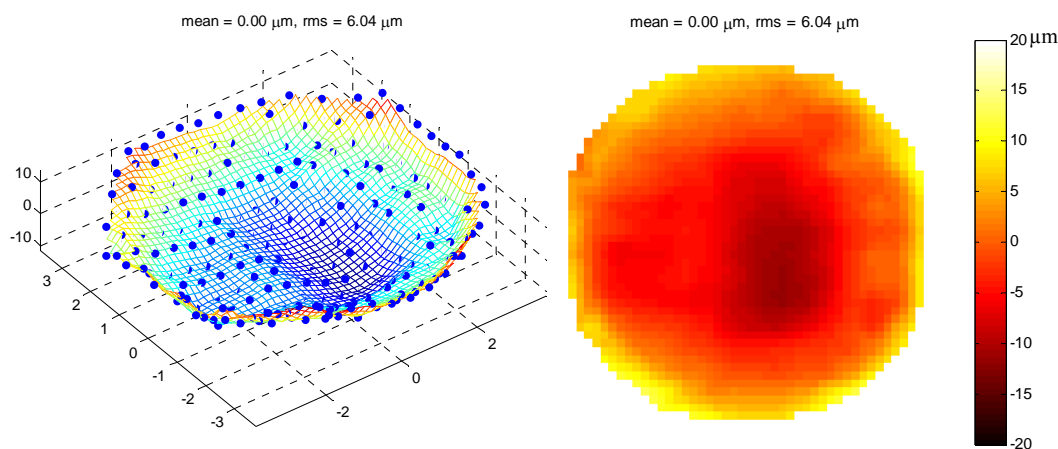


Figure 7-5: Figure of the GMT mirror taken on October 29, 2009 to guide the figuring during polishing.

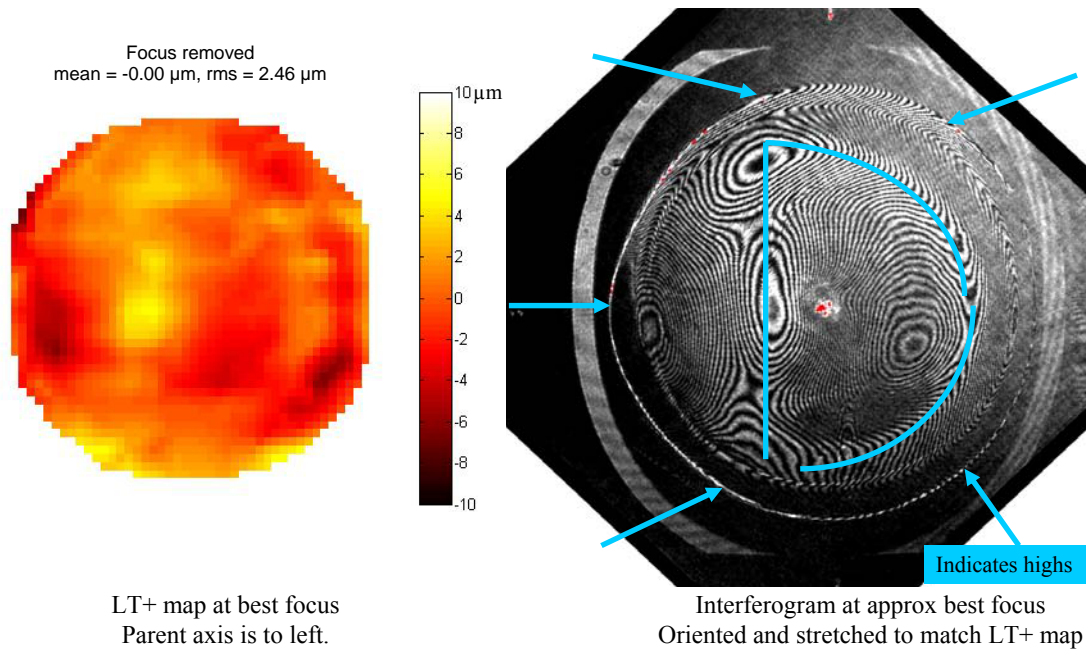


Figure 7-6: Comparison of Laser Tracker Plus measurements made on October 29, 2009 with fringes obtained by the GMT principal test during the same time period.

Figure 7-7 shows the GMT mirror under the SOML test tower set up for a Laser Tracker Plus measurement. All four external references are set up around the circumference of the mirror and aligned to the DMI laser beams shining down from the Laser Tracker Plus instrument platform at the top of the tower (not visible in the picture). The air puck is visible on the mirror surface, and with close inspection, the air hose and the strings can be seen leading back to the SMR positioning system. The mirror is sitting on the primary mirror positioner (PMP) that is used to support the mirror under the test tower during testing and provide six degrees of motion. One corner of the air cart that is used to move the mirror can be seen sticking out from beneath the mirror.

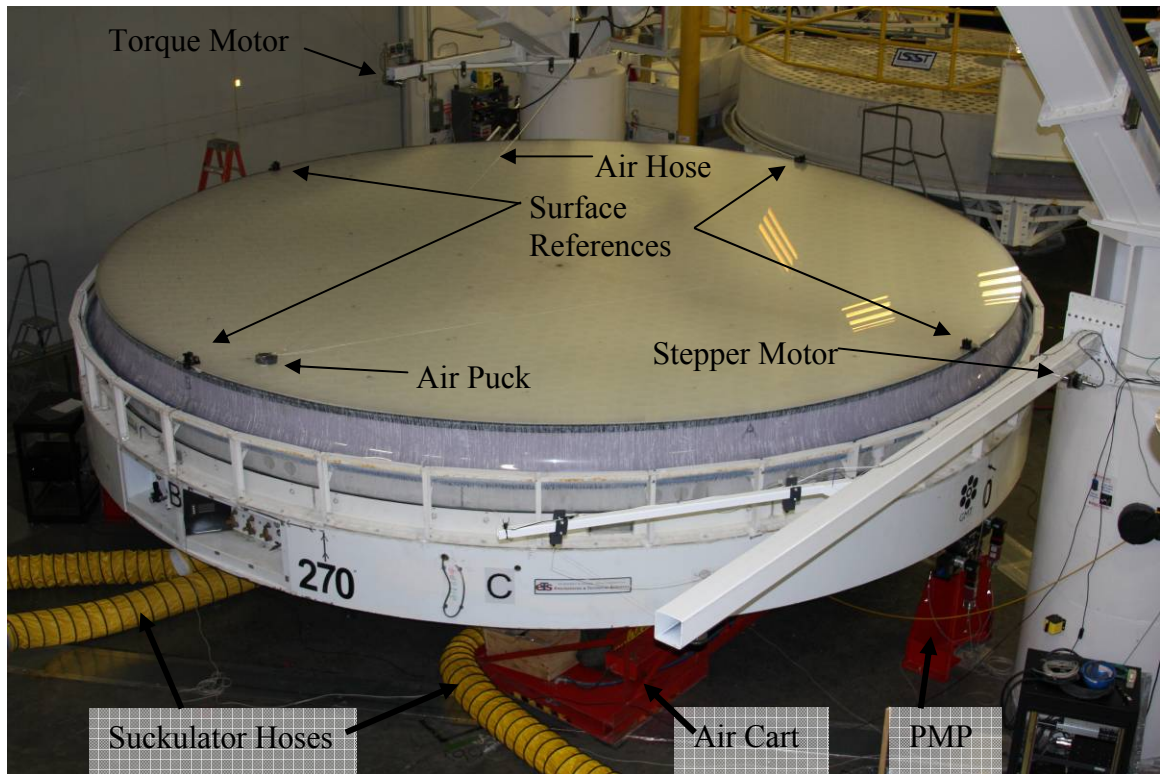


Figure 7-7: GMT mirror set up under the SOML test tower for a surface measurement with the Laser Tracker Plus system [45].

7.3 Analysis of Performance

The ultimate performance of the system is hard to assess because there is not yet an independent test to compare it with. This section will describe tests that were made in an attempt to estimate the system accuracy, discuss error sources that affect the measurement accuracy, and relate the final system performance to the system performance goals stated in Chapter 1.

7.3.1 Tests of System Accuracy

Comparison of Laser Tracker Plus measurement data to interferometric measurements made with the GMT principal test will ultimately determine the final system accuracy; however, the answer to that test will have to wait a while longer. In lieu of GMT optical data, let's start by recapping the results from the measurements of the LFS. At the time of the measurements of the LFS, it was a finished optic. The errors in the surface figure were considerably smaller than the measurement resolution of the Laser Tracker Plus system, so for all practical purposes, the surface was perfect. The measurement results shown in Figure 7-2 show that after applying the DMI reference correction, the residual rms error is only 0.38 μm , and the P-V is less than 4 μm .

Most of the individual point deviations are consistent with measurement noise observed in measurement of other surfaces; however, the three points with the largest deviations have the appearance of dust contaminants, such as a speck of lint trapped between the SMR and the mirror surface. The LFS had been sitting out under the test tower for two days prior to these measurements, and a substantial amount of lint had settled on the mirror surface. If the mirror had been cleaned earlier in the day prior to the measurements, as is typically done, the measurements may have been even better. However, because dust is a common source of measurement error (discussed in more detail in Section 7.3.2), it is reasonable to leave its effects in when evaluating the Laser Tracker Plus system's performance.

Based on the LFS measurement results, the Laser Tracker Plus system is capable of measuring an optical surface with an accuracy down to 0.38 μm . A caveat must be

made though, because the RoC of the LFS is 25.5 m, and it was positioned approximately 22 m below the Laser Tracker Plus system, so the laser tracker head was very close to the center of curvature of the LFS, making the measurements less sensitive to angular errors. From Equation 2.3, the sensitivity of the surface measurements to angular errors is $0.24 \mu\text{m} / \mu\text{rad}$ at the edge of the mirror. Combining this with the laser tracker's angular measurement accuracy of $0.5 \mu\text{rad rms}$ results in a potential surface error of only $0.12 \mu\text{m}$ at the edge. The GMT segment is about six times more sensitive to angular errors.

One common way of assessing a measuring system's accuracy is to rotate the part being measured with respect to the measurement instrument. As was discussed in Section 2.5, when the NST mirror was rotated by 90° between laser tracker measurements, it revealed a systematic error of $3 \mu\text{m rms}$ in the 45° component of astigmatism. A similar test was done with the GMT mirror to test for systematic errors in the Laser Tracker Plus measurements.

Eight sets of measurements were made of the GMT mirror over several consecutive days. Three measurements were made with the mirror oriented with the 0° clocking reference due west, then the mirror was rotated 90° , three more measurement sets were made, then the mirror was rotated back to the 0° position and two more set of measurements were made, for a total of five measurements at 0° and three measurements at 90° . Two of the 0° measurements were made the first day, but thermal data measured that same day indicated that the mirror was not well equilibrated and there were thermal gradients across the mirror that would affect the mirror's figure significantly. For this reason, those two data sets are not included in this analysis. A side by side comparison of a measurement in each orientation is shown in Figure 7-8. The coefficients from Zernike

polynomial fits of the three 90° orientation measurements were averaged and then subtracted from the average of coefficients from the three remaining 0° measurements. The fits and subtraction are done in mirror coordinates, so the differences of all coefficients would be zero in the absence of measurements error. The results are provided in Table 7-2.

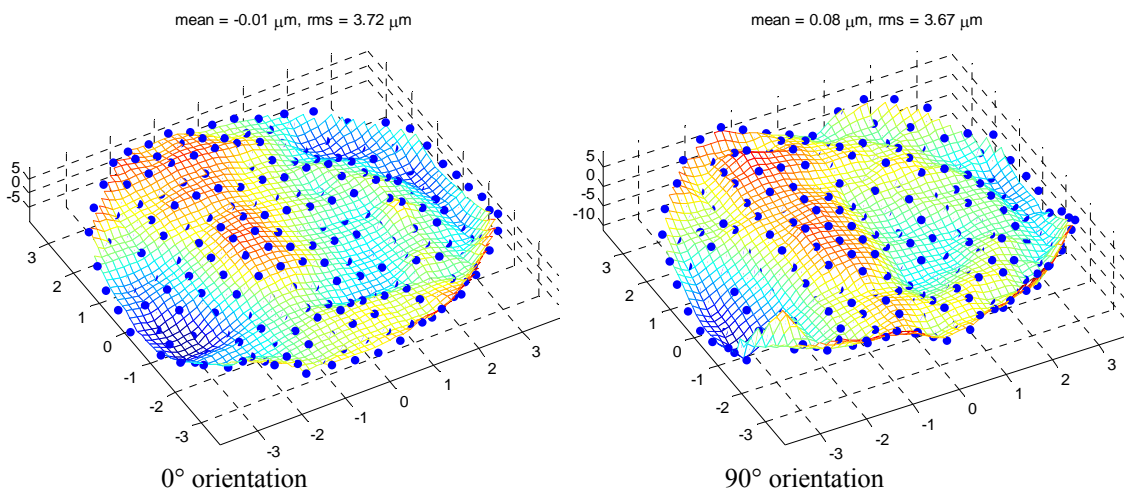


Figure 7-8: Results of two consecutive GMT measurements made with the Laser Tracker Plus system with the mirror rotated 90° between measurements. Both measurements are shown in the standard mirror orientation, with the parent axis toward the negative x direction. Power, which is a rotationally symmetric aberration, has been removed to emphasize the comparison of the non-symmetric aberrations.

For most polynomials listed, the values in the table represent an upper limit on the systematic errors that can be expected in a Laser Tracker Plus measurement. The angular calibration correction has not yet been applied to this data, and we expect this correction to reduce the error. The angular calibration correction was applied to both the 0° measurement and the 90° measurement, and again the polynomial coefficients of the 90° measurement were subtracted from those of the 0° measurement. Some of the angular calibration coefficients listed in Table 4-1 have mean values smaller than the standard

deviation between the three sets of angular calibration measurements, so these coefficients might not be significant. Two sets of corrections were made, first applying the angular calibration for just those coefficients that have a smaller standard deviation than the mean, and then using all the coefficients listed in Table 4-1.

Table 7-2: Worst case comparison of GMT figure measurements made with the Laser Tracker Plus system when the mirror is rotated 90° between measurements. Fits and the subtractions are done in mirror coordinates.

0° Average microns	90° Average microns	Average microns	Difference microns	Aberrations rms surface
-0.91	-2.21	-1.56	1.30	Astigmatism 0°
8.42	8.43	8.43	-0.01	Power
-2.27	-0.67	-1.47	-1.60	Astigmatism 45°
0.98	0.58	0.78	0.40	Trefoil 0°
0.52	0.35	0.43	0.17	Coma 0°
-1.14	-1.08	-1.11	-0.05	Coma 90°
0.10	0.27	0.19	-0.17	Trefoil 30°
-0.75	-0.67	-0.71	-0.08	Tetrafoil 0°
0.83	0.78	0.80	0.05	2 nd Astigmatism 0°
1.63	1.75	1.69	-0.13	Primary Spherical
0.02	-0.07	-0.02	0.09	2 nd Astigmatism 45°
-0.05	-0.08	-0.07	0.03	Tetrafoil 22.5°
0.05	0.10	0.08	-0.05	Pentafoil 0°
-0.31	-0.54	-0.43	0.22	2 nd Trefoil 0°
-0.50	-0.67	-0.59	0.17	2 nd Coma 0°
-0.04	-0.15	-0.09	0.12	2 nd Coma 90°
-0.22	-0.15	-0.19	-0.07	2 nd Trefoil 30°
0.37	0.28	0.33	0.10	Pentafoil 18°
0.01	-0.07	-0.03	0.08	Hexafoil 0°
-0.03	0.02	-0.01	-0.05	2 nd Tetrafoil 0°
0.55	0.53	0.54	0.01	3 rd Astigmatism 0°
1.16	1.22	1.19	-0.06	2 nd Spherical
0.09	0.13	0.11	-0.04	3 rd Astigmatism 45°
0.06	0.10	0.08	-0.04	2 nd Tetrafoil 22.5°
-0.25	-0.15	-0.20	-0.09	Hexafoil 15°

Figure 7-9 shows the plots for the 0° average, the 90° average, and the difference for the three cases of no angular correction, correcting with just the significant coefficients (those whose mean is greater than their standard deviation), and correcting with all coefficients. Piston, tilt and all of the rotationally symmetric aberrations have been removed from the plots to emphasize the asymmetric aberrations that will be

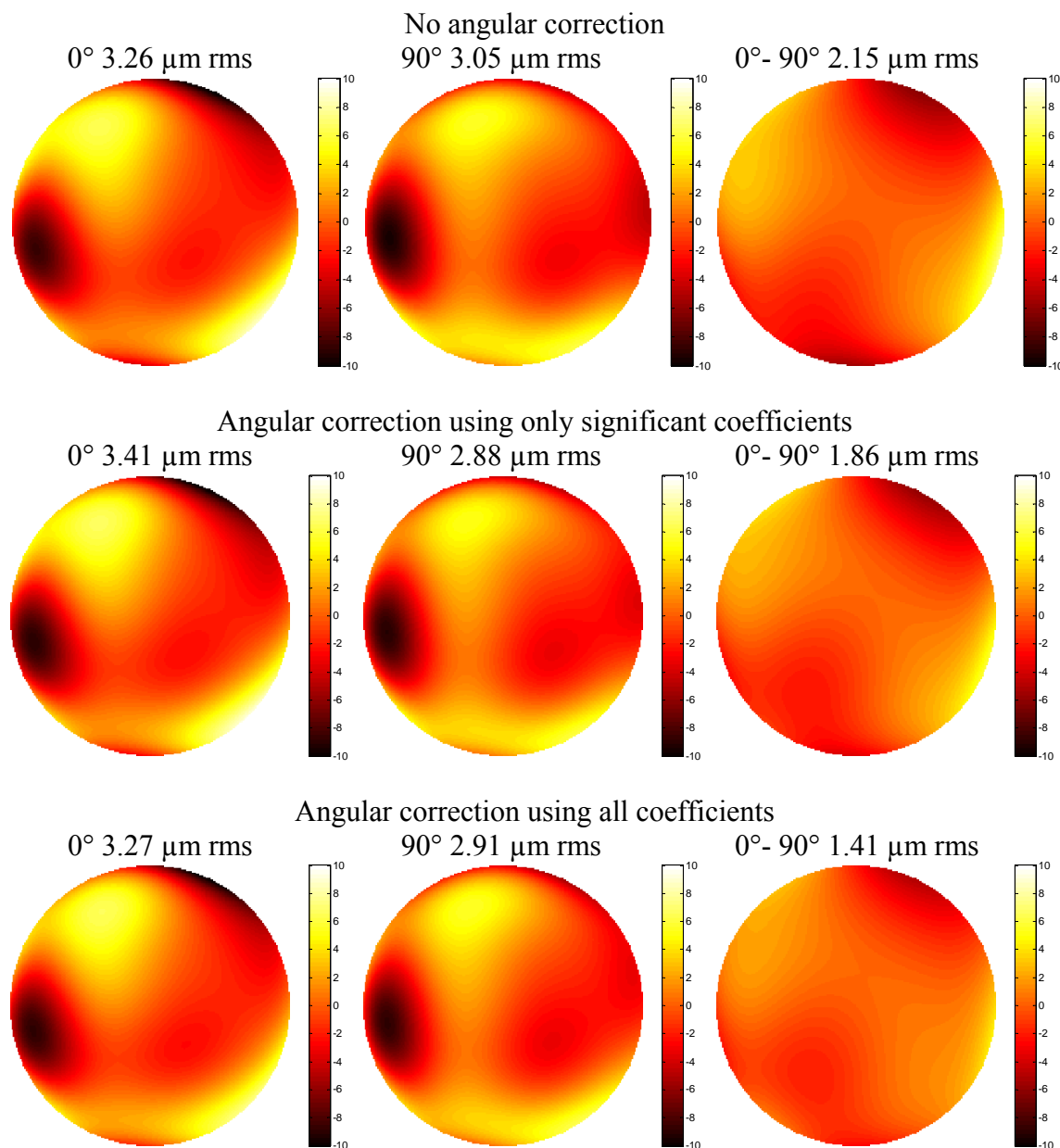


Figure 7-9: The left hand plots show the average of the 0° rotation measurements, the center plots show the average of the 90° rotation measurements, and the right hand plots shows the differences. The top row of plots is without applying the angular calibration correction. The center row is for the case when only the calibration coefficients from Table 4-1 with a mean greater than the standard deviation are used. The bottom row of plots is when all the coefficients are used. The right hand plots show that error between the two orientations is reduced more by using all of the angular calibration coefficients. Piston, tilt and all rotationally symmetric aberrations have been removed from the plots.

affected by the rotation. The difference plots show a significant reduction in the residual error between the two orientations, indicating that the measurements are improved by using all of the angular calibration coefficients in the correction. Using only the subset of coefficients gives an improvement, but not as much as using all coefficients. Table 7-3 lists the corrected coefficients after applying angular calibration correction using all the coefficients.

Table 7-3: Comparison of GMT figure measurements made with the Laser Tracker Plus system with the mirror rotated 90° between measurements and the angular calibration correction applied.

0° microns	90° microns	Average Microns	Difference microns	Aberrations rms surface
-1.24	-1.88	-1.56	0.64	Astigmatism 0°
8.26	8.27	8.26	-0.01	Power
-1.99	-0.94	-1.46	-1.05	Astigmatism 45°
1.10	0.61	0.86	0.49	Trefoil 0°
0.50	0.57	0.53	-0.07	Coma 0°
-1.34	-1.10	-1.22	-0.24	Coma 90°
0.12	0.15	0.13	-0.03	Trefoil 30°
-0.58	-0.50	-0.54	-0.08	Tetrafoil 0°
0.80	0.80	0.80	0.00	2 nd Astigmatism 0°
1.66	1.79	1.72	-0.12	Primary Spherical
0.06	-0.11	-0.02	0.17	2 nd Astigmatism 45°
-0.06	-0.09	-0.07	0.03	Tetrafoil 22.5°
0.05	0.10	0.08	-0.05	Pentafoil 0°
-0.31	-0.54	-0.43	0.22	2 nd Trefoil 0°
-0.48	-0.65	-0.57	0.17	2 nd Coma 0°
-0.05	-0.13	-0.09	0.07	2 nd Coma 90°
-0.22	-0.15	-0.19	-0.07	2 nd Trefoil 30°
0.38	0.28	0.33	0.10	Pentafoil 18°
0.01	-0.07	-0.03	0.08	Hexafoil 0°
-0.03	0.02	-0.01	-0.05	2 nd Tetrafoil 0°
0.55	0.53	0.54	0.01	3 rd Astigmatism 0°
1.10	1.16	1.13	-0.05	2 nd Spherical
0.09	0.13	0.11	-0.04	3 rd Astigmatism 45°
0.06	0.10	0.08	-0.04	2 nd Tetrafoil 22.5°
-0.25	-0.15	-0.20	-0.09	Hexafoil 15°

In addition to guiding the loose-abrasive grinding phase of the GMT fabrication, the Laser Tracker Plus system is also intended as a verification system for the GMT principal test. With the exception of the primary astigmatism, all the aberrations listed in

Table 7-3 have values $< 0.5 \mu\text{m rms}$. This indicates there are no large intrinsic errors in the system (aside from possibly astigmatism), which provides confidence that the system will meet its verification design goals when the time comes. The astigmatism term is unique in that it is the easiest aberration to bend into the mirror from improper support forces. Unfortunately, during the rotation measurements, the support forces were never measured for the 90° orientation, so it is unclear if the astigmatism is the result of errors in the Laser Tracker Plus measurements, or in the shape of the mirror due to improper support forces. Note that the difference between the 0° and 90° measurements give twice the magnitude of the error in astigmatism, so the indicated error is $\frac{1}{2} [(0.64 \mu\text{m})^2 + (1.05\mu\text{m})^2]^{\frac{1}{2}} = 0.6 \mu\text{m rms}$.

The most important aberration that is not validated by the 90° rotation test is power. Sources of errors that could couple into power are errors measuring absolute distance between the laser tracker and the mirror segment, errors in measuring relative distance changes across the mirror, and axisymmetric angular errors producing surface errors that change as a function of angle of incidence. According to the manufacturer's specifications, the ADM accuracy of the laser tracker is $9.8 \mu\text{m} + 0.4 \mu\text{m/m} \approx 20 \mu\text{m}$ of radius error. This uncertainty in distance results in about 35 nm P-V power, so this is negligible. The IFM accuracy of the laser tracker is stated to be $0.4 \mu\text{m/m}$. The radial displacement across the mirror surface is only about 0.25 m, so the error in displacement is about $0.1 \mu\text{m P-V}$, also negligible. If a conservative assumption is made that there is a rotationally symmetric angular error of $1 \mu\text{rad}$ at the edge of the mirror, this results in $1.6 \mu\text{m P-V}$ power or $0.5 \mu\text{m rms}$.

7.3.2 Other Sources of Error

The ultimate accuracy of an individual surface measurement is limited by the intrinsic accuracy of the measurement instrument, environmental effects, and other miscellaneous effects that couple in errors. The accuracy of the laser tracker is remarkably good, and the external reference system compensates for most of the environmental effects, but there are a number of other error sources that have been identified that can adversely affect the quality of the surface measurements if efforts are not made to better control them.

The first major error source identified is actually the SMR positioning system. If it is not properly tuned, it is capable of introducing a considerable amount of error into the measurements. If the control algorithm for the torque motors is not properly tuned, the force imbalance can result in lifting the puck off the mirror, which causes large flares in the data (typically near the edge of the mirror), or tilting of the puck as it moves, causing a washboard effect in the data. The plots in Figure 7-10 show an extreme example of this washboard effect, which was measured early on with the SMR positioner using the Teflon puck, before the control algorithm was improved and the flexure modification discussed in Section 3.4.1 was made. The ridges are aligned with direction of the raster scan. The puck is lifted or tilted when it is pulled only in one direction. When the air puck is used, a similar error can occur as a result of the air hose. Because the air hose uses gravity to reel in the slack, it responds significantly slower than the motors, resulting in some hysteresis in the applied forces that must be compensated for in the control algorithm. The system is now tuned to the point that these effects are rare

when measuring GMT, but some consideration needs to be made when the system is used for testing future mirrors.

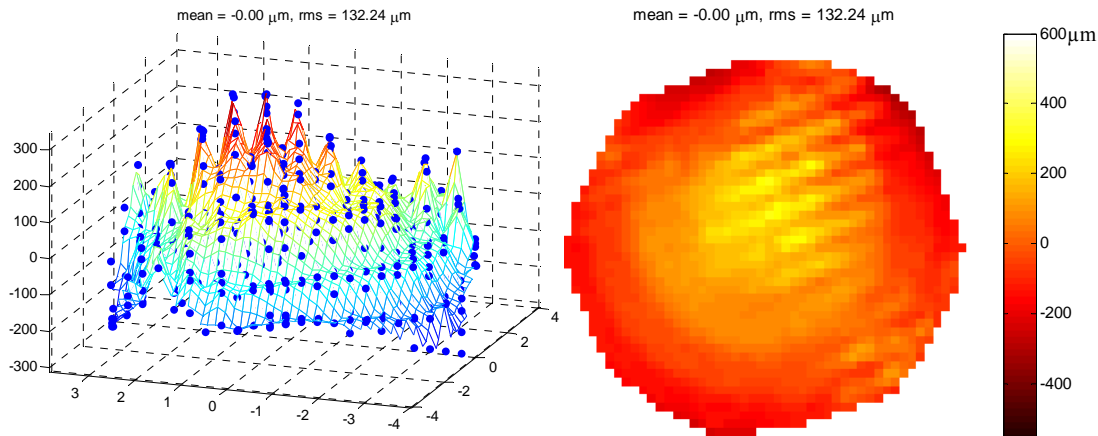


Figure 7-10: Alternating ridges and valleys in the data similar to a washboard due to excessive torque motor forces tilting the puck as it scans back and forth across the mirror. The left plot show a side view of the ridges, which are on the order of 150 μm P-V.

Another error source that has plagued the measurements throughout loose-abrasive grinding is related to the cleanliness of the mirror surface during testing. Because the Laser Tracker Plus system relies on direct contact with the optical surface, any residual grinding compound or dust on the mirror during testing can cause large errors in the individual measurement points. The effects seen in the measurement data from dust contamination can range from isolated high spots if an individual particle gets between the SMR and the surface, but remains in position after the puck moves on, to streaks in the data similar to those in the plots in Figure 7-11 if the particle remains stuck on the SMR for several consecutive measurements. This has been a problem for GMT because its long RoC means the mirror is relatively flat in the center, where it only has a 2 inch diameter drain hole. As a result, when the mirror is washed, the water drains very

slowly and much of the grinding compound settles out on the mirror surface. This problem is probably less severe with the on-axis telescope mirrors fabricated in the past, because they have more curvature and a large central Cassegrain hole. The cleaning procedures used on previous mirrors proved inadequate on GMT, so new procedures had to be implemented. The problem has been significantly reduced as a result of the new procedures and the fabrication progressing to finer and finer grit sizes.

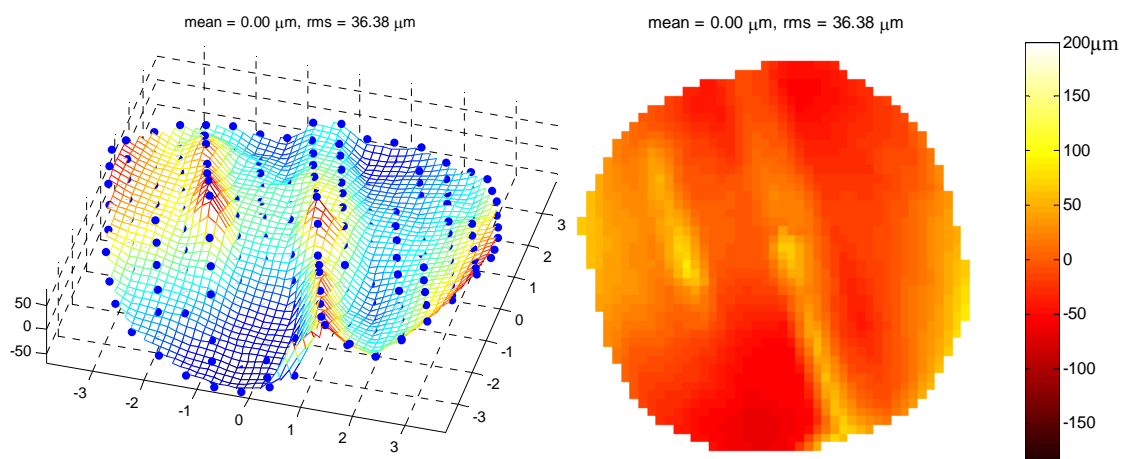


Figure 7-11: Plots showing streaks in the data caused by dust contaminants on the mirror surface during testing. It appears that particles stuck to the SMR and prevented direct contact with the mirror surface for several consecutive measurement positions.

Another interesting measurement error would result from measuring the mirror surface with the laser tracker in absolute distance measurement (ADM) mode, rather than interferometric measurement (IFM) mode. The advertised accuracy in ADM is $\pm 9.8 \pm 0.4 \mu\text{m/m}$, or $\pm 19 \mu\text{m}$ at the distance of 22.3 m. This is clearly inadequate to meet the goals, so the tracker must be used in IFM. Figure 7-12 show the results of measurement in ADM. The concentric pattern of rings indicates that the distance error is

a systematic function of distance. This ADM error could probably be characterized and reduced through a custom calibration if required.

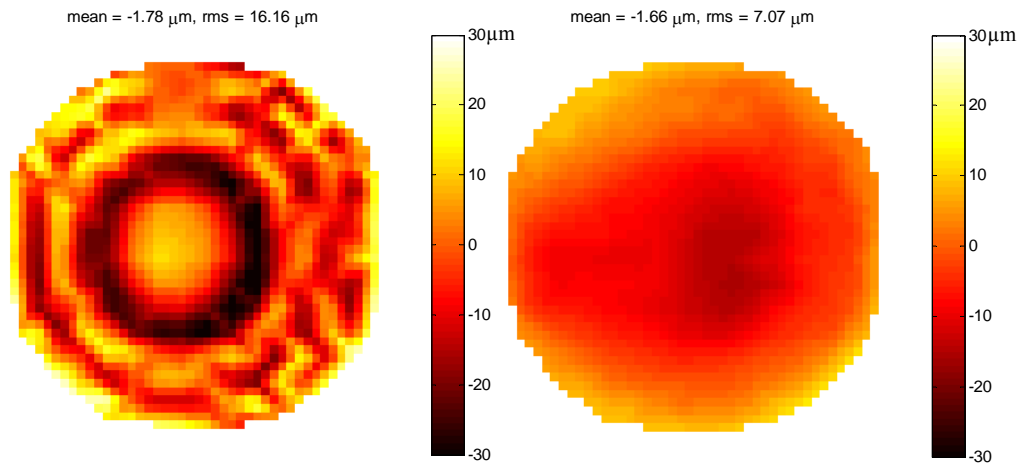


Figure 7-12: Two consecutive measurements of GMT using the Laser Tracker Plus system, where the left hand plot was measuring with the laser tracker in absolute distance mode, while the right hand plot was measured in interferometric mode.

The Faro laser trackers have a distance measurement setting option called “interferometer set by ADM”, where ADM is used to measure the first position, but all subsequent positions are measured using IFM. Because the laser tracker is mounted 22.3 m above the mirror, this is the method that must be used to take advantage of the higher accuracy of the laser tracker’s interferometer. A value of $\pm 19 \mu\text{m}$ is expected for the error in an ADM measurement over this distance. This error affects the measurement of the RoC, so it will produce a small systematic error that looks like power, but this error is very small and contributes $< 0.05 \mu\text{m}$ rms of error in the power coefficient. The more common problem is that the SMR positioning system could jerk the puck abruptly during a measurement run, causing the laser tracker to lose lock on the SMR momentarily and have to reacquire the base distance with the ADM. The ADM error then causes a

discontinuity between the surface data measured before and after the ADM reset occurred, giving the appearance of a step in the mirror surface, as seen in Figure 7-13. This error is easily recognized, so a scan can be repeated if it occurs. Additionally, an error code is reported to the operator's console so the scan can be aborted and restarted if desired.

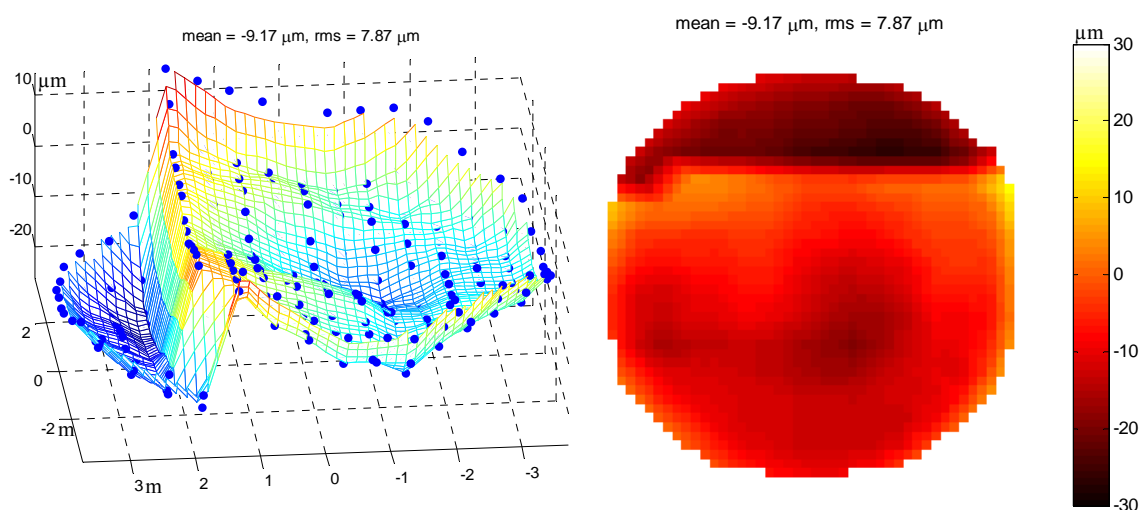


Figure 7-13: Example of a discontinuity in a surface measurement caused by the laser tracker losing lock on the SMR and performing an ADM reset to reacquire the distance.

The last major category of measurement error sources is related to the deformation of the mirror shape itself. This can happen as a result of improper support forces, temperature gradients across the mirror, and leaving the pressure seal inflated. These effects are not errors in the Laser Tracker Plus system, but errors in the test procedure.

In order to allow the mirror to be pressurized with air matching the polishing pressure (and consequently minimize print-through of the honeycomb structure on the polished surface), there are two seals similar to inertubes between the mirror and the

cell, one in the center of the mirror around the drain hole, and the other around the diameter. When inflated, these seals squeeze the mirror and can change the power and astigmatism. Figure 7-14 shows two consecutive measurements of the GMT segment, the first with the seals inflated, and the second after they were deflated. The resulting change in the mirror's shape is over 6 μm rms power.

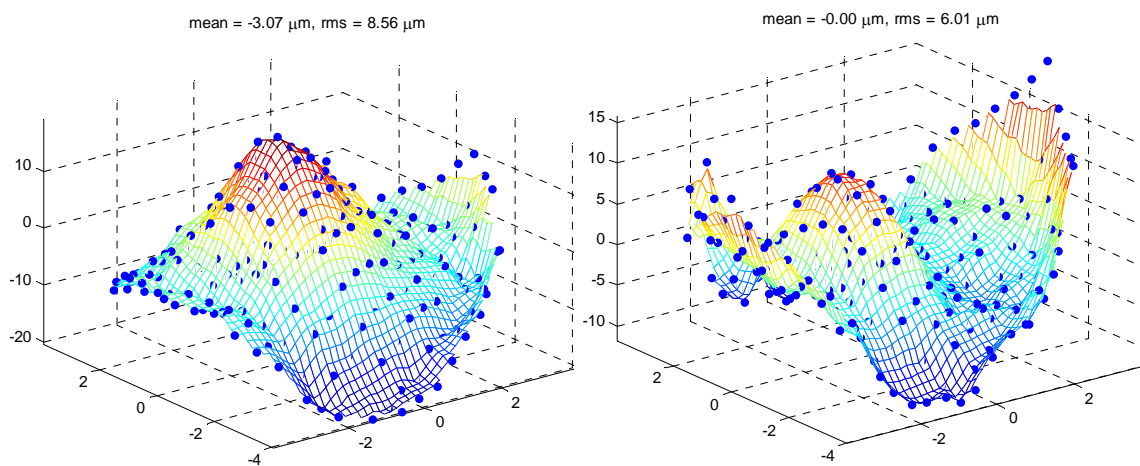


Figure 7-14: Two consecutive sets of measurements of GMT. The set on the left still has the seals inflated, while they were deflated before measuring the set on the right. A change of over 6 μm rms power was measured.

It was mentioned earlier in this chapter that the GMT segment is very sensitive to temperature gradients. The importance of thermal effects during loose-abrasive grinding was not appreciated at the beginning of the process because the interferometer measurements used for previous mirrors are blind to power; special radius measurements were made with a steel tape and the mirrors were generally in better thermal equilibrium for these radius measurements than for routine measurements. Furthermore, the GMT segment has a very tight tolerance for the measurement of radius of curvature: 0.5 mm, which corresponds to 0.9 μm rms power.

The mirror has about 80 thermocouples bonded to the inner surfaces of the honeycomb structure. This temperature information had not been monitored closely until inconsistencies in the power measurement were determined to be temperature dependent. Figure 7-15 shows a set of temperature measurements of GMT with roughly 0.4 K thermal gradient between the front and back faces of the mirror, and variations of about 0.5 K across the back plate. The front to back gradient causes the mirror to bend in power, changing the RoC. A lateral gradient across the mirror can change the astigmatism and other non-symmetric aberrations.

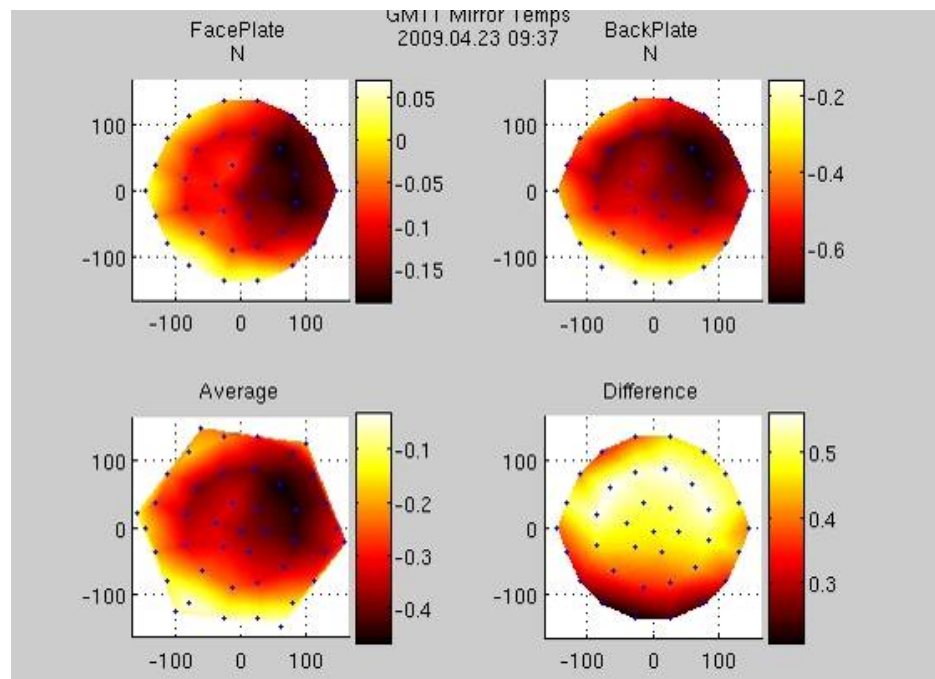


Figure 7-15: Temperature measurements of the GMT mirror showing a 0.4 K thermal gradient between the front and back faces of the mirror and a 0.5 K variation across the back plate. Values represent difference from ambient, in K.

Figure 7-16 shows two consecutive measurements of GMT with significantly different amounts of power. The plot on the left shows $-19 \mu\text{m}$ P-V of power (edge is

low) when the front face of the mirror was warmer than the back face by nearly 1 K. The mirror was then allowed to passively equilibrate overnight and was remeasured in the morning. The plot on the right now shows +12 μm P-V power (edge is high) while the thermal gradient was reduced to 0.4 K. Analysis indicates that a temperature difference of 1 K between the front and back faces of the GMT mirror causes a 44 μm P-V change in power, which corresponds to a change in RoC of ~ 7 mm. The measured change (31 μm P-V power for 0.6 K temperature difference) is roughly consistent with the analysis.

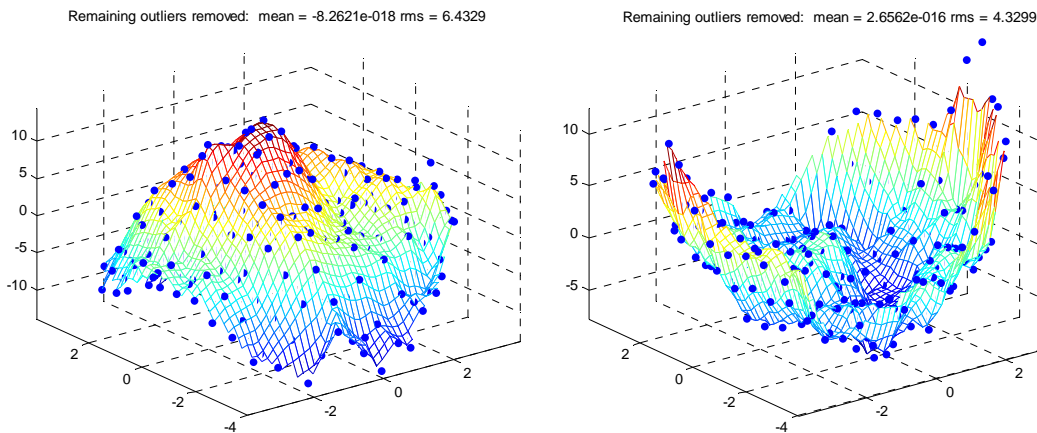


Figure 7-16: Plots of the GMT mirror segment with significantly different amounts of power due to changes in the thermal gradients across the mirror. The measurement on the left was taken shortly after washing the front surface and had a measured thermal gradient of ~ 1 K front to back. The measurement on the right was taken after the mirror was allowed to passively equilibrate overnight, reducing the thermal gradient to 0.4 K, which changed the power by 31 μm .

Given the strong dependence of RoC on temperature gradients, effort is made to decrease the temperature difference across the mirror to < 0.1 K for each measurement. This is not easy to achieve because the electronics in the cell can produce localized hot spots, and passive cooling is inefficient. For this reason, the mirror is actively ventilated

before each measurement to attempt to equilibrate it. This is done by attaching three large hoses to the mirror cell and using industrial squirrel cage fans to suck air through the cell. These can be seen in the photo of the underside of the GMT mirror cell shown in Figure 7-17.



Figure 7-17: The underside of the GMT mirror cell, with the hoses from the “suckulators” that are used to actively ventilate the mirror cell.

The last potential source of measurement error to be conscious of is the support forces. Again, this is not an error in the Laser Tracker Plus system, but an effect that must be controlled in the test procedure. During fabrication, the mirror sits on a set of passive hydraulic supports intended to duplicate the axial support forces in the telescope. The passive supports can develop errors due to friction, bending of the support cell, and tilt. The support forces are typically measured before a surface measurement. The plots in Figure 7-18 show a typical set of force measurements for GMT. Generally, if force errors more than ± 5 pounds develop, the supports are adjusted to redistribute the load.

One issue to keep in mind is that the loadcells that are used to measure the axial support forces are located within the mirror cell and produce heat when operating. For this reason, the forces are typically measured just briefly before the surface measurements, and possibly again after the surface measurement.

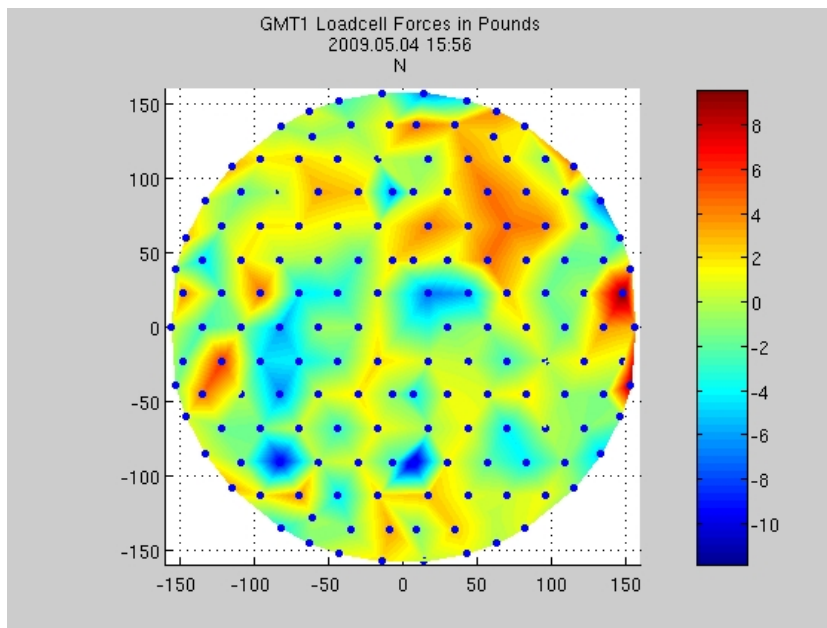


Figure 7-18: Errors in the GMT axial support forces measured by loadcells in the mirror cell.

7.3.3 Performance vs. Goals

Back in Chapter 1, the performance goals for the system were discussed, and the requirements were listed in Table 1-2. Now that the Laser Tracker Plus system has been in operation for over a year, it is time to evaluate how well it meets these goals. The stated minimum requirements were to “guide figuring to within capture range of principal optical test”, and to “reduce geometric errors to ... $\sim 10 \mu\text{m}$ P-V surface”. The system is

capable of meeting both of these requirements, although due to the decision to end loose-abrasive grinding early, the geometric errors in the mirror (radius of curvature) are still about 30 μm P-V surface, and other errors are about 3 μm rms surface. The mirror or the interferometer can be shifted from the nominal positions to compensate for the power. The comparison of a Laser Tracker Plus map and a visible interferogram in Figure 7-6 shows that fringes are resolved over most of the surface. The figure error that limits the ability to resolve fringes are present in the Laser Tracker Plus map, so the Laser Tracker Plus measurements are adequate to guide the figuring further. Likewise, the Laser Tracker Plus measurements of power agrees with that of the optical test within 3 μm P-V. (The Laser Tracker Plus measures power directly while the optical test sees power as a change in the position of the mirror at best focus.) Both power and residual errors will continue to be reduced by figuring, guided by the Laser Tracker Plus measurements until optical tests can be made routinely.

The right-hand side of Table 1-2 lists the implied requirements for the system. Addressing these requirements is probably the best way to evaluate how well the Laser Tracker Plus system meets its performance goals. The results presented in Tables 7-2 and 7-3 are used to address most of these requirements.

- The root-sum-square of the first 15 Zernike polynomials in Table 7-3 is 1.2 μm rms, which meets the system's net accuracy requirement.
- The radial calibration does not provide information about power, so the accuracy in power must be inferred from the manufacture's specifications for ADM distance and IFM displacement accuracies and the angular calibration

measurements. From these, the power measurement accuracy is estimated to be better than 0.5 μm rms surface, which satisfies the basic requirements and the goals.

- Table 7-3 indicates that the measurement of astigmatism is accurate to $\sim 0.6 \mu\text{m}$ rms, which satisfies the goals, but is just shy of the ambitious goals the system. More tests including 90° rotations of the mirror are needed to evaluate the accuracy in astigmatism.
- The coma measurement is only accurate to $\sim 0.25 \mu\text{m}$ rms based on Table 7-3, so it does not meet the ambitious goals, but satisfies the basic requirements.
- The laser tracker measurements of the geometry references on the mirror consistently have fitting errors that are less than 0.5 mm, which indicates that the measurement meets the ambitious goal.
- The specifications listed in Table 3-1 state the ADM accuracy of the laser tracker is better than 20 μm over the ~ 22 m distance from the laser tracker to the mirror, which is 10 times better than the ambitious goal.

Table 7-4 contains the tabulations of all of the error sources for a Laser Tracker Plus measurement with their expected values obtained from the custom laser tracker calibration and the correlation study. The expected system accuracy is computed, showing that the system meets all stated goals for system accuracy. In all cases, the Laser Tracker Plus system exceeds the basic performance requirements stated in Chapter 1.

Table 7-4: Laser Tracker Plus system accuracy.

Laser Tracker Plus System Measurement Accuracy					
Category	Source	Type	Direct surface microns	Angle microrad	Net surface microns
Tracker Calibration					
Distance vs angle:	Error in correction	systematic	0.0		0.0
	Uncorrected systematics	systematic	0.1		0.1
Angle vs angle:	Error in correction	systematic		0.2	0.2
	Uncorrected systematics	systematic		0.2	0.2
Tracker Noise					
	Distance	random	0.1		0.1
	Angle	random		0.5	0.6
Compensation					
Distance:	DMI noise	random	0.2		0.2
	Non-linear spatial variation	random	0.1		0.1
Angle:	Uncompensated motion	random		0.3	0.4
SMR Centering					
	Depth error	systematic	0.1		0.1
	Runout error	random		0.0	0.0
Net Error			0.3	0.6	0.8

The radial calibration measurements showed that the error in the laser tracker's measurement of radial distance as a function of angle is $< 0.1 \mu\text{m}$ rms without any correction. The results from the angular calibration show that the residual error in the laser tracker's measurement of angle as a function angle can be reduced significantly through calibration, resulting in $< 0.2 \mu\text{rad}$ rms of uncorrected repeatable errors after calibration, with the assumption that there is $< 0.2 \mu\text{rad}$ rms error in the correction itself. The noise in a typical laser tracker measurement is $< 0.1 \mu\text{m}$ rms in distance and $< 0.5 \mu\text{rad}$ rms in angle. The correlation study showed that when DMI compensation is performed, a large amount of relative motion error is removed from the laser tracker measurements, but $< 0.2 \mu\text{m}$ rms error is added to the laser tracker measurements due to the noise in the DMI measurements. Likewise, only rigid-body relative motion is corrected with the DMIs, but analysis of the non-planar component of the data shows that

the non-linear spatial variations are $< 0.1 \mu\text{m rms}$. Analysis of a typical GMT surface measurement shows that since the PSD compensation is not being performed, there is lateral relative motion that is not being corrected, equivalent to $< 0.3 \mu\text{rad rms}$. Errors in the centering of the retroreflector in the SMR can couple into surface errors, but for the SMR used for these test, there is not runout error and the 0.00007 inch depth error multiplied by the maximum tilt of the SMR with respect to the laser tracker line of sight (4.4° from Table 2-1) results in $< 0.1 \mu\text{m rms}$ of surface error.

The radial errors directly contribute to errors in the surface measurements, while the angular errors couple to surface errors through the sensitivity relationship described in Equation 2.3. For GMT, the average sensitivity is $1.2 \mu\text{m}/\mu\text{rad}$, which multiplies the angular errors in Table 7-4 to determine the resulting net surface errors. These errors are than root-sum-squared to determine the expected net error for the entire system. The result is that each individual measurement is expected to be accurate to better than $0.8 \mu\text{m rms}$.

An estimate was performed to determine how the error sources listed in Table 7-4 couple into the low-order Zernike polynomials that the Laser Tracker Plus system is expected to verify for the principal test. The error sources were each classified as either random or systematic, and their magnitude was multiplied by a scale factor to determine the coupling of the error into each polynomial coefficient. The random errors contribute equally to all the polynomials by a scale factor of $1/\sqrt{N} \approx 0.07$, where N , the number of measurement points, is 216 for a typical surface measurement. Coupling factors for systematic errors must be estimated. The worst case for any aberration would be a

coupling factor of 1.0, leaving no systematic error in any other aberration. Instead, the assumption was made that systematic errors will couple more strongly into the simpler and more systematic aberrations: 0.5 for power, 0.3 for astigmatism, and 0.2 for coma. Table 7-5 lists the expected error in the fit for these three critical Zernike polynomials as a result of the individual measurement errors.

Table 7-5: Expected errors in the fit of low-order Zernike polynomials to a GMT surface measurement due to the errors listed in Table 7-4 for individual Laser Tracker Plus measurements. These values meet the system design specifications listed in Table 1-2.

Error Contributions to Zernike Polynomials					
Category	Source	Type	Power microns	Astigmatism microns	Coma microns
Tracker Calibration					
Distance vs angle:	Error in correction	systematic	0.00	0.00	0.00
	Uncorrected systematics	systematic	0.05	0.03	0.02
Angle vs angle:	Error in correction	systematic	0.12	0.07	0.05
	Uncorrected systematics	systematic	0.12	0.07	0.05
Tracker Noise					
	Distance	random	0.01	0.01	0.01
	Angle	random	0.04	0.04	0.04
Compensation					
Distance:	DMI noise	random	0.01	0.01	0.01
	Non-linear spatial variation	random	0.01	0.01	0.01
Angle:	Uncompensated motion	random	0.02	0.02	0.02
SMR Centering					
	Depth error	systematic	0.07	0.04	0.03
	Runout error	random	0.00	0.00	0.00
ADM Error					
	Initial distance measurement	systematic	0.03		
rms Surface Error			0.20	0.12	0.09

The ADM error is a special case that only affects the power term, so it was not listed in Table 7-4. This error affects the RoC measurement, producing a systematic error that looks like power at a rate of 0.0018 μm rms of defocus for each micron of distance error. Table 3-1 lists the Faro tracker's ADM accuracy as $\pm 9.8 \mu\text{m} + 0.4 \mu\text{m}/\text{m}$, which at

a distance of 22.3 m works out to an initial distance uncertainty of $\pm 18.7 \mu\text{m}$, which agrees with the values typically observed, as shown in Figure 7-13. This error is very small and contributes $< 0.03 \mu\text{m}$ rms of error in the power coefficient.

Chapter 8

FINAL COMMENTS

As scientific demands continue to push the frontiers of astronomy, larger telescopes with faster optics will be required. One repercussion of those demands is that the optical surfaces can become highly aspheric, making the testing extremely difficult. The main thrust of this dissertation was to develop a system that can guide the loose-abrasive grinding of large telescope mirrors, while having sufficient accuracy to be used as a verification instrument to validate the optical interferometric results obtained by the GMT principal test.

It was a challenging research project to determine how to combine multiple commercially available metrology systems, develop custom calibrations to improve an individual system's performance beyond the manufacture's specifications, and properly combine the measurement data in a manner that improves the total system accuracy enough to meet the requirements. The project involved extensive evaluation and testing of the different commercially available laser trackers and distance measuring interferometry systems, to identify those that would work best for the combined system. From there, custom calibrations were employed to identify intrinsic errors that remained after following the manufacturers' recommended calibration. Studies were performed to evaluate the measurement environment and the sensors' accuracies, the results of which were used to determine how best to combine the individual measurements to improve the total system accuracy. System level tests were performed to evaluate the final accuracy

of the system, and this accuracy was compared with the design requirements. The final conclusion based on those results is that the system will meet or exceed its requirements in all categories.

Several useful lessons were learned along the way. First of all, making accurate measurements with a contact probe instrument at the micron level is hard! Mechanically, things move around a lot at that level. The realization that the weight of the puck moving around on the mirror surface can cause micron level motion of the GMT mirror was surprising. The extreme temperature dependence of the mirror's shape makes accurate testing difficult, and may make meeting the final RoC goals challenging. A number of error sources that affect the measurement accuracy were determined during the study, and explanations of the techniques used to mitigate them were presented.

In addition to the GMT measurements, this system will be used to provide the feedback for the loose-abrasive grinding of the combined primary and tertiary mirrors for the Large Synoptic Survey Telescope. Because that mirror substrate consists of two optical surfaces in one, more work needs to go into developing the techniques required to make Laser Tracker Plus measurement of both surfaces. Measurements of the LSST primary, the outer annulus of the mirror, should be fairly accurate and straightforward using the Laser Tracker Plus system. On the other hand, the LSST tertiary, the central portion of the mirror, is a deep bowl in the center, with a short RoC and steep surface slopes. It will be difficult to get the SMR positioner, as it stands now, to work reliably on that surface. Coupling of angular errors into surface errors is more severe due to the large angle of incidence for the tertiary. Meeting the accuracy requirements for this

surface will rely heavily on the angular calibration techniques developed for this dissertation.

The angular calibration procedure discussed in Chapter 4 works, but it is tedious to perform and has drawbacks due to the time required to perform the measurements. It takes over an hour to measure a single scan of 21 point, during which drift can significantly affect the results. To improve the accuracy, more points should be taken per scan, and more scan angles measured, both of which require longer measurement times. An earlier idea was to use a 10 m long precision rail with either a distance measuring interferometer or another laser tracker mounted at the one end. This idea was later rejected due to cost and other constraints. One of the baseline beliefs that we had going into this project was that it would be difficult to install and remove the laser tracker from the tower. This belief drove our requirement that the calibrations be performed *in situ*, but during the first year of operation, we determined that it is possible for two people to install or remove the laser tracker head from the system in about ½ hour. The reality is that it will be far easier to perform the calibrations at ground level rather than 85 feet in the air, so I propose the following modification to the calibration procedures outlined in Chapter 4. The tracker stand used for mounting the floor tracker in the angular calibration test could be easily modified to hold the calibration mirror at the proper distance to align the CoC and the tracker's gimbal for performing the radial calibration at floor level. The angular calibration could also be performed at floor level by using a shorter precision rail system similar to the "Laser Rail", a 2.8 m rail with integral laser interferometer and carriage for holding two SMRs manufactured by API, pictured in Figure 8-1 [2]. This system was designed by API as a verification tool, rather than a

calibration tool, but this tool or one of similar design could be used to perform the angular calibration by following the same general guidelines previously discussed in this dissertation, but with the laser tracker mounted 1-3 m above the rail. The DMI accuracy is listed as 0.5ppm, so at a distance of 2 m, the carriage would need to scan 0.4 m along the rail to traverse the 10.7° (~ 0.2 rad) subtended by GMT at 22.3 m, resulting in a DMI accuracy of $0.2 \mu\text{m}$. This gives an angular accuracy of $0.1 \mu\text{rad}$ for this configuration, which is sufficiently accurate for the angular calibration. This option would significantly improve the ease and precision of the calibration process.



Figure 8-1: Laser Rail system manufactured by API for verifying that laser tracking systems meet their performance requirements as specified in the ASME B89 standard.[2]

On the whole, the system performance is very good and it runs quite reliably. The SOML should get many years of useful service out of it for testing GMT, LSST, and any future telescope mirrors.

Appendix A

COMPETING TECHNOLOGIES

Ever since the advent of lasers in the 1960's, many useful metrology instruments have been developed making use of laser technology, of which, laser trackers are one. Gallagher's thesis provides a useful summary of many of these instruments, including a discussion of the history and evolution of the laser tracker [15]. A number of these technologies can perform highly accurate measurements similar to the Laser Tracker Plus system and are discussed in some detail below. Several of these systems were considered for the GMT testing, but were rejected due to cost or performance limitations. Table A-1 shows a comparison of the Laser Tracker Plus system and the competing technologies, which include:

- Laser tracker – The Laser Tracker Plus system utilizes a standard laser tracker, which has been successfully used to guide the loose-abrasive grinding of smaller mirrors, such as the New Solar Telescope 1.7 m primary mirror, which is a 1/5 scale prototype of the GMT mirror [31]. However, without the external reference system to back out errors that scale with the system, a standard laser tracker would not have the required accuracy. The errors that the external reference system help mitigate include an increased sensitivity to relative motion between the mirror and tracker head because of the increased separation, larger lateral errors due to the limitations in the angular encoders over the longer path lengths,

and decreased radial accuracy because of air effects over the increased optical path length.

- Multilateration System – Utilizes four laser trackers that all monitor the same target and determine its location strictly from the four radial measurements to eliminate the angular errors which limit a stand alone laser tracker. The radial errors caused by the air effects now limit the system accuracy. The National Physical Laboratory proposed a multilateration system for testing GMT [21]. Their proposal built on the heritage of the Surfitek system built in the 1980's [19, 20]. The proposal was ultimately rejected due to cost and complexity.
- Standard CMM – A probe tip is moved with linear X-Y stages and mechanically measures the height of an object that sits atop the granite table surface that is part of the machine. These systems are typically expensive and commonly are only used for measuring smaller objects to high precision, but would be impossible to implement on the order of the GMT.
- Joint-Arm CMM – This is type of portable CMM uses a probe tip on the end of a multi jointed arm. Encoders at each joint record the angle between each adjacent arm segment, coupled with the segment length will determine the location of the probe tip with respect to the base of the arm. The angular errors in the encoders limit the accuracy of this system more than a standard laser tracker because the increased number of encoders required. Mechanical limits set the practical length of the arm and thus limit the size to surfaces smaller than GMT.

- Swing-Arm Profilometer – Utilizes a probe (either optical or mechanical) at the end of a long rigid arm that sweeps a circular arc above the measurement surface. The probe measures the height difference between the measurement surface and the circular arc. Uncertainty in the knowledge of the arc followed limits the accuracy in the measured surface.

The Steward Observatory Mirror Lab (SOML) has a swing-arm profilometer that is capable of measuring both convex and concave optics up to 2 m in diameter. This profilometer has been used to guide the loose-abrasive grinding on a number of symmetric telescope secondary mirrors. The Optical Sciences Center has built swing-arm profilometers that are capable of measuring convex and concave mirrors up to 4 m. It is possible to make a swing-arm profilometer that would be capable of measuring an 8.4 m mirror such as GMT, but there are additional issues to address than just size. The SOML profilometer can measure asphericity with an accuracy of about 50 nm rms, but it is relatively insensitive to average curvature (power) [31]. For an off-axis mirror like GMT, the profilometer cannot measure the difference in sag between the two orthogonal diameters within an accuracy of a few microns, as is needed to make the transition from loose-abrasive grinding to polishing and testing at 633 nm.

Table A-1: A comparison of competing technologies with similar accuracy and range to the Laser Tracker Plus system.

Competing Technologies	Accuracy	Range	Angular Errors	Air Effects	Relative Motion Effects	Test Area Size	Cost
Laser Tracker Plus	Very High	Broad	Moderate	Low	Small	Large	Higher
Laser Tracker	Higher	Broad	High	High	Large	Large	High
Multilateration System	Very High	Limited	None	High	Large	Moderate	Very High
Standard CMM	Higher	Very Limited	None	None	Moderate	Very Small	Higher
Jointed-Arm CMM	High	Very Limited	Very High	None	Moderate	Small	Moderate
Profilometer (Swing-arm)	High	Limited	None	None	Moderate	Small	Moderate

Appendix B

HARDWARE TECHNICAL DETAILS AND SPECIFICATIONS

To prevent Chapter 3 from becoming overly burdened with all the technical details of the individual components that make up the external reference system, the details were extracted from that chapter and included in this appendix for completeness.

B.1 Heterodyne Laser Head

A heterodyne laser emits a coherent light beam composed of two slightly different optical frequencies, f_1 and f_2 , with orthogonal linear polarization states, horizontal and vertical respectively. This is achieved by means of the Zeeman Effect, where an intense axial magnetic field is used to split degenerate electron energy levels of an atom into separate sublevels based on the electron spin state. For a helium-neon laser, the degenerate energy levels of the $3s_2 \rightarrow 2p_4$ lasing transition of the neon atoms in the gain medium are split, causing two separate lasing transitions with slightly different energy and photon frequencies. Because the two transition energy levels have opposite spin states, the emitted photons from those lasing transitions have opposite circular polarization states. A quarter-wave plate within the laser head converts the beam's circularly polarized components to orthogonal linearly polarized components before the beam leaves the laser head.

Before exiting the laser head, the beam passes through a beam splitter where a small fraction of the light is sampled. This portion of the beam is used to generate an electronic reference signal between 1.9 and 2.4 MHz, which is outputted to the PC Axis board measurement electronics. The difference in the beam component optical frequencies f_2-f_1 is used to produce the reference signal.

The laser head selected for the Laser Tracker Plus system is an Agilent 5517B. Table **B-1** lists the specifications for the laser, while Figure **B-1** provides the laser head

Table **B-1**: Agilent 5517B laser head specifications [1].

PHYSICAL CHARACTERISTICS	
Dimensions:	See Figure B-1
Weight:	3.4 kg (7.5 pounds)
POWER	
Power Input Requirements:	+15 V \pm 0.3 V at 2.2 Amps Maximum -15 V \pm 0.3 V at 0.02 Amps Maximum
Heat Dissipation:	35 watts during warm-up 23 watts during operation
Warm-up Time:	Less than 10 minutes (4 minutes typical)
Equilibrium Time:	30 minutes typical
LASER BEAM CHARACTERISTICS	
Type:	HeNe, continuous wave, two-frequency
Maximum Beam Power Output:	1 milliwatts
Minimum Beam Power Output:	120 microwatts
Measured Beam Power Output:	635 microwatts
Beam Diameter:	6 millimeter (0.25 inch) typical
Vacuum Wavelength Accuracy:	\pm 0.1 ppm (3 sigma, lifetime)
Vacuum Wavelength Stability:	\pm 0.002 ppm (typical 1 hour) \pm 0.02 ppm (typical lifetime)
Nominal Vacuum Wavelength:	0.63299137 μ m
Pointing Stability:	< 2 arc-minutes (during warm-up) A few arc-seconds (after thermal equilibrium)
Range:	40 meters (130 feet)
Laser Tube Lifetime:	> 50,000 hours of operation
ELECTRONIC OUTPUT	
Reference Frequency (f_2-f_1):	Between 1.9 – 2.4 MHz

dimensions. To accommodate the nearly 25 m working distance from the interferometers, mounted in the top of the tower, to the floor, the laser was ordered with a 6 mm diameter beam that has an operational range of 40 m. The laser head was ordered with option H10, a $>400 \mu\text{W}$ power output (measured to be $635 \mu\text{W}$), to provide sufficient power to split the laser output into four reference arms.

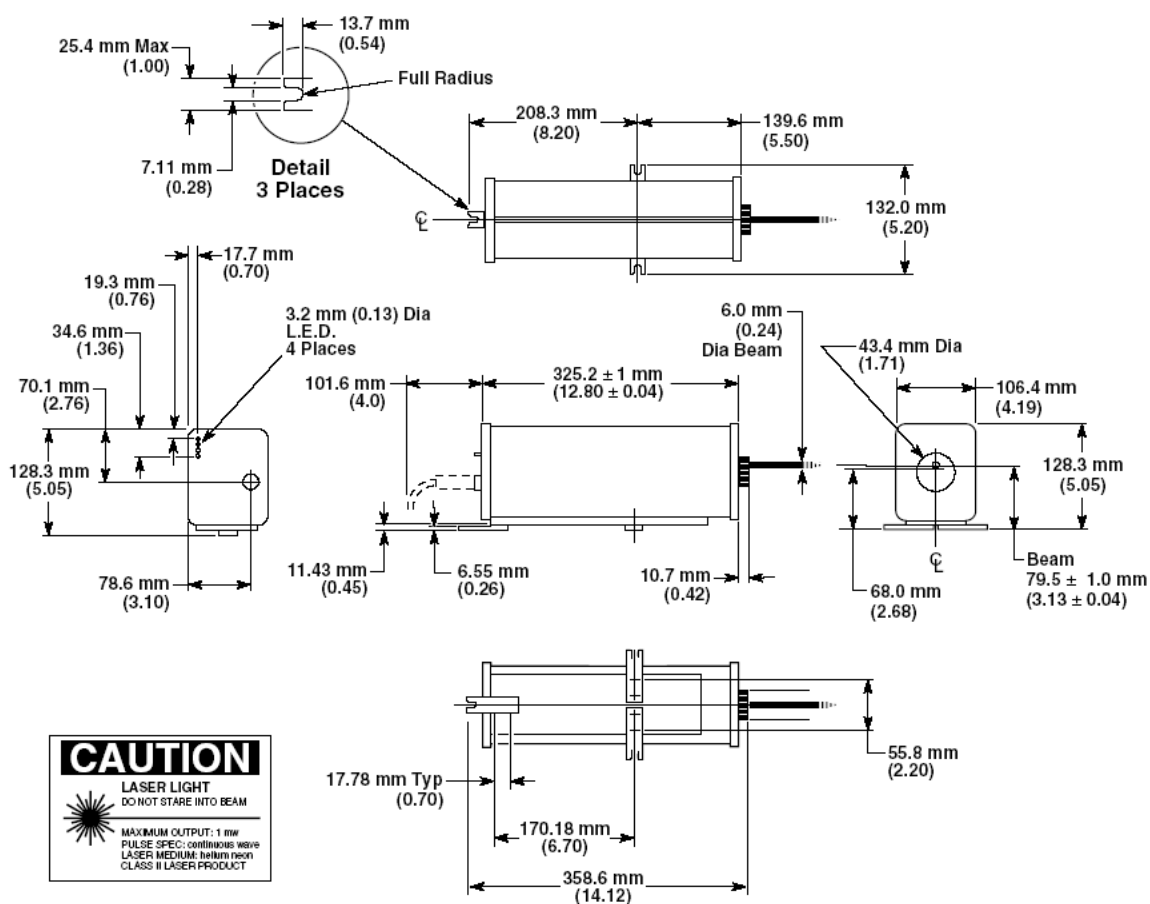


Figure B-1: Agilent 5517B laser head dimensions [1]. Image used with permission from Agilent Technologies, Inc.

Heterodyne lasers are generally used with displacement measuring interferometers (DMI) because they have four main advantages over homodyne lasers, which only producing a single frequency laser output [25].

1. The interference signal is insensitive to intensity fluctuations in the laser light.
2. They have high measurement accuracy independent of displacement speed.
3. Heterodyne lasers can be split into more beams, allowing more axes per laser.
4. The design is absent of laser tube noise.

The maximum slew rate that a heterodyne laser can measure is limited by the frequency difference between the two polarization states; the larger the frequency separation f_2-f_1 , the faster the response time of the system. The maximum motion speed achievable with the laser selected is considerably faster than the motions being monitored by the external references for the Laser Tracker Plus system, so that the maximum speed would not be a limitation.

B.2 Single Beam Interferometer and Retroreflectors

The linear interferometers used for the DMI system were Agilent 10705A single beam interferometers, shown in Figure **B-2**. These interferometers are intended for use in low-mass or space-limited application. The single beam interferometer is called that because the outgoing and returning beams are superimposed on each other, giving the appearance of a single beam traveling between the interferometer and retroreflector.

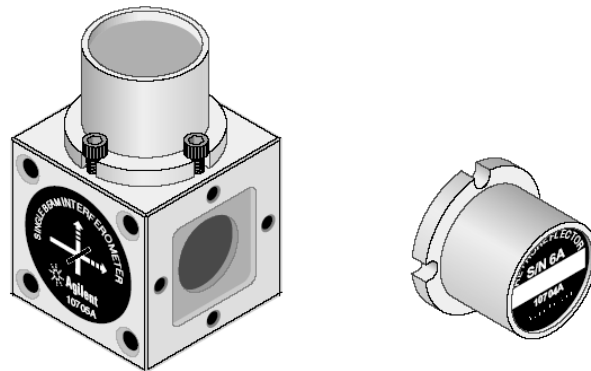


Figure B-2: Agilent 10705A single beam interferometer (left) and Agilent 10704A retroreflector (right) [1]. Image used with permission from Agilent Technologies, Inc.

The Agilent 10705A single beam interferometer is composed of a polarization beam splitter and two quarter-wave plates mounted in a 1 inch cube housing of stainless steel (the dimensions of the Agilent 10705A interferometer are provided in Figure B-3), with a retroreflector mounted at one of the outputs to act as a reference mirror. The two

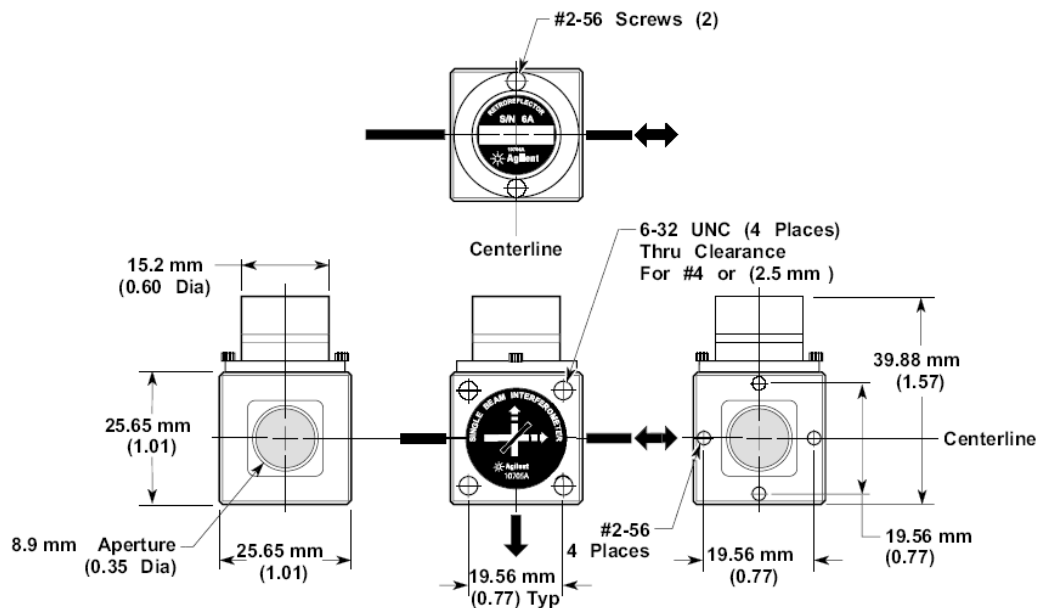


Figure B-3: Agilent 10705A single beam interferometer dimensions [1]. Image used with permission from Agilent Technologies, Inc.

linear orthogonally polarized outputs from the laser are split by the polarizing beam splitter into two separate beams, each having only one of the two frequencies (f_1 & f_2) of the original beam from the laser.

The interferometer must be aligned to within 1° of the incoming linearly polarized light to minimize cross-talk between the two polarized frequencies. Rotating the interferometer by 90° switches which optical frequency (f_1 or f_2) is in the reference path, thus changing the displacement direction sense. For the arrangement used in the Laser Tracker Plus system, the interferometer was oriented so that the horizontally polarized beam from the laser (the lower frequency: f_1) was reflected by the beam splitter to become the reference beam. Likewise, the vertically polarized beam (the higher frequency: f_2) was transmitted straight through the beam splitter to become the measurement beam.

After leaving the beam splitter, the two linearly polarized beams pass through the quarter-wave plates and become right-hand and left-hand circularly polarized as they leave the interferometer. The reference beam immediately strikes the retroreflector mounted to the side of the interferometer cube, and is reflected back through the interferometer, while the measurement beam travels a longer distance through the air to a retroreflector mounted on the surface of the optic being tested with the Laser Tracker Plus system, before being reflected back to the interferometer. When each of the circularly polarized beams strikes the retroreflectors, the directions of their polarizations switch, so when the beams pass back through the quarter-wave plate when reentering the interferometer, they become linearly polarized with the opposite sense they previously

had. Where the reference beam was reflected by the polarizing beam splitter the first time, it will now pass straight through the beam splitter to the receiver. Likewise, the measurement beam initially passed straight through the beam splitter, but because its polarization has been flipped, it will now be reflected by the beam splitter so that it too is incident on the receiver. Figure B-4 shows a diagram of the laser beam paths through the interferometer.

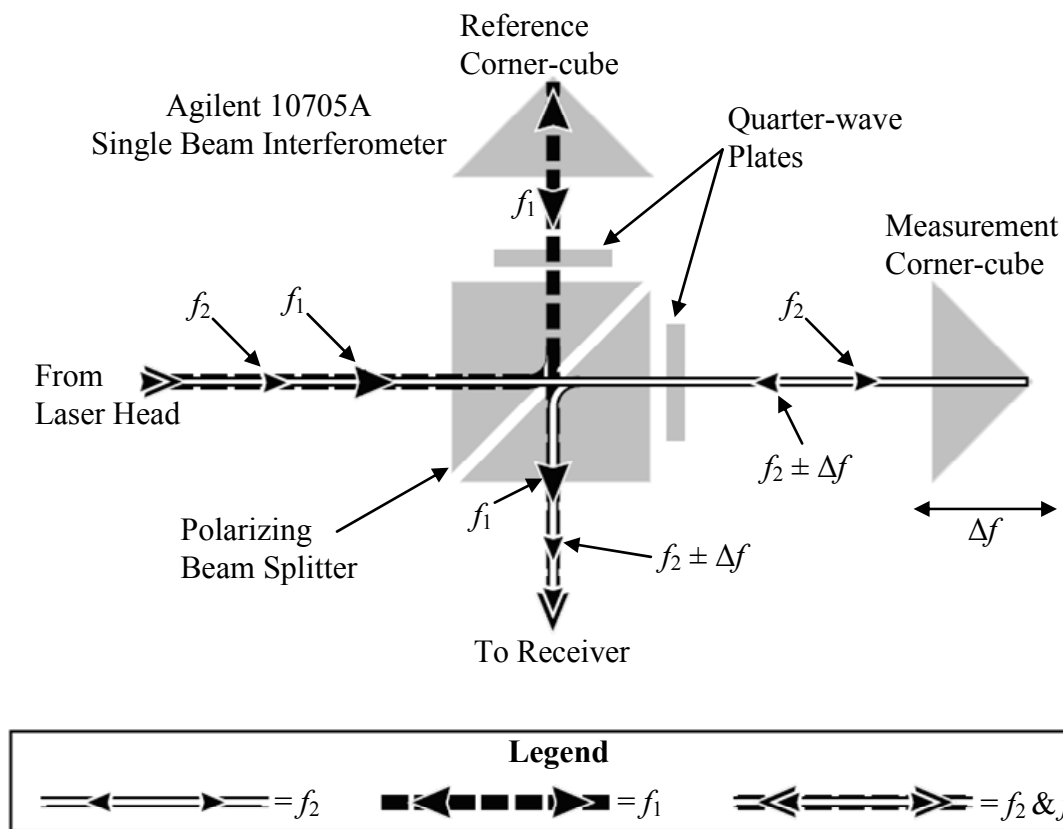


Figure B-4: Single beam interferometer reference and measurement laser beam paths [1]. Image used with permission from Agilent Technologies, Inc.

The retroreflector for the reference beam is mounted directly on the interferometer, and is therefore stationary. The measurement beam retroreflector is

mounted on the optic being tested, and moves with respect to the interferometer. When this happens, the optical frequency of the measurement beam f_2 gets Doppler-shifted by an amount Δf , causing the reflected beam to have a slightly different frequency $f_2 \pm \Delta f$. If the system is properly aligned, the measurement and reference beams are both coincident on the receiver, but have opposite linear polarizations, so the two beams do not interfere. An analyzer screen (a linear polarizer oriented at 45° to the two incident beams) in the receiver caused the two beams to interfere, allowing the measurement electronics to determine the difference frequency ($f_2 - f_1 \pm \Delta f$) between the measurement and reference beams, corresponding to the change in the optical path difference (OPD) between the two beams. The receivers are described in more detail in Section **B.4**, while the measurement electronics are described in Section **B.5**.

Table **B-2** lists the technical specifications of the Agilent 10705A single beam interferometer. From this, the fundamental optical resolution of a single beam interferometer is listed as $\lambda/2$ ($0.3165 \mu\text{m}$), where $\lambda = 0.633 \mu\text{m}$ for the Agilent 5517B Laser Head. When coupled with $32\times$ electronic resolution extension, this gives a system resolution of $\lambda/64$ ($0.01 \mu\text{m}$), which is ten times better than what is required to meet the Laser Tracker Plus system design requirements.

Table B-2: Agilent 10705A single beam interferometer technical specifications [1].

PHYSICAL CHARACTERISTICS	
Dimensions:	See Figure B-3
Weight:	85.5 grams (3.0 ounces)
MATERIALS USED	
Housing:	Stainless Steel (416)
Apertures:	Plastic (Nylon)
Optics:	Optical Grade Glass
Adhesives:	Low Volatility (Vacuum Grade)
OPTICAL CHARACTERISTICS	
Transmitted Beam Deviation:	± 30 arc-minutes (maximum)
Optical Efficiency:	62% (typical)
(includes retroreflector losses)	59% (worse case)
Fundamental Optical Resolution:	$\lambda/2$
Non-linear Error:	$< 0.0042 \mu\text{m}$
Beam Roll Alignment Tolerance:	$\pm 1^\circ$ (with respect to laser head axes)

This interferometer was used with the Agilent 10704A retroreflector, shown in Figure B-2. This is a glass prismatic retroreflector with a clear aperture of 10.2 mm. The retroreflector is mounted in a stainless steel housing that can be bolted directly to the output of the polarizing beam splitter of the Agilent 10705A single beam interferometer to function as the reference beam retroreflector. Table B-3 lists the specification for the retroreflector, while the dimensions are provided in Figure B-5.

Table B-3: Agilent 10704A retroreflector technical specifications [1].

PHYSICAL CHARACTERISTICS	
Dimensions:	See Figure B-5
Weight:	10.5 grams (0.37 ounce)
MATERIALS USED	
Housing:	Stainless Steel (416)
Optics:	Optical Grade Glass
Adhesives:	Low Volatility (Vacuum Grade)

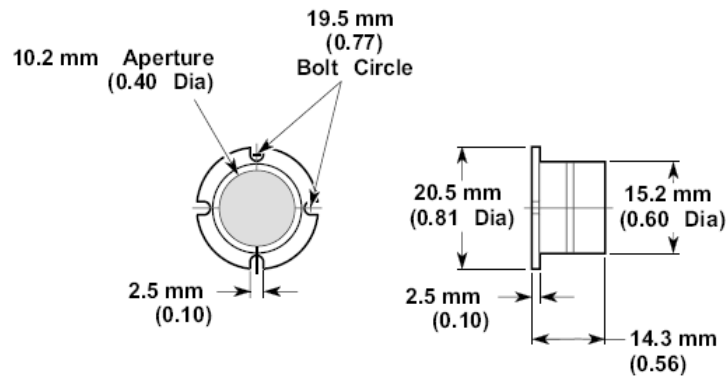


Figure B-5: Agilent 10704A retroreflector dimensions [1]. Image used with permission from Agilent Technologies, Inc.

B.3 Beam Directing Optics

Additional beam directing optical components were used to split the beam from the laser into four separate beams and steer them into the four interferometers. Three Agilent 10701A 50% beam splitters were used to divide the laser head output beam into four beams of equal intensity. Additionally, two Agilent 10707A beam benders were used to redirect two of the beams 90° to align with their intended interferometers. The dimensions for these two optical components are provided in Figure B-6, while the technical specifications are provided in Table B-4.

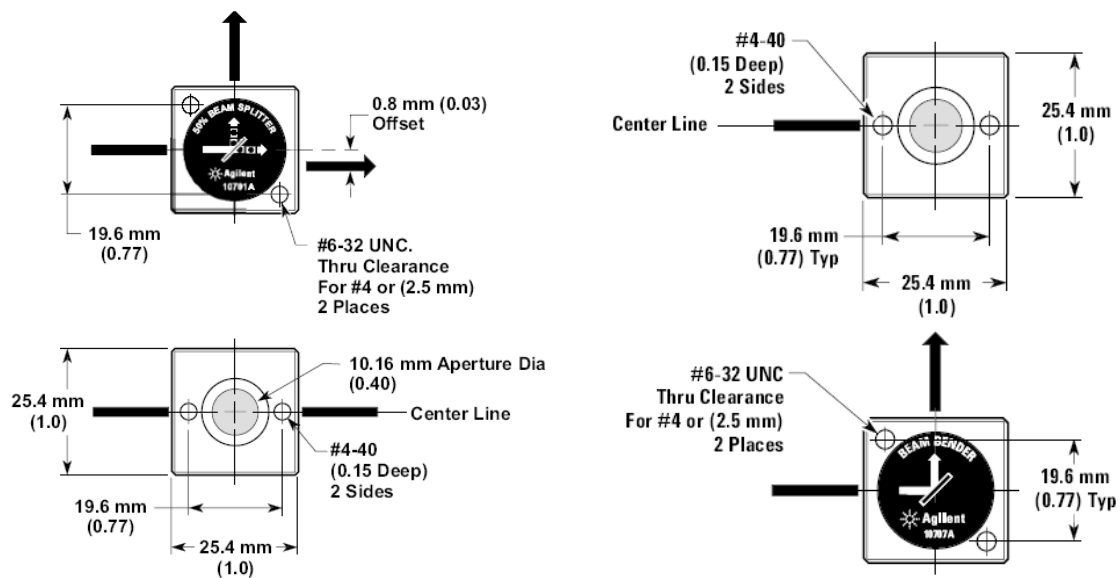


Figure B-6: Dimensions of the Agilent 10701A 50% beam splitter (left) and Agilent 10707A beam bender (right) [1]. Image used with permission from Agilent Technologies, Inc.

After the four measurement beams leave each interferometer, they must be redirected towards the edges of the optic under test at floor level beneath the test tower. For this purpose, 1 inch diameter flat mirrors (PF10-03-G01) with protected aluminum coatings were ordered from Thor Labs, which were mounted in 90° cage block mirror mounts (KCB1) [40]. The mirror coating, specified by an application engineer at Zygo, allows the DMI beams to be steered without adversely affecting their polarization states. The KCB1 cage block is designed to deviate an optical beam 90° while providing $\pm 4^\circ$ of tip/tilt adjustment using 100 threads-per-inch, manual-adjust screws for smooth movement and high resolution. The cage blocks are each mounted on a 10.7° wedge plate to nominally tilt the four beams to the four compass points along the circumference of the mirror under test. The steering mirrors only need to be manually adjusted once to

the nominal reference location on the surface of the test optics. Thereafter, the surface references (shown in Figure 3-6) are manually positioned on the surface of the optic to center the retroreflector on the measurement beam.

Table B-4: Technical specifications for the Agilent 10701A 50% beam splitter and the Agilent 10707A beam bender [1].

BEAM DIRECTING OPTIC:	AGILENT 10701A	AGILENT 10707A
PHYSICAL CHARACTERISTICS		
Dimensions:	See Figure B-6	
Weight:	62 grams (2.2 ounces)	58 grams (2.1 ounces)
MATERIALS USED		
Housing:	Stainless Steel (416)	
Optics:	Optical Grade Glass	
Adhesives:	Low Volatility (Vacuum Grade)	
OPTICAL CHARACTERISTICS		
Transmitted Beam Deviation:	0.8 mm (0.03 in) offset	N/A
Optical Efficiency (typical):	45% (each beam)	99%
(worse case):	39% (each beam)	98%
Beam Roll Alignment Tolerance:	$\pm 3^\circ$ (with respect to laser head axes)	

B.4 Receivers

The purpose of the receivers is to convert the Doppler-shifted laser light from the interferometers into an electrical signal that is sent to the PC axis board for comparison with the reference signal from the laser head. The receivers used for this task were Excel Precision model 1031F receivers, which are dimensionally and functionally identical to the Agilent 10780F remote receiver pictured in Figure B-7. The light enters through a lens and analyzer contained in a small assembly, called the remote sensor, that is bolted

directly to the interferometer, to maintain optical alignment, and connected to the receiver's electrical housing via a 2 m long fiber optic cable.

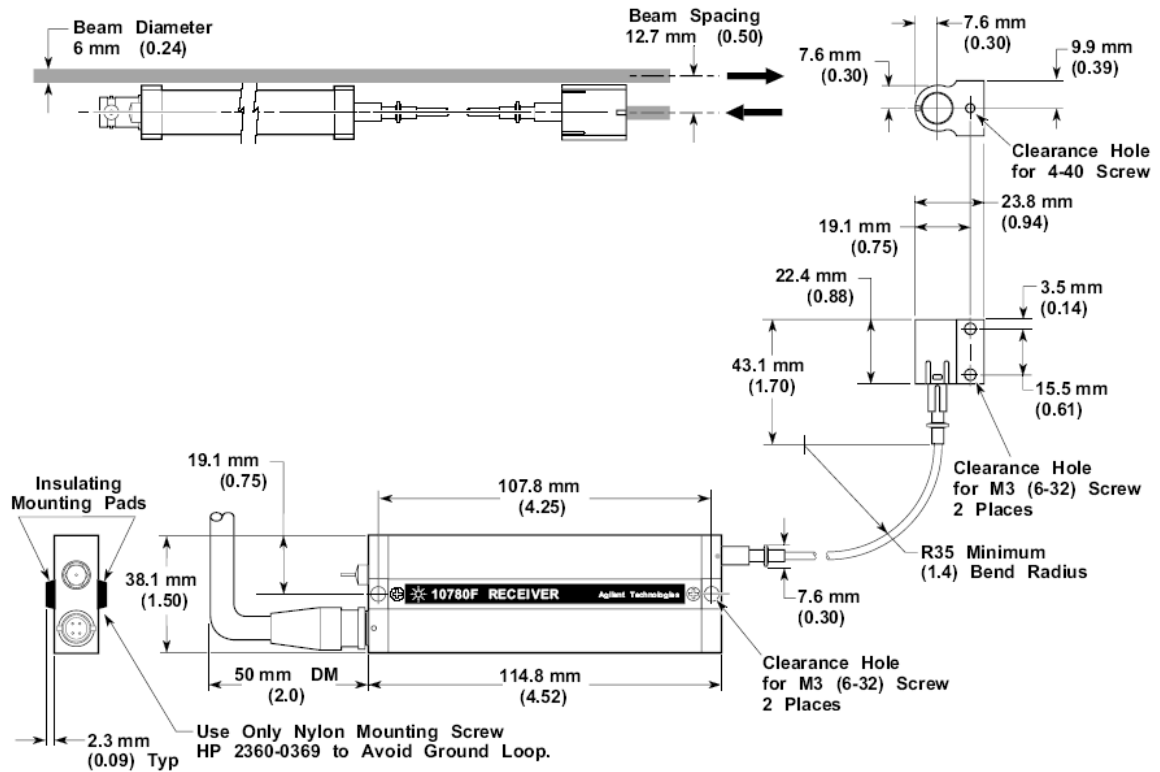


Figure B-7: Dimensions of the Agilent 10780F remote receiver with 2 meter fiber optic and remote sensor [1]. Image used with permission from Agilent Technologies, Inc.

The fiber optic cable allows the receiver module to be mounted in a location remote from the interferometers, removing a source of heat from the measurement area. Each receiver, of which there are four, dissipate 2.3 W of heat (see technical specification in Table B-5), while the remote sensors do not dissipate any. For this reason, the receivers were mounted in a separate ventilated compartment along with the laser head.

Table B-5: Technical specifications for Excel Precision model 1031F remote receiver [13].

PHYSICAL CHARACTERISTICS	
Dimensions:	See Figure B-7 above
Weight:	139 grams (4.9 ounces)
POWER	
Power Input Requirements:	+15 V at 150 milliamps Maximum
Heat Dissipation:	2.3 watts Typical for receiver 0 watts for remote sensor
Maximum Cable length	20 meters (65 feet)
OPTICAL CHARACTERISTICS	
Maximum Fiber Optic Length:	10 meters
Minimum Fiber Bend Radius:	64 mm (2.5 inches)
Minimum Optical Input Power:	2.2 microwatts (with 2-meter cable)
Remote Sensor Alignment Tolerances:	$\pm 3^\circ$ (Roll)
(with respect to laser head axes)	$\pm 1^\circ$ (Pitch)
	$\pm 1^\circ$ (Yaw)
ELECTRONIC OUTPUT	
Measurement Frequency ($f_2-f_1\pm\Delta f$):	Differential square wave at Doppler-shifted split frequency (100 kHz – 5 MHz)

When the remote sensor is properly oriented (with its vertical axis parallel or perpendicular to the laser head axes), the analyzer passes one-half of the incident power from each of the two incoming orthogonally polarized components of the received laser beam. The output from the remote sensor, an amplitude-modulated sine wave caused by the interference between the f_1 and f_2 polarizations, is sent through the fiber optic cable to a photodiode chip in the receiver's electronic housing. The frequency of the signal is the Doppler-shifted split frequency $f_2-f_1\pm\Delta f$, while the amplitude is proportional to the product of the incident power of the two orthogonal components. The photodiode generates an AC current, which is converted to an AC voltage with a frequency between 100 kHz – 5 MHz. This is converted to a TTL-level signal that is outputted as a differential square wave at the Doppler-shifted split frequency to the PC axis board. The

receiver also generates a DC voltage output which indicates incoming laser beam intensity. The DC voltage output is monitored by the MicroPC (discussed in Section **B.9**) mounted with the DMI electronics, which reports the voltage signal to the master control console to indicate the quality of the optical alignment of the measurement beam retroreflector.

The receiver photodiode only measures the overlapping portion of the reference and measurement laser beams. For maximum signal strength, the interferometer and retroreflector must be aligned so that the reference beam from the interferometer and the measurement beam from the retroreflector exactly overlap each other and are centered on the photodiode during recombination. If the interferometer or the retroreflector is misaligned (see Figure **B-8**), the reference and measurement beams will no longer completely overlap, resulting in signal loss. Typically a lateral offset of $\frac{1}{4}$ of the beam diameter between the beams is allowable for adequate signal strength, but optimizing the beam overlap will improve the performance [1].

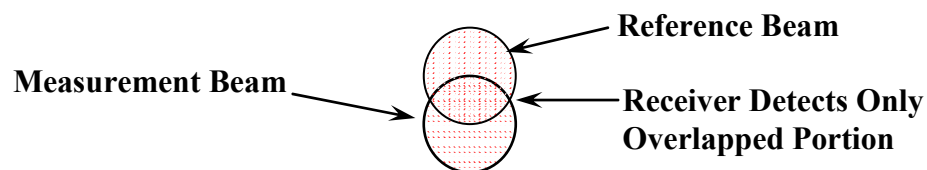


Figure **B-8**: Optical misalignment resulting in lateral displacement of the measurement beam with respect to the reference beam at recombination results in signal loss.

A couple of notes useful to mention:

1. The receiver's electronics housing is mounted using nylon screws. This serves two purposes. The first is that it electrically isolates the receivers from

the mounting fixtures so that ground loops do not introduce noise into the signal. Furthermore, the receivers are AC-coupled to the rest of the measurement electronics with shielded twisted-pair cable and powered by the same power supply as the laser head and PC axis board to further isolate noise. The second function of the nylon screws is to thermally isolate the receivers to reduce problems with heat conduction. The receivers typically dissipate between 2.0 and 2.7 W of power, so the plastic mounting feet provide an air gap around the receiver housing to act as a thermal isolator.

2. The Excel Precision model 1031F receiver used for this system has a variable sensitivity to the intensity of the incident optical power. Its maximum sensitivity is 2.2 μW when using its standard 2 m long fiber optic. The original design was to use an Agilent E1709A remote high-performance receiver with a 2 m cable and sensitivity between 0.2 - 0.8 μW depending on AC signal strength. It had numerous other strengths as well, but it was for this added sensitivity that it was selected. The belief was that the added sensitivity would provide a large safety margin to offset misalignments, dirty optics, and decreased laser power with age. One of the Agilent E1709A receivers was purchased for initial testing, but determined that the light returned by the system would saturate the detector without additional absorptive optics before the receiver. This, coupled with increased difficulty to align and optimize, demonstrated that a standard receiver was a better initial choice, and a high-

gain receiver should be reserved as a last resort. The Excel Precision model 1031F receivers used instead have proven to be more than adequate for the job

B.5 PC Axis Board

The signal processing for the DMI system is done using an Agilent 10885A PC axis board, shown in Figure B-9. These boards conform to ISA specifications used with PC-compatible computers. The Agilent 10885A axis board's primary function is to convert reference and measurement signals from the laser head and a measurement receiver into a 32-bit digital position word (the count) that can be read by the software via the PC's I/O backplane.

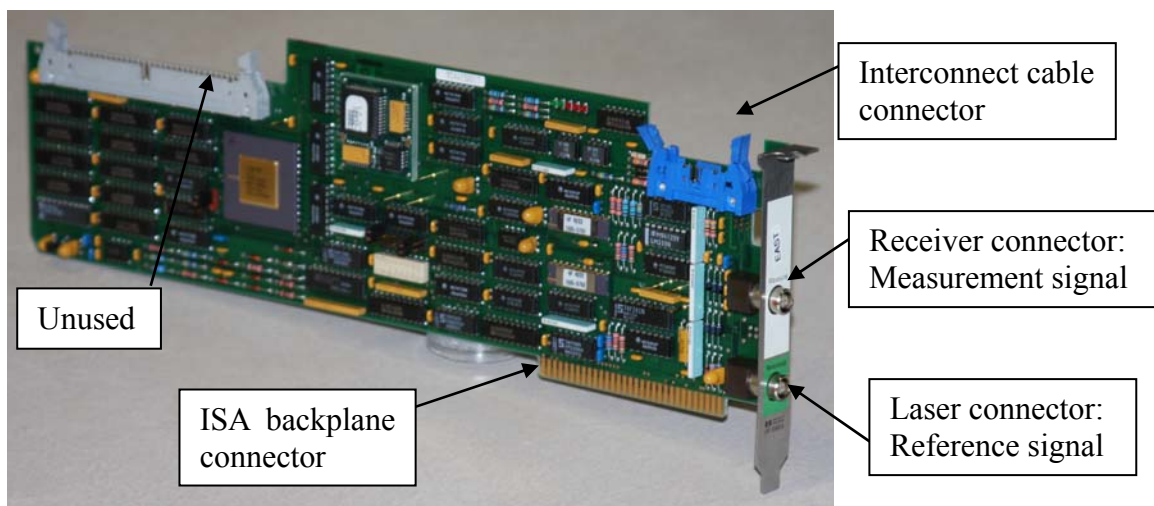


Figure B-9: Agilent 10885A PC axis board used to process the signals from the DMI used in the Laser Tracker Plus system.

For the Agilent 10885A using single beam interferometers, 64 counts add up to one wavelength of motion of the retroreflector. Therefore, to calculate the motion of the

retroreflector in microns, the exact wavelength of the laser and the index of the air must be known to high precision. The index n is calculated using the temperature, humidity and barometric pressure values measured by the laser tracker's built in weather station and following the procedure described in Section 6.3.5. The orientation of the interferometer to the laser affects the measurement direction sense. Because the Laser Tracker Plus system uses the lower frequency output (f_1) of the heterodyne laser for the reference beam, this means as the optical path length difference of the measurement beam gets larger, the fringe counts will decrease.

Each of the measurement signals outputted from the four receivers, go to a separate PC axis board to be combined with the reference signal from the laser head. Because one measurement board is required for each axis, they are daisy-chained together internally (requires 4-axis interconnect cable, Agilent part number 10895-60203) to pass the laser's reference signal to all four axis boards. The boards electronically subtract the laser's reference signal f_2-f_1 from the receiver's measurement signal $f_2-f_1\pm\Delta f$, to isolate the frequency of the Doppler-shift, which is used to determine the direction and magnitude of the retroreflector motion. The output of the PC axis boards is read by the software as register counts, which must be converted into microns using the procedure described in Section 6.3.5.

The Agilent 10885A PC axis board is powered by +5 V and ± 12 V from the ISA backplane. An external power supply (Agilent 10884A power supply) is required to provide the ± 15 V to power the laser head and the receivers. The power supply connects to the 20 m long laser head cable (Agilent 10881C laser head cable) that runs from the

laser head to the lower jack on the back of the axis board (see Figure **B-9**). The cable carries the reference signal from the laser head to the master axis board (first one in the daisy chain), while providing ± 15 V of power to both. The ± 15 V and the reference signal are shared by all four axis boards via the interconnect cable. The remote receivers are connected to the upper jack on the axis boards using 20 m long cables (Agilent 10880C receiver cable) that carries the ± 15 V to the receivers and the measurement signals back to the PC axis boards.

B.6 Position Sensing Module

For the Laser Tracker Plus system, four On-Trak Photonics PSM 2-10 duolateral position sensing modules were used. The performance specifications are provided in Table **B-6**. Each module contains a 10 mm \times 10 mm PSD chip mounted in a rugged aluminum housing (see Figure **B-10**). The detector is recessed to allow mounting of a 1 inch diameter filter to be mounted in front of the detector to block the ambient room light. A Melles Griot interference filter (03 FIL 006: 1 nm bandwidth, 633 nm center wavelength) was used.

Table B-6: Technical specifications for the On-Trak Photonics PSM 2-10 position sensing module [33].

PHYSICAL CHARACTERISTICS	
Module Dimensions:	See Figure B-10 below
DETECTOR SPECIFICATIONS	
Model:	2L10SP
Active Area:	10 mm × 10 mm
Responsivity @ 940 nm	0.63 A/W
Dark Current:	100 nA typical (500 nA max)
Noise Current:	1.3 pA/Hz ^{1/2} typical (2.5 pA/Hz ^{1/2} max)
Capacitance @ 15 V:	90 pF typical (110 pF max)
Rise Time (10-90% @ 15 V):	0.40 μs typical (0.80 μs max)
Reverse Bias:	15 V typical (5 V min, 20 V max)
Detector Resistance:	10 kΩ typical (7 kΩ min, 16 kΩ max)
Thermal Drift:	40 ppm/C° typical (200 ppm/C° max)
Position Non-linearity:	±0.3% typical (±0.8% max)

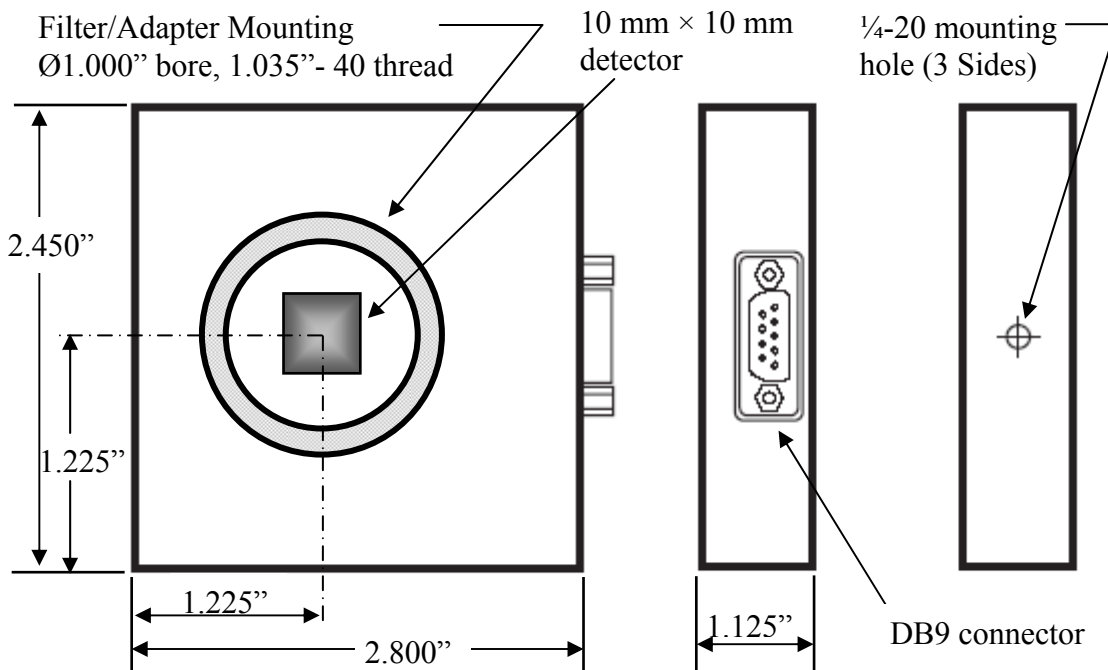


Figure B-10: On-Trak Photonics PSM 2-10 position sensing module dimensions [33].

A position sensing detector (PSD) consists of a p-type resistive layer on the front face and an n-type resistive layer on the back face with a p-n junction in between. A duolateral PSD has four terminals, two on the back side positioned perpendicular to two more on the front side. When light is incident on the PSD, charge separation occurs in the square silicon surface, generating a photoelectric current. A bias voltage is applied to the detector, allowing the electrons to flow through the p-layer (along the X axis) to one set of edge electrodes, while the holes flow through the n-layer (along the Y axis) to the other set of edge electrodes, giving the appearance of two input currents (X_1 & X_2) and two output currents (Y_1 & Y_2).

The ratio of the input currents provides the light's position X along one dimension, while the ratio of the output currents provides the light's position Y along the other dimension. This is because the resistance through the resistive layers is linearly proportional to the distance traveled through layer, which is inversely proportional to the current. The four currents signals produced by the PSD modules are then converted to voltage signals by the position sensing amplifiers.

B.7 Position Sensing Amplifier

On-Trak Photonics OT-301 S504 high gain position sensing amplifiers are used with the Laser Tracker Plus system. These amplifiers are effectively identical to the standard OT-301 versatile position sensing amplifier pictured in Figure **B-11**, but the gain range is higher. A radiometric calculation (discussed in Section **3.3**) performed for the

external reference system indicated that the light levels received at the PSDs were at the limit of what the OT-301 could handle. An increased safety margin is provided by using high gain amplifiers to accommodate a decrease in the DMI laser intensity with age. Table B-7 lists the technical specifications of the OT-301 S504 amplifier.



Figure B-11: Images of the front and rear panels of the On-Trak Photonics OT-301 versatile position sensing amplifier, dimensionally identical to the OT-301 S504 high gain position sensing amplifier used for the Laser Tracker Plus system.

The On-Trak position sensing amplifier takes the photocurrent from each electrode of a PSD module and processes the signals to provide X and Y outputs independent of light intensity. The output is a normalized ± 10 V analog signal that indicates the position of the beam centroid on the detector, with 0 V indicates the center.

The output signal passes through a 16-bit analog-to-digital converter (ADC) (discussed in Section **B.8**) before being read by the measurement software.

Table **B-7**: On-Trak Photonics OT-301 S504 high gain position sensing amplifier specifications [33].

PHYSICAL CHARACTERISTICS	
Dimensions:	1.5 × 5.5 × 6.0 inches (H×W×D)
ELECTRICAL SPECIFICATIONS	
Power Requirement:	±12V DC @ 300 mA
Input Connector:	9 Pin SubD (DB9)
Output Connector	BNC (3)
Transimpedance Gain:	5×10 ⁴ to 5×10 ⁷
Input Current Range:	0.1 μA to 1.5 mA
Output Voltage:	± 10 V Position X, Y 0-6 V SUM
Null Offset:	±1 V each axis
Calibration Adjustment:	±10% of reading
Detector Bias:	0 V ± 5 V
Non-linearity:	±0.1%
Frequency Responce:	DC to 15 kHz (range dependent)
GAIN-BANDWIDTH	
Gain 1:	5×10 ⁴ V/A – 15 kHz
Gain 2:	2×10 ⁵ V/A – 15 kHz
Gain 3:	8×10 ⁵ V/A – 5 kHz
Gain 4:	4×10 ⁶ V/A – 1.25 kHz
Gain 5:	1×10 ⁷ V/A – 310 Hz
Gain 6:	5×10 ⁷ V/A – 80 Hz

The amplifier outputs the motion of the centroid in volts, but ultimately it is that motion in angle space that is desired. The calibration procedure discussed in Appendix **G** determines the conversion factors required to convert the PSD outputs into angular motions of the reference beams. Section **6.3.6** discusses the details of applying the reported PSD motions to correct the laser tracker surface measurement data.

The amplifier also generates a 0-6 V **SUM** signal that indicates the intensity of the incident light on the PSD module. If the **GAIN** setting is too high, such that the **SUM** voltage is greater than 6 V, the amber **H** light will illuminate to indicate that the detector is saturated and the gain needs to decrease. If the **SUM** voltage drops below 1 V, the green **L** light will illuminate to indicate that the gain needs to increase. The **SUM** should be approximately 5 V for optimum performance. The **SUM** voltage output is run through a 12-bit ADC and monitored by the control software for diagnostic purposes to indicate if the alignment of the PSD to the reference beam is poor or changes during a measurement.

The amplifiers have an additional set of controls to allow an electronic offset of ± 1 V in each axis to move the relative position of the zero point on the PSD by using the **ZERO** knobs on the front. The **CAL** knobs can be used to adjust the **GAIN** $\pm 10\%$ of full scale in each axis to calibrate the volts out in terms of displacement. To enable these features, the **CAL/ZERO** switch on the back must be set to the **ON** position. For the Laser tracker Plus system, these features were not used, and therefore the switch was set to **OFF**.

The position sensing modules are connected to the amplifiers via a standard male-male DB9 serial patch cord, which plugs into the DB9 receptacle labeled **PSD** on the front of the amplifier. The pinout for the 9 pin connector is listed in Table **B-8**. The OT-301 series amplifiers must be internally configured for use with a specific PSD module (if they are ordered together, this will be done at the factory). For the PSM 2-10 position sensing modules used, Table **B-9** lists the amplifier internal switch settings

Table **B-8**: Pinout for the 9 pin D connector used by On-Trak Photonics for connecting their PSD modules to their amplifiers.

PIN #	PSD
1	PSD Electrode: X_1
2	PSD Electrode: X_2
3	PSD Electrode: Y_1
4	PSD Electrode: Y_2
5	Ground
6	Not Connected
7	Not Connected
8	Bias for Common Cathode/Anode
9	Ground

Table **B-9**: OT-301 series PSD amplifier internal switch settings for use with a PSM 2-10 duo-lateral position sensing module.

PSD TYPE	DIP SW 8: ON	DIP SW 7: ON	BIAS	POLARIZATION
Duo-lateral	1,3,6,9	1,3,7,9	-5 V (JP2)	SW1: Negative

B.8 Compact FieldPoint for PSD System

Three analog voltage signals are output from the PSD system amplifiers: two that varies between ± 10 V to indicate the location of the centroid of the incident light in each axis, and a 0-6 V signal indicating the magnitude of the incident light. To input these signals into the computer where they can be accessed and manipulated with software, the analog signals needed to be digitized. National Instruments provides a line of products called Compact FieldPoint, which allows the signals from remote instruments to be read by a computer via Ethernet or serial port. The system uses an Ethernet/serial interface (shown in Figure **B-12**), where different combinations of modules to be plugged into its

chassis. The interface converts between the input/output of each type of module to the digital signal transmitted through the Ethernet or serial line to the computer. For the Laser Tracker Plus system, a cFP-1804 four-chassis Ethernet/serial interface was used with the PSD system and connected to the master control computer via Ethernet. Its specifications are listed in Table **B-10**. The cFP-1804 interface is powered by the same 12 VDC power supply that powers all four of the PSD amplifiers.



Figure **B-12**: National Instruments cFP-1804 Ethernet/serial interface for Compact FieldPoint, which has slots for four modules for inputting or outputting digital or analog signals, for interfacing remote instruments with a compute via Ethernet or serial port connection.

Two different types of modules were used. The first was a cFP-AI-118 analog input module. This module has a high-end 16-bit analog-to-digital converter (ADC) that had eight completely isolated channels, allowing the eight PSD position voltages (X & Y output from all four PSDs) to be read and digitized with high resolution and minimal noise from ground loops or cross talk between the different channels. The module has the option of a 10 Hz filter that provides 55 dB of rejection at every multiple of 10 Hz, which can significantly reduce 60 Hz noise from the electrical mains, but it limits the sampling rate so it was nominally deactivated. The module was connected to the X & Y outputs of the PSD amplifiers (see Figure **B-11**) with BNC patch cables wired into a

cFP-CB-1 connector block, and set up with a maximum input range of ± 10 V. The specifications for this module are listed in Table **B-11**.

Table **B-10**: National Instruments cFP-1804 Compact FieldPoint Ethernet/serial interface specifications.

PHYSICAL CHARACTERISTICS	
Weight:	935 g (2 lbs 1 oz)
Dimensions:	127 mm×246 mm×88 mm 5 inch×9.7 inch×3.5 inch
Cable Clearance Requirement:	76 mm (3 inch)
Screw-Terminal Wiring:	14- 22 AWG copper conductor wire
Torque for Screw-Terminals	0.5-0.6 N·m (4.4-5.3 in·lb)
POWER	
Power Supply Voltage:	11-30 VDC (range)
Power Supply Actual:	12 VDC (actual)
Recommended Power Supply:	20 W
Power Consumption:	6.1 W + 1.1(I/O module power requirement) 7.7 W (actual)
Maximum Power to I/O Modules	9 W
NETWORK	
Network Interface:	10BaseT & 100BaseTX Ethernet
Communication Rates:	10 Mbps, 100 Mbps, auto-negotiate
Maximum Cable Distance:	100 m / segment

Table B-11: National Instruments cFP-AI-118 analog input module specifications.

PHYSICAL CHARACTERISTICS	
Weight:	117 g (4.1 oz)
POWER	
Power from Network Module:	1.125 Watts
Warmup Time:	30 minutes
INPUT CHARACTERISTICS	
Number of Channels:	8
Maximum Signal Input Range:	± 10 V
ADC Resolution:	16 bit
Effective resolution:	320 μ V
RMS Noise:	100 μ V
Peak-to-Peak Noise:	700 μ V
Accuracy:	$\pm 0.037\%$ of reading $\pm 0.001\%$ of full scale
Signaling Time Delay:	2.1 ms
All-Channel Sampling Rate:	3.45 kHz (with 10 Hz filter) 10.42 kHz (without filtering)
Input Bandwidth (-3dB):	3 kHz minimum
Common-mode Rejection at 60 Hz:	100 dB channel-to-channel 100 dB channel-to-ground
Cross-talk attenuation:	>100 dB
Input Resistance:	1 M Ω
Input Capacitance:	<50 pF
Over Voltage Protection:	± 250 V
Gain Error Drift:	7.4 ppm/ $^{\circ}$ C
Offset Error Drift:	3 μ V/ $^{\circ}$ C

The second module, a cFP-AI-110 analog input module, was used to monitor the light intensity incident on the four PSDs. This module does not have as high-end of an ADC, despite also being 16-bit, because it has eight single-ended inputs which all have a common cathode. Therefore, to get isolation between the four PSD amplifiers, each SUM output was wired into two input channels of the module and measured in differential mode, thereby avoiding the use of a common ground. This module was

configured for a maximum input range of 0-10 V. The specifications for this module are listed in Table B-12.

Table B-12: National Instruments cFP-AI-110 analog input module specifications.

PHYSICAL CHARACTERISTICS	
Weight:	110 g (3.7 oz)
POWER	
Power from Network Module:	0.35 Watts
INPUT CHARACTERISTICS	
Number of Channels:	8 single-ended 4 differential
Maximum Signal Input Range:	0-10 V
ADC Resolution:	16 bit
Effective resolution:	190 μ V
Peak-to-Peak Input Noise:	$\pm 153 \mu$ V
Accuracy:	$\pm 0.04\%$ of reading $\pm 0.003\%$ of full scale
Signaling Time Delay:	2.8 ms
All-Channel Sampling Rate:	5 Hz
Input Bandwidth (-3dB):	130 Hz
Common-mode Rejection at 60 Hz:	95 dB
Input Resistance:	>100 M Ω
Over Voltage Protection:	± 40 V
Gain Error Drift:	20 ppm/ $^{\circ}$ C
Offset Error Drift:	6 μ V/ $^{\circ}$ C

B.9 MicroPC for DMI Monitoring

To provide diagnostic information about the DMI alignment, temperature fluctuations within the DMI electronic and optics enclosure, and information about the location of the bridge crane, a MicroPC (shown in Figure B-13) was installed in with the DMI electronics. The MicroPC is a TS-7300 single board computer manufactured by Technologic Systems, which is PC/104 compatible and runs on a 32-bit 200 MHz ARM9

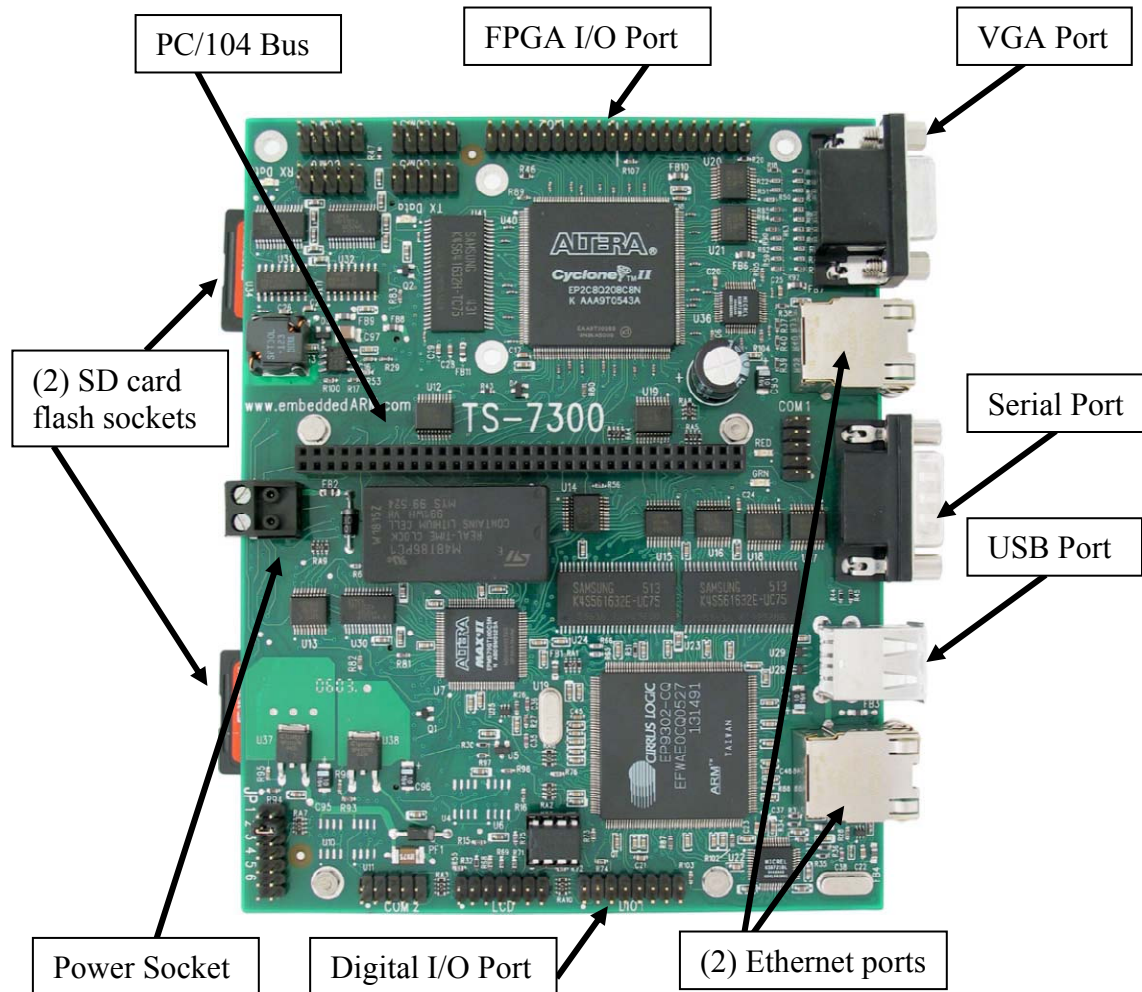


Figure B-13: The TS-7300 single board computer MicroPC used for diagnostic monitoring of the Laser Tracker Plus system instrument cluster atop the bridge crane.

processor. The MicroPC runs on a full installation of LINUX, which is stored on a flash card in one of the two hot-swappable flash card sockets, allowing the second card socket for additional program storage. Table B-13 contains a list of the TS-7300 specifications.

The MicroPC is equipped with:

- Two Ethernet ports for connectivity to the rest of the Laser Tracker Plus system;
- Serial, VGA, and USB ports that were not used;

- A bank of digital I/O ports that were used to determine when the bridge crane was in the proper position via a switch mounted on the crane rails.

Table B-13: Technologic Systems TS-7300 single board computer specifications.

PHYSICAL CHARACTERISTICS	
Dimensions:	
POWER	
Power Requirements:	Regulated 5 VDC @ 450 mA
Power Consumption:	1.8 W
FEATURES	
200 MHz ARM9 Processor	
32 MB SDRAM	
User-programmable Altera 2C8 Cyclone II FPGA	
2 SD Card flash sockets	
TS-VIDCORE VGA video-out with 8 MB dedicated video RAM	
2 USB 2.0 compatible OHCI ports	
2 10/100 Ethernet ports	
10 RS232 serial ports	
55 DIO ports	
PC/104 expansion bus	
Fast boot to LINUX prompt-shell in 1.69 s	

Because the TS-7300 has a PC/104 expansion bus, additional PC/104 cards can be plugged into the MicroPC for increased functionality. PC/104 is a standard form-factor that many electronics manufactures can use to maintain compatibility between their products and those of others. A PC/104 compatible analog-to-digital converter was used to read the voltage signals from the DMI receivers, which indicate the signal quality and alignment of the surface reference to the DMI reference beam, and the thermocouple voltages, which measure temperature stability around the DMI electronics and optics. This was a Technologic Systems TS-9700 eight channel 12-bit ADC PC/104 daughter board. All eight channels were used: four of them for reading the DMI receivers (wire up

through the 12-pin terminal block), three for reading thermocouple outputs (wired up through the 10-pin header), and the last monitors the supply voltage for the MicroPC (jumper PJ5). Table **B-14** lists the input sources and connectors used for each ADC channel, and its analog input voltage range and the expected nominal signal voltage.

Table **B-14**: List of the input sources, expected nominal signal voltage, and voltage ranges used with each channel of the TS-9700 analog-to-digital converter used with the MicroPC. Channel 7 was set to monitor the supply voltage by setting jumper PJ5, the thermocouple voltages were input through the 10-pin header, and the DMI receiver voltages were input through the terminal block. The appropriate set of pin numbers is noted for each channel.

ADC Channel	Connector Input	Input Source	Voltage Range	Nominal Signal
1	H1 & H10	DMI Laser Head Thermocouple	0-2.5 V	~1.0 V
2	T2 & T3	North DMI Receiver	0-2.5 V	~0.8 V
3	H5 & H10	DMI Electronics Thermocouple	0-2.5 V	~1.0 V
4	T5 & T6	South DMI Receiver	0-2.5 V	~0.8 V
5	H9 & H10	DMI Optics Thermocouple	0-2.5 V	~1.0 V
6	T8 & T9	East DMI Receiver	0-2.5 V	~0.8 V
7	PJ5	Power Supply Voltage Monitor	0-10 V	~5.0 V
8	T11 & T12	West DMI Receiver	0-2.5 V	~0.8 V

The TS-7300 MicroPC is powered by +5 VDC which can be supplied either through the power socket on the board, or through the PC/104 bus. Because +5 VDC was not available on the bridge crane, the MicroPC used a Technologic Systems TS-12W power supply that plugged into the PC/104 bus. The TS-12W is used to convert the +24 VDC powering the indicator light on the bridge crane to +5 VDC to power the MicroPC. The TS-12W can supply a maximum of 12 W of power at +5 VDC, which was used to power both the MicroPC and the thermocouple amplification circuitry used for monitoring the temperatures around the DMI electronics and optics

B.10 Electronic Circuit for Temperature Monitoring

During the starting measurement of the Correlation study, it was noted that reference beam motions observed by the PSDs were greater than the motion observed by the laser tracker under the same seeing conditions. This resulted in poor correlation between the PSD system and the laser tracker for angular motion. This indicated that there was some additional mechanism that was causing the apparent increased motion of the reference beams. One possibility considered was that the pointing stability of the DMI laser was not stable over time. During a conversation with an application engineer from Agilent Technologies, it was stated if there were pointing instability in the DMI laser, it would be temperature dependent and the suggestion was made to install a ventilation system and to monitor the temperature around the DMI laser, electronics, and optics. For this reason, the temperature monitoring system was installed.

The decision was made to use thermocouples because simple, rugged, and inexpensive. They do have the disadvantages of being non-linear, producing low voltages, and requiring a reference; two of these issues were not a problem. Because the test tower is temperature controlled, the thermocouples only needed to work over a narrow temperature range, over which their thermoelectric response is effectively linear. An absolute reference would not be required because the laser tracker's weather station already measures the temperature outside the DMI enclosure, so a reference thermocouple could be placed adjacent to the laser tracker's temperature sensor and the relative difference could be measured between that and the temperatures in and around the DMI laser to monitor for changes. To compensate to the low voltage output of a

thermocouple, an amplification circuit was required. A schematic of this circuit is shown in Figure B-14.

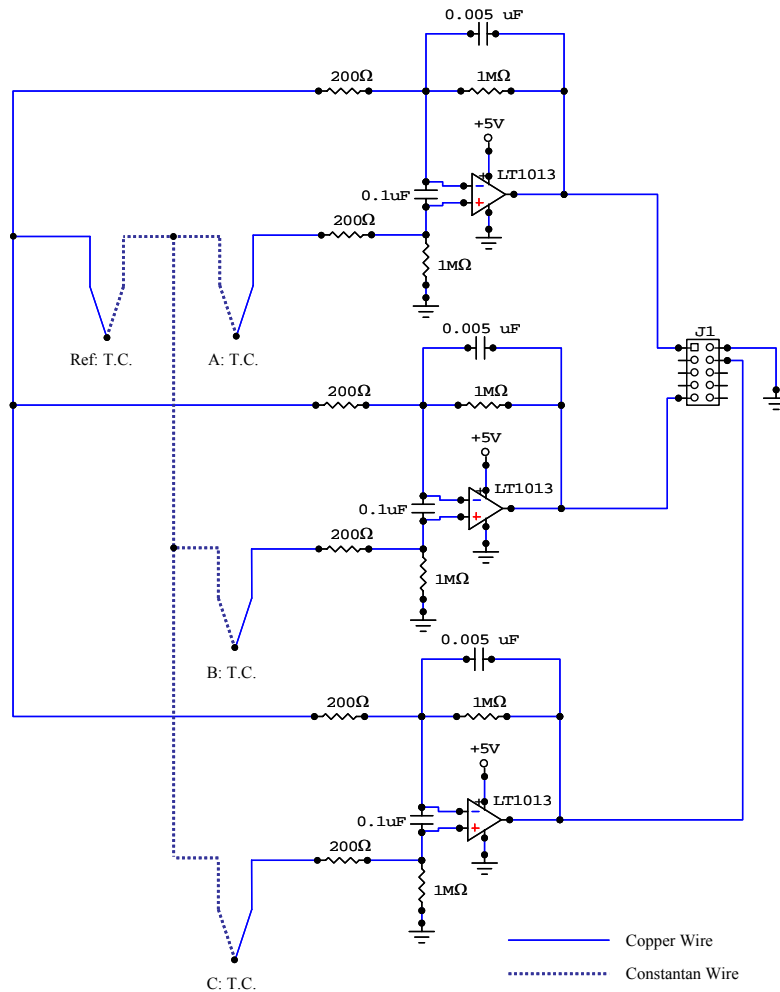


Figure B-14: Schematic of the thermocouple amplification circuit used to monitor changes in the temperature in and around the Distance Measuring Interferometer laser head, receiver electronics, and optics. The circuit produces a nominal gain of 5001, which for the type T thermocouples used, results in a temperature constant of 200 mV/°C.

During the design process, commercially available monolithic thermocouple amplifiers, such as the Analog Devices AD594, were considered for amplifying the thermocouple voltage signals, but they all were set with a standard temperature

proportional output of 10 mV/°C, which coupled with a 16 bit ADC reported about 1°C change per digital step. The goal was to have measurement sensitivity on the order of ~0.1°C, so the custom differential amplifier circuit shown Figure B-14 in was developed instead. This circuit uses Linear Technology LT1013 operational amplifiers, set up in tandem to measure the differential voltage between a reference thermocouple adjacent to the laser tracker's temperature probe, and three other thermocouples (one in the DMI laser head, one in the DMI electronics housing, and one in with the DMI optics). The pinout for the chip is shown in Figure B-15, while Table B-15 lists the electrical characteristics when powered with +5 VDC and operated at around 25°C.

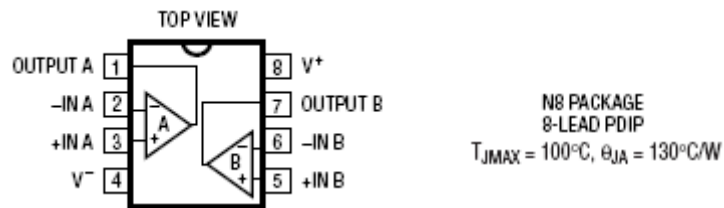


Figure B-15: Pinout for the Linear Technology LT1013 dual precision op amp used in the thermocouple amplification circuit shown in Figure B-14.

Table B-15: Linear Technology LT1013 dual precision op amp specifications at 25°C, $V^+ = +5$ VDC, and $V^- = 0$ V [22].

ELECTRICAL CHARACTERISTICS		
Input Offset Voltage:	90 μ V (typ)	450 μ V (max)
Input Offset Current:	0.3 nA (typ)	2.0 nA (max)
Input Bias Current:	18 nA (typ)	50 nA (max)
Large Signal Voltage Gain:	1.0 V/ μ V (typ)	
Input Voltage Range:	-0.3 to +3.8 V (typ)	0 to +3.5 V (min)
Output Voltage Swing:	5 mV to 4.4 V (typ)	
Supply Current	0.32 mA (typ)	0.50 mA (max)

The amplifier circuit has a gain of

$$\text{Gain} = \frac{1\text{M}\Omega}{200\Omega} + 1 = 5001. \quad (\text{B.1})$$

To reduce the noise in the circuit, a 0.1 μF capacitor is wired across the inputs to the amplifiers, while the feedback loop contains a low-pass filter with a cut-off frequency of

$$f_c = \frac{1}{2\pi RC} = \frac{1}{2\pi(1\text{M}\Omega \cdot 0.005\mu\text{F})} = 32 \text{ Hz}. \quad (\text{B.2})$$

The circuit is powered the +5 VDC power supply from the MicroPC from wires run to the power socket shown in Figure **B-13**. The three amplifier outputs are run to a 10 pin header cable that is then plugged into the TS-9700 ADC board in the MicroPC through the connections shown in Table **B-14**. The ADC is configured with 65536 steps between 0 – 2.5 VDC, or 0.038 mV/step.

The thermocouples used were type T, which are copper and constantan. This variety was selected because it eliminated the need for an isothermal block since the constantan wire only contacted copper at the thermocouples' junctions, and copper wire was used throughout the rest of the circuit. Type T thermocouple characteristics are also well suited for most ambient environments and has a fairly linear temperature proportional output of 0.041 mV/ $^{\circ}\text{C}$ at 25 $^{\circ}\text{C}$, which after amplification is

$$0.041 \text{ mV}/^{\circ}\text{C} \times 5001 = 0.205 \text{ mV}/^{\circ}\text{C}. \quad (\text{B.3})$$

Therefore the temperature resolution for the system is

$$0.038 \text{ mV/step} \div 0.205 \text{ mV}/^{\circ}\text{C} = 0.185^{\circ}\text{C/step}, \quad (\text{B.4})$$

which is sufficient to determine if temperature changes are affecting the DMI system.

Appendix C

LASER TRACKER PLUS MEASUREMENT PROCEDURE

1. Insure all system components are powered up
 - a. Check power on components in tower:
 - i. Laser Tracker
 - ii. DMI laser
 - iii. Laser Tracker Plus control computer
 - iv. Laser Tracker Plus micro computer
 - b. Check power on components at floor level
 - i. GMT operator's consol (GMTopera)
 - ii. PSD amplifiers
 - iii. TrackerPC computer
 - iv. Ball Mover computer
 - v. Ball Mover motor controllers (the AC POWER light should be lit, but the 75 VOLTS and POWER lights will remain off until enabled in software)
2. Open safety net
3. Move bridge crane into position using one of the following methods:
 - a. Move bridge crane East-West until the laser from the laser tracker is in line with the GMT center spot on floor
 - b. Move bridge crane East-West until the blue light on the bridge crane is illuminated
 - c. If mirror is already on tower, then move bridge crane East-West until all four DMI laser spots are equal distance from the edge of the mirror
4. Confirm that the trolley of the bridge crane is all the way to the South end of the bridge
5. Initialize tracker
 - a. Connect to tracker with TrackerPC computer using Faro utilities software
 - b. Open *Tracker Pad*
 - i. *Initialize* tracker
 - ii. *Set Distance Mode* to ADM Only
 - iii. *Home* tracker with 1.5" SMR
 - iv. *Set Distance Mode* to Interferometer Set By ADM
 - c. Run *Startup Checks*
 - d. Run *Health Checks*
 - e. Run *CompIT*
 - i. Run *Self Compensation*
 - ii. When Self Compensation is complete, *Update* parameters

- iii. Check *No* for Angular Accuracy Checks
 - iv. *Close CompIT*
 - v. Close tracker pad
 - f. *Disconnect* from tracker
- 6. At the GMT operator's (GMTopera) consol, open "GMT Monitor" from Applications.
- 7. Press *Show GMT Process Status*
 - a. Press the *Start* buttons for:
 - i. *GMT Sa GUI*
 - ii. *Tracker Plus Gui*
 - iii. *LT Position Display GUI*
 - iv. *Tracker Plus Big Status GUI*
 - v. *Faro Control*
 - vi. *Faro Java Thread*
 - vii. *TP Control*
 - viii. *DMI Control*
 - ix. *PSD Control*
 - x. *Trackerp Send Update*
 - xi. *Catch Update*
 - xii. *GMT Executive*
 - xiii. *Ball Mover GUI*
 - xiv. *Ball Mover Control*
 - xv. *Ball Mover State*
 - xvi. *Ball Mover Send Update*
 - xvii. *Mirror Cell Positioner GUI*
 - xviii. *(PMP/FMP) GUI*
 - b. Close the "Monitor" window
- 8. Setup the mirror for testing
 - a. Move mirror onto tower
 - b. Position Mirror with Primary Mirror Positioner (PMP)
 - i. Check positioning switches are off
 - ii. Turn on PMP Power
 - iii. Move the PMP stages until centered under mirror
 - iv. Lower air cart until mirror rests on PMP
 - v. In the Mirror Cell Positioner GUI window on GMTopera
 - 1. Press the "Save" button
 - 2. Type in a name in the box such as "Lift_091027" to indicate this is the values that the PMP read at the time the mirror was removed from the air cart (this is important for the mirror needs to be returned to this position after the test to set the mirror back onto the air cart)
 - 3. Press the "Load" button
 - 4. Press the "LT+_091001" option, then press →, then press "Abs Move" to move the mirror into position for a LT+ test

- c. Deflate seals
9. Remove puck from storage drawer and inspect for contaminants on the pads and clean as required.
10. String Ball Mover system
- a. In the Ball Mover Control window (“mover_disp”):
 - i. *Power On* Overall Controls (The 75 VOLTS and POWER lights on the Bal Mover motor controller panel should light up)
 - ii. *Disable* torque motors (“Torque Status” should read “Fault” in red)
 - iii. Feed out both stepper motors:
 - 1. Typing 11 in the white boxes under “North”
 - 2. Typing 7 in the white boxes under “South”
 - 3. Press the *Start Relative Move* button

(Note: if the Stepper Status is red and reads “latch”, the limit override switch on electronics rack needs to be tripped to clear the error)
 - b. Feed the strings from the stepper motors over the string that runs between the two limit switches at the ends of each ball mover arm
 - c. Pull stepper strings to the South side of the mirror
 - d. Feed the strings from the torque motors over the string that runs between the two limit switches at the ends of each ball mover arm
 - e. Pull each torque string to the South side of the mirror
 - f. Attach all four strings to the puck
 - g. Attach the air line for the air puck
 - h. Draw in the slack in the strings
 - i. Check latch override
 - ii. For the stepper strings, in the Ball Mover Control window:
 - 1. Typing “-0.5” in the North and “-2” in the South
 - 2. Press the *Start Relative Move* button
 - iii. For the torque strings, in the Ball Mover Control window:
 - 1. Type “0.3” in the white boxes by “Torque CMD” and press *Go* for each
 - 2. *Enable* both torque motors
 - 3. Once strings are taught, increase torque to “1.0”
 - i. Press the *Select Air Puck* button
 - j. Press the *Air Puck On* button
11. Install External References (PSD/DMI references)
- a. Extend the PSD cable to the appropriate sides of the mirror (North, South, East, or West).
 - b. Remove the external references from the drawer in the Ball Mover rack and place at the appropriate compass points around the circumference of the mirror.
 - c. Wrap the cable around the guardrail on the cell to support the weight of the cable.
 - d. Plug the cable into the PSD.

12. Align External references

- a. Adjust the references on the mirror so that the DMI laser beams are centered on the beamsplitter hole.
- b. Place a small plane-parallel mirror onto the beamsplitter and adjust the three nylon tipped feet of each reference until each laser beam reflects back on itself.
- c. Fine adjust the centering of the laser beam to the beamsplitter hole until well aligned.
 - i. This can be done by holding a sheet of paper so that the edge of the paper blocks half the DMI laser beam, allowing the other half to retroreflects off the reference
 - ii. Look at the underside of the sheet of paper, the light from the half of the laser beam blocked by the paper should be visible through the paper as a diffuse red semicircle
 - iii. The reflected half of the beam will look like half a sliced pie due to the facets in the retroreflector
 - iv. Shift the reference along the edge of the mirror and radially until the reflected half of the laser beam overlaps on the underside of the paper with the half blocked by the top of the paper
 Note: The beam from the DMI is stationary, while the reflected beam moves with the reference, so shift the reference in the direction to move the reflected spot to be concentric with the stationery spot
 - v. Check the concentricity of the two beams by moving the sheet of paper to bisect the beam on each side to insure that the reflected beam overlaps the incident beam everywhere
- d. Repeat steps b & c until satisfied with alignment
- e. In the “DMI Data” section of “trackerp” window
 - i. Press the *Reset* button after every adjustment
 - ii. Check the “Power Lever” boxes to ensure that the values for each DMI is greater than 0.9.

13. Connect to laser tracker using the GMT “Sa” GUI window

- a. Make sure the “First Faro Tracker Control” is checked *Enabled*
- b. Press the *Connect* button
- c. Press the *Initialize* button
 (Tracker Status will read “Initializing” for a couple minutes until the “Status” box changes to “Initialized” in green and is ready for the next step)

14. Start setting up Ball Mover software
 - a. In the “Measurement Controls” section of the “GMT Sa GUI” window
 - i. Press *View Parameters* button
 1. Set “First Faro Tracker” to *Enabled* with 1024 Samp/Point
 2. Set “DMI/PSD Controls” to *Enabled* with 1000 msec Integration time and 20 msec Sample time
 3. Set “Second Faro Tracker” to *Disabled*
 4. Minimize window
 - ii. Place a file name for the measurements to be made in the “File” box (example: gmt1_091027_1 for the first measurement on October 27, 2009 of the 1st segment of GMT)
 - iii. Press the *Set Parameters* button
 - b. In the “Faro Basic Controls” section of the “GMT Sa GUI” window
 - i. Press the *Set Target 1 ½ inch SMR* button
 - ii. Press the *Inter Set By ADM* button
 - iii. Press the *Home Front Sight* button
 - c. In “Tracker XY Display” window, press *Initial Ball Mover Setup* button
 - d. In the new “Initial Ballmover Setup” window that appears
 - i. Press the *All* button to measure the locations of all four DMI/PSD references
 1. If any of the references fail to measure, then measure their locations by placing an SMR on the beamsplitter entrance and measure with the laser tracker.
 2. In the software, add 60 mm to the radial length of the references that were measured with the SMR
 - ii. Set path to data file by either
 1. Pressing *Data File:* button and browsing through the file system to the appropriate file
 2. Typing in the route to the desired file (example: “/data/gmt1_091027_1.csv”)
 - iii. Press the *Load Data List from file* button
 - e. In “Tracker XY Display” window, check
 - i. *Draw command list on cartoon*
(If magenta pattern on display is incorrect or does not appear, then)
 1. Press *Show Command Position List* button
 2. In the new “Commanded Positions” window that appears:
 - a. Press *Clear List* to remove all current points
 - b. Press *Load List from file* to browse for new list positions
 - c. Select the desired measurement pattern (such as “a_master_grid_new.txt”) then press the *Open* button
 - d. Close “Commanded Positions” window

- e. Uncheck and Recheck *Draw command list on cartoon* in the “Tracker XY Display” window
 - ii. *Show Data points on cartoon*
(The North, South, East, & West PSD/DMI reference positions should appear near the edge of the circle)
 - iii. *Auto update from datafile*
 - iv. *Show puck position on Cartoon*
(A black dot should appear indicating the location of the puck)
- 15. Lock tracker onto 1.5” SMR
 - a. Steer tracker to South edge of mirror using the “Faro Basic Controls” section of the GMT “Sa” GUI window
 - i. Type in:
 1. Az: “-0.188”
 2. Zi: “1.5708”
 3. Dist: “22.3”
 - ii. Press *Move*
 - b. Hold the 1.5” SMR in tracker laser beam until the tracker locks on
 - c. Set SMR in Ball Mover puck
 - d. Press *Measure and Set Ball Mover Encoders* button in the “Initial Ballmover Setup” window
- 16. In the Ball Mover Control window (“mover_disp”):
 - a. Type “3” in the white boxes by “Torque CMD” and press *Go* for each
 - b. Press *Auto* for the North Torque motor
 - c. Press *Auto* for the South Torque motor
 - d. Press *Measure and Set Ball Mover Encoders* button in the “Initial Ballmover Setup” window
- 17. Measure clocking references
 - a. Retrieve the clocking references fixture from the drawer over the PSD amplifiers
 - b. Locate the 0 degree reference on the mirror cell and align the fixture to the mark scribed in the glass edge
 - c. Move the Ball Mover puck with the SMR to a position near ref0 by:
 - i. Click the mouse cursor on the “Tracker XY Display” approximately near ref0
 - ii. Press either the
 1. *Move to Tag* button if a measurement point is near ref0
 2. *Move to XY* to move to the exact XY position on the mirror
 - d. Remove the SMR from the puck and place in Clocking fixture and align
 - e. In the “Initial Ballmover Setup” window, press the *ref0* button to measure 0 degree reference location
 - f. When measurement is done replace SMR in puck
 - g. Repeat process for 90 degree, 180 degree and 270 degree references
 - h. After all four references are measured, in the “Initial Ballmover Setup” window:

- i. Press the *Calc Offsets from Ref positions* button to calculate the x & y offset values and shift the measured points to the appropriate positions on the display
 - ii. Make sure the SMR is in the puck, then press *Measure and Set Ball Mover Encoders* to update the encoder values to account for the correct offsets
 - iii. Press *Done*
- 18. Take thermal and load cell force measurements
- 19. Clear equipment away from around the mirror and set up the barricades
- 20. Start measurements
 - a. *Reset* the DMIs
 - b. In the “Ball Mover Controls” window, Press the *Start Mover at Tag:* starting at “Measurement_001”
 - c. The ball mover will stop:
 - i. If the Puck trips a limit switch, then either
 - 1. Press *Back out of Limit and retry* if the black dot for puck position is partway between magenta measurement points
 - 2. Press *Measure and move to next point* if the black dot is approximately at the magenta measurement position
 - ii. If the laser tracker loses lock on the SMR, the ball mover will stop and report “ERROR Faro lost lock, aborting measurement” in the “GMT Monitor” window, at which point the data set is no good, so follow the instructions to start another set of measurements described below
 - iii. If “WARNING Airon delta ## exceeds limits” is encountered, This indicates that there is a chance the Air Puck did not lift the SMR off the mirror surface when the air pressure was turned back on after a measurement
 - 1. Look at the puck to make sure that all three feet of the puck are still attached and sitting directly on the mirror
(This error can occur if the Air Puck goes over the edge of the mirror such that one foot falls off the mirror surface, or the string tension gets too high because the air hose got bound up and the Air Puck gets partially lifted off the mirror surface)
 - 2. If everything looks fine, then look at the “GMT Monitor” log file to see the measurement number that the error occurred at
 - 3. Type this number in the white box next to the *Start Mover tag:* button in the “Tracker XY Display” window and then press button the restart the ball mover at its last location
 - iv. Automatically at the end of the measurement run and a ding-dong sound will be made to signal the successful completion of the measurement set

21. After the measurement is complete, either setup for another measurement or put everything away
 - a. To set up for another measurement:
 - i. In the “GMT Sa GUI” window
 1. Change “File” name for new measurements set (example: gmt1_091027_2”)
 2. Press *Set Parameter* button to update that change to the Ball Mover
 - ii. In “Tracker XY Display” window
 1. Type “Measurement_001” in the “Nearest Command tag:” box and press *Move to Tag* button
 2. Uncheck “Show Data points on cartoon” box
 3. Press *Initial Ball Mover Setup* button
 - iii. In “Initial Ballmover Setup” window that pops up
 1. Press *Clear List* button
 2. Make sure the filename in the white box at the top matches the name for the new data set to be measured, and change to match if necessary (example: “/data/gmt1_091027_2.csv”)
 3. Press *Load Data List from file* button
 4. Press *Done*
 - iv. Press the *Reset* button for the DMIs in the “trackerp” window
 - v. In “Tracker XY Display” window
 1. Check “Show Data points on cartoon” box
 2. Check “Auto update from datafile” box
 3. Type “Measurement_001” in the white box next to *Start Mover at tag:* button, and press button to start new set of measurements
 - b. To put everything away:
 - i. In “Tracker XY display” window
 1. Type “Measurement_001” in the white box beside “Nearest Command Tag:” and press *Move to Tag* button
 2. Wait until puck is in position, then close window
 - ii. In “Mover_disp” window
 1. Press *Disable* for both torque motors
 2. Press *Air Puck Off* button
 3. Press *Select Non-Air Puck* button
 - iii. Remove Air Puck from mirror
 1. Disconnect air hose from Air Puck and let retract
 2. Disconnect all four strings
 3. Remove Air Puck from mirror surface
 4. Remove SMR from Air Puck and put it in the plastic storage container
 5. Inspect Air Puck for contaminants on feet and clean as needed

6. Put SMR and Air Puck back into drawer in electronics rack
- iv. In “Mover_disp” window
 1. Retract torque motor strings
 - a. Type “0.2” into white box by “Torque Cmd” and press *Go* for both torque motors
 - b. Press *Enable* for both torque motors to retract torque motor strings
 - c. Once both torque motor strings are fully retracted, press *Disable* button for both motors
 2. Retract stepper motor strings
 - a. Press the *Set Retract Strings* button to set appropriate retract values into the stepper motor input boxes
 - b. Press *Start Relative Move* button to begin retracting stepper strings

Note: The override button on the electronics rack may need to be pressed if the limit switches get tripped to remove the “Latch” error

 - c. Once both stepper strings are fully retracted, press *Power Off* button
 3. Close window
- v. Put away references
 1. Remove DMI references from mirror surface and put away
 2. Close “trackerp” window
 3. coil up PSD cables
 4. Power off PSD amplifier chassis
- vi. In the “GMT Sa GUI” window
 1. Press *Disconnect* button in “Faro Basic Controls” section
 2. Close window
- vii. Close “Tracker Plus Big Status” window
- viii. Move the bridge crane all the way to the East to park it out of the way in the event that an optical test will be performed
- ix. Use the Primary Mirror Positioner (PMP) controls to move mirror back to Lift location if desired
 1. In the Mirror Cell Positioner GUI window on GMTopera
 - a. Press the “Load” button
 - b. Press the “Lift_091027” option, then press →, then press “Abs Move” to move the mirror into position for the mirror to be lifted off the PMPs with the air cart
 - c. Press *Power Off* button for PMP
 - d. close window
 2. Physically turn off the power to each of the PMP chassis

22. Analyzing the data

- a. Copy file from GMTopera computer to the TrackerPC computer in the /GMT/data/segment1 folder
- b. Open in excel
 - i. Delete non-data points
(For instance, the “encoder_setup” points)
 - ii. Arrange measurements so points 1-4 are ref0, ref90, ref180, and ref 270, and points 5-8 are North, South, East, and West, then the surface data starts at point 9
 - iii. Save file as an excel file with underscores replaced with spaces and “mod” added to indicate the data has been modified from the original.
(Example: “gmt1_091027_1.csv” becomes “gmt1 091027 1 mod.xls”)
 - iv. Close file
- c. Open MATLAB
 - i. Run the command:
`ltPlusGmt('gmt1 091027 1 mod',90,340,-90,0,0,-22,1,6,-.1,.1,1,.12)`
 Where
 1. The quantity in single quotes is the file name
 2. The first six numbers are the initial guess at the coordinate transformation of the data (3 rotations and 3 translations)
 3. The 7th number is 1 if DMI correction and 0 without DMI correction
 4. The 8th number is the order of the Zernike fit (in this case, up through 6th order, or the first 28 Zernike coefficients)
 5. The 9th and 10th numbers are the lower and upper scale bar limits for the surface maps
 6. The 11th and 12th numbers are the course and fine outlier correction values respectively in units of microns
 - ii. Nine plots are generated
 1. Examine plots 1-4 to make sure the course outlier value is appropriate and not chopping off valid data points
 2. Compare plots 4 & 5 to make sure the fine outlier value is appropriate to remove any remaining outliers between the two plots
 3. Plots 5 & 6 show the data as a 3 dimensional surface and a surface map respectively
(These two plots should be included in the report)
 4. Plot 7 is a surface map of the Zernike fit to the data
(This plot should be in the report)
 5. Plots 8 & 9 are the same as plots 5 & 6 with power removed

- iii. The Zernike polynomial coefficients are calculated
 - 1. A list is provided in the command line
 - 2. Two excel files are also created
 - a. A file containing the coefficients of the same name as the data with the suffix “ fit”
(Example: “gmt1 091027 1 mod.xls” becomes “gmt1 091027 1 mod fit.xls”)
 - b. A file containing the residuals from the fit with the same name as the data with the suffix “ Residuals”
(Example: “gmt1 091027 1 mod.xls” becomes “gmt1 091027 1 mod Residuals.xls”)
 - c. The values of the coefficients should be included in the report

23. Create the report

- a. It should contain from the MATLAB analysis
 - i. Date of the measurement
 - ii. The last five plots:
 - 1. The “Remaining outliers removed” mesh plot
 - 2. The “Remaining outliers removed” contour plot
 - 3. The “Polynomial fit” plot
 - 4. The “Focus removed” mesh plot
 - 5. The “Focus removed” contour plot

Note: if multiple measurement sets are made, display one representative set of plots
 - iii. A list of Zernike coefficients
Note: if multiple measurement sets are made, list the coefficients for each set, along with the mean of the sets and either the difference if only two sets, or the standard deviation if three or more sets
 - iv. Number of surface points in measurement (for each set)
 - v. Min and Max values (use mean values)
 - vi. Residual RMS after fit (use mean values)
- b. If force actuator measurements are made, include in report as well
- c. Include the thermal maps of the mirror at the time of the start of each measurement set
- d. Send report to
 - i. Buddy Martin
 - ii. Steve Warner
 - iii. Kevin Law
 - iv. Kirk O’Laughlin
 - v. Bill Hubble
 - vi. Mike Tuell
 - vii. Tom Zobrist
 - viii. Anyone else that wants it

24. Also send to Buddy

- a. The Excel files of the surface data
(Example: "gmt1 091027 1 mod.xls" & "gmt1 091027 2 mod.xls")
- b. The Excel files with Zernike coefficients
(Example: "gmt1 091027 1 mod fit.xls" & "gmt1 091027 2 mod fit.xls")

Appendix D

MATLAB DATA ANALYSIS CODE

Throughout this dissertation, much of the data analysis has been done using MATLAB scripts. In the sections below are copies of the MATLAB scripts that have been used to generate most of the plots throughout this dissertation. The first major section lists the code for analyzing GMT surface measurements and many of the subroutines. Next is the code for evaluating the radial and angular calibration data, followed by the code for the correlation study.

D.1 GMT Surface Measurement Analysis Code

At the time of the writing of this dissertation, the data analysis is done offline using MATLAB scripts. The expectation is that the data analysis will eventually be incorporated into the control software so that it can be done real-time as the data is being collected. In the sections below are copies of the MATLAB scripts that are currently used.

D.1.1 ltPlusGMT.m

```
function
ltPlusGmt(fileName,phiT,thetaT,psiT,deltaXT,deltaYT,deltaZT,...
    dmiCorrection,fitDegree,zmin,zmax,coarseThresh,fineThresh)
% ltPlusGmt(fileName,phiT,thetaT,psiT,deltaXT,deltaYT,deltaZT,...
%   dmiCorrection,fitDegree,zmin,zmax,coarseThresh,fineThresh)
%
% Compares LT+ measurements with ideal GMT surface. Corrects
% tracker data based on DMIs.
```

```

%
% Reads data from spreadsheet. Tracker data are in m and rad. DMI data
% are in counts which gets converted to microns. Convert everything to
% microns after transforming to mirror coordinates.
%
% Next 6 arguments are initial guess at transformation of coordinate
% axes from tracker coordinates to mirror coordinates with +ve x axis
% west. Rotations of coordinate axes follow right-hand rule and are
% entered in degrees. Rotations follow the xyz-convention of Goldstein,
% p 147:
%
% phiT = rotation of coordinate axes around original z axis:
% puts new y axis in a plane perpendicular to target x axis
% thetaT = rotation of coordinate axes around new y axis:
% makes new x axis parallel to target x axis
% psiT = rotation of coordinate axes around new x axis:
% makes new y and z axes parallel to target y and z axes
%
% Translations come after rotations and are entered in m:
% deltaXT = translation of coordinate axes along new x axis:
% deltaYT = translation of coordinate axes along new y axis:
% deltaZT = translation of coordinate axes along new z axis:
%
% fitDegree = highest degree for polynomial fit
% zmin,zmax = plot scale limits (microns)
%
% Remove points with displacements > coarseThresh before removing
% plane. Remove points with displacements > fineThresh after removing
% plane. Thresholds are in microns.
%
% Tracker data are in spherical polar coordinates:
% phi = azimuth angle measured from center of mirror (down) to north
% (rad)
% theta = angle measured from pole (east) (rad)
% r = radial coordinate (m)
%
% DMI data are radial displacements in counts which is converted to
% microns. Both DMI displacements and DMI tracker coordinates are in
% order N, S, E, W.
%
close all
DegPerRad = 180 / pi;
R = 36; % m
k = -0.998286;
x_c = 8.71; % off-axis distance (m)
D = 8.417; % m
tiltAngle = 13.522; % tilt of surface relative to optical axis, deg
R_r = R * (1 - k * (x_c/R)^2)^(3/2); % radial RoC at x_c
R_t = R * (1 - k * (x_c/R)^2)^(1/2); % tangential RoC at x_c
z_c = x_c^2 / (R + sqrt(R^2 - (k+1)*x_c^2)); % surface height at x_c
a = D/2;
r_ball = 0.01905; % m
% r_ball = 0.02; % m, adding 1 mm for puck
%
% Read and sort data.

```

```

%
folder = 'C:\My Documents\GMT\Data\Segment1';
file = fullfile(folder,fileName);
Time = xlsread(file,'g:g');
StartTime = Time(9,1);
deltaTime = Time(9:end,1)-ones(size(Time(9:end,1)))*StartTime;
Time_initial = (StartTime-1191628923)/86400+733320.70975694;
S = datestr(Time_initial,21);
fprintf('\nMeasurement initiated at %s.\n',S);
data = xlsread(file,'i:k');
weather = xlsread(file,'q:s');
n = size(data,1);
fprintf('\n%d rows of data read.\n',n);
r = data(:,3)'; % row vector
theta = data(:,2)'; % row vector
phi = data(:,1)'; % row vector
Temp = weather(:,1); % column vector
Pressure = weather(:,2); % column vector
RH = weather(:,3); % column vector
Index = CalcIndex(Temp,Pressure,RH)*[1 1 1 1]; % calculates the index
for j = 1:n
    if Index(j,:)>mean(Index)+0.0000025
        Index(j,)=(Index(j-1,)+Index(j+1,))/2;
    end
end

%
% Convert to tracker Cartesian coordinates.
%
x_t = r .* sin(theta) .* cos(phi); % increases down
y_t = r .* sin(theta) .* sin(phi); % increases to N
z_t = r .* cos(theta); % increases to E
xyz_t = [x_t; y_t; z_t]; % 3 x n
%
% First 4 points are ref pts on mirror in order 0, 90, 180, 270 deg.
%
refData = xyz_t(:,1:4);
%
% Find local mirror coordinates of 4 reference points. Local mirror
% system has origin at center of mirror surface, 0 and 180 degree edges
% at same height. x points away from optical axis. z is given by
surface
% sag along appropriate axis + correction for z distance from surface
% to center of ball.
%
% Reference points are at 4 compass points, displaced from edge by dr
% and from surface by ds.
%
dr = 0.0360; % radial distance from OD to center of tracker ball, m
ds = 0.01905; % normal distance from mirror surface to center of ball, m
rToBall = a - dr;
zToBall_r = rToBall^2/(2*R_r) + ds/cos(atan(rToBall/R_r));
zToBall_t = rToBall^2/(2*R_t) + ds/cos(atan(rToBall/R_t));
x_ref = [rToBall 0 -rToBall 0];
y_ref = [0 rToBall 0 -rToBall];

```

```

z_ref = [zToBall_r zToBall_t zToBall_r zToBall_t];
refNom = [x_ref; y_ref; z_ref];
fprintf('\nNominal reference coordinates in mm:\n')
for i=1:3
    for j=1:4
        fprintf('%10.1f',refNom(i,j)*1000);
    end
    fprintf('\n');
end
%
% Use 4 reference points to find best-fit coordinate transformation
% from tracker coordinates to mirror coordinates.
%
initTrans = [phiT/DegPerRad; thetaT/DegPerRad; psiT/DegPerRad;...
    deltaXT; deltaYT; deltaZT];
[trans,displacement,it] = nPtFitxyz(refData,refNom,initTrans,1e-6);
phiT = trans(1);
thetaT = trans(2);
psiT = trans(3);
deltaXT = trans(4);
deltaYT = trans(5);
deltaZT = trans(6);
fprintf('\nBest-fit transformation to mirror reference points after')
fprintf('%d iterations:\n',it)
fprintf('rotation %9.3f %9.3f %9.3f deg\n',phiT*DegPerRad,...
    thetaT*DegPerRad,psiT*DegPerRad);
fprintf('translation %9.4f %9.4f %9.4f m\n',deltaXT,deltaYT,deltaZT);
fprintf('\nResidual displacements in mm:\n')
for i=1:3
    for j=1:4
        fprintf('%10.1f',displacement(i,j)*1000);
    end
    fprintf('\n');
end
%
% Apply this transformation to surface data.
%
Rz = [cos(phiT) sin(phiT) 0; -sin(phiT) cos(phiT) 0; 0 0 1];
Ry = [cos(thetaT) 0 -sin(thetaT); 0 1 0; sin(thetaT) 0 cos(thetaT)];
Rx = [1 0 0; 0 cos(psiT) sin(psiT); 0 -sin(psiT) cos(psiT)];
Tvec = [deltaXT; deltaYT; deltaZT];
T = repmat(Tvec,1,n); % 3 x nSurf
xyz_r = Rx*Ry*Rz*xyz_t - T;% contains n column vectors in mirror coords
%
% Next 4 points are DMI locations.
%
dmiCoords = xyz_r(:,5:8);
r_dmi = r(:,5:8);
firstSurfRow = 9;
%
% Remaining points are surface data.
%
xyz = xyz_r(:,firstSurfRow:n);
nSurf = n - firstSurfRow + 1;
x = xyz(1,:);

```

```

y = xyz(2,:); % 1 x nSurf row vectors
z = xyz(3,:);
fprintf('\n%d surface data points.\n',n);
%
% Use DMI data to correct for rigid-body motion.
%
if dmiCorrection
    fprintf('\nCorrecting for DMI displacements.\n');
    z_u = z;
%
% Read DMI displacements.
%
dmiDispC = zeros(n,4);
dmiDispC(:,1) = xlsread(file,'y:y'); % North DMI counts
dmiDispC(:,2) = xlsread(file,'aa:aa'); % South DMI counts
dmiDispC(:,3) = xlsread(file,'ac:ac'); % West DMI counts
dmiDispC(:,4) = xlsread(file,'ae:ae'); % East DMI counts
dmiDisp = DMICountsToMicrons(dmiDispC,Index,r_dmi); % converts DMI
% from counts to microns
dmiDisp = dmiDisp(9:8+nSurf,:); % nSurf x 4 matrix (meters)
DMIzCoef=zeros(nSurf,4);

% [Index(10:20,:) dmiDispC(10:20,:) dmiDisp(10:20,:)]
if size(dmiDisp,1) ~= nSurf
    error(['Number of DMI data do not match number of',...
        ' tracker data.\n'])
end
%
% Find tracker position in mirror coordinates.
%
z_tracker = -deltaZT;
%
% Find normalized cylindrical polar coordinates of DMI positions.
%
x_dmi = dmiCoords(1,:);
y_dmi = dmiCoords(2,:);
z_dmi = dmiCoords(3,:);
[angle,rho] = cart2pol(x_dmi',y_dmi'); % 4 x 1 col vectors
rho = rho / a;
%
% Initialize matrices for fit of plane to 4 DMIs, and residual
% displacements of 4 DMIs.
%
dmiCoef = zeros(nSurf,3);
dmiResid = zeros(nSurf,4);
correction = zeros(1,nSurf); % row vector
%
% For each surface point...
%
for i=1:nSurf
    dz = zeros(4,1); % 4 x 1 col vector
%
% ...convert DMI displacements to vertical displacements (microns).
% Divide by cos(alpha) where alpha = angle betw line of sight and
% mirror's z axis.

```

```

%
    for j=1:4
        dz(j) = r_dmi(j) / (z_tracker - z_dmi(j)) * dmiDisp(i,j);
    end
%
% ...fit a plane to vertical displacements.
%
    [zCoef,zMatrix] = zFit4(rho,angle,dz,1);
    DMIzCoef(i,:) = zCoef;
%
% ...save Zernike coefficients and residual displacements.
%
    for kk=1:3
        dmiCoef(i,kk) = zCoef(kk);
    end
    outOfPlane = dz - zMatrix * zCoef; % 4 x 1 col vector
    for j=1:4
        dmiResid(i,j) = outOfPlane(j); % nSurf x 4 matrix
    end
%
% Apply correction to each surface point.
%
%     correction = zeros(size(z_u));
%     correction(i) = zCoef(1) + zCoef(2) * x(i)/a ...
%         + zCoef(3) * y(i)/a;
% How do you correct for the astigmatism component from the DMIs?
%     z(i) = z_u(i) - correction(i) / 1e6; % It is -ve and in microns
    end
    xyz = [x; y; z];
%
% Plots the first four Zernike terms to the DMI data to monitor the
% planar vs nonplanar components of the measurement
%
figure
plot((Index(9:end,1)-1)*10^4)
title('(Index-1)*10^4')
DMIzCoef = [DMIzCoef(:,1),DMIzCoef(:,2)/2,DMIzCoef(:,3)/2,...
    DMIzCoef(:,4)/sqrt(6)];
figure
plot(DMIzCoef(9:end,:))
legend('piston','X tilt','Y tilt','astigmatism',0)
axis tight
title('DMI correction components')
ylabel('RMS Zernike Coeficents [microns]')
xlabel('Measurement number')
end
%
% Transform from mirror coordinates to parent coordinates.
%
beta = tiltAngle/DegPerRad;
Ry = [cos(beta) 0 -sin(beta); 0 1 0; sin(beta) 0 cos(beta)]; % rotation
Tvec = [-x_c; 0; -z_c]; % 3 x 1 translation vector
T = repmat(Tvec,1,nSurf); % 3 x nSurf translation matrix
xyz_p = Ry*xyz - T; % contains nSurf column vectors in parent coords
%

```

```

% Compensate for radius of tracker ball, i. e. find contact points on
% mirror surface (still in parent coordinates).
%
xyz_p = radiusComp(xyz_p,r_ball,R,k);
%
% Find displacements d from nominal surface, in microns.
%
x_p = xyz_p(1,:);
y_p = xyz_p(2,:); % Nx1 col vectors
z_p = xyz_p(3,:);
rsq = x_p.^2 + y_p.^2;
r = sqrt(rsq);
z_nom = rsq ./ (R + sqrt(R^2 - (k+1)*rsq));
dzdr = r ./ (R - (k+1)*z_nom);
d = 1e6 * (z_p-z_nom).*cos(atan(dzdr)); % col vector
%
% Apply angular calibration results to LT data
%
MeanCoefficients = [0;-0.0905;0.1935;0.3982;0.7382;-0.2702;0.1993;...
    -0.2661;-0.6919;0.0541;-0.3183;0.1235;-0.6020;-0.1814;...
    0.1849;-0.1261;0.3747];
% MeanCoefficients = [0;-0.0905;0.1935;0.3982;0.7382;0;0;...
%     0;-0.6919;0;0;0;-0.6020;0;0;0;0.3747];
[THETA,RHO] = cart2pol(z_t',y_t');
sensitivity = RHO*(38-22.3)/38;
znknum = 25;
slp = Slope([z_t',y_t']/a,THETA,znknum);
slp = [slp(:,1:14) slp(:,18:19) slp(:,25)];
d = d-slp(9:end,:)...
    *MeanCoefficients(1:size(slp,2),:).*sensitivity(9:end,:);
%
% Put x and y for contact points in mirror coordinates.
% Keep d as displacements normal to surface.
%
Ry = [cos(beta) 0 sin(beta); 0 1 0; -sin(beta) 0 cos(beta)];
Tvec = [-x_c; 0; -z_c];
T = repmat(Tvec,1,nSurf);
xyz_m = Ry * (xyz_p + T);
x = xyz_m(1,:); % col vector
y = xyz_m(2,:);

%
% Plot displacements vs x and y (in mirror coordinates).
%
meshPlot3(x,y,d,50)
avg = mean(d);
rms = std(d,1);
title(['transformed per reference points:'],...
    ['mean = ',num2str(avg,'%2f'),' \mum, rms = ',...
    num2str(rms,'%2f'),' \mum']);
%
% Delete points with displacements > coarse threshold.
%
dd = d;
[deltaTime,x,y,d,newN] = skim(deltaTime,x,y,d,coarseThresh);

```

```

nRemoved = nSurf - newN;
nSurf = newN;
fprintf('\nRemoved %d points with displacement > %.3f\n',...
        nRemoved,coarseThresh);
fprintf('\n%d surface points remaining.\n',nSurf);
avg = mean(d);
rms = std(d,1);
%
% Plot displacements vs x and y.
%
meshPlot3(x,y,d,50)
title(['Worst outliers removed:  '],...
      ['mean = ',num2str(avg,'%.2f'),' \mum, rms = ',...
      num2str(rms,'%.2f'),' \mum']]);
%
% Fit and remove piston, tip and tilt.
%
[angle,rho] = cart2pol(x,y); % col vectors
rho = rho / a;
[zCoef,zMatrix,nVec,elVec] = zFit(rho,angle,d,1);
[Coef,Matrix] = zFitD(rho,angle,d,deltaTime);
d_d = d - Matrix * Coef;
d = d - zMatrix * zCoef;
driftError = d-d_d;
meshPlot3(x,y,driftError,50)
avg = mean(d-d_d);
rms = std(d-d_d,1);
title(['Drift Error in GMT Surface Measurements'],...
      ['mean = ',num2str(avg,'%.2f'),' \mum, rms = ',...
      num2str(rms,'%.2f'),' \mum']]);
xlabel('meters')
ylabel('meters')
zlabel('\mum')
fprintf('\n');
% d = d_d;
listCoefs(nVec,elVec,zCoef);
avg = mean(d);
rms = std(d,1);
%
% Plot residual error vs x and y.
%
meshPlot3(x,y,d,50)
title(['Plane removed:  '],...
      ['mean = ',num2str(avg,'%.2f'),' \mum, rms = ',...
      num2str(rms,'%.2f'),' \mum']]);
imagescWithLims(x,y,d,0,a,50,zmin,zmax)
title(['Plane removed:  '],...
      ['mean = ',num2str(avg,'%.2f'),' \mum, rms = ',...
      num2str(rms,'%.2f'),' \mum']]);
%
% Delete points with displacements > fine threshold.
%
[deltaTime,x,y,d,newN] = skim(deltaTime,x,y,d,fineThresh);
nRemoved = nSurf - newN;
nSurf = newN;

```

```

fprintf('\nRemoved %d points with displacement > %.1f\n',...
        nRemoved,fineThresh);
fprintf('\n%d surface points remaining.\n',nSurf);
avg = mean(d);
rms = std(d,1);
fprintf('\nrms = %.1f micron\n',rms);
%
% Plot residual error vs x and y.
%
meshPlot3(x,y,d,50)
title(['Remaining outliers removed:  '],...
       ['mean = ',num2str(avg,'%.2f'),' \mum, rms = ',...
        num2str(rms,'%.2f'),' \mum']);
imagescWithLims(x,y,d,0,D/2,50,zmin,zmax)
title(['Remaining outliers removed:  '],...
       ['mean = ',num2str(avg,'%.2f'),' \mum, rms = ',...
        num2str(rms,'%.2f'),' \mum']);
%
% Fit polynomials and display coefficients.
%
[angle,rho] = cart2pol(x,y); % col vectors
rho = rho / a;
[zCoef,zMatrix,nVec,elVec] = zFit(rho,angle,d,fitDegree);
rmsCoef = edge2rms(nVec,elVec,zCoef);
rmsOfFit = norm(rmsCoef);
fprintf('\n');
listBothCoefs(nVec,elVec,zCoef,rmsCoef);
zDisplay(zCoef,fitDegree,0,a,'hot',[zmin,zmax],zmax)
title(['Polynomial fit:  rms = ',...
       num2str(rmsOfFit,'%.2f'),' \mum']);
fprintf('rms of fit = %.1f micron\n',rmsOfFit);
%
% Find residual from fit.
%
residFromFit = d - zMatrix * zCoef;
rms = std(residFromFit,1);
fprintf('residual rms = %.1f micron\n',rms);
%
% Write coefficients in microns to spreadsheet.
%
excelFilename = [fileName,' Fit'];
excelFile = fullfile(folder,excelFilename);
xlswrite(excelFile,[nVec elVec zCoef rmsCoef])
%
% Write displacements and DMI information to spreadsheet.
%
if dmiCorrection
    excelFilename = [fileName,' Residuals'];
    excelFile = fullfile(folder,excelFilename);
    xlswrite(excelFile,[dd dmiCoef dmiResid]);
end
%
% Remove focus. Fit through degree 2 but only subtract P, T, T & F.
%
[zCoef,zMatrix] = zFit(rho,angle,d,2);

```

```

zCoef(4) = 0;
zCoef(6) = 0;
d = d - zMatrix * zCoef;
avg = mean(d);
rms = std(d,1);
%
% Plot residual error vs x and y.
%
meshPlot3(x,y,d,50)
title(['Focus removed:  '],...
      ['mean = ',num2str(avg,'%2f'),' \mum, rms = ',...
      num2str(rms,'%2f'),' \mum']);
imagescWithLims(x,y,d,0,a,50,zmin,zmax)
title(['Focus removed:  '],...
      ['mean = ',num2str(avg,'%2f'),' \mum, rms = ',...
      num2str(rms,'%2f'),' \mum']);
%
%
%
function a_s = radiusComp(a_p,r_b,R,k)
% a_s = radiusComp(a_p,r_b,R,k)
%
% Corrects points on a conic section for probe tip radius. Input
% points are in parent coordinates with origin at vertex of parent and
% z = optical axis.
%
% a_p = 3xN matrix of points corresponding to center of probe tip
% r_b = radius of probe tip
% R = radius of curvature of conic section
% k = conic constant
%
% a_s = 3xN matrix of points on surface
%
x = a_p(1,:);
y = a_p(2,:); % 1xN row vectors
z = a_p(3,:);
R_p = R-r_b; % approx radius of conic section through input points
%
% Go polar and project normal to surface of ball-center points. Project
% toward mirror surface.
%
r = sqrt(x.^2+y.^2);
theta = atan2(y,x);
z_nom = r.^2 ./ (R_p + sqrt(R_p^2 - (k+1)*r.^2));
dzdr = r ./ (R_p - (k+1)*z_nom); % Should I use z or z_nom?
deltar = r_b*sin(atan(dzdr));
deltaz = -r_b*cos(atan(dzdr));
r = r + deltar;
z = z + deltaz;
x = r .* cos(theta);
y = r .* sin(theta);
%
% Repackage as 3xN matrix.
%
a_s = cat(1,x,y,z);

```

D.1.2 CalcIndex.m

```

function Index = CalcIndex(Temp,Pressure,RH);
% Calculates the Index of Refraction for air given Temperature in
% Degrees Centegrade, Pressure in mmHG, and Relative Humidity in
% decimal form.

% Additional parameters that can be changed by user
wavelengthV = 0.63299137; % Vacuum wavelength of a HeNe laser [um]
CO2Concentration = 0.000450; % CO2 concentration, 400ppm is standard
% for a lab room, Faro uses 450ppm []

% Coefficients used to calculate Saturation Pressure
SPCoefA = 0.000012378847; % [1/K^2]
SPCoefB = -0.019121316; % [1/K]
SPCoefC = 33.93711; % []
SPCoefD = -6343.1645; % [K]

PressurePa = Pressure*101325/760; % Converts Press in units of mmHg
% into Pascals [Pa]
% TempC = (Temp-32)*5/9; % Temperature converted to Centegrade [C]
TempC = Temp; % Temperature converted to Centegrade [C]
TempK = 273.15 + TempC; % Temperature converted to Kelvin [K]
SatPress = exp(SPCoefA*TempK.^2 + SPCoefB.*TempK +
SPCoefC.*ones(size(TempK)) + SPCoefD./TempK); % Saturation Pressure [Pa]
PartPress = SatPress.*RH; % Partial Pressure []
STPRefract = 1 + 10^-8*(8091.37 + 2333983/(130 - wavelengthV^-2) ...
+ 15518/(38.9 - wavelengthV^-2)); % Refractivity of air at STP
RefDepCO2 = (STPRefract - 1)*(1 + 0.5327*(CO2Concentration-0.0004));
% Dependence of Refractivity to CO2 Concentrations
RefTempPressDep = RefDepCO2.*PressurePa./93214.6.*(1+10^(-8)). ...
*(0.5953-0.009876.*TempC).*PressurePa)./(1+0.003661.*TempC);
% Dependence of Refractivity to Temp and Pressure
RefHumDep = RefTempPressDep+1-PartPress. ...
*(3.802-0.0384.*wavelengthV.^-2)*10^-10; % Dependence of
% refractivity to Relative Humidity

% Outputed parameter
Index = RefHumDep; % Index of Refraction of air at the provided
% Temperature, Pressure and RH

% Additional Parameter
WavelengthA = wavelengthV/Index; % Wavelength of the HeNe laser in air
% at the Index calculated above

```

D.1.3 DMICountsToMicrons.m

```

function DMIm = DMICountsToMicrons(DMlc,Index,r_dmi);
% DMIm = DMICountsToMicrons(DMlc,Index,r_dmi) converts from Distance
% Measuring Interferometer counts into microns using the index at each
% point.
%
% DMlc is the outputted counts form the four DMIs. It is an n x 4
% matrix where one column for each DMI and n row for the n
% measurements.
% Index it the index of refraction for each measurement point. It is
% also an n x 4 matrix.
% r_dmi is the Deadpath length measured in meters radially from the
% laser tracker to the surface references. This is a 1 x 4 array.
%
% Typical values:
% % DMlc = [-2.67E+02 -2.84E+02 -2.97E+02 -2.68E+02];
% % Index = [1.00024904175809 1.00024904175809 1.00024904175809
% % 1.00024904175809];
% % r_dmi = [22.443456667860200 22.465887364628500 22.419107220363099
% % 22.474938580258101];

One = ones(size(DMlc,1),1);
DMlc = DMlc-One*DMlc(9,:); % starts the DMI counts at zero
N = 64; % the number of counts per wavelength
wavelength = 0.63299137; % wavelength of the DMI laser in microns
DeadPath = -r_dmi*10^6; % distance from the DMI to the retroreflector
% at the mirror surface in microns
DeadCounts = DeadPath.*Index(9,:)*N/wavelength; % the number of counts
% over the DeadPath
DMIm = (wavelength*(DMlc + One*DeadCounts)./(N*Index))-One*DeadPath;
% the DMI reading in microns
return

```

D.1.4 nPtFitxyz.m

```

function [trans,displacement,it] = ...
nPtFitxyz(measuredPts,targetPts,initTrans,rmsTol)
% [trans,displacement,it] =
% nPtFitxyz(measuredPts,targetPts,initTrans,rmsTol)
%
% Finds best fit coordinate transformation of measured points to target
% points.
%
% measuredPts = 3xN matrix of measured (x,y,z) coordinates
% targetPts = 3xN matrix of target coordinates in transformed coord
% system initTrans = initial guess at coordinate transformation (See
% trans below.)rmsTol: Iterate until change in rms residual
% displacement < rmsTol
%

```

```

% trans = column vector of 3 rotations and 3 translations, using
% Goldman xyz convention, in the order z, y, x or yaw, pitch, roll:
%
% phi = rotation of coordinate axes around original z axis (yaw)
% theta = rotation of coordinate axes around new y axis (pitch)
% psi = rotation of coordinate axes around new x axis (roll)
%
% The 3 rotations are followed by 3 translations
%
% deltaX = translation of coordinate axes along new x axis
% deltaY = translation of coordinate axes along new y axis
% deltaZ = translation of coordinate axes along new z axis
%
% Angles are in rad and displacements are in same units as data.
%
% displacement = 3xN matrix of residual displacements
% it = number of iterations
%
N = size(measuredPts,2); % number of points
%
% Take first cut at transformation.
%
trans = initTrans;
phi = trans(1);
theta = trans(2);
psi = trans(3);
deltaX = trans(4);
deltaY = trans(5);
deltaZ = trans(6);
%
% Form three 3x3 rotation matrices and one 3xN translation matrix.
%
Rz = [cos(phi) sin(phi) 0; -sin(phi) cos(phi) 0; 0 0 1];
Ry = [cos(theta) 0 -sin(theta); 0 1 0; sin(theta) 0 cos(theta)];
Rx = [1 0 0; 0 cos(psi) sin(psi); 0 -sin(psi) cos(psi)];
Tvec = [deltaX; deltaY; deltaZ];
T = Tvec;
for i=1:N-1
    T = cat(2,T,Tvec);
end % T should be 3xN now
%
% Apply coordinate transformation and find residual displacements.
%
newPts = Rx*Ry*Rz*measuredPts - T;
displacement = newPts-targetPts;
dispSq = displacement .* displacement;
rmsDist = sqrt(sum(sum(dispSq))/N);
%
% Find coordinate transformation that minimizes displacements from
% target points. Must iterate because derivatives of displacements with
% respect to rotations and translations depend on current values of
% rotations and translations.
%
% First find influence functions for rotations and translations.
%

```

```

dPhi = 0.001; % rad
dTheta = 0.001; % rad
dPsi = 0.001; % rad
dDeltaX = 1; % mm
dDeltaY = 1; % mm
dDeltaZ = 1; % mm
maxIterations = 10;
for it=1:maxIterations
%
% Start with rotation around z axis.
%
    phil = phi+dPhi;
    RzAtPhil = [cos(phil) sin(phil) 0; -sin(phil) cos(phil) 0; 0 0 1];
    pts = Rx*Ry*RzAtPhil*measuredPts - T;
    dXYZdPhi = (pts-newPts)/dPhi;
%
% Then rotation around new y axis.
%
    thetal = theta+dTheta;
    RyAtThetal = [cos(thetal) 0 -sin(thetal); ...
        0 1 0; sin(thetal) 0 cos(thetal)];
    pts = Rx*RyAtThetal*Rz*measuredPts - T;
    dXYZdTheta = (pts-newPts)/dTheta;
%
% Then rotation around new x axis.
%
    psil = psi+dPsi;
    RxAtPsil = [1 0 0; 0 cos(psil) sin(psil); 0 -sin(psil) cos(psil)];
    pts = RxAtPsil*Ry*Rz*measuredPts - T;
    dXYZdPsi = (pts-newPts)/dPsi;
%
% Then translation in x'.
%
    deltaX1 = deltaX+dDeltaX;
    TvecAtDeltaX1 = [deltaX1; deltaY; deltaZ];
    TAtDeltaX1 = TvecAtDeltaX1;
    for i=1:N-1
        TAtDeltaX1 = cat(2,TAtDeltaX1,TvecAtDeltaX1);
    end
    pts = Rx*Ry*Rz*measuredPts - TAtDeltaX1;
    dXYZdDeltaX = (pts-newPts)/dDeltaX;
%
% Then translation in y'.
%
    deltaY1 = deltaY+dDeltaY;
    TvecAtDeltaY1 = [deltaX; deltaY1; deltaZ];
    TAtDeltaY1 = TvecAtDeltaY1;
    for i=1:N-1
        TAtDeltaY1 = cat(2,TAtDeltaY1,TvecAtDeltaY1);
    end
    pts = Rx*Ry*Rz*measuredPts - TAtDeltaY1;
    dXYZdDeltaY = (pts-newPts)/dDeltaY;
%
% And translation in z'.
%

```

```

deltaZ1 = deltaZ+dDeltaZ;
TvecAtDeltaZ1 = [deltaX; deltaY; deltaZ1];
TAtDeltaZ1 = TvecAtDeltaZ1;
for i=1:N-1
    TAtDeltaZ1 = cat(2,TAtDeltaZ1,TvecAtDeltaZ1);
end
pts = Rx*Ry*Rz*measuredPts - TAtDeltaZ1;
dXYZdDeltaZ = (pts-newPts)/dDeltaZ;
% Form 3N x 6 matrix A to solve equation A*c = d for c.
% Each column of A is the influence function for one rotation or
% translation, i. e. the changes in x, y and z for all
% N data points due to a unit change in that parameter.
% Elements of vector c are 3 rotations and 3 translations.
% Elements of vector d are the 3N differences between current
% coordinates and target coordinates.
% The solution is the transformation that minimizes the sum of squares
% of residual displacements.
%
A(:,1) = reshape(dXYZdPhi,3*N,1);
A(:,2) = reshape(dXYZdTheta,3*N,1);
A(:,3) = reshape(dXYZdPsi,3*N,1);
A(:,4) = reshape(dXYZdDeltaX,3*N,1);
A(:,5) = reshape(dXYZdDeltaY,3*N,1);
A(:,6) = reshape(dXYZdDeltaZ,3*N,1);
d = reshape(displacement,3*N,1);
c = A\d;
%
% New rotations and translations are sums of old ones and (-) changes
% required to match current displacements.
%
trans = trans-c;
phi = trans(1);
theta = trans(2);
psi = trans(3);
deltaX = trans(4);
deltaY = trans(5);
deltaZ = trans(6);
%
% Try coordinate transformation again with new parameters.
%
Rz = [cos(phi) sin(phi) 0; -sin(phi) cos(phi) 0; 0 0 1];
Ry = [cos(theta) 0 -sin(theta); 0 1 0; sin(theta) 0 cos(theta)];
Rx = [1 0 0; 0 cos(psi) sin(psi); 0 -sin(psi) cos(psi)];
Tvec = [deltaX; deltaY; deltaZ];
T = Tvec;
for i=1:N-1
    T = cat(2,T,Tvec);
end % T is 3xN now
%
% Apply transformation and find residual displacements.
%
newPts = Rx*Ry*Rz*measuredPts - T;
displacement = newPts-targetPts;
dispSq = displacement .* displacement;
newRmsDist = sqrt(sum(sum(dispSq))/N);

```

```

%
% See if convergence is complete.
%
    if (rmsDist-newRmsDist < rmsTol)
        return
    end
    rmsDist = newRmsDist;
end

```

D.1.5 zFit.m

```

function [zCoef,zMatrix,nVec,elVec] = zFit(rho,theta,z,maxDegree)
% [zCoef,zMatrix,nVec,elVec] = zFit(rho,theta,maxDegree)
%
% Least-squares fit of Zernike polynomials to data.
%
% rho = column vector of normalized radius
% theta = column vector of angles (rad)
% z = col vector of data
% maxDegree = maximum degree of radial polynomials. All polynomials
% through maxDegree are fit.
%
% zCoef = col vector of fitted coefficients (same units as z)
% zMatrix = matrix whose columns are the Zernike polynomials evaluated
% over the data (useful for subtracting the fitted polynomials)
% nVec = col vector of radial degrees of polynomials
% elVec = col vector of angular orders of polynomials
%
% Polynomials are normalized to +/-1 at edge of pupil.
%
[zMatrix,nVec,elVec] = zEval(rho,theta,maxDegree);
zCoef = zMatrix \ z;

```

D.1.6 zFit4.m

```

function [zCoef,zMatrix,nVec,elVec] = zFit4(rho,theta,z,maxDegree)
% [zCoef,zMatrix,nVec,elVec] = zFit(rho,theta,maxDegree)
%
% Performs Least-squares fit of DMI values to the first four Zernike %
% polynomials to get piston, tip, tilt, and non-planar motions of mirror.
%
% rho = column vector of normalized radius
% theta = column vector of angles (rad)
% z = col vector of data
% maxDegree = this is not actually used since only the first 4 Zernike
% terms are fit.
%
% zCoef = col vector of fitted coefficients (same units as z)

```

```

% zMatrix = matrix whose columns are the Zernike polynomials evaluated
% over the data (useful for subtracting the fitted polynomials)
% nVec = col vector of radial degrees of polynomials
% elVec = col vector of angular orders of polynomials
%
% Polynomials are normalized to +/-1 at edge of pupil.
%
[zMatrix,nVec,elVec] = zEval(rho,theta,2);
Astig = zMatrix(:,4) + zMatrix(:,6);
zMatrix = [zMatrix(:,1:3) Astig];
zCoef = zMatrix \ z;

```

D.1.7 zEval.m

```

function [zMatrix,nVec,elVec] = zEval(rho,theta,maxDegree)
% [zMatrix,nVec,elVec] = zEval(rho,theta,maxDegree)
%
% Evaluates Zernike polynomials over the points specified by col
% vectors rho and theta.
%
% rho = column vector of normalized radius
% theta = column vector of angles (rad)
% maxDegree = maximum degree of radial polynomials. All polynomials
% through maxDegree are evaluated.
%
% zMatrix contains polynomials as its columns.
% nVec = col vector of radial degrees of polynomials
% elVec = col vector of angular orders of polynomials
%
% Polynomials are normalized to +/-1 at edge of pupil.
%
% Use notation of Born & Wolf, Appendix VII, with the additional
% convention that el>0 represents cosine term and el<0 represents sine
% term. (el because I can't tell an l from a 1)
% Put polynomials in the order in which they appear in Durango, which
% uses m for what I call el.
points = length(rho);
i = 1; % index for polynomials
for n = 0:maxDegree % degree of radial polynomial
    for el = n:-2:-n
        m = abs(el); % angular order
        radialPoly = zeros(points,1);
        for s = 0:(n-m)/2
            coef = (-1)^s*factorial(n-s) / ...
                (factorial(s)*factorial((n+m)/2-s) ...
                 *factorial((n-m)/2-s));
            power = n-2*s;
            radialPoly = radialPoly + coef * rho.^power;
        end
        if el>0
            zMatrix(:,i) = radialPoly .* cos(m*theta);

```

```

        nVec(i,1) = n;
        elVec(i,1) = el;
    elseif el==0
        zMatrix(:,i) = radialPoly;
        nVec(i,1) = n;
        elVec(i,1) = el;
    else
        zMatrix(:,i) = radialPoly .* sin(m*theta);
        nVec(i,1) = n;
        elVec(i,1) = el;
    end
    i = i+1;
end
end
end

```

D.1.8 skim.m

```

function [xSkimmed,ySkimmed,zSkimmed,nSkimmed] = skim(x,y,z,threshold)

% [xSkimmed,ySkimmed,zSkimmed,nSkimmed] = skim(x,y,z,threshold)
%
% Removes data whose absolute z value exceeds threshold.
%
% x, y, z are 3 separate vectors of data
% threshold = threshold value
% xSkimmed, ySkimmed, zSkimmed = 3 vectors of remaining data
% nSkimmed = number of remaining data points
%
index = find(abs(z)<threshold);
nSkimmed = length(index);
xSkimmed = zeros(nSkimmed,1);
ySkimmed = zeros(nSkimmed,1);
zSkimmed = zeros(nSkimmed,1);
for i=1:nSkimmed
    xSkimmed(i) = x(index(i));
    ySkimmed(i) = y(index(i));
    zSkimmed(i) = z(index(i));
end

```

D.1.9 meshPlot3.m

```

function meshPlot3(x,y,z,meshSize)
% meshPlot3(x,y,z,meshSize)
%
% Plots points (x,y,z) overlaid on mesh plot of z(x,y).
%
% x, y, z are 3 separate vectors of coordinates.
% meshSize = number of rows and columns in mesh plot

```

```

xlin = linspace(min(x),max(x),meshSize);
ylin = linspace(min(y),max(y),meshSize);
[X,Y] = meshgrid(xlin,ylin);
figure
zGrid = griddata(x,y,z,X,Y);
mesh(X,Y,zGrid)
axis tight
hold on
plot3(x,y,z, '.', 'MarkerSize',15)
hold off

```

D.1.10 imagescWithLims.m

```

function imagescWithLims(x,y,z,rmin,rmax,meshSize,zmin,zmax)

% imagescWithLims(x,y,z,rmin,rmax,meshSize,zmin,zmax)
%
% Makes color contour plot of points (x,y,z).
%
% x, y, z are 3 separate vectors of coordinates.
% rmin, rmax define mask and extent of image.
% meshSize = number of rows and columns in plot
% zmin,zmax set color scale.
%
% Make 2-D grid of x and y values. Put max y in first row.
%
xlin = linspace(-rmax,rmax,meshSize);
ylin = linspace(rmax,-rmax,meshSize);
[X,Y] = meshgrid(xlin,ylin);
R = sqrt(X.*X+Y.*Y);
onMirror = (R<=rmax & R>=rmin);
Z = griddata(x,y,z,X,Y);
%
% Mask out area off mirror and NaNs.
%
mask = onMirror .* ~isnan(Z);
%
% Paint background.
%
for row=1:meshSize
    for col=1:meshSize
        if ~mask(row,col)
            Z(row,col) = zmax;
        end
    end
end
figure
imagesc(Z,[zmin,zmax])
axis equal tight
axis off
colormap('hot');colorbar

```

```
rectangle('Position',[0.5,0.5,50,50],'Curvature',[1],...
          'LineWidth',2,'LineStyle','-')
daspect([1,1,1])
```

D.1.11 edge2rms.m

```
function rmsCoef = edge2rms(nVec,elVec,zCoef)

% rmsCoef = edge2rms(nVec,elVec,zCoef)
%
% Converts Zernike coefficients normalized to +/- 1 at edge to
% coefficients normalized to rms = 1.
%
% Use notation of Born & Wolf, Appendix VII, with the additional
% convention that el>0 represents cosine term and el<0 represents sine
% term. (el because I can't tell an l from a 1)
%
terms = length(zCoef);
rmsCoef = zeros(terms,1); % column vector
for i=1:terms
    if elVec(i)==0
        rmsCoef(i) = zCoef(i) / sqrt(nVec(i) + 1);
    else
        rmsCoef(i) = zCoef(i) / sqrt(2 * (nVec(i) + 1));
    end
end
```

D.1.12 listCoefs.m

```
function listCoefs(nVec,elVec,zCoef)
% listCoefs(nVec,elVec,zCoef)
%
% Makes a neat listing of polynomial coefficients.
%
% zCoef = coefficients, in whatever units and normalization
% nVec = col vector of radial degrees of polynomials
% elVec = col vector of angular orders of polynomials
%
fprintf(' n l   coef\n')
for i=1:size(zCoef)
    fprintf('%2d %2d %10.3f\n',nVec(i),elVec(i),zCoef(i))
end
```

D.1.13 listBothCoefs.m

```
function listBothCoefs(nVec,elVec,zCoef,rmsCoef)
% listBothCoefs(nVec,elVec,zCoef,rmsCoef)
%
% Makes a neat listing of polynomial coefficients.
%
% zCoef = coefficients, in whatever units and normalized to edge value
% rmsCoef = ditto normalized to rms value
% nVec = col vector of radial degrees of polynomials
% elVec = col vector of angular orders of polynomials
%
fprintf(' n l      edge coef  rms coef\n')
for i=1:size(zCoef)
    fprintf('%2d %2d %10.3f %10.3f\n', ...
        nVec(i),elVec(i),zCoef(i),rmsCoef(i));
end
```

D.1.14 zDisplay.m

```
function zDisplay(zCoef,maxDegree,rMin,rMax,palette,scale,maskVal)
%
% zDisplay(zCoef,maxDegree,rMin,rMax,palette,scale,maskVal)
%
% Displays map made of Zernike polynomials.
%
% INPUT
% zCoef      Zernike coefficients (standard form, column vector)
% maxDegree  of Zernike polynomials
% rMin       mask out area inside this radius
% rMax       mask out area outside this radius; normalizing radius
% palette    Matlab colormap (string)
% scale      [min,max] for color map
% maskVal    value to display for region outside aperture

% Set up arrays for map.
%
rows = 200;
cols = 200;
points = rows*cols;
dX = 2*rMax/cols;
Xvec = -rMax+dX/2:dX:rMax-dX/2;
Yvec = rMax-dX/2:-dX:-rMax+dX/2;
[X,Y] = meshgrid(Xvec,Yvec);
R = sqrt(X.*X+Y.*Y);
onMirror = R<=rMax & R>=rMin;
%
% Evaluate polynomials over map.
%
polys = size(zCoef);
```

```

if polys ~= (maxDegree+1)*(maxDegree+2)/2
    error('Wrong number of coefficients.')
end
rho = reshape(R/rMax,points,1);
theta = reshape(atan2(Y,X),points,1);
[zMatrix,nVec,e1Vec] = zEval(rho,theta,maxDegree);
map = reshape(zMatrix*zCoef,rows,cols);
map = onMirror .* map;
%
% Assign values to masked areas.
%
for i=1:rows
    for j=1:cols
        if ~onMirror(i,j)
            map(i,j) = maskVal;
        end
    end
end
%
% Display map.
%
figure
imagesc(map,scale)
axis equal tight
axis off
colormap(palette)
colorbar
%
% Display min and max.
%
map = onMirror .* map;
minVal = min(min(map));
maxVal = max(max(map));
rms = std(map(:),1);
fprintf('\nmin = %.3f\n',minVal);
fprintf('max = %.3f\n',maxVal);
fprintf('RMS = %.3f\n',rms);

```

D.2 LFS Surface Measurement Analysis Code

The MATLAB scripts used to analyze the large fold sphere data are included in this section.

D.2.1 ltPlusFoldSphere.m

```
function ltPlusFoldSphere(fileName,D,R,phiT,thetaT,psiT,...
    deltaXT,deltaYT,deltaZT,zmin,zmax,fitDegree,fitmin,fitmax)
% ltPlusFoldSphere(fileName,D,R,phiT,thetaT,psiT,...
%   deltaXT,deltaYT,deltaZT,zmin,zmax,fitDegree,fitmin,fitmax)
%
% Fits a sphere to LT+ measurements of a surface. Corrects
% tracker data based on DMIs.
%
% Reads data from spreadsheet. Tracker data are in m and rad. DMI data
% are in microns. Convert everything to mm after transforming to mirror
% coordinates.
%
% D = diameter of mirror (m)
% R = nominal radius of curvature (m)
%
% Next 6 arguments are initial guess at transformation of coordinate
% axes from tracker coordinates to mirror coordinates with +ve x axis
% west. Rotations of coordinate axes follow right-hand rule and are
% entered in degrees. Rotations follow the xyz-convention of Goldstein,
% p 147:
%
% phiT = rotation of coordinate axes around original z axis:
%   puts new y axis in a plane perpendicular to target x axis:
% thetaT = rotation of coordinate axes around new y axis:
%   makes new x axis parallel to target x axis
% psiT = rotation of coordinate axes around new x axis:
%   makes new y and z axes parallel to target y and z axes
%
% Translations come after rotations and are entered in m:
% deltaXT = translation of coordinate axes along new x axis:
% deltaYT = translation of coordinate axes along new y axis:
% deltaZT = translation of coordinate axes along new z axis:
%
% zmin,zmax = plot scale limits for data
% fitDegree = highest degree for polynomial fit
% fitmin,fitmax = plot scale limits for fit
%
% Tracker data are in spherical polar coordinates:
% phi = azimuth angle measured from center of mirror (down) to north
% theta = angle measured from pole (east)
```

```

% r = radial coordinate
%
% DMI data are radial displacements. Both DMI displacements and DMI
% tracker coordinates are in order N, S, E, W.
%
close all
DegPerRad = 180 / pi;
a = D/2;
r_ball = 0.01905; % m
%
% Read and sort data.
%
folder = 'C:\My Documents\GMT\Data\Fold Sphere';
file = fullfile(folder,fileName);
surfaceData = xlsread(file,'a:c');
N = size(surfaceData,1);
fprintf('\n%d data points read.\n',N);
r = surfaceData(:,3)'; % row vector
theta = surfaceData(:,2)'; % row vector
phi = surfaceData(:,1)'; % row vector
%
% Convert to tracker Cartesian coordinates.
%
x_t = r .* sin(theta) .* cos(phi); % increases down
y_t = r .* sin(theta) .* sin(phi); % increases to N
z_t = r .* cos(theta); % increases to E
xyz_t = [x_t; y_t; z_t]; % 3 x N
%
% Use DMI retros as references to define mirror coordinate system. Does
% not need to be accurate. But I should look at surface errors after
% transformation of surface data, to refine dr and ds.
%
% Read tracker coordinates of DMI retros.
%
dmiCoords = xlsread(file,'j:1');
if size(dmiCoords,1) ~= 4
    error ('Did not read 4 sets of DMI coordinates.\n')
end
r_dmi = dmiCoords(:,3)'; % 1 x 4 row vector
theta_dmi = dmiCoords(:,2)'; % 1 x 4 row vector
phi_dmi = dmiCoords(:,1)'; % 1 x 4 row vector
x_dmi = r_dmi .* sin(theta_dmi) .* cos(phi_dmi); % 1 x 4 row vector
y_dmi = r_dmi .* sin(theta_dmi) .* sin(phi_dmi); % 1 x 4 row vector
z_dmi = r_dmi .* cos(theta_dmi); % 1 x 4 row vector
refData = [x_dmi; y_dmi; z_dmi]; % 3 x 4
%
% Define mirror coordinates of 4 reference points.
% Reference points are at 4 compass points, displaced from edge by dr
% and from surface by ds, which are determined by trial and error.
% x axis points to west. Order of points is N, S, E, W.
%
dr = 0.025; % radial distance from OD to center of tracker ball, m
ds = 0.07; % normal distance from mirror surface to center of ball, m
rToBall = a-dr;
zToBall = R - sqrt((R-ds)^2 - rToBall^2);

```

```

x_ref = [0 0 -rToBall rToBall];
y_ref = [-rToBall rToBall 0 0];
z_ref = [zToBall zToBall zToBall zToBall];
refNom = [x_ref; y_ref; z_ref]; % 3 x 4
%
% Use 4 reference points to find best-fit coordinate transformation
% from tracker coordinates to mirror coordinates.
%
initTrans = [phiT/DegPerRad; thetaT/DegPerRad; psiT/DegPerRad;...
             deltaXT; deltaYT; deltaZT];
[trans,displacement,it] = nPtFitxyz(refData,refNom,initTrans,1e-6);
phiT = trans(1);
thetaT = trans(2);
psiT = trans(3);
deltaXT = trans(4);
deltaYT = trans(5);
deltaZT = trans(6);
fprintf('\nBest-fit transformation to mirror reference points after ...
        %d iterations:\n',it)
fprintf('rotation    %9.3f %9.3f %9.3f  deg\n',phiT*DegPerRad,...
        thetaT*DegPerRad,psiT*DegPerRad);
fprintf('translation %9.4f %9.4f %9.4f  m\n',deltaXT,deltaYT,deltaZT);
fprintf('\nResidual displacements in mm:\n')
for i=1:3
    for j=1:4
        fprintf('%10.1f',displacement(i,j)*1000);
    end
    fprintf('\n');
end
%
% Apply this transformation to surface data.
%
Rz = [cos(phiT) sin(phiT) 0; -sin(phiT) cos(phiT) 0; 0 0 1];
Ry = [cos(thetaT) 0 -sin(thetaT); 0 1 0; sin(thetaT) 0 cos(thetaT)];
Rx = [1 0 0; 0 cos(psiT) sin(psiT); 0 -sin(psiT) cos(psiT)];
Tvec = [deltaXT; deltaYT; deltaZT];
T = repmat(Tvec,1,N); % 3 x N
xyz = Rx*Ry*Rz*xyz_t - T; % contains N column vectors in mirror coord
% sys
x = xyz(1,:);
y = xyz(2,:); % 1 x N row vectors
z = xyz(3,:);
%
% Fit sphere to surface data.
%
center = [0; 0; R];
radius = R;
conv = 0;
it = 0;
while conv == 0
    [center,radius,resid, sigmaH, conv, Vx0n, urn, GNlog, Opt, J] ...
    = lssphere(xyz',center,radius,1E-3,1e-9);
    it = it + 1;
end
fprintf('\nBefore DMI correction:\n')

```

```

fprintf('Best-fit sphere after %d iterations:\n',it)
fprintf('center %9.4f %9.4f %9.4f  m\n',center');
fprintf('R = %9.5f m\n',radius);
fprintf('R + ball radius = %9.5f m\n',radius+r_ball);
%
% Plot residual error (in microns) vs x and y (in m).
%
resid = 1e6 * resid;
xlin = linspace(-a,a,50);
ylin = linspace(-a,a,50);
[X,Y] = meshgrid(xlin,ylin);
figure
residGrid = griddata(x,y,resid,X,Y);
mesh(X,Y,residGrid)
axis tight
hold on
plot3(x,y,resid, '.', 'MarkerSize',15)
hold off
axis([-a a -a a zmin zmax])
fprintf('\nmean = %.2f micron\n',mean(resid));
fprintf('rms = %.2f micron\n',std(resid,1));
%
% Use DMI data to correct for rigid-body motion.
%
    dmiCoef = zeros(N,3);
    dmiResid = zeros(N,4);
%
% Read DMI displacements.
%
    dmiDisp = xlsread(file,'d:g'); % N x 4 matrix (microns)
    if size(dmiDisp,1) ~= N
        error('Number of DMI data do not match number of tracker
data.\n')
    end
%
% Find tracker position in mirror coordinates.
%
    z_tracker = -deltaZT;
%
% Find normalized cylindrical polar coordinates of DMI positions.
%
    [angle,rho] = cart2pol(x_ref',y_ref'); % 4 x 1 col vectors
    rho = rho / a;
%
% For each data point...
%
    for i=1:N
        dz = zeros(4,1); % 4 x 1 col vector
%
% ...convert DMI displacements to vertical displacements (microns).
%
        for j=1:4
            dz(j) = r_dmi(j) / (z_tracker - z_ref(j)) * dmiDisp(i,j);
        end
    end
%

```

```

% ...fit a plane to vertical displacements.
%
    [zCoef,zMatrix] = zFit4(rho,angle,dz,1);
    DMIZCoef(i,:) = zCoef;
%
% ...save Zernike coefficients and residual displacements.
%
    for k=1:3
        dmiCoef(i,k) = zCoef(k);
    end
    outOfPlane = dz - zMatrix * zCoef; % 4 x 1 col vector
    for j=1:4
        dmiResid(i,j) = outOfPlane(j); % N x 4 matrix
    end
% Apply correction to each tracker point.
%
    correction = zCoef(1) + zCoef(2) * x(i)/a + zCoef(3) * y(i)/a;
    z(i) = z(i) - correction / 1e6;
end
%
% Plots the first four Zernike terms to the DMI data to monitor the
% planar vs nonplanar components of the measurement
%
    DMIZCoef = [DMIZCoef(:,1),DMIZCoef(:,2)/2,DMIZCoef(:,3)/2,...
        DMIZCoef(:,4)/sqrt(6)];
    figure
    plot(DMIZCoef)
    legend('piston','X tilt','Y tilt','astigmatism',0)
    axis tight
    title('DMI correction components')
    ylabel('RMS Zernike Coeficents [microns]')
    xlabel('Measurement number')

%
% Fit sphere to corrected coordinates.
%
    xyz = [x; y; z];
    it = 0;
    conv = 0;
    while conv == 0
        [center,radius,correctedResid, sigmah, conv, Vx0n, urn, ...
        GNlog, Opt, J] = lssphere(xyz',center,radius,1E-3,1e-9);
        it = it +1;
    end
    fprintf('\nAfter DMI correction:')
    fprintf('\nBest-fit sphere after %d iterations:\n',it)
    fprintf('center %9.4f %9.4f %9.4f m\n',center');
    fprintf('R = %9.5f m\n',radius);
    fprintf('R + ball radius = %9.5f m\n',radius+r_ball);
%
% Plot residual error (in microns) vs x and y (in m).
%
    correctedResid = 1e6 * correctedResid;
    figure
    residGrid = griddata(x,y,correctedResid,X,Y);

```

```

mesh(X,Y,residGrid)
axis tight
hold on
plot3(x,y,correctedResid, '.', 'MarkerSize',15)
hold off
axis([-a a -a a zmin zmax])
fprintf('\nmean = %.2f micron\n',mean(correctedResid));
    fprintf('rms = %.2f micron\n',std(correctedResid,1));
%
% Write residual errors and DMI information to spreadsheet.
%
    excelFilename = [fileName, ' residuals'];
    excelFile = fullfile(folder,excelFilename);
    xlswrite(excelFile,[resid, correctedResid, dmiCoef, dmiResid]);
%
% Fit Zernike polynomials to residual error and plot.
%
    [angle,r] = cart2pol(x',y'); % Change to column vectors.
    rho = r / a;
    [zCoef,zMatrix,nVec,elVec] = ...
    zFit(rho,angle,correctedResid,fitDegree);
    fprintf('\n');
    listCoefs(nVec,elVec,zCoef);
    zDisplay(zCoef,fitDegree,0,D/2, 'hot', [fitmin,fitmax],2)
%
% Find residual from fit.
%
residFromFit = correctedResid - zMatrix * zCoef;
rms = std(residFromFit,1);
fprintf('\nresidual rms = %.3f micron\n',rms);

```

D.2.2 lssphere.m

```

function [x0n, rn, d, sigmah, conv, Vx0n, urn, GNlog, a, R] = ...
    lssphere(X, x0, r, tolp, tolg, w)
% -----
% LSSPHERE.M Least-squares sphere using Gauss-Newton.
%
% Version 1.0
% Last amended I M Smith 27 May 2002.
% Created I M Smith 08 Mar 2002
% -----
% Input
% X Array [x y z] where x = vector of x-coordinates,
% y = vector of y-coordinates and z = vector of z-coordinates.
% Dimension: m x 3.
%
% x0 Estimate of the sphere centre.
% Dimension: 3 x 1.
%
% r Estimate of the sphere radius.

```

```

%          Dimension: 1 x 1.
%
% tolp    Tolerance for test on step length.
%          Dimension: 1 x 1.
%
% tolg    Tolerance for test on gradient.
%          Dimension: 1 x 1.
%
% <Optional...
% w       Weights.
%          Dimension: m x 1.
% ...>
%
% Output
% x0n     Estimate of the sphere centre.
%          Dimension: 3 x 1.
%
% rn      Estimate of the sphere radius.
%          Dimension: 1 x 1.
%
% d       Vector of radial distances from the points
%          to the sphere.
%          Dimension: m x 1.
%
% sigmah  Estimate of the standard deviation of the weighted
%          residual errors.
%          Dimension: 1 x 1.
%
% conv    If conv = 1 the algorithm has converged,
%          if conv = 0 the algorithm has not converged
%          and x0n, rn, d, and sigmah are current estimates.
%          Dimension: 1 x 1.
%
% Vx0n    Covariance matrix of sphere centre.
%          Dimension: 3 x 3.
%
% urn     Uncertainty in sphere radius.
%          Dimension: 1 x 1.
%
% GNlog   Log of the Gauss-Newton iterations.
%          Rows 1 to niter contain
%          [iter, norm(f_iter), |step_iter|, |gradient_iter|].
%          Row (niter + 1) contains
%          [conv, norm(d), 0, 0].
%          Dimension: (niter + 1) x 4.
%
% a       Optimisation parameters at the solution.
%          Dimension: 4 x 1.
%
% R       Upper-triangular factor of the Jacobian matrix
%          at the solution.
%          Dimension: 4 x 4.
%
% Modular structure: NLSS11.M, GNCC2.M, FGSPHERE.M.
%

```

```

% [x0n, rn, d, sigmah, conv, Vx0n, urn, GNlog, a, R] = ...
%   lssphere(X, x0, r, tolp, tolg <, w >)
% -----

% check number of data points
m = size(X, 1);
if m < 4
    error('At least 4 data points required: ' )
end

%
% if no weights are specified, use unit weights
if nargin == 5
    w = ones(m, 1);
end % if nargin

%
% find the centroid and translate the data and
% centre estimate
xb = mean(X)';
%
xt = X(:, 1) - xb(1);
yt = X(:, 2) - xb(2);
zt = X(:, 3) - xb(3);
Xt = [xt yt zt];
x0b = x0 - xb;
%
ai = [x0b; r];
tol = [tolp; tolg];
%
% Gauss-Newton algorithm to find estimate of centre and radius
[a, d, R, GNlog] = nlss11(ai, tol, 'fgsphere', Xt, w);
%
x0n = a(1:3);
% translate sphere centre
x0n = x0n + xb;
rn = a(4);
%
nGN = size(GNlog, 1);
conv = GNlog(nGN, 1);
if conv == 0
    beep;
    warning('*** Gauss-Newton algorithm has not converged ***');
end % if conv

%
% calculate statistics
dof = m - 4;
sigmah = norm(d)/sqrt(dof);
G = eye(4);
Gt = R\'(sigmah * G); % R' * Gt = sigmah * G'
Va = Gt'*Gt;
Vx0n = Va(1:3, 1:3); % covariance matrix for x0n
urn = sqrt(Va(4, 4)); % uncertainty in rn
% -----
% See A B Forbes: Least-squares best-fit geometric elements,
%               NPL Report DITC 140/89.
%

```

```

% -----
% Author   A B Forbes
%          National Physical Laboratory
%          England
%
% Created  November 1988
% Version  2.0       93/07/09
% Crown Copyright
% -----
% End of LSSPHERE.M.

```

D.2.3 nlss11.m

```

function [a, f, R, GNlog] = nlss11(ai,tol,fguser,p1,p2,p3,p4,p5, ...
    p6,p7,p8,p9,p10,p11,p12,p13,p14,p15,p16,p17,p18,p19,p20)
% -----
% NLSS11.M   Nonlinear least squares solver:
%            Minimise f'*f where
%            [f, J] = fguser(a, p1, p2,...).
%
% Author     A B Forbes, CMSC, NPL.
% Amendment history
% v1.1 2002-05-03 IMS Prepared for MetroS.
% v1.1 2002-01-04 ABF Output a, f, GNlog set to latest value.
% v1.1 2001-07-09 ABF Optional input arguments increased.
% v1.1 2000-12-19 ABF Better convergence criteria. Column scaling.
% v1.0a 1999-07-16 ABF Statistics removed.
% v1.0a 1999-07-16 ABF Created.
% -----
% Input
% ai       Optimisation parameters, intial estimates.
%          Dimension: n x 1
%
% tol      Convergence tolerances [tolr tols]', where
%          tolr = relative tolerance, and
%          tols = scale for function values.
%          Dimension: 2 x 1.
%
% fguser   Module to calculate function and gradients with
%          signature
%          [f, J] = fguser(a, p1, p2,...).
%
% p1,...   Additional parameters to be passed to fguser
%          without change.
%          Note: The number of additional parameters supported is 20.
%
% Output
% a        Solution estimates of the optimisation parameters.
%          Dimension: n x 1.
%
% f        Functions evaluated at a.

```

```

%          Dimension: m x 1.
%          Constraint: m >= n.
%
% R          Triangular factor of the Jacobian matrix evaluated at a.
%          Dimension: n x n.
%
% GNlog      Log of the Gauss-Newton iterations.
%          Rows 1 to niter contain
%          [iter, norm(f_iter), |step_iter|, |gradient_iter|].
%          Row (niter + 1) contains
%          [conv, norm(d), 0, 0].
%          Dimension: (niter + 1) x 4.
%
% Modular structure: GNCC2.M.
%
% [a, f, R, GNlog] = nlss11(a, tol, 'fguser', p1, p2, p3, ...)
% -----

a0 = ai;
%
n = length(a0);
%
if n == 0
    error('Empty vector of parameter estimates:')
end
%
% Set up call to fguser:
% [f0, J ] = fguser(a0,p1,p2,....);
callfg0 = [fguser,'(a0',,];
for k = 1:nargin-3
    callfg0 = [callfg0,'p',int2str(k),,];
end % for k
callfg0 = [callfg0,')'];
%
% [f1, J ] = fguser(a1,p1,p2,....);
callfg1 = [fguser,'(a1',,];
for k = 1:nargin-3
    callfg1 = [callfg1,'p',int2str(k),,];
end % for k
callfg1 = [callfg1,')'];
%
mxiter = (100+ceil(sqrt(n)));
conv = 0;
niter = 0;
%
eta = 0.01;
%
GNlog = [];
%
% G-N iterations
while niter < mxiter & conv == 0
%
    [f0, J] = eval(callfg0);
    if niter == 0 % scale by norm of columns of J
        [mJ,nJ] = size(J);
    end
end

```

```

        scale = zeros(nJ,1);
        for j = 1:nJ;
            scale(j) = norm(J(:,j));
        end
    end % if niter
%
    m = length(f0);
% Check on m, n.
    if niter == 0 & m < n
        error('Number of observation less than number of parameters')
    end
%
% Calculate update step and gradient.
    F0 = norm(f0);
    Ra = triu(qr([J, f0]));
    R = Ra(1:nJ,1:nJ);
    q = Ra(1:nJ,nJ+1);
    p = -R\q;
    g = 2*R'*q;
    G0 = g'*p;
    a1 = a0 + p;
    niter = niter + 1;
%
% Check on convergence.
    [f1] = eval(callfg1);
    F1 = norm(f1);
    [c, conv, sp, sg] = gncc2(F0, F1, p, g, scale, tol(1), tol(2));
%
    if conv ~= 1
%
% ...otherwise check on reduction of sum of squares.
%
% Evaluate f at a1.
        rho = (F1 - F0)*(F1 + F0)/(G0);
        if rho < eta
            tmin = max([0.001; 1/(2*(1-rho))]);
            a0 = a0 + tmin*p;
        else
            a0 = a0 + p;
        end % if rho
%
    end % if conv
%
    GNlog = [GNlog; [niter, F0, sp, sg]];
%
end % while niter
%
a = a0+p;
f = f1;
%
GNlog = [GNlog; [conv, F1, 0, 0]];
%
% -----
% End of NLSS11.M.

```

D.2.4 gncc2.m

```

function [c, iconv, sp, sg] = gncc2(f0, f1, p, g, scale, tolr, scalef)
% -----
% GNCC2   Gauss-Newton convergence conditions.
%
% Version 1.0
% Last amended   I M Smith 27 May 2002.
% Created        I M Smith 08 Mar 2002
% -----
% Input
% f0           Norm of residuals at old point: norm(f(a))
%              Dimension: 1 x 1.
%
% f1           Norm of residuals at new point: norm(f(a + p))
%              Dimension: 1 x 1.
%
% p            Step
%              Dimension: n x 1.
%
% g            Gradient
%              Dimension: n x 1.
%
% scale        Scale for columns of Jacobian matrix.
%              Dimension: n x 1.
%
% tolr         Relative tolerance.
%              Dimension: 1 x 1.
%
% scalef       Scale for function values.
%              Dimension: 1 x 1.
%
% Output
% c            Convergence indices in the form of ratio of value over
%              scaled tolerance.
%              c(1) size of step
%              c(2) change in function value
%              c(3) size of gradient
%              c(4) sum of squares near zero
%              c(5) gradient near zero
%              Dimension: 1 x 5.
%
% iconv        = 1 if convergence criteria have been met, i.e.,
%              C(1), C(2), C(3) < 1 or
%              C(4) < 1 or
%              C(5) < 1.
%              = 0 otherwise.
%              Dimension: 1 x 1.
%
% sp           Scaled size of the step.
%              Dimension: 1 x 1.
%
% sg           Scaled size of the gradient.

```

```

%           Dimension: 1 x 1.
%
% [c, iconv, sp, sg] = gncc2(f0, f1, p, g, scale, tolr, scalef)
% -----

iconv = 0;
%
sp = max(abs(p .* scale));
sg = max(abs(g ./ scale));
%
c(1) = sp/(scalef * tolr^(0.7));
%
delf = f0 - f1;
c(2) = abs(delf)/(tolr * scalef);
%
d3 = (tolr^(0.7)) * (scalef);
d4 = scalef * (eps^(0.7));
d5 = (eps^(0.7)) * (scalef);
%
c(3) = sg/d3;
c(4) = f1/d4;
c(5) = sg/d5;
%
if c(1) < 1 & c(2) < 1 & c(3) < 1
    iconv = 1;
elseif (c(4)) < 1
    iconv = 1;
elseif (c(5) < 1)
    iconv = 1;
end
% -----
% End of GNCC2.M.

```

D.2.5 fgsphere.m

```

function [f, J] = fgsphere(a, X, w)
% -----
% FGSPHERE.M   Function and gradient calculation for
%               least-squares sphere fit.
%
% Version 1.0
% Last amended   I M Smith 27 May 2002.
% Created       I M Smith 08 Mar 2002
% -----
% Input
% a           Parameters [x0 y0 z0 r0]'.
%             Dimension: 4 x 1.
%
% X           Array [x y z] where x = vector of x-coordinates,
%             y = vector of y-coordinates and z = vector of z-coordinates.
%             Dimension: m x 3.

```

```

%
% <Optional...
% w      Weights.
%        Dimension: m x 1.
% ...>
%
% Output
% f      Signed distances of points to sphere:
%        f(i) = sqrt((x(i)-x0)^2 + (y(i)-y0)^2 + (z(i)-z0)^2) - r0.
%        Dimension: m x 1.
%
% <Optional...
% J      Jacobian matrix df(i)/da(j).
%        Dimension: m x 4.
% ...>
%
% [f <, J >] = fgsphere(a, X <, w >)
% -----

m = size(X, 1);
% if no weights are specified, use unit weights
if nargin == 2
    w = ones(m, 1);
end % if nargin
%
xt = X(:,1) - a(1);
yt = X(:,2) - a(2);
zt = X(:,3) - a(3);
%
ri = sqrt(xt.*xt + yt.*yt + zt.*zt);
f = ri - a(4);
f = w .* f; % incorporate weights
%
if nargin > 1 % form the Jacobian matrix
    J = - [xt./ri, yt./ri, zt./ri ones(length(xt), 1)];
    W = diag(w);
    J = W * J; % incorporate weights
end % if nargin
% -----
% End of FGSPHERE.M.

```

D.3 Radial Calibration Analysis Code

The MATLAB code for analyzing the radial calibration data from the custom laser tracker calibration is provided in this section.

D.3.1 RadialCalibration.m

```
function RadialCalibration(inFileName,maxDegree,coarseThresh,...
    fineThresh)
% Modified version xlsFitFilter (written originally by Buddy Martin),
% to include referencing data to polishing table rotation center and
% known axes on the mirror For now this will be a fixed axis on the
% polishing table but later incorporate using the fiducials on the
% mirror edge. Also include other analysis pieces from Buddy's various
% codes to help with our tracker data reduction.

% Throw out points with displacements > coarseThresh before removing
% plane.
% Throw out points with displacements > fineThresh after removing
% plane.

% Call this initially with coarseThresh = fineThresh = 1000 or some
% value that won't throw out any data. Inspect plots and choose
% suitable thresholds for a second iteration.

% Mods by Ping Zhou and Matt Novak to various pieces during Fall 2007

%close all

%D = 150;    % diameter, mm
R = 243.86;  % nominal radius of curvature of parent, mm
k = 0;
rmin = 0;   % inner hole radius of the mirror, mm
rmax = 45.925; % semidiameter subtended by GMT, mm
r_b = 6.35;  % radius of tracker ball
%lambda = 10.6; %% unit in microns

%pathstr = 'C:\Documents and Settings\tzobrist\Desktop\GMT\...
% Laser Trackers\FARO\FARO Data\test data\set4';

%inFile = fullfile(pathstr,inFileName);
%[point,Radial,Theta,Phi,Time] = ImportFaroSAData(inFile);
[point,Radial,Theta,Phi,Time,InitialTime] = ...
    ImportFaroSAData(inFileName); % Time in Days
Radial = Radial + r_b;
Time = (point-point(1,1))/1200; %Time in Minutes
```

```

N = size(Radial,1);
clear point

Threshold = 3*std(Radial);
One = ones(N,1);
A=[Time One];
coefficients = A\Radial;
Drift = A*coefficients;
d = Radial - Drift;
dd = Radial - One*coefficients(2);
figure(7)
plot(Time,1000*dd,'-sq','MarkerSize',2)
xlabel('time (minutes)')
ylabel('Deviation (um)')
N_d = N;
mean_d = 1000*sum(d)/N;
rms_d = 1000*sqrt(dot(d,d)/N);
Coefficients = [N;1000*Threshold;1000*coefficients];
Values = [...
    ' Number of Points';...
    ' Threshold          ';...
    ' Linear Drift       ';...
    ' Constant Offset   '];

[Radial,Theta,Phi,Time] = OutlierCorrect2(d,Radial,Theta,Phi,Time);
Threshold = 3*std(Radial);
N = size(Radial,1);
One = ones(N,1);
A=[Time One];
coefficients = A\Radial;
Drift = A*coefficients;
dd = Radial - Drift;
Radial = Radial - Time*coefficients(1);
Coefficients2 = [N;1000*Threshold;1000*coefficients];
%figure(7)
ZeroLine = zeros(size(Time,1),1);
hold on
mean = 1000*sum(dd)/N;
rms = 1000*sqrt(dot(dd,dd)/N);
plot(Time,1000*Time*coefficients(1),'g-',Time,1000*(dd),...
    'r-sq',Time,ZeroLine(1:N,:), 'k-', 'MarkerSize',2)
title(['d = Uncorrection data  N = ',num2str(N_d,4),...
    ' mean = ',num2str(mean_d,2), ' um ',...
    'rms = ',num2str(rms_d,2), ' um '];...
    ['dd = Drift corrected data  N = ',num2str(N,4),...
    ' mean = ',num2str(mean,2), ' um ',...
    'rms = ',num2str(rms,2), ' um '];...
    [' Measurement start time: ',InitialTime]], 'FontSize',8);
legend('d','Drift','dd',0);
hold off
coef = [num2str([Coefficients, Coefficients2],8),Values]

[x y z] = SphereToCart(Radial,Theta,Phi);
a = [x';y';z'];

```

```

%%%%%%%%%%%%%%%%%%%%%%%%%%%%%%%%%%%%%%%%%%%%%%%%%%%%%%%%%%%%%%%%%%%%%%%%
%%%%%%%% STEP1: Compensate for radius of tracker ball. %%%%%%%%%
%%%%%%%%%%%%%%%%%%%%%%%%%%%%%%%%%%%%%%%%%%%%%%%%%%%%%%%%%%%%%%%%%%%%%%%%
a_m = a;

%
% Fit points to sphere
%
tolp = 0.0001;
tolg = 0.0001;
x0 = [0;0;0];
r0 = R;
[x0n, rn, d, sigmah, conv, Vx0n, urn, GNlog, aa, Rub] = ...
    lssphere(a_m', x0, r0, tolp, tolg);
R = rn
x0 = x0n - [0;0;R];
T = repmat(x0,1,N);
a_m = a_m - T;

x = a_m(1,:)' ;
y = a_m(2,:)' ; % Nx1 col vectors
z = a_m(3,:)' ;
s = z;
%
%
%%%%%%%%%%%%%%%%%%%%%%%%%%%%%%%%%%%%%%%%%%%%%%%%%%%%%%%%%%%%%%%%%%%%%%%%
%%%%%%%% STEP2: Fit piston and tilt to data so the surface normal at vertex
%%%%%%%% is pointing z axis %%%%%%%%%
r = sqrt(x.^2 + y.^2);
rho = r / max(r); % normalized radial coordinate
angle = atan2(y,x); % angular coordinate
[zCoef,zMatrix,nVec,elVec] = zFit(rho,angle,s,1);
% Translate the data by the amount of piston
% And rotate the data by the angles indicated by the amount of tilt

Tvec = [0; 0; zCoef(1)];
T = repmat(Tvec,1,N);

newa = a_m - T;
x = newa(1,:)' ;
y = newa(2,:)' ; % Nx1 col vectors
z = newa(3,:)' ;
s = z;

xlin = linspace(min(x),max(x),50);
ylin = linspace(min(y),max(y),50);
[X,Y] = meshgrid(xlin,ylin);

figure(1)
sGrid = griddata(x,y,s,X,Y);
mesh(X,Y,sGrid);axis tight; hold on
plot3(x,y,s, '.', 'MarkerSize',15)
title({'Transformed to mirror center coordinate frame';...
    ['Sampled points: ', num2str(N)]}); hold off

```

```

%%%%%%%%%%%%%%%%%%%%%%%%%%%%%%%%%%%%%%%%%%%%%%%%%%%%%%%%%%%%%%%%%%%%%%%%
%%%%%% STEP3: Subtract out the ideal surface %%%%%%%%%
%%%%%%%%%%%%%%%%%%%%%%%%%%%%%%%%%%%%%%%%%%%%%%%%%%%%%%%%%%%%%%%%%%%%%%%%
s = d;
meandata = sum(s)/N;    rms = std(s);

xlin = linspace(min(x),max(x),50);
ylin = linspace(min(y),max(y),50);
[X,Y] = meshgrid(xlin,ylin);

figure(2)
sGrid = griddata(x,y,s,X,Y);
mesh(X,Y,sGrid);axis tight;hold on
plot3(x,y,s, '.', 'MarkerSize',15)
title(['Transformed per ref points: ',...
       'mean = ',num2str(1000*meandata,3),' um ',...
       'rms = ',num2str(1000*rms,2),' um'];...
      ['Sampled points: ', num2str(N)]]; hold off
%%%%%%%%%%%%%%%%%%%%%%%%%%%%%%%%%%%%%%%%%%%%%%%%%%%%%%%%%%%%%%%%%%%%%%%%
%%%%%% STEP4: Delete points with displacements > coarse threshold %%%%%
%%%%%%%%%%%%%%%%%%%%%%%%%%%%%%%%%%%%%%%%%%%%%%%%%%%%%%%%%%%%%%%%%%%%%%%%
x = x(abs(s)<coarseThresh);
y = y(abs(s)<coarseThresh);
s = s(abs(s)<coarseThresh);
N = length(s);

% Fit piston and tilt to data, and remove them now
rho = sqrt(x.^2 + y.^2) / max(r);    % normalized radial coordinate
angle = atan2(y,x);                  % angular coordinate
[zCoef,zMatrix,nVec,elVec] = zFit(rho,angle,s,1);
s = s - zMatrix * zCoef;

meandata = sum(s)/N;    rms = std(s);

xlin = linspace(min(x),max(x),100);
ylin = linspace(min(y),max(y),100);
[X,Y] = meshgrid(xlin,ylin);

figure(3)
sGrid = griddata(x,y,s,X,Y);
mesh(X,Y,sGrid); axis tight; hold on;
plot3(x,y,s, '.', 'MarkerSize',15)
title(['Worst outliers removed: ',...
       'mean = ',num2str(1000*meandata,3),' um ',...
       'rms = ',num2str(1000*rms,2),' um'];...
      ['Sampled points: ', num2str(N)]]; hold off
%%%%%%%%%%%%%%%%%%%%%%%%%%%%%%%%%%%%%%%%%%%%%%%%%%%%%%%%%%%%%%%%%%%%%%%%
%%%%%% STEP5: Delete points with displacements > fine threshold %%%%%
%%%%%%%%%%%%%%%%%%%%%%%%%%%%%%%%%%%%%%%%%%%%%%%%%%%%%%%%%%%%%%%%%%%%%%%%
x = x(abs(s)<fineThresh);
y = y(abs(s)<fineThresh);
s = s(abs(s)<fineThresh);

```

```

N = length(s);
meandata = sum(s)/N;
rms = std(s);

xlin = linspace(min(x),max(x),100);
ylin = linspace(min(y),max(y),100);
[X,Y] = meshgrid(xlin,ylin);

figure(4)
sGrid = griddata(x,y,s,X,Y);
mesh(X,Y,sGrid); axis tight; hold on
plot3(x,y,s, '.', 'MarkerSize',15)
title(['Remaining outliers removed: ',...
      'mean = ', num2str(1000*meandata,3), ' um ',...
      'rms = ', num2str(1000*rms,2), ' um'];...
      ['Sampled points: ', num2str(N)]); hold off

%%%%%%%%%%%%%%%%%%%%%%%%%%%%%%%%%%%%%%%%%%%%%%%%%%%%%%%%%%%%%%%%%%%%%%%%%%%%%%
%%%%%%%%% STEP6: Final Zernike fit through maxDegree over full aperture %%%
%%%%%%%%%%%%%%%%%%%%%%%%%%%%%%%%%%%%%%%%%%%%%%%%%%%%%%%%%%%%%%%%%%%%%%%%%%%%%%
r = sqrt(x.^2 + y.^2);
rho = r / max(r);      % normalized radial coordinate
angle = atan2(y,x);    % angular coordinate

zCoef
[zCoef,zMatrix,nVec,elVec] = zFit(rho,angle,s,maxDegree);

Residual = s - zMatrix * zCoef;    % zCoef units in mm
Residual_rms = std(Residual)*1000; % unit in microns
zCo6 = zCoef(1:6);
zMat6 = zMatrix(:,1:6);
zCo6(4) = 0; % astigmatism 1
zCo6(6) = 0; % astigmatism 2

s = s - zMat6 * zCo6;
meandata = sum(s)/N
rms = std(s)

figure(5)
subplot(2,1,1)
sGrid = griddata(x,y,s,X,Y);
mesh(X,Y,sGrid); axis tight; hold on
plot3(x,y,s, '.', 'MarkerSize',15)
title(['Focus and final outliers removed: ',...
      'mean = ', num2str(1000*meandata,3), ' um ',...
      'rms = ', num2str(1000*rms,2), ' um'];...
      hold off

subplot(2,1,2)
nGrid = griddata(x,y,Residual,X,Y);
mesh(X,Y,nGrid); axis tight; hold on
plot3(x,y,Residual, '.', 'MarkerSize',15)
title(['Residual error after Zernike fit'],...
      ['rms = ', num2str(Residual_rms,3), ' um'])

```

```

%%%%%%%%%%%%%%%%%%%%%%%%%%%%%%%%%%%%%%%%%%%%%%%%%%%%%%%%%%%%%%%%%%%%%%%%
%%%%%%%% STEP7: Display the surface map and interferogram %%%%%%%%%
%%%%%%%%%%%%%%%%%%%%%%%%%%%%%%%%%%%%%%%%%%%%%%%%%%%%%%%%%%%%%%%%%%%%%%%%
[map,rms] = zDisplay_PZ(1000*zCoef, max(r), rmin, maxDegree);
rmsCoef = 1000*edge2rms(nVec,elVec,zCoef)
figure(6)
imagesc(map); axis equal tight; colorbar;
title(['File: ' num2str(inFileName) ...
      ' Measured: ' num2str(InitialTime)],...
      ['Piston/Tilt/Power removed RMS = ' num2str(rms) ' Microns'],...
      ['Zernike fit up through order ' num2str(maxDegree)...
      '; N = ',num2str(N) ]]);

% figure(7)
% I = 0.5+0.5*cos(4*pi*map/lambda); % double-pass config
% imagesc(I); axis equal tight; axis off; colormap(gray);
% title('Synthetic interferogram');

%%%%%%%%%%%%%%%%%%%%%%%%%%%%%%%%%%%%%%%%%%%%%%%%%%%%%%%%%%%%%%%%%%%%%%%%
%%%%%%%% STEP8: Final Zernike fit through maxDegree over GMT footprint %
%%%%%%%%%%%%%%%%%%%%%%%%%%%%%%%%%%%%%%%%%%%%%%%%%%%%%%%%%%%%%%%%%%%%%%%%
[N,s,x,y] = RadialOutlierCorrect(rmax,s,x,y);
r = sqrt(x.^2 + y.^2);
rho = r / max(r); % normalized radial coordinate
angle = atan2(y,x); % angular coordinate
xlin = linspace(min(x),max(x),100);
ylin = linspace(min(y),max(y),100);
[X,Y] = meshgrid(xlin,ylin);

[zCoef,zMatrix] = zFit(rho,angle,s,maxDegree);

Residual = s - zMatrix * zCoef; % zCoef units in mm
Residual_rms = std(Residual)*1000; % unit in microns
zCo6 = zCoef(1:6);
zMat6 = zMatrix(:,1:6);
zCo6(4) = 0; % astigmatism 1
zCo6(6) = 0; % astigmatism 2

s = s - zMat6 * zCo6;
meandata = sum(s)/N;
rms = std(s);

figure(8)
subplot(2,1,1)
sGrid = griddata(x,y,s,X,Y);
mesh(X,Y,sGrid); axis tight; hold on
plot3(x,y,s, '.', 'MarkerSize',15)
title(['Focus and final outliers removed: '],...
      ['mean = ',num2str(1000*meandata,3), ' um ',...
      'rms = ',num2str(1000*rms,2), ' um']); hold off

subplot(2,1,2)

```

```

nGrid = griddata(x,y,Residual,X,Y);
mesh(X,Y,nGrid); axis tight; hold on
plot3(x,y,Residual, '.', 'MarkerSize',15)
title(['Residual error after Zernike fit'],...
      ['rms = ',num2str(Residual_rms,3), ' um'])
%%%%%%%%%%%%%%%%%%%%%%%%%%%%%%%%%%%%%%%%%%%%%%%%%%%%%%%%%%%%%%%%%%%%%%%%
%%%%%%%% STEP9: Display the surface map through maxDegree %%%%%%%%%
%%%%%%%%%%%%%%%%%%%%%%%%%%%%%%%%%%%%%%%%%%%%%%%%%%%%%%%%%%%%%%%%%%%%%%%%
[map,rms] = zDisplay_PZ(1000*zCoef, max(r), rmin, maxDegree);
rmsCoef = 1000*edge2rms(nVec,elVec,zCoef)
figure(9)
imagesc(map); axis equal tight; colorbar;
title(['File: ' num2str(inFileName) ...
      ' Measured: ' num2str(InitialTime)],...
      ['Piston/Tilt/Power removed RMS = ' num2str(rms) ' Microns'],...
      ['Zernike fit up through order ' num2str(maxDegree)...
      '; N = ',num2str(N) ]});

%%%%%%%%%%%%%%%%%%%%%%%%%%%%%%%%%%%%%%%%%%%%%%%%%%%%%%%%%%%%%%%%%%%%%%%%
%%%%%%%% STEP10: Display the surface map up through Degree 3 %%%%%%%%%
%%%%%%%%%%%%%%%%%%%%%%%%%%%%%%%%%%%%%%%%%%%%%%%%%%%%%%%%%%%%%%%%%%%%%%%%
[map,rms] = zDisplay_PZ(1000*zCoef(1:10), max(r), rmin, 3);
figure(10)
imagesc(map); axis equal tight; colorbar;
title(['File: ' num2str(inFileName) ...
      ' Measured: ' num2str(InitialTime)],...
      ['Piston/Tilt/Power removed RMS = ' num2str(rms) ' Microns'],...
      ['Zernike fit up through order 3; N = ',num2str(N) ]});

```

D.3.2 ImportFaroSADData.m

```

function [point,R,Theta,Phi,Time,InitialTime] = ImportFaroSADData(file)
% Imports an ASCII text file (.txt) containing the X, Y, Z & Time
% stamped data which is space delimited, and outputs X, Y, Z & Time
% based on the type of tracker used to collect the data. Time starts
% at zero for the first measured point and increments up in units of
% Minutes for each successive measurement.
%
% file = input('Type file name to open in single quotes');

% file = 'surface3.txt';
fid = fopen(file);
C = textscan(fid,...
            '%f %f %f %f %2f /%2f /%2f %2f :%2f :%2f', 'delimiter', ' ', ...
            'commentStyle', '//','multipledelimsasone', 1);
fclose(fid);
point = cell2mat(C(1));
R = cell2mat(C(2));
Theta = cell2mat(C(3));
Phi = cell2mat(C(4));

```

```

M = cell2mat(C(5));
D = cell2mat(C(6));
Y = cell2mat(C(7));
H = cell2mat(C(8));
MN = cell2mat(C(9));
S = cell2mat(C(10));

FileHeader = importdata(file, ' ', 3)
% file = textread(File, '%s');
%
% [m,n] = size(file);
% file = file(4:m,1:n);

%[point,X,Y,Z,Days] = textread(file, '%d %f %f %f %f');
% [point,R,Theta,Phi,M,D,Y,H,MN,S] = textread(file,...
%      '%d %f %f %f %2d /%2d /%2d %2d :%2d :%2d');
Days = datenum(Y, M, D, H, MN, S);%time in Days
InitialTime = datestr(Days(1,1),21);

Time = 1440*Days;%time in minutes

Time = Time - Time(1,1);

```

D.3.3 SphereToCart

```

function [x,y,z] = SphereToCart(R,T,P);
% Converts data from R, Theta, Phi to X, Y, Z. Time starts at zero for
% the first measured point and increments up in units of Minutes for
% each successive measurement.

z = R.*cos(P*pi/180);
x = cos(T*pi/180).*sqrt(R.^2-z.^2);
y = sin(T*pi/180).*sqrt(R.^2-z.^2);

```

D.3.4 zDisplay_PZ.m

```

function [map,rms] = zDisplay(zCoef, rmax, rmin, maxDegree)
%
% Displays map made of Zernike polynomials.
% A variation of zDisplay.m modified by Ping Zhou that additionally
% outputs a matrix containing the map and the rms of the map
%
% INPUT

```

```

% zCoef      Zernike coefficients (standard form, column vector)
% maxDegree of Zernike polynomials
% rMin      mask out area inside this radius
% rMax      mask out area outside this radius; normalizing radius

rows = 431; % sets dimension of array to display Zernike surface
points = rows*rows;

    dX = 2*rmax/rows;
Xvec = -rmax+dX/2:dX:rmax;
    Yvec = Xvec';
[X,Y] = meshgrid(Xvec,Yvec);

R = sqrt(X.^2+Y.^2);
onMirror = R<=rmax & R>=rmin;

rho = reshape(R/rmax,points,1);
theta = reshape(atan2(Y,X),points,1);
[zMatrix,nVec,e1Vec] = zEval(rho,theta,maxDegree);

% subtract out various aberration terms...
    TzCoef = zCoef;

TzCoef(1:3)=0; % remove piston and tilt
TzCoef(5)=0; % remove power

map = reshape(zMatrix*TzCoef,rows,rows);

% Shift data to be positive everywhere on the mirror, and negative for
% points not on mirror

map = onMirror.*map;
minVal = min(min(map));
maxVal = max(max(map));

offset = abs(minVal)+0.001;

map = map + offset;
map = (onMirror .* map)-0.001;

PtsOnMirror = map(onMirror);
rms = std(PtsOnMirror(:));

```

D.3.5 RadialOutlierCorrect.m

```

function [N,d,x,y] = RadialOutlierCorrect(rmax,d,x,y);

r = sqrt(x.^2 + y.^2);
N = size(d,1);

```

312

```
oldN = N;
newN = N + 1;
while oldN~=newN
    oldN = N;
    index = find(r<rmax);
    newN = length(index);
    newd = zeros(newN,1);
    newr = zeros(newN,1);
    newx = zeros(newN,1);
    newy = zeros(newN,1);
    for i=1:newN
        newx(i) = x(index(i));
        newr(i) = r(index(i));
        newd(i) = d(index(i));
        newy(i) = y(index(i));
    end
    N = newN;
    x = newx;
    r = newr;
    d = newd;
    y = newy;
end

N = size(d,1)
oldN = N;
newN = N + 1;

while oldN~=newN
    oldN = N;
    Threshold = 3*std(d);
    index = find(abs(d)<Threshold);
    newN = length(index);
    newx = zeros(newN,1);
    newy = zeros(newN,1);
    newd = zeros(newN,1);
    for i=1:newN
        newx(i) = x(index(i));
        newy(i) = y(index(i));
        newd(i) = d(index(i));
    end
    N = newN;
    x = newx;
    y = newy;
    d = newd;
end
N
```

D.3.6 RadialCalibrationPlot.m

```

%
% Import data
%
file = 'surfacel.txt';
[point,R,Theta,Phi,Time,InitialTime] = ImportFaroSAData(file);
FitRadius = 243.859287*ones(length(R),1);
%
% Convert to tracker Cartesian coordinates.
%
[x,y,z] = SphereToCart(R,Theta,Phi);

meshPlot3(x,y,z,50)
avg = mean(z);
rms = std(z,1);
title(['Raw surface data of calibration sphere:  '],...
      ['mean = ',num2str(avg,'%0.2f'),' \mum, rms = ',...
      num2str(rms,'%0.2f'),' \mum']);

d = z+FitRadius;
meshPlot3(x,y,d,50)
avg = mean(d);
rms = std(d,1);
title(['Surface error after fitting to calibration sphere:  '],...
      ['mean = ',num2str(avg,'%0.2f'),' \mum, rms = ',...
      num2str(rms,'%0.2f'),' \mum']);

```

D.4 Angular Calibration Analysis Code

The MATLAB code for analyzing the angular calibration data from the custom laser tracker calibration is provided in this section.

D.4.1 AngularCalibration.m

```
function AngularCalibration
%
% Function evaluates the radial errors of one tracker by comparing a
% common set of measurements with another tracker. The script reads
% data for both trackers from spreadsheet. Tracker data are in m and
% rad.
%

close all
DegPerRad = 180 / pi;
NumScan=4;% number of scans
pps = 21; % points per scan
ppp = 4; % points per point: measurements made at each location
newDelta2 = zeros(4,pps);
Surf = zeros(3,NumScan*pps);
for set = 1:3
    if set == 1
        direction = 'F';
        Col = 'b';
        dataset = '1';
    elseif set == 2
        direction = 'F';
        Col = 'g';
        dataset = '2';
    else
        direction = 'R';
        Col = 'r';
        dataset = '2';
    end
    for p=1:NumScan
        folder = 'C:\My Documents\GMT\Data\Angular Calibration';
        phiT = 270;
        thetaT = 180;
        deltaXT = -24.5;
        if p == 1
            fullFileName = ...
                ['angular_calibration_set' dataset direction '_EW'];
            psiT = 90;
            deltaYT = 0;
            deltaZT = -6;
```

```

elseif p == 2
    fullFileName = ...
        ['angular_calibration_set' dataset direction '_NS'];
    psiT = 180;
    deltaYT = -5.5;
    deltaZT = 0;
elseif p == 3
    fullFileName = ...
        ['angular_calibration_set' dataset direction '_SE'];
    psiT = 225;
    deltaYT = -4.2;
    deltaZT = 4.3;
elseif p == 4
    fullFileName = ...
        ['angular_calibration_set' dataset direction '_NE'];
    psiT = 315;
    deltaYT = 4.4;
    deltaZT = 4.5;
end
if direction == 'R'
    psiT = psiT - 180;
    deltaYT = -deltaYT;
    deltaZT = -deltaYT;
end
file = fullfile(folder,fullFileName);
data1 = xlsread(file,'i:k');
n = size(data1,1);
time = xlsread(file,'g13:g96');
time = reshape(time,ppp,pps);
Time = time(1,:)- time(1,1);
data2 = xlsread(file,'w:y');
fprintf('\n%d rows of data read.\n',n);
r1 = data1(:,3)'; % row vector
thetal = data1(:,1)'; % row vector
phil = data1(:,2)'; % row vector
r2 = data2(:,3)'; % row vector
theta2 = data2(:,1)'; % row vector
phi2 = data2(:,2)'; % row vector
%
% Convert to tracker Cartesian coordinates.
%
x_t1 = r1 .* cos(thetal) .* sin(phil); % increases down
y_t1 = r1 .* sin(thetal) .* sin(phil); % increases to N
z_t1 = r1 .* cos(phil); % increases to E
xyz_t1 = [x_t1; y_t1; z_t1]; % 3 x n
x_t2 = r2 .* cos(theta2) .* sin(phi2); % increases down
y_t2 = r2 .* sin(theta2) .* sin(phi2); % increases to N
z_t2 = r2 .* cos(phi2); % increases to E
xyz_t2 = [x_t2; y_t2; z_t2]; % 3 x n
%
% First 6 points are LT+ nominal points.
%
refNom = xyz_t1(:,1:6);
%
% Next 6 points are LT2 reference points.

```

```

%
refData = xyz_t1(:,7:12);
%
% Remaining points are surface data.
%
Data1=[data1(:,3)';data1(:,1)';data1(:,2)'];
A = reshape(Data1(:,13:n),3,pps,pps);
scanData1 = reshape(mean(A,2),3,pps);
A = reshape(xyz_t2(:,13:n),3,pps,pps);
scanData2 = reshape(mean(A,2),3,pps);
nScan = n - 12;
fprintf('\n%d scan data points.\n',nScan);
fprintf('\nNominal reference coordinates in mm:\n')
for i=1:3
    for j=1:6
        fprintf('%10.1f',refNom(i,j)*1000);
    end
    fprintf('\n');
end
%
% Use 4 reference points to find best-fit coordinate
% transformation from tracker coordinates to mirror
% coordinates.
%
initTrans = [phiT/DegPerRad; thetaT/DegPerRad; ...
             psiT/DegPerRad; deltaXT; deltaYT; deltaZT];
[trans,displacement,it] = ...
    nPtFitxyz(refData,refNom,initTrans,1e-6);
phiT = trans(1);
thetaT = trans(2);
psiT = trans(3);
deltaXT = trans(4);
deltaYT = trans(5);
deltaZT = trans(6);
fprintf('\nBest-fit transformation to mirror reference points')
fprintf(' after %d iterations:\n',it)
fprintf('rotation    %9.3f %9.3f %9.3f deg\n',...
        phiT*DegPerRad,thetaT*DegPerRad,psiT*DegPerRad);
fprintf('translation %9.4f %9.4f %9.4f m\n',deltaXT,...
        deltaYT,deltaZT);
fprintf('\nResidual displacements in microns:\n')
for i=1:3
    for j=1:6
        fprintf('%10.1f',displacement(i,j)*1000000);
    end
    fprintf('\n');
end
%
% Apply this transformation to scan data.
%
Rz = [cos(phiT) sin(phiT) 0; -sin(phiT) cos(phiT) 0; 0 0 1];
Ry = [cos(thetaT) 0 -sin(thetaT);...
      0 1 0; sin(thetaT) 0 cos(thetaT)];
Rx = [1 0 0; 0 cos(psiT) sin(psiT); 0 -sin(psiT) cos(psiT)];
Tvec = [deltaXT; deltaYT; deltaZT];

```

```

T = repmat(Tvec,1,pps); % 3 x nScan
xyz = Rx*Ry*Rz*scanData2 - T; % contains nScan column vectors
%      in mirror coord sys
x2 = xyz(1,:);
y2 = xyz(2,:);
z2 = xyz(3,:);
rt = sqrt(x2.^2+y2.^2+z2.^2);
pt = acos(z2./rt);
tt = asin(y2./(rt.*sin(pt)));
rtp = [rt;tt;pt];
delta = (scanData1-rtp)*1000; % in mm & mrad
tpd(:,pps*(p-1)+1:p*pps) = [tt;pt;delta(1,:)];
Delta=((delta)-mean(delta,2)*ones(1,pps))*1000;
% Units of Delta in microns & urad
ScanAngle = (atan2(y2(1,1),z2(1,1)));
ScanData = Delta(2,:).*sin(ScanAngle) ...
    + Delta(3,:).*cos(ScanAngle);
ScanDirection = (y2*sin(ScanAngle) + z2*cos(ScanAngle));
drift = ([Time' ones(21,1)]\ScanData');
Drift = drift(1,:)*Time+drift(2,:);
newDelta2(p,:) = ScanData-Drift;
Surf(:,pps*(p-1)+1:p*pps)=[ScanData-Drift;tt;pt];
figure(p)
hold on
NewRes = newDelta2(p,)-newDelta2(p,6);
plot(ScanDirection,NewRes,'.-','color',Col)
ylabel('microradians')
xlabel('meters')

index = (1:10);

if p<3
    scancor(pps*(p-1)+1:p*pps,:) = sortrows([z2' y2'],-p);
else
    scancor(pps*(p-1)+1:p*pps,:) = sortrows([z2' y2'],p-2);
end
theta(pps*(p-1)+1:p*pps,:) = ScanAngle*ones(pps,1);
d=fliplr([fliplr(NewRes(1:11)); 0 NewRes(12:21)]);
d = d(1:21);
d(index)=-d(index);
MeasuredValues(pps*(p-1)+1:p*pps,:) = d';

z(pps*(p-1)+1:p*pps,:) = z2';
y(pps*(p-1)+1:p*pps,:) = y2';
x_dist(pps*(p-1)+1:p*pps,)=...
    (scanData1(3,)-pi/2)'/max(scanData1(3,:))*10^6;
y_dist(pps*(p-1)+1:p*pps,:) = ...
    (scanData1(2,)-pi/2)'/max(scanData1(3,:))*10^6;
end
Scancor = scancor;
znknum = 25;
[thetall,RRHO] = cart2pol(scancor(:,1),scancor(:,2));
slpA = Slope((Scancor/5),thetall,znknum); % is this correct?
slpA = [slpA(:,1:14) slpA(:,18:19) slpA(:,25)];

```

```

PistCorrection = zeros(pps*NumScan,2*NumScan);
for p=1:NumScan
    PistCorrection(pps*(p-1)+1:p*pps,p) = ones(1:21,1);
end
NslpA = [slpA PistCorrection];
coefficients(:,set) = NslpA\MeasuredValues;
U = NslpA*coefficients(:,set);
V = NslpA(:,1:17)*coefficients(1:17,set);
ANslpA(1+(set-1)*pps*NumScan:pps*NumScan+(set-1)*pps*NumScan,:)...
    =NslpA;
meshPlot3(scancor(:,1),scancor(:,2),MeasuredValues,50)
meshPlot3(scancor(:,1),scancor(:,2),V,50)

figure(100)

for p=1:NumScan
    subplot(2,2,p)
    hold on
    plot(Scancor(pps*(p-1)+1:p*pps,1)...
        .*cos(theta(pps*(p-1)+1:p*pps,:))...
        +Scancor(pps*(p-1)+1:p*pps,2)...
        .*sin(theta(pps*(p-1)+1:p*pps,:)),...
        MeasuredValues(pps*(p-1)+1:p*pps,:),'.','color',Col)
    plot(Scancor(pps*(p-1)+1:p*pps,1)...
        .*cos(theta(pps*(p-1)+1:p*pps,:))...
        +Scancor(pps*(p-1)+1:p*pps,2)...
        .*sin(theta(pps*(p-1)+1:p*pps,:)),...
        U(pps*(p-1)+1:p*pps,:), '-','color',Col)
    ylabel('microradians')
    xlabel('meters')
    title([num2str(ScanAngle*DegPerRad,'%2f'), ...
        ' degrees rms = ',...
        num2str(std(NewRes,1),'%2f'),' \murad']);
    axis([-5.1 5.1 -3 3])

end

ylin = linspace(-5,5,50);
xlin = linspace(-5,5,50);
[X,Y] = meshgrid(xlin,ylin);
[THETA,RHO] = cart2pol(X,Y);
Xx = reshape(X,2500,1);
Yy = reshape(Y,2500,1);
THETAt = reshape(THETA,2500,1);
slpB = Slope([Xx,Yy]/5,THETAt,znknum);
slpB = [slpB(:,1:14) slpB(:,18:19) slpB(:,25)];
Zz = slpB*coefficients(1:size(slpB,2),set);
Z = reshape(Zz,50,50);
figure; mesh(X,Y,Z./IMCIRCLE(50))

rho = RHO*5*22.3/24.6;
sensitivity = rho*(38-22.3)/38;
AllMeasuredValues(:,set)=MeasuredValues;
Alltheta(:,set)=theta;

```

```

ASC1(:,set)=scancor(:,1);
ASC2(:,set)=scancor(:,2);
u(:,set)=MeasuredValues.*cos(thetall);
v(:,set)=MeasuredValues.*sin(thetall);

for rs=1:NumScan
    s = 1+(rs-1)*pps;
    ss = 11 +(rs-1)*pps;
    sss = 21 +(rs-1)*pps;
    Rscan(s+(rs-1):ss+(rs-1),:)=...
        [MeasuredValues(s:ss,:),scancor(s:ss,:),thetall(s:ss,:)];
    Rscan(ss+rs:sss+rs,:)=[-MeasuredValues(ss:sss,:),...
        scancor(ss:sss,:),thetall(ss:sss,)+pi];
end

end

MeanCoeficents = mean(coeficents,2)

AAngle = [0 90 135 45];
AMV1 = AllMeasuredValues(1:21,:);
AMV1 = AMV1(:);
AMV2 = AllMeasuredValues(22:42,:);
AMV2 = AMV2(:);
AMV3 = AllMeasuredValues(43:63,:);
AMV3 = AMV3(:);
AMV4 = AllMeasuredValues(64:84,:);
AMV4 = AMV4(:);
AMV = [AMV1 AMV2 AMV3 AMV4];

AU=ANslpA*MeanCoeficents;
AveCorr = reshape(AU,84,set);
residuals = AllMeasuredValues-AveCorr;

figure(101)

for p=1:NumScan
    subplot(2,2,p)
    AR=residuals(pps*(p-1)+1:p*pps,:);
    plot(ASC1(pps*(p-1)+1:p*pps,:)...
        .*cos(Alltheta(pps*(p-1)+1:p*pps,:))...
        +ASC2(pps*(p-1)+1:p*pps,:)...
        .*sin(Alltheta(pps*(p-1)+1:p*pps,:)),AR, '.'),'color',Col)
    hold on
    ylabel('microradians')
    xlabel('meters')
    axis([-5.1 5.1 -3 3])
    plot(-5:5:5,[0,0,0],'k-','LineWidth',2)
    title([num2str(AAngle(p),'%.0f'),...
        ' degrees rms = ',num2str(std2(AR),'%.2f'),' \murad']);
end

figure(100)

```

```

for p=1:NumScan
    subplot(2,2,p)
    hold on
    box on
    title([num2str(AAngle(p), '%.0f'), ' degrees rms = ', ...
        num2str(std(AMV(:,p),1), '%.2f'), ' \murad']);
    plot(ASC1(pps*(p-1)+1:p*pps,1)...
        .*cos(Alltheta(pps*(p-1)+1:p*pps,1))...
        +ASC2(pps*(p-1)+1:p*pps,1)...
        .*sin(Alltheta(pps*(p-1)+1:p*pps,1))...
        ,AU(pps*(p-1)+1:p*pps,1), 'k-', 'LineWidth', 2)
end

rec=5*22.3/24.6;
coeficients
rho = RHO;%*4.2/5;
sensitivity = rho*(38-22.3)/38;
figure; surf(X,Y,sensitivity./IMCIRCLE(50))
daspect([1,1,1])
shading interp
colormap hot
colorbar

Zz = slpB*MeanCoeficients(1:size(slpB,2),:);
Z = reshape(Zz,50,50);
index = find(sqrt(X.^2+Y.^2)>5);
Z(index)=nan;
index = find(sqrt(X.^2+Y.^2)<rec);

figure; surf(X,Y,Z.*sensitivity./IMCIRCLE(50))
daspect([1,1,1])
shading interp
colormap hot
colorbar

figure; pcolor(X,Y,Z.*sensitivity./IMCIRCLE(50))
rectangle('Position', [-rec,-rec,2*rec,2*rec], ...
    'Curvature', [1], 'LineWidth', 3, 'LineStyle', '-')
daspect([1,1,1])
shading interp
colormap hot
colorbar
title(['rms = ', num2str(std(Z(index)).*sensitivity(index),1), ...
    '%.2f'), ' \mum']);

figure(99)
quiver([scancor(:,1);-5],[scancor(:,2);-5],[mean(u,2);1],[mean(v,2);0])
title('Vector plot showing relative magnitude and direction', ...
    ' of angular error');
axis([-6 6 -6 6])
hold on
rectangle('Position', [-rec,-rec,2*rec,2*rec], 'Curvature', [1], ...
    'LineWidth', 3, 'LineStyle', '-')
daspect([1,1,1])

```

```

xlabel({'West <==> East'},['meters'])
ylabel({'South <==> North'},['meters'])

    [junk,X,Y] = textread(fullfile(folder,...
        'ahalf_grid_air_puck_flipped.txt'), '%s %f %f');
    [THETA,RHO] = cart2pol(X,Y);
    slpB = Slope([X,Y]/rec,THETA,znknum);
    slpB = [slpB(:,1:14) slpB(:,18:19) slpB(:,25)];
    Z = slpB*MeanCoeficents(1:size(slpB,2),:);
    figure(102)
    quiver([X;-5],[Y;-5],[Z.*cos(THETA);1],[Z.*sin(THETA);0])
    title({'Vector plot showing relative magnitude and direction',...
        ' of angular error',...
        ['at each measurement location for a typical GMT Laser',...
        ' Tracker Plus test']});
    axis([-6 6 -6 6])
    hold on
    rectangle('Position',[-rec,-rec,2*rec,2*rec], 'Curvature',[1],...
        'LineWidth',3, 'LineStyle', '-')
    daspect([1,1,1])
    xlabel({'West <==> East'},['meters'])
    ylabel({'South <==> North'},['meters'])

Sz = 21;
    ylin = linspace(-5,5,Sz);
    xlin = linspace(-5,5,Sz);
    [X,Y] = meshgrid(xlin,ylin);
    [THETA,RHO] = cart2pol(X,Y);
    index = find(RHO<5);
    Xx = reshape(X,Sz^2,1);
    Yy = reshape(Y,Sz^2,1);
    THETAt = reshape(THETA,Sz^2,1);
    slpB = Slope([Xx,Yy]/5,THETAt,znknum);
    slpB = [slpB(:,1:14) slpB(:,18:19) slpB(:,25)];
    Zz = slpB*MeanCoeficents(1:size(slpB,2),:);
    Z = reshape(Zz,Sz,Sz);
    figure; quiver([Xx(index);-5],[Yy(index);-5],...
        [Zz(index).*cos(THETAt(index));1],...
        [Zz(index).*sin(THETAt(index));0])
    title({'Vector plot showing relative magnitude and direction',...
        ' of angular error',...
        ['across the entire test area for GMT']});
    axis([-6 6 -6 6])
    hold on
    rectangle('Position',[-rec,-rec,2*rec,2*rec], 'Curvature',[1],...
        'LineWidth',3, 'LineStyle', '-')
    daspect([1,1,1])
    xlabel({'West <==> East'},['meters'])
    ylabel({'South <==> North'},['meters'])

```

end

D.4.2 Slope.m

```
function slpA = Slope(scancor,thetall,zknum);

for i=1:length(scancor)
    x=scancor(i,1);
    y=scancor(i,2);
    [dzdx,dzdy] =ZernSlopeStandardNorm(zknum,x,y);
    cosphi=cos(thetall(i));
    sinphi=sin(thetall(i));
    slpA(i,:) = dzdx*cosphi+dzdy*sinphi;
end
return
```

D.4.3 ZernSlopeStandardNorm.m

```
function [dzdx,dzdy] = ZernSlopeStandardNorm(zNum,x,y)
% computes zernikes and their slopes
% x and y are normalized to +/- 1 at the edge
% for real values:
% if z and D are in m dzdy/(D/2) will be radians

    % these coefficients have same dimension as D
r2 = x*x + y*y;

% z = 0;
dzdx = 0;
dzdy = 0;

% piston
% z = z + ZC(1,1)*1;
dzdx(1) = 0;
dzdy(1) = 0;

% tilt in x
dzdx(2) = 1;
dzdy(2) = 0;

% tilt in y
dzdx(3) = 0;
dzdy(3) = 1;

% cos Astig
% z = z + ZC(1,6)*(2*x*y);
dzdx(4)= (2*x)/2;
dzdy(4)= (-2*y)/2;

% Power
dzdx(5) = 4*x/4;
dzdy(5) = 4*y/4;
```

```

% sin Astig
% z = z + ZC(1,5)*(x*x - y*y);
dzdx(6)= (2*y)/2;
dzdy(6)= (2*x)/2;

% Cos 3 Theta
% z = z + ZC(1,10)*(x*x*x - 3*x*y*y);
dzdx(7)= (3*x*x - 3*y*y)/3;
dzdy(7)= (-6*x*y)/3;

% cos Coma
dzdx(8)= (9*x*x + 3*y*y - 2)/7;
dzdy(8)= (6*x*y)/7;

% sin Coma
dzdx(9)= (6*x*y)/7;
dzdy(9)= (9*y*y + 3*x*x - 2)/7;

% Sin 3 Theta
% z = z + ZC(1,11)*(3*x*x*y - y*y*y);
dzdx(10)= (6*x*y)/3;
dzdy(10)= (3*x*x - 3*y*y)/3;

% z = z + ZC(1,12)*(x^4-y^4-4x^4y^2-4x^2y^4);
dzdx(11)= (4*x^3 - 12*x*y^2)/4;
dzdy(11)= (4*y^3 - 12*x^2*y)/4;

%z=sqrt(10)*(4x^4-4y^4-3x^2+3y^2)
dzdx(12)= (16*x^3 - 6*x)/10;
dzdy(12)= (-16*y^3+6*y)/10;

% Spherical
% z = z + ZC(1,9)*(6*r2*r2 - 6*r2 +1);
dzdx(13)= (24*r2*x - 12*x)/12;
dzdy(13)= (24*r2*y - 12*y)/12;

%z=sqrt(10)*(8x^3y+8xy^3-6xy)
dzdx(14)= (24*x^2*y + 8*y^3-6*y)/10;
dzdy(14)= (8*x^3+24*x*y^2-6*x)/10;

%z=sqrt(10)*(4x^3y-4xy^3)
dzdx(15)= (12*x^2*y -4*y^3)/4;
dzdy(15)= (4*x^3-12*x*y^2)/4;

dzdx(16)= (5*x^4 - 30*x^2*y^2 + 5*y^4)/5;
dzdy(16)= (-20*x^3*y + 20*x*y^3)/5;

dzdx(17)= (-12*x^2 + 25*x^4 + 12*y^2 - 30*x^2*y^2 - 15*y^4)/13;
dzdy(17)= (24*x*y - 20*x^3*y - 60*x*y^3)/13;

```

```
%z=sqrt(12)*(10*x^5+10*y^4*x+20*x^3*y^2-12*x^3-12*y^2*x+3*x)
dzdx(18)= (50*x^4+10*y^4+60*x^2*y^2-36*x^2-12*y^2+3)/17;
dzdy(18)= (40*y^3*x+40*x^3*y-24*y*x)/17;
```

```
%z=sqrt(12)*(10*x^4*y+10*y^5+20*x^2*y^3-12*x^2*y-12*y^3+3*y)
dzdx(19)= (40*x^3*y+40*x*y^3-24*x*y)/17;
dzdy(19)= (10*x^4+50*y^4+60*x^2*y^2-12*x^2-36*y^2+3)/17;
```

```
dzdx(20)= (-24*x*y + 60*x^3*y + 20*x*y^3)/13;
dzdy(20)= (-12*x^2 + 15*x^4 + 12*y^2 + 30*x^2*y^2 - 25*y^4)/13;
```

```
dzdx(21)= (20*x^3*y - 20*x*y^3)/5;
dzdy(21)= (5*x^4 - 30*x^2*y^2 + 5*y^4)/5;
```

```
dzdx(22)= (6*x^5 - 60*x^3*y^2 + 30*x*y^4)/6;
dzdy(22)= (-30*x^4*y + 60*x^2*y^3 - 6*y^5)/6;
```

```
dzdx(23)= (-20*x^3 + 36*x^5 + 60*x*y^2 - 120*x^3*y^2 ...
- 60*x*y^4)/16;
dzdy(23)= (60*x^2*y - 60*x^4*y - 20*y^3 - 120*x^2*y^3 ...
+ 36*y^5)/16;
```

```
dzdx(24)= (12*x - 80*x^3 + 90*x^5 + 60*x^3*y^2 - 30*x*y^4)/22;
dzdy(24)= (-12*y + 30*x^4*y + 80*y^3 - 60*x^2*y^3 - 90*y^5)/22;
```

```
dzdx(25)= (24*x - 120*x^3 + 120*x^5 - 120*x*y^2 ...
+ 240*x^3*y^2 + 120*x*y^4)/24;
dzdy(25)= (24*y - 120*x^2*y + 120*x^4*y - 120*y^3 ...
+240*x^2*y^3 + 120*y^5)/24;
```

```
dzdx(26)= (12*y - 120*x^2*y + 150*x^4*y - 40*y^3 ...
+180*x^2*y^3 + 30*y^5)/22;
dzdy(26)= (12*x - 40*x^3 + 30*x^5 - 120*x*y^2 ...
+ 180*x^3*y^2 +150*x*y^4)/22;
```

```
dzdx(27)= (-60*x^2*y + 120*x^4*y + 20*y^3 - 24*y^5)/16;
dzdy(27)= (-20*x^3 + 24*x^5 + 60*x*y^2 - 120*x*y^4)/16;
```

```
dzdx(28)= (30*x^4*y - 60*x^2*y^3 + 6*y^5)/6;
dzdy(28)= (6*x^5 - 60*x^3*y^2 + 30*x*y^4)/6;
```

```
dzdx(29)= (7*x^6-105*x^4*y^2+105*x^2*y^4-7*y^6)/7;
dzdy(29)= (-42*x^5*y+140*x^3*y^3-42*x*y^5)/7;
```

```
dzdx(30)= (-30*x^4+49*x^6+180*x^2*y^2-315*x^4*y^2 ...
-30*y^4-105*x^2*y^4+35*y^6)/19;
dzdy(30)= (120*x^3*y-126*x^5*y-120*x*y^3 ...
-140*x^3*y^3+210*x*y^5)/19;
```

```
dzdx(31)= (30*x^2-150*x^4+147*x^6-30*y^2+180*x^2*y^2 ...
-105*x^4*y^2+90*y^4-315*x^2*y^4-63*y^6)/27;
dzdy(31)= (-60*x*y+120*x^3*y-42*x^5*y+360*x*y^3 ...
```

```

-420*x^3*y^3-378*x*y^5)/27;

dzdx(32)= (-4+90*x^2 -300*x^4 + 245*x^6+30*y^2 ...
-360*x^2*y^2+525*x^4*y^2-60*y^4+315*x^2*y^4+35*y^6)/31;
dzdy(32)= (60*x*y-240*x^3*y+210*x^5*y ...
-240*x*y^3+420*x^3*y^3+210*x*y^5)/31;

dzdx(33)= (60*x*y - 240*x^3*y + 210*x^5*y - 240*x*y^3 ...
+420*x^3*y^3 + 210*x*y^5)/31;
dzdy(33)= (-4+30*x^2 - 60*x^4 + 35*x^6 + 90*y^2 ...
- 360*x^2*y^2+315*x^4*y^2 - 300*y^4 + 525*x^2*y^4 + 245*y^6)/31;

dzdx(34)= (60*x*y-360*x^3*y+378*x^5*y ...
-120*x*y^3+420*x^3*y^3+42*x*y^5)/27;
dzdy(34)= (30*x^2-90*x^4+63*x^6-30*y^2 ...
-180*x^2*y^2+315*x^4*y^2+150*y^4+105*x^2*y^4-147*y^6)/27;

dzdx(35)= (-120*x^3*y+210*x^5*y+120*x*y^3-140*x^3*y^3 ...
-126*x*y^5)/19;
dzdy(35)= (-30*x^4+35*x^6+180*x^2*y^2-105*x^4*y^2-30*y^4 ...
-315*x^2*y^4+49*y^6)/19;

dzdx(36)= (42*x^5*y-140*x^3*y^3+42*x*y^5)/7;
dzdy(36)= (7*x^6-105*x^4*y^2+105*x^2*y^4-7*y^6)/7;

dzdx(37)= (-40*x+360*x^3- 840*x^5+560*x^7+360*x*y^2 ...
-1680*x^3*y^2+1680*x^5*y^2-840*x*y^4+1680*x^3*y^4+560*x*y^6)/40;
dzdy(37)= (-40*y+360*x^2*y-840*x^4*y+560*x^6*y+360*y^3 ...
-1680*x^2*y^3+1680*x^4*y^3-840*y^5+1680*x^2*y^5 + 560*y^7)/40;

%z56
dzdx(38)= (60*x-840*x^3+3360*x^5-5040*x^7+2520*x^9 ...
-840*x*y^2+6720*x^3*y^2-15120*x^5*y^2+10080*x^7*y^2+3360*x*y^4 ...
-15120*x^3*y^4+15120*x^5*y^4...
-5040*x*y^6+10080*x^3*y^6+2520*x*y^8)/60;
dzdy(38)= (60*y-840*x^2*y+3360*x^4*y-5040*x^6*y+2520*x^8*y ...
-840*y^3+6720*x^2*y^3-15120*x^4*y^3 10080*x^6*y^3+3360*y^5 ...
-15120*x^2*y^5+15120*x^4*y^5 ...
-5040*y^7+10080*x^2*y^7+2520*y^9)/60;

%79
dzdx(39)= (-84*x+1680*x^3-10080*x^5+25200*x^7 ...
-27720*x^9+11088*x^11+ 1680*x*y^2-20160*x^3*y^2+75600*x^5*y^2 ...
-110880*x^7*y^2+55440*x^9*y^2-10080*x*y^4+75600*x^3*y^4...
-166320*x^5*y^4+110880*x^7*y^4+25200*x*y^6 -110880*x^3*y^6 ...
+110880*x^5*y^6-27720*x*y^8+55440*x^3*y^8+11088*x*y^10)/84;
dzdy(39)= (-84*y+1680*x^2*y-10080*x^4*y+25200*x^6*y ...
-27720*x^8*y+11088*x^10*y+1680*y^3-20160*x^2*y^3 ...
+75600*x^4*y^3-110880*x^6*y^3+55440*x^8*y^3 -10080*y^5 ...
+75600*x^2*y^5-166320*x^4*y^5+110880*x^6*y^5+25200*y^7 ...
-110880*x^2*y^7+110880*x^4*y^7-27720*y^9+55440*x^2*y^9...
+11088*y^11)/84;

%106
dzdx(40)= (112*x-3024*x^3+25200*x^5-92400*x^7+166320*x^9 ...

```

$$\begin{aligned}
& -144144*x^{11}+48048*x^{13}-3024*x*y^2+50400*x^3*y^2 \dots \\
& -277200*x^5*y^2+665280*x^7*y^2-720720*x^9*y^2+288288*x^{11}*y^2 \dots \\
& +25200*x*y^4-277200*x^3*y^4+997920*x^5*y^4-1441440*x^7*y^4 \dots \\
& +720720*x^9*y^4-92400*x*y^6+665280*x^3*y^6-1441440*x^5*y^6 \dots \\
& +960960*x^7*y^6+166320*x*y^8-720720*x^3*y^8+720720*x^5*y^8 \dots \\
& -144144*x*y^{10}+288288*x^3*y^{10}+48048*x*y^{12})/112; \\
dzdy(40) = & (112*y-3024*x^2*y + 25200*x^4*y - 92400*x^6*y \dots \\
& + 166320*x^8*y -144144*x^{10}*y + 48048*x^{12}*y - 3024*y^3 \dots \\
& + 50400*x^2*y^3 - 277200*x^4*y^3 + 665280*x^6*y^3 \dots \\
& -720720*x^8*y^3 + 288288*x^{10}*y^3 + 25200*y^5 - 277200*x^2*y^5 \dots \\
& + 997920*x^4*y^5 - 1441440*x^6*y^5 + 720720*x^8*y^5 - 92400*y^7 \dots \\
& + 665280*x^2*y^7 - 1441440*x^4*y^7 + 960960*x^6*y^7 \dots \\
& +166320*y^9 -720720*x^2*y^9 + 720720*x^4*y^9 - 144144*y^{11} \dots \\
& + 288288*x^2*y^{11} + 48048*y^{13})/112;
\end{aligned}$$

%137

$$\begin{aligned}
dzdx(41) = & (-144*x+5040*x^3-55440*x^5+277200*x^7-720720*x^9 \dots \\
& +1009008*x^{11}-720720*x^{13}+205920*x^{15}+5040*x*y^2-110880*x^3*y^2 \dots \\
& +831600*x^5*y^2-2882880*x^7*y^2+5045040*x^9*y^2-4324320*x^{11}*y^2 \dots \\
& +1441440*x^{13}*y^2-55440*x*y^4+831600*x^3*y^4-4324320*x^5*y^4 \dots \\
& +10090080*x^7*y^4-10810800*x^9*y^4+4324320*x^{11}*y^4+277200*x*y^6 \dots \\
& -2882880*x^3*y^6+10090080*x^5*y^6-14414400*x^7*y^6 \dots \\
& +7207200*x^9*y^6-720720*x*y^8+5045040*x^3*y^8-10810800*x^5*y^8 \dots \\
& +7207200*x^7*y^8+1009008*x*y^{10}-4324320*x^3*y^{10}+4324320*x^5*y^{10} \dots \\
& -720720*x*y^{12}+1441440*x^3*y^{12}+205920*x*y^{14})/144; \\
dzdy(41) = & (-144*y+5040*x^2*y-55440*x^4*y+277200*x^6*y \dots \\
& -720720*x^8*y+1009008*x^{10}*y-720720*x^{12}*y+205920*x^{14}*y+5040*y^3 \dots \\
& -110880*x^2*y^3+831600*x^4*y^3-2882880*x^6*y^3+5045040*x^8*y^3- \dots \\
& 4324320*x^{10}*y^3+1441440*x^{12}*y^3-55440*y^5+831600*x^2*y^5 \dots \\
& -4324320*x^4*y^5+10090080*x^6*y^5-10810800*x^8*y^5 \dots \\
& +4324320*x^{10}*y^5 +277200*y^7-2882880*x^2*y^7+10090080*x^4*y^7 \dots \\
& -14414400*x^6*y^7+7207200*x^8*y^7-720720*y^9+5045040*x^2*y^9 \dots \\
& -10810800*x^4*y^9+7207200*x^6*y^9+1009008*y^{11}-4324320*x^2*y^{11} \dots \\
& +4324320*x^4*y^{11}-720720*y^{13}+1441440*x^2*y^{13}+205920*y^{15})/144;
\end{aligned}$$

%172

$$\begin{aligned}
dzdx(42) = & (180*x-7920*x^3+110880*x^5-720720*x^7+2522520*x^9 \dots \\
& -5045040*x^{11}+5765760*x^{13}-3500640*x^{15}+875160*x^{17}-7920*x*y^2 \dots \\
& +221760*x^3*y^2-2162160*x^5*y^2+10090080*x^7*y^2 \dots \\
& -25225200*x^9*y^2 +34594560*x^{11}*y^2-24504480*x^{13}*y^2 \dots \\
& +7001280*x^{15}*y^2+110880*x*y^4-2162160*x^3*y^4+15135120*x^5*y^4 \dots \\
& -50450400*x^7*y^4+86486400*x^9*y^4-73513440*x^{11}*y^4 \dots \\
& +24504480*x^{13}*y^4-720720*x*y^6+10090080*x^3*y^6 \dots \\
& -50450400*x^5*y^6+115315200*x^7*y^6-122522400*x^9*y^6 \dots \\
& +49008960*x^{11}*y^6+2522520*x*y^8-25225200*x^3*y^8 \dots \\
& +86486400*x^5*y^8-122522400*x^7*y^8+61261200*x^9*y^8 \dots \\
& -5045040*x*y^{10}+34594560*x^3*y^{10}-73513440*x^5*y^{10} \dots \\
& +49008960*x^7*y^{10}+5765760*x*y^{12}-24504480*x^3*y^{12} \dots \\
& +24504480*x^5*y^{12}-3500640*x*y^{14}+7001280*x^3*y^{14} \dots \\
& +875160*x*y^{16})/180;
\end{aligned}$$

$$\begin{aligned}
dzdy(42) = & (180*y-7920*x^2*y + 110880*x^4*y - 720720*x^6*y \dots \\
& + 2522520*x^8*y - 5045040*x^{10}*y + 5765760*x^{12}*y \dots \\
& - 3500640*x^{14}*y + 875160*x^{16}*y - 7920*y^3 + 221760*x^2*y^3 \dots \\
& - 2162160*x^4*y^3 + 10090080*x^6*y^3- 25225200*x^8*y^3 \dots
\end{aligned}$$

```

+ 34594560*x^10*y^3 - 24504480*x^12*y^3 + 7001280*x^14*y^3 ...
+ 110880*y^5 -2162160*x^2*y^5 + 15135120*x^4*y^5...
- 50450400*x^6*y^5 + 86486400*x^8*y^5 - 73513440*x^10*y^5 ...
+ 24504480*x^12*y^5 - 720720*y^7 + 10090080*x^2*y^7 ...
- 50450400*x^4*y^7 + 115315200*x^6*y^7 - 122522400*x^8*y^7 ...
+ 49008960*x^10*y^7 + 2522520*y^9 - 25225200*x^2*y^9 ...
+ 86486400*x^4*y^9 - 122522400*x^6*y^9 + 61261200*x^8*y^9...
- 5045040*y^11 + 34594560*x^2*y^11 - 73513440*x^4*y^11 ...
+ 49008960*x^6*y^11 + 5765760*y^13 - 24504480*x^2*y^13 ...
+ 24504480*x^4*y^13 - 3500640*y^15 + 7001280*x^2*y^15 ...
+ 875160*y^17)/180;

%211
dzdx(43)= (-220*x + 11880*x^3 - 205920*x^5 + 1681680*x^7 ...
- 7567560*x^9 + 20180160*x^11 - 32672640*x^13 + 31505760*x^15 ...
- 16628040*x^17 + 3695120*x^19 + 11880*x*y^2 - 411840*x^3*y^2 ...
+ 5045040*x^5*y^2 - 30270240*x^7*y^2 + 100900800*x^9*y^2 ...
- 196035840*x^11*y^2 + 220540320*x^13*y^2 - 133024320*x^15*y^2 ...
+ 33256080*x^17*y^2 - 205920*x*y^4 + 5045040*x^3*y^4 ...
- 45405360*x^5*y^4 + 201801600*x^7*y^4 - 490089600*x^9*y^4 ...
+ 661620960*x^11*y^4 - 465585120*x^13*y^4 + 133024320*x^15*y^4 ...
+ 1681680*x*y^6 - 30270240*x^3*y^6 + 201801600*x^5*y^6 ...
- 653452800*x^7*y^6 + 1102701600*x^9*y^6 - 931170240*x^11*y^6 ...
+ 310390080*x^13*y^6 - 7567560*x*y^8 +100900800*x^3*y^8...
- 490089600*x^5*y^8 + 1102701600*x^7*y^8 - 1163962800*x^9*y^8 ...
+ 465585120*x^11*y^8 + 20180160*x*y^10 - 196035840*x^3*y^10 ...
+ 661620960*x^5*y^10 - 931170240*x^7*y^10 + 465585120*x^9*y^10 ...
- 32672640*x*y^12 + 220540320*x^3*y^12 - 465585120*x^5*y^12 ...
+ 310390080*x^7*y^12 + 31505760*x*y^14 - 133024320*x^3*y^14 ...
+ 133024320*x^5*y^14 - 16628040*x*y^16 + 33256080*x^3*y^16 ...
+ 3695120*x*y^18)/220;

dzdy(43)= 220*y + 11880*x^2*y - 205920*x^4*y ...
+ 1681680*x^6*y - 7567560*x^8*y + 20180160*x^10*y ...
- 32672640*x^12*y + 31505760*x^14*y - 16628040*x^16*y ...
+ 3695120*x^18*y + 11880*y^3 - 411840*x^2*y^3 + 5045040*x^4*y^3 ...
- 30270240*x^6*y^3 + 100900800*x^8*y^3 - 196035840*x^10*y^3 ...
+ 220540320*x^12*y^3 - 133024320*x^14*y^3 + 33256080*x^16*y^3 ...
- 205920*y^5 +5045040*x^2*y^5 - 45405360*x^4*y^5 ...
+ 201801600*x^6*y^5 -490089600*x^8*y^5 + 661620960*x^10*y^5 ...
- 465585120*x^12*y^5 + 133024320*x^14*y^5 + 1681680*y^7 ...
- 30270240*x^2*y^7 + 201801600*x^4*y^7 -653452800*x^6*y^7 ...
+ 1102701600*x^8*y^7 - 931170240*x^10*y^7 + 310390080*x^12*y^7 ...
- 7567560*y^9 + 100900800*x^2*y^9 - 490089600*x^4*y^9 ...
+ 1102701600*x^6*y^9 - 1163962800*x^8*y^9 + 465585120*x^10*y^9 ...
+ 20180160*y^11 - 196035840*x^2*y^11 + 661620960*x^4*y^11 ...
- 931170240*x^6*y^11 + 465585120*x^8*y^11 - 32672640*y^13 ...
+ 220540320*x^2*y^13 - 465585120*x^4*y^13 + 310390080*x^6*y^13 ...
+ 31505760*y^15 -133024320*x^2*y^15 + 133024320*x^4*y^15 ...
- 16628040*y^17 + 33256080*x^2*y^17 + 3695120*y^19)/220;

dzdx=dzdx(1:zNum);
dzdy=dzdy(1:zNum);
return

```

D.4.4 IMCIRCLE.m

```

function y = imcircle(n)

% y = imcircle(n);
%
% Draw a solid circle of ones with diameter n pixels
% in a square of zero-valued pixels.
%
% Example: y = imcircle(128);

if rem(n,1) > 0,
    disp(sprintf('n is not an integer and has been rounded to'),...
        sprintf(' %1.0f',round(n)))
    n = round(n);
end

if n < 1      % invalid n
    error('n must be at least 1')
end

elseif n < 4 % trivial n
    y = ones(n);
end

elseif rem(n,2) == 0, % even n
    DIAMETER = n;
    diameter = n-1;
    RADIUS = DIAMETER/2;
    radius = diameter/2;
    height_45 = round(radius/sqrt(2));
    width = zeros(1,RADIUS);
    semicircle = zeros(DIAMETER,RADIUS);

    for i = 1 : height_45
        upward = i - 0.5;
        sine = upward/radius;
        cosine = sqrt(1-sine^2);
        width(i) = ceil(cosine * radius);
    end

    array = width(1:height_45)-height_45;

    for j = max(array):-1:min(array)
        width(height_45 + j) = max(find(array == j));
    end

    if min(width) == 0
        index = find(width == 0);
        width(index) = round(mean([width(index-1) width(index+1)]));
    end

    width = [fliplr(width) width];

```

```

for k = 1 : DIAMETER
    semicircle(k,1:width(k)) = ones(1,width(k));
end

y = [fliplr(semicircle) semicircle];

else % odd n
    DIAMETER = n;
    diameter = n-1;
    RADIUS = DIAMETER/2;
    radius = diameter/2;
    semicircle = zeros(DIAMETER,radius);
    height_45 = round(radius/sqrt(2) - 0.5);
    width = zeros(1,radius);

    for i = 1 : height_45
        upward = i;
        sine = upward/radius;
        cosine = sqrt(1-sine^2);
        width(i) = ceil(cosine * radius - 0.5);
    end

    array = width(1:height_45) - height_45;

    for j = max(array):-1:min(array)
        width(height_45 + j) = max(find(array == j));
    end

    if min(width) == 0
        index = find(width == 0);
        width(index) = round(mean([width(index-1) width(index+1)]));
    end

    width = [fliplr(width) max(width) width];

    for k = 1 : DIAMETER
        semicircle(k,1:width(k)) = ones(1,width(k));
    end

    y = [fliplr(semicircle) ones(DIAMETER,1) semicircle];

end

```

D.5 Correlation Study Analysis Code

```

% CorrStrucCalc is the Matlab file used to evaluate the correlation
% data. It creates plots from the data showing the change in the
% radial direction for the laser tracker and the DMIs with time, as
% will as plots of the correlation between them. It also generates
% plots for the angular changes of the laser tracker and PSDs with
% time, as well as plots of the correlation between them.

clc
clear all
close all
fileName = 'Correlation_AHon.xls';
folder = 'C:\My Documents\GMT\Data\Correlation\20081207';
fileToRead1 = fullfile(folder,fileName);
ImportFile(fileToRead1);
ImportFile(fileName);
Index = CalcIndex(Temp,Pressure,RH);
count30=(1:30) '*10-5;
count300=(1:300)';
%
% Convert to tracker Cartesian coordinates.
%
x_t = Tracker_R .* sin(Tracker_Ze) .* cos(Tracker_Az); % increases down
y_t = Tracker_R .* sin(Tracker_Ze) .* sin(Tracker_Az); % increases to N
z_t = Tracker_R .* cos(Tracker_Ze); % increases to E
xyz_t = [x_t; y_t; z_t]; % 3 x n
sets = length(Index)/300;
r_DMI = mean(reshape(r_dmi,300,sets),1);
Separation = [9.3 7.3 5.3 3.3 1.3 0.3]; % Separation of the N & S
% references for different sets [m]
gainN = 500; % Conversion factor for the PSDs [microns/Volt]
gainS = -500; % Conversion factor for the PSDs [microns/Volt]
ThetaN = -13*pi/180;
ThetaS = -13*pi/180;
PSD_Nn = gainN*(PSD_Nx-mean(PSD_Nx))*cos(ThetaN)...
    -gainN*(PSD_Ny-mean(PSD_Ny))*sin(ThetaN);
PSD_Ne = gainN*(PSD_Nx-mean(PSD_Nx))*sin(ThetaN)...
    +gainN*(PSD_Ny-mean(PSD_Ny))*cos(ThetaN);
PSD_Sn = gainS*(PSD_Sx-mean(PSD_Sx))*cos(ThetaS)...
    -gainS*(PSD_Sy-mean(PSD_Sy))*sin(ThetaS);
PSD_Se = gainS*(PSD_Sx-mean(PSD_Sx))*sin(ThetaS)...
    +gainS*(PSD_Sy-mean(PSD_Sy))*cos(ThetaS);
%% Radial correlation Calculations %%

% For 1 second intervals
Nr = reshape(DMI_N,300,sets);
Sr = reshape(DMI_S,300,sets);
Tr = reshape(Tracker_R,300,sets);
MeanTr = mean(Tr);
Index = reshape(Index,300,sets);
Nr = Nr-ones(300,1)*mean(Nr);
Sr = Sr-ones(300,1)*mean(Sr);

```

```

Tr = Tr-ones(300,1)*mean(Tr);
Nrm = DMICountsToMicrons(Nr, Index, r_DMI);
Nrm = Nrm - ones(size(Nrm,1),1)*Nrm(1,:);
Srm = DMICountsToMicrons(Sr, Index, r_DMI);
Srm = Srm - ones(size(Srm,1),1)*Srm(1,:);
Trm = Tr*1000000;
STDrn = std(Nrm);
STDrt = std(Trm);
NSDiff_r = sqrt(mean((Nrm-Srm).^2));
NTDiff_r = sqrt(mean((Nrm-Trm).^2));
for m=1:4
    factor = [1 2 5 10];
    color = [[0 0 1];[0 1 0];[0 0 0];[1 0 0]];
    Trml = reshape(mean(reshape(Trm(:,1),...
        factor(m),300/factor(m)),1),300/factor(m),1);
    T_std(m) = std(Trml);
    Nrml = reshape(mean(reshape(Nrm(:,1),...
        factor(m),300/factor(m)),1),300/factor(m),1);
    N_std(m) = std(Nrml);
    Srml = reshape(mean(reshape(Srm(:,1),...
        factor(m),300/factor(m)),1),300/factor(m),1);
    S_std(m) = std(Srml);
    figure(500)
    subplot(3,1,1)
    title(['Plots of radial motion for laser tracker (top)'],...
        {' North DMI (middle) and South DMI (bottom)'}], 'FontSize',12)
    plot(1:factor(m):300,Trml-mean(Trml), 'color',color(m,:))
    hold on
    subplot(3,1,2)
    ylabel('Motion in Microns', 'FontSize',12)
    plot(1:factor(m):300,-(Nrml-mean(Nrml)), 'color',color(m,:))
    hold on
    subplot(3,1,3)
    xlabel('Time in seconds', 'FontSize',12)
    plot(1:factor(m):300,-(Srml-mean(Srml)), 'color',color(m,:))
    hold on
    figure(501)
    title('Plots of radial motion for laser tracker', 'FontSize',12)
    ylabel('Motion in Microns', 'FontSize',12)
    xlabel('Time in seconds', 'FontSize',12)
    plot(1:factor(m):300,Trml-mean(Trml), 'color',color(m,:))
    legend('1 sec. ave', '2 sec. ave', '5 sec. ave', '10 sec. ave',0)
    hold on
    figure(502)
    title('Plots of radial motion for the North DMI ', 'FontSize',12)
    ylabel('Motion in Microns', 'FontSize',12)
    xlabel('Time in seconds', 'FontSize',12)
    plot(1:factor(m):300,-(Nrml-mean(Nrml)), 'color',color(m,:))
    legend('1 sec. ave', '2 sec. ave', '5 sec. ave', '10 sec. ave',0)
    hold on
    figure(503)
    title('Plots of radial motion for the South DMI', 'FontSize',12)
    xlabel('Time in seconds', 'FontSize',12)
    ylabel('Motion in Microns', 'FontSize',12)
    plot(1:factor(m):300,-(Srml-mean(Srml)), 'color',color(m,:))

```

```

legend('1 sec. ave','2 sec. ave','5 sec. ave','10 sec. ave',0)
hold on
figure(504)
NSr_std(m) = std((- (Nrml-mean(Nrml)))-(- (Srml-mean(Srml))));
title('Plots of differential motion between the North & South...
      DMI','FontSize',12)
xlabel('Time in seconds','FontSize',12)
ylabel('Differential Motion in Microns','FontSize',12)
plot(1:factor(m):300,(- (Nrml-mean(Nrml)))-(- (Srml-mean(Srml))),...
      'color',color(m,:))
legend('1 sec. ave','2 sec. ave','5 sec. ave','10 sec. ave',0)
hold on
figure(505)
NTr_std(m) = std((- (Nrml-mean(Nrml)))- (Trml-mean(Trml)));
title('Plots of differential motion between the North DMI ',...
      '& laser tracker','FontSize',12)
xlabel('Time in seconds','FontSize',12)
ylabel('Differential Motion in Microns','FontSize',12)
plot(1:factor(m):300,(- (Nrml-mean(Nrml)))- (Trml-mean(Trml)),...
      'color',color(m,:))
legend('1 sec. ave','2 sec. ave','5 sec. ave','10 sec. ave',0)
hold on
figure(506)
title('Plots of differential motion between the South DMI ',...
      '& laser tracker','FontSize',12)
xlabel('Time in seconds','FontSize',12)
ylabel('Differential Motion in Microns','FontSize',12)
plot(1:factor(m):300,(- (Srml-mean(Srml)))- (Trml-mean(Trml)),...
      'color',color(m,:))
legend('1 sec. ave','2 sec. ave','5 sec. ave','10 sec. ave',0)
hold on

end
figure(507)
subplot(2,1,1)
plot(Separation,NSDiff_r,Separation,STDrn)
axis([0 10 0 2])
title(['North DMI - South DMI'],...
      {'Plot of the motion in Radial direction with 1 second ',...
      'intervals'}], 'FontSize',12)
ylabel('Magnitude [\mum]')
legend('RMS Difference','RMS of North DMI',0);
subplot(2,1,2)
plot(Separation,NSDiff_r./STDrn,Separation,STDrn./STDrn)
axis([0 10 0 2])
ylabel('Magnitude/Standard Deviation')
xlabel('Separation [m]')
legend('RMS Difference','RMS of North DMI',0);

figure(508)
subplot(2,1,1)
plot(Separation,NTDiff_r,Separation,STDrt)
axis([0 10 0 2])
title(['North DMI - Laser Tracker'],...

```

```

        {'Plot of the motion in Radial direction with 1 second ',...
        'intervals'}], 'FontSize',12)
legend('RMS Difference', 'RMS of Tracker',0);
ylabel('Magnitude [\mum]')
subplot(2,1,2)
plot(Separation,NTDiff_r./STDrt,Separation,STDrt./STDrt)
axis([0 10 0 6])
ylabel('Magnitude/Standard Deviation')
xlabel('Separation [m]')
legend('RMS Difference', 'RMS of Tracker',0);

%% Angular correlation Calculations %%

% For 1 second intervals
PSD_Nn = reshape(PSD_Nn,300,sets)./(ones(300,1)*MeanTr);
PSD_Ne = reshape(PSD_Ne,300,sets)./(ones(300,1)*MeanTr);
PSD_Sn = reshape(PSD_Sn,300,sets)./(ones(300,1)*MeanTr);
PSD_Se = reshape(PSD_Se,300,sets)./(ones(300,1)*MeanTr);
Tn = reshape(Tracker_Az,300,sets);
Te = reshape(Tracker_Ze,300,sets);
PSD_Nn = PSD_Nn-ones(300,1)*mean(PSD_Nn);
PSD_Ne = PSD_Ne-ones(300,1)*mean(PSD_Ne);
PSD_Sn = PSD_Sn-ones(300,1)*mean(PSD_Sn);
PSD_Se = PSD_Se-ones(300,1)*mean(PSD_Se);
Tn = (Tn-ones(300,1)*mean(Tn))*1000000;
Te = (Te-ones(300,1)*mean(Te))*1000000;
STDn = std(PSD_Nn);
STDe = std(PSD_Ne);
STDtn = std(Tn);
STDte = std(Te);
NSDiff_n = sqrt(mean((PSD_Nn-PSD_Sn).^2));
NSDiff_e = sqrt(mean((PSD_Ne-PSD_Se).^2));
NTDiff_n = sqrt(mean((PSD_Nn-Tn).^2));
NTDiff_e = sqrt(mean((PSD_Ne-Te).^2));
m = 1;
for m=1:4
    factor = [1 2 5 10];
    color = [[0 0 1];[0 1 0];[0 0 0];[1 0 0]];
    Tnl = reshape(mean(reshape(Tn(:,1),factor(m),...
        300/factor(m)),1),300/factor(m),1);
    Tn_std(m) = std(Tnl);
    Tel = reshape(mean(reshape(Te(:,1),factor(m),...
        300/factor(m)),1),300/factor(m),1);
    Te_std(m) = std(Tel);
    PSD_Nnl = reshape(mean(reshape(PSD_Nn(:,1),factor(m),...
        300/factor(m)),1),300/factor(m),1);
    Nn_std(m) = std(PSD_Nnl);
    PSD_Nel = reshape(mean(reshape(PSD_Ne(:,1),factor(m),...
        300/factor(m)),1),300/factor(m),1);
    Ne_std(m) = std(PSD_Nel);
    PSD_Snl = reshape(mean(reshape(PSD_Sn(:,1),factor(m),...
        300/factor(m)),1),300/factor(m),1);
    Sn_std(m) = std(PSD_Snl);
    PSD_Sel = reshape(mean(reshape(PSD_Se(:,1),factor(m),...

```

```

    300/factor(m)),1),300/factor(m),1);
Se_std(m) = std(PSD_Sel);
figure(301)
subplot(2,1,1)
title(['Plots of angular motion for laser tracker in'],...
      {'North-South direction (upper), ',...
       '& East-West dircetion (lower)'}], 'FontSize',12)
ylabel('Motion [\murad]', 'FontSize',12)
plot(1:factor(m):300,Tnl-mean(Tnl), 'color',color(m,:))
hold on
subplot(2,1,2)
plot(1:factor(m):300,Tel-mean(Tel), 'color',color(m,:))
xlabel('Time in seconds', 'FontSize',12)
ylabel('Motion [\murad]', 'FontSize',12)
legend('1 sec. ave', '2 sec. ave', '5 sec. ave', '10 sec. ave',0)
hold on
figure(302)
subplot(2,1,1)
title(['Plots of angular motion for North PSD in'],...
      {'North-South direction (upper), ',...
       '& East-West dircetion (lower)'}], 'FontSize',12)
ylabel('Motion [\murad]', 'FontSize',12)
plot(1:factor(m):300,PSD_Nnl-mean(PSD_Nnl), 'color',color(m,:))
hold on
subplot(2,1,2)
plot(1:factor(m):300,PSD_Nel-mean(PSD_Nel), 'color',color(m,:))
xlabel('Time in seconds', 'FontSize',12)
ylabel('Motion [\murad]', 'FontSize',12)
legend('1 sec. ave', '2 sec. ave', '5 sec. ave', '10 sec. ave',0)
hold on
figure(303)
subplot(2,1,1)
title(['Plots of angular motion for South PSD in'],...
      {'North-South direction (upper), ',...
       '& East-West dircetion (lower)'}], 'FontSize',12)
ylabel('Motion [\murad]', 'FontSize',12)
plot(1:factor(m):300,PSD_Snl-mean(PSD_Snl), 'color',color(m,:))
hold on
subplot(2,1,2)
plot(1:factor(m):300,PSD_Sel-mean(PSD_Sel), 'color',color(m,:))
xlabel('Time in seconds', 'FontSize',12)
ylabel('Motion [\murad]', 'FontSize',12)
legend('1 sec. ave', '2 sec. ave', '5 sec. ave', '10 sec. ave',0)
hold on
figure(304)
NSn_std(m) = std((PSD_Nnl-mean(PSD_Nnl))-(PSD_Snl-mean(PSD_Snl)));
subplot(2,1,1)
title(['Plots of differential motion between the North ',...
      '& South PSD in'], {'North-South direction (upper), ',...
      '& East-West dircetion (lower)'}], 'FontSize',12)
ylabel('Differential Motion [\murad]', 'FontSize',12)
plot(1:factor(m):300,(PSD_Nnl-mean(PSD_Nnl))...
      -(PSD_Snl-mean(PSD_Snl)), 'color',color(m,:))
hold on
NSE_std(m) = std((PSD_Nel-mean(PSD_Nel))-(PSD_Sel-mean(PSD_Sel)));

```

```

subplot(2,1,2)
plot(1:factor(m):300,(PSD_Nel-mean(PSD_Nel))...
    -(PSD_Sel-mean(PSD_Sel)), 'color',color(m,:))
xlabel('Time in seconds','FontSize',12)
ylabel('Differential Motion [\murad]','FontSize',12)
legend('1 sec. ave','2 sec. ave','5 sec. ave','10 sec. ave',0)
hold on
figure(305)
NTn_std(m) = std((PSD_Nnl-mean(PSD_Nnl))-(Tnl-mean(Tnl)));
subplot(2,1,1)
title(['Plots of differential motion between the North PSD '...
    '& laser tracker in'],{'North-South direction (upper), '...
    '& East-West dircetion (lower)'}], 'FontSize',12)
ylabel('Differential Motion [\murad]','FontSize',12)
plot(1:factor(m):300,(PSD_Nnl-mean(PSD_Nnl))-(Tnl-mean(Tnl)),...
    'color',color(m,:))
hold on
NTE_std(m) = std((PSD_Nel-mean(PSD_Nel))-(Tel-mean(Tel)));
subplot(2,1,2)
plot(1:factor(m):300,(PSD_Nel-mean(PSD_Nel))-(Tel-mean(Tel)),...
    'color',color(m,:))
xlabel('Time in seconds','FontSize',12)
ylabel('Differential Motion [\murad]','FontSize',12)
legend('1 sec. ave','2 sec. ave','5 sec. ave','10 sec. ave',0)
hold on
end

figure(306)
subplot(2,1,1)
plot(Separation,NSDiff_n,Separation,STDn)
axis([0 10 0 2])
ylabel('Magnitude [\murad]')
title(['North PSD - South PSD'],{'Plot of the motion in ',...
    'North-South direction with 1 second intervals'}], 'FontSize',12)
legend('RMS Difference','RMS of North PSD',0);
subplot(2,1,2)
plot(Separation,NSDiff_n./STDn,Separation,STDn./STDn)
axis([0 10 0 2])
ylabel('Magnitude/Standard Deviation')
xlabel('Separation [m]')
legend('RMS Difference','RMS of North PSD',0);

figure(307)
subplot(2,1,1)
plot(Separation,NSDiff_e,Separation,STDe)
axis([0 10 0 2])
ylabel('Magnitude [\murad]')
title(['North PSD - South PSD'],{'Plot of the motion in ',...
    'East-West direction with 1 second intervals'}], 'FontSize',12)
legend('RMS Difference','RMS of North PSD',0);
subplot(2,1,2)
plot(Separation,NSDiff_e./STDe,Separation,STDe./STDe)
axis([0 10 0 2])
ylabel('Magnitude/Standard Deviation')

```

```
xlabel('Separation [m]')
legend('RMS Difference', 'RMS of North PSD', 0);

figure(308)
subplot(2,1,1)
plot(Separation,NTDiff_n,Separation,STDtn)
axis([0 10 0 2])
ylabel('Magnitude [\murad]')
title(['North PSD - Laser Tracker'], {'Plot of the motion in ', ...
    'North-South direction with 1 second intervals'}], 'FontSize', 12)
legend('RMS Difference', 'RMS of Tracker', 0);
subplot(2,1,2)
plot(Separation,NTDiff_n./v,Separation,STDtn./STDtn)
axis([0 10 0 6])
ylabel('Magnitude/Standard Deviation')
xlabel('Separation [m]')
legend('RMS Difference', 'RMS of Tracker', 0);

figure(309)
subplot(2,1,1)
plot(Separation,NTDiff_e,Separation,STDte)
axis([0 10 0 2])
ylabel('Magnitude [\murad]')
title(['North PSD - Laser Tracker'], {'Plot of the motion in ', ...
    'East-West direction with 1 second intervals'}], 'FontSize', 12)
legend('RMS Difference', 'RMS of Tracker', 0);
subplot(2,1,2)
plot(Separation,NTDiff_e./STDte,Separation,STDte./STDte)
axis([0 10 0 6])
ylabel('Magnitude/Standard Deviation')
xlabel('Separation [m]')
legend('RMS Difference', 'RMS of Tracker', 0);
```

Appendix E

ORTHOGONAL POLYNOMIALS

Orthogonal polynomials are used as basis functions for fitting measurement data into a number of discrete polynomials. This is useful for comparing multiple data sets by comparing the values of the coefficients of each polynomial in the fit. Two different sets of orthogonal polynomials are used throughout this dissertation, and are discussed in the sections below.

E.1 Zernike Polynomials

Zernike polynomials are a set of orthogonal scalar functions commonly used to represent wavefront phase or surface irregularity. In this dissertation, Zernike polynomials are fit to the measured laser tracker data of the GMT surface, the distance measuring interferometer data for the radial correction, and the data of the intrinsic radial errors the laser tracker. By fitting each of these data sets into Zernike polynomials, the coefficients from the respective sets can be mathematically combined to calculate a more accurate representation of the true GMT segment surface.

Listed in Table E-1 below are the equations for the first 66 RMS Zernike polynomials (up through 10th degree). Zernike polynomials are defined over a unit circle where R is the radial distance from the center and φ is the clocking angle around the

circle. The RMS Zernike polynomials have an rms amplitude that is normalized to unity over the pupil.

Table E-1: List of the first 66 functions for the RMS Zernike polynomials up through 10th degree. The coefficient for each function is listed in the form $Z_{n,m}$ where n is the degree of the polynomial, and m describes the rotational dependence. If $m > 0$, the function has an $m\varphi$ cosine-dependence, if $m < 0$, the function has an $m\varphi$ sine-dependence, and if $m = 0$, the function is rotationally symmetric.

$Z_{n,m}$	Standard Zernike Polynomials	Aberration
$Z_{0,0}$	1	Piston
$Z_{1,1}$	$\sqrt{4} \rho \cos(\varphi)$	Tilt 0°
$Z_{1,-1}$	$\sqrt{4} \rho \sin(\varphi)$	Tilt 90°
$Z_{2,2}$	$\sqrt{6} \rho^2 \cos(2\varphi)$	Astigmatism 0°
$Z_{2,0}$	$\sqrt{3} (2\rho^2 - 1)$	Power
$Z_{2,-2}$	$\sqrt{6} \rho^2 \sin(2\varphi)$	Astigmatism 45°
$Z_{3,3}$	$\sqrt{8} \rho^3 \cos(3\varphi)$	Trefoil 0°
$Z_{3,1}$	$\sqrt{8} (3\rho^3 - 2\rho) \cos(\varphi)$	Coma 0°
$Z_{3,-1}$	$\sqrt{8} (3\rho^3 - 2\rho) \sin(\varphi)$	Coma 90°
$Z_{3,-3}$	$\sqrt{8} \rho^3 \sin(3\varphi)$	Trefoil 30°
$Z_{4,4}$	$\sqrt{10} \rho^4 \cos(4\varphi)$	Tetrafoil 0°
$Z_{4,2}$	$\sqrt{10} (4\rho^4 - 3\rho^2) \cos(2\varphi)$	2 nd Astigmatism 0°
$Z_{4,0}$	$\sqrt{5} (6\rho^4 - 6\rho^2 + 1)$	Primary Spherical
$Z_{4,-2}$	$\sqrt{10} (4\rho^4 - 3\rho^2) \sin(2\varphi)$	2 nd Astigmatism 45°
$Z_{4,-4}$	$\sqrt{10} \rho^4 \sin(4\varphi)$	Tetrafoil 22.5°
$Z_{5,5}$	$\sqrt{12} \rho^5 \cos(5\varphi)$	Pentafoil 0°
$Z_{5,3}$	$\sqrt{12} (5\rho^5 - 4\rho^3) \cos(3\varphi)$	2 nd Trefoil 0°
$Z_{5,1}$	$\sqrt{12} (10\rho^5 - 12\rho^3 + 3\rho) \cos(\varphi)$	2 nd Coma 0°
$Z_{5,-1}$	$\sqrt{12} (10\rho^5 - 12\rho^3 + 3\rho) \sin(\varphi)$	2 nd Coma 90°
$Z_{5,-3}$	$\sqrt{12} (5\rho^5 - 4\rho^3) \sin(3\varphi)$	2 nd Trefoil 30°
$Z_{5,-5}$	$\sqrt{12} \rho^5 \sin(5\varphi)$	Pentafoil 18°
$Z_{6,6}$	$\sqrt{14} \rho^6 \cos(6\varphi)$	Hexafoil 0°
$Z_{6,4}$	$\sqrt{14} (6\rho^6 - 5\rho^4) \cos(4\varphi)$	2 nd Tetrafoil 0°
$Z_{6,2}$	$\sqrt{14} (15\rho^6 - 20\rho^4 + 6\rho^2) \cos(2\varphi)$	3 rd Astigmatism 0°
$Z_{6,0}$	$\sqrt{7} (20\rho^6 - 30\rho^4 + 12\rho^2 - 1)$	2 nd Spherical
$Z_{6,-2}$	$\sqrt{14} (15\rho^6 - 20\rho^4 + 6\rho^2) \sin(2\varphi)$	3 rd Astigmatism 45°
$Z_{6,-4}$	$\sqrt{14} (6\rho^6 - 5\rho^4) \sin(4\varphi)$	2 nd Tetrafoil 22.5°
$Z_{6,-6}$	$\sqrt{14} \rho^6 \sin(6\varphi)$	Hexafoil 15°
$Z_{7,7}$	$\sqrt{16} \rho^7 \cos(7\varphi)$	Heptafoil 0°

$Z_{7,5}$	$\sqrt{16} (7\rho^7 - 6\rho^5) \cos(5\varphi)$	2 nd Pentafoil 0°
$Z_{7,3}$	$\sqrt{16} (21\rho^7 - 30\rho^5 + 10\rho^3) \cos(3\varphi)$	3 rd Trefoil 0°
$Z_{7,1}$	$\sqrt{16} (35\rho^7 - 60\rho^5 + 30\rho^3 - 4\rho) \cos(\varphi)$	3 rd Coma 0°
$Z_{7,-1}$	$\sqrt{16} (35\rho^7 - 60\rho^5 + 30\rho^3 - 4\rho) \sin(\varphi)$	3 rd Coma 90°
$Z_{7,-3}$	$\sqrt{16} (21\rho^7 - 30\rho^5 + 10\rho^3) \sin(3\varphi)$	3 rd Trefoil 30°
$Z_{7,-5}$	$\sqrt{16} (7\rho^7 - 6\rho^5) \sin(5\varphi)$	2 nd Pentafoil 18°
$Z_{7,-7}$	$\sqrt{16} \rho^7 \sin(7\varphi)$	Heptafoil 12.857°
$Z_{8,8}$	$\sqrt{18} \rho^8 \cos(8\varphi)$	Octafoil 0°
$Z_{8,6}$	$\sqrt{18} (8\rho^8 - 7\rho^6) \cos(6\varphi)$	2 nd Hexafoil 0°
$Z_{8,4}$	$\sqrt{18} (28\rho^8 - 42\rho^6 + 15\rho^4) \cos(4\varphi)$	3 rd Tetrafoil 0°
$Z_{8,2}$	$\sqrt{18} (56\rho^8 - 105\rho^6 + 60\rho^4 - 10\rho^2) \cos(2\varphi)$	4 th Astigmatism 0°
$Z_{8,0}$	$\sqrt{9} (70\rho^8 - 140\rho^6 + 90\rho^4 - 20\rho^2 + 1)$	3 rd Spherical
$Z_{8,-2}$	$\sqrt{18} (56\rho^8 - 105\rho^6 + 60\rho^4 - 10\rho^2) \sin(2\varphi)$	4 th Astigmatism 45°
$Z_{8,-4}$	$\sqrt{18} (28\rho^8 - 42\rho^6 + 15\rho^4) \sin(4\varphi)$	3 rd Tetrafoil 22.5°
$Z_{8,-6}$	$\sqrt{18} (8\rho^8 - 7\rho^6) \sin(6\varphi)$	2 nd Hexafoil 15°
$Z_{8,-8}$	$\sqrt{18} \rho^8 \sin(8\varphi)$	Octafoil 11.25°
$Z_{9,9}$	$\sqrt{20} \rho^9 \cos(9\varphi)$	Nonafoil 0°
$Z_{9,7}$	$\sqrt{20} (9\rho^9 - 8\rho^7) \cos(7\varphi)$	2 nd Heptafoil 0°
$Z_{9,5}$	$\sqrt{20} (36\rho^9 - 56\rho^7 + 21\rho^5) \cos(5\varphi)$	3 rd Pentafoil 0°
$Z_{9,3}$	$\sqrt{20} (84\rho^9 - 168\rho^7 + 105\rho^5 - 20\rho^3) \cos(3\varphi)$	4 th Trefoil 0°
$Z_{9,1}$	$\sqrt{20} (126\rho^9 - 280\rho^7 + 210\rho^5 - 60\rho^3 + 5\rho) \cos(\varphi)$	4 th Coma 0°
$Z_{9,-1}$	$\sqrt{20} (126\rho^9 - 280\rho^7 + 210\rho^5 - 60\rho^3 + 5\rho) \sin(\varphi)$	4 th Coma 90°
$Z_{9,-3}$	$\sqrt{20} (84\rho^9 - 168\rho^7 + 105\rho^5 - 20\rho^3) \sin(3\varphi)$	4 th Trefoil 30°
$Z_{9,-5}$	$\sqrt{20} (36\rho^9 - 56\rho^7 + 21\rho^5) \sin(5\varphi)$	3 rd Pentafoil 18°
$Z_{9,-7}$	$\sqrt{20} (9\rho^9 - 8\rho^7) \sin(7\varphi)$	2 nd Heptafoil 12.857°
$Z_{9,-9}$	$\sqrt{20} \rho^9 \sin(9\varphi)$	Nonafoil 10°
$Z_{10,10}$	$\sqrt{22} \rho^{10} \cos(10\varphi)$	Decafoil 0°
$Z_{10,8}$	$\sqrt{22} (10\rho^{10} - 9\rho^8) \cos(8\varphi)$	2 nd Octafoil 0°
$Z_{10,6}$	$\sqrt{22} (45\rho^{10} - 72\rho^8 + 28\rho^6) \cos(6\varphi)$	3 rd Hexafoil 0°
$Z_{10,4}$	$\sqrt{22} (120\rho^{10} - 252\rho^8 + 168\rho^6 - 35\rho^4) \cos(4\varphi)$	4 th Tetrafoil 0°
$Z_{10,2}$	$\sqrt{22} (210\rho^{10} - 504\rho^8 + 420\rho^6 - 140\rho^4 + 15\rho^2) \cos(2\varphi)$	5 th Astigmatism 0°
$Z_{10,0}$	$\sqrt{11} (252\rho^{10} - 630\rho^8 + 560\rho^6 - 210\rho^4 + 30\rho^2 - 1)$	4 th Spherical
$Z_{10,-2}$	$\sqrt{22} (210\rho^{10} - 504\rho^8 + 420\rho^6 - 140\rho^4 + 15\rho^2) \sin(2\varphi)$	5 th Astigmatism 45°
$Z_{10,-4}$	$\sqrt{22} (120\rho^{10} - 252\rho^8 + 168\rho^6 - 35\rho^4) \sin(4\varphi)$	4 th Tetrafoil 22.5°
$Z_{10,-6}$	$\sqrt{22} (45\rho^{10} - 72\rho^8 + 28\rho^6) \sin(6\varphi)$	3 rd Hexafoil 15°
$Z_{10,-8}$	$\sqrt{22} (10\rho^{10} - 9\rho^8) \sin(8\varphi)$	2 nd Octafoil 11.25°
$Z_{10,-10}$	$\sqrt{22} \rho^{10} \sin(10\varphi)$	Decafoil 9°

E.2 Zernike Slope Polynomials

Another useful set of basis functions are the Zernike slope polynomials, which are the derivatives of the Zernike polynomials, listed in Table E-1, with respect to both x and y . This relationship takes the form of

$$\vec{\nabla}Z_{n,m} = \frac{\partial}{\partial x}(Z_{n,m})\hat{x} + \frac{\partial}{\partial y}(Z_{n,m})\hat{y}. \quad (\text{E.1})$$

Because the derivative of the Zernike polynomials are gradients, the Zernike slope polynomials are vector polynomials, and must therefore be projected into the direction of the scans to determine the radial component:

$$\vec{\nabla}Z_{n,m} = \left(\frac{\partial}{\partial x}(Z_{n,m})\cos\varphi + \frac{\partial}{\partial y}(Z_{n,m})\sin\varphi \right)\hat{r}. \quad (\text{E.2})$$

Table E-2 contains a list of the first 36 Zernike slope polynomials used in this dissertation. One drawback with the Zernike slope polynomials is that they are not orthogonal, so a least-squares fit must be performed, and the resulting coefficient values will change if the number of polynomials in the fit is changed.

Table E-2: List of the first 36 functions for the Zernike slope polynomials up through 6th degree. The coefficient $\vec{\nabla}Z_{n,m}$ is the gradient of the Standard Zernike polynomial $Z_{n,m}$, where n is the order of the polynomial, and m describes the rotational dependence. These coefficients are normalized to ± 1 at the edge.

$$\vec{\nabla}Z_{n,m} = \frac{\partial}{\partial x}(Z_{n,m})\hat{x} + \frac{\partial}{\partial y}(Z_{n,m})\hat{y}$$

$$\vec{\nabla}Z_{0,0} = 0\hat{x} + 0\hat{y}$$

$$\vec{\nabla}Z_{1,1} = \hat{x} + 0\hat{y}$$

$$\vec{\nabla}Z_{1,-1} = 0\hat{x} + \hat{y}$$

$$\vec{\nabla}Z_{2,2} = 2^{-1}(2x)\hat{x} + 2^{-1}(-2y)\hat{y}$$

$$\vec{\nabla}Z_{2,0} = 4^{-1}(4x)\hat{x} + 4^{-1}(4y)\hat{y}$$

$$\begin{aligned}
\bar{V}Z_{2,-2} &= 2^{-1}(2y)\hat{x} + 2^{-1}(2x)\hat{y} \\
\bar{V}Z_{3,3} &= 3^{-1}(3x^2 - 3y^2)\hat{x} + 3^{-1}(-6xy)\hat{y} \\
\bar{V}Z_{3,1} &= 7^{-1}(9x^2 - 3y^2 - 2)\hat{x} + 7^{-1}(6xy)\hat{y} \\
\bar{V}Z_{3,-1} &= 7^{-1}(6xy)\hat{x} + 7^{-1}(9y^2 + 3x^2 - 2)\hat{y} \\
\bar{V}Z_{3,-3} &= 3^{-1}(6xy)\hat{x} + 3^{-1}(3x^2 - 3y^2)\hat{y} \\
\bar{V}Z_{4,4} &= 4^{-1}(4x^3 - 12xy^2)\hat{x} + 4^{-1}(4y^3 - 12x^2y)\hat{y} \\
\bar{V}Z_{4,2} &= 10^{-1}(16x^3 - 6x)\hat{x} + 10^{-1}(-16y^3 + 6y)\hat{y} \\
\bar{V}Z_{4,0} &= 12^{-1}(24x^3 + 24xy^2 - 12x)\hat{x} + 12^{-1}(24x^2y + 24y^3 - 12y)\hat{y} \\
\bar{V}Z_{4,-2} &= 10^{-1}(24x^2y + 8y^3 - 6y)\hat{x} + 10^{-1}(8x^3 + 24xy^2 - 6x)\hat{y} \\
\bar{V}Z_{4,-4} &= 4^{-1}(12x^2y - 4y^3)\hat{x} + 4^{-1}(4x^3 - 12xy^2)\hat{y} \\
\bar{V}Z_{5,5} &= 5^{-1}(5x^4 - 30x^2y^2 + 5y^4)\hat{x} + 5^{-1}(-20x^3y + 20xy^3)\hat{y} \\
\bar{V}Z_{5,3} &= 13^{-1}(-12x^2 + 25x^4 + 12y^2 - 30x^2y^2 - 15y^4)\hat{x} + 13^{-1}(24xy - 20x^3y - 60xy^3)\hat{y} \\
\bar{V}Z_{5,1} &= 17^{-1}(50x^4 + 10y^4 + 60x^2y^2 - 36x^2 - 12y^2 + 3)\hat{x} + 17^{-1}(40xy^3 + 40x^3y - 24xy)\hat{y} \\
\bar{V}Z_{5,-1} &= 17^{-1}(40x^3y + 40xy^3 - 24xy)\hat{x} + 17^{-1}(10x^4 + 50y^4 + 60x^2y^2 - 12x^2 - 36y^2 + 3)\hat{y} \\
\bar{V}Z_{5,-3} &= 13^{-1}(-24xy + 60x^3y + 20xy^3)\hat{x} + 13^{-1}(-12x^2 + 15x^4 + 12y^2 + 30x^2y^2 - 25y^4)\hat{y} \\
\bar{V}Z_{5,-5} &= 5^{-1}(20x^3y - 20xy^3)\hat{x} + 5^{-1}(5x^4 - 30x^2y^2 + 5y^4)\hat{y} \\
\bar{V}Z_{6,6} &= 6^{-1}(6x^5 - 60x^3y^2 + 30xy^4)\hat{x} + 6^{-1}(-30x^4y + 60x^2y^3 - 6y^5)\hat{y} \\
\bar{V}Z_{6,4} &= 16^{-1}(-20x^3 + 36x^5 + 60xy^2 - 120x^3y^2 - 60xy^4)\hat{x} \\
&\quad + 16^{-1}(60x^2y - 60x^4y - 20y^3 - 120x^2y^3 + 36y^5)\hat{y} \\
\bar{V}Z_{6,2} &= 22^{-1}(12x - 80x^3 + 90x^5 + 60x^3y^2 - 30xy^4)\hat{x} \\
&\quad + 22^{-1}(-12y + 30x^4y + 80y^3 - 60x^2y^3 - 90y^5)\hat{y} \\
\bar{V}Z_{6,0} &= 24^{-1}(24x - 120x^3 + 120x^5 - 120xy^2 + 240x^3y^2 + 120xy^4)\hat{x} \\
&\quad + 24^{-1}(24y - 120x^2y + 120x^4y - 120y^3 + 240x^2y^3 + 120y^5)\hat{y} \\
\bar{V}Z_{6,-2} &= 22^{-1}(12y - 120x^2y + 150x^4y - 40y^3 + 180x^2y^3 + 30y^5)\hat{x} \\
&\quad + 22^{-1}(12x - 40x^3 + 30x^5 - 120xy^2 + 180x^3y^2 + 150xy^4)\hat{y} \\
\bar{V}Z_{6,-4} &= 16^{-1}(-60x^2y + 120x^4y + 20y^3 - 24y^5)\hat{x} + 16^{-1}(-20x^3 + 24x^5 + 60xy^2 - 120xy^4)\hat{y} \\
\bar{V}Z_{6,-6} &= 6^{-1}(30x^4y - 60x^2y^3 + 6y^5)\hat{x} + 6^{-1}(6x^5 - 60x^3y^2 + 30xy^4)\hat{y}
\end{aligned}$$

E.3 Zhao Vector Polynomials

Zhao developed two sets of orthogonal polynomials defined over a unit circle that together form a complete set of basis functions for representing vector quantities, such as mapping distortion or wavefront gradient [41,42]. The \vec{S} polynomials are generated from gradients of Zernike polynomials, made orthonormal using the Gram-Schmidt technique. This set provides a complete basis for representing vector fields that can be defined as a gradient of some scalar function. The \vec{S} polynomials have zero curl, which makes them an incomplete set of vector polynomials such that an arbitrary continuously differentiable vector function defined over a unit circle cannot be represented by linear combinations of these polynomials. Additional vector polynomials must be added to make a complete set. The other set of vector functions \vec{T} consist of only rotational terms with zero divergence. The complete set of orthogonal vector polynomials that fully spans the circular domain can be written as the combined set of \vec{S} polynomials and independent \vec{T} polynomials since the Laplacian type functions are included in both sets.

The \vec{S} and \vec{T} polynomials can be thought of as vector fields in a unit circle. In vector calculus, \vec{S} is known as the irrotational vector fields, which have zero curl everywhere, and \vec{T} is known as the solenoidal vector fields which have zero divergence everywhere. There is some overlap between the two sets, as represented in Figure E-1, so they must be combined in such a way that the overlapped subset is counted only once. The functions are used in this dissertation for fitting angular errors in the measurements,

which are similar to mapping errors from distortion. Table **E-3** lists the first 10 functions for both the \vec{S} and the \vec{T} polynomial sets.

Table **E-3**: Analytic expression for the first 10 functions for both the \vec{S} and the \vec{T} polynomial sets, expressed in terms of the Zernike polynomials listed in Table **E-1**.

$\vec{S}_1 = 0$, trivial	$\vec{T}_1 = 0$, trivial
$\vec{S}_2 = Z_{0,0}\hat{x}$	$\vec{T}_2 = -Z_{0,0}\hat{y} = -\vec{S}_3$
$\vec{S}_3 = Z_{0,0}\hat{y}$	$\vec{T}_3 = Z_{0,0}\hat{x} = \vec{S}_2$
$\vec{S}_4 = \frac{1}{\sqrt{2}}(Z_{1,1}\hat{x} + Z_{1,-1}\hat{y})$	$\vec{T}_4 = \frac{1}{\sqrt{2}}(Z_{1,-1}\hat{x} - Z_{1,1}\hat{y})$
$\vec{S}_5 = \frac{1}{\sqrt{2}}(Z_{1,-1}\hat{x} + Z_{1,1}\hat{y})$	$\vec{T}_5 = \frac{1}{\sqrt{2}}(Z_{1,1}\hat{x} - Z_{1,-1}\hat{y}) = \vec{S}_6$
$\vec{S}_6 = \frac{1}{\sqrt{2}}(Z_{1,1}\hat{x} - Z_{1,-1}\hat{y})$	$\vec{T}_6 = \frac{-1}{\sqrt{2}}(Z_{1,-1}\hat{x} + Z_{1,1}\hat{y}) = -\vec{S}_5$
$\vec{S}_7 = \frac{1}{2}(Z_{2,-2}\hat{x} + (\sqrt{2}Z_{2,0} - Z_{2,2})\hat{y})$	$\vec{T}_7 = \frac{1}{2}((\sqrt{2}Z_{2,0} - Z_{2,2})\hat{x} - Z_{2,-2}\hat{y})$
$\vec{S}_8 = \frac{1}{2}((\sqrt{2}Z_{2,0} + Z_{2,2})\hat{x} + Z_{2,-2}\hat{y})$	$\vec{T}_8 = \frac{1}{2}(Z_{2,-2}\hat{x} - (\sqrt{2}Z_{2,0} + Z_{2,2})\hat{y})$
$\vec{S}_9 = \frac{1}{\sqrt{2}}(Z_{2,-2}\hat{x} + Z_{2,2}\hat{y})$	$\vec{T}_9 = \frac{1}{\sqrt{2}}(Z_{2,2}\hat{x} - Z_{2,-2}\hat{y}) = \vec{S}_{10}$
$\vec{S}_{10} = \frac{1}{\sqrt{2}}(Z_{2,2}\hat{x} - Z_{2,-2}\hat{y})$	$\vec{T}_{10} = \frac{-1}{\sqrt{2}}(Z_{2,-2}\hat{x} + Z_{2,2}\hat{y}) = -\vec{S}_9$

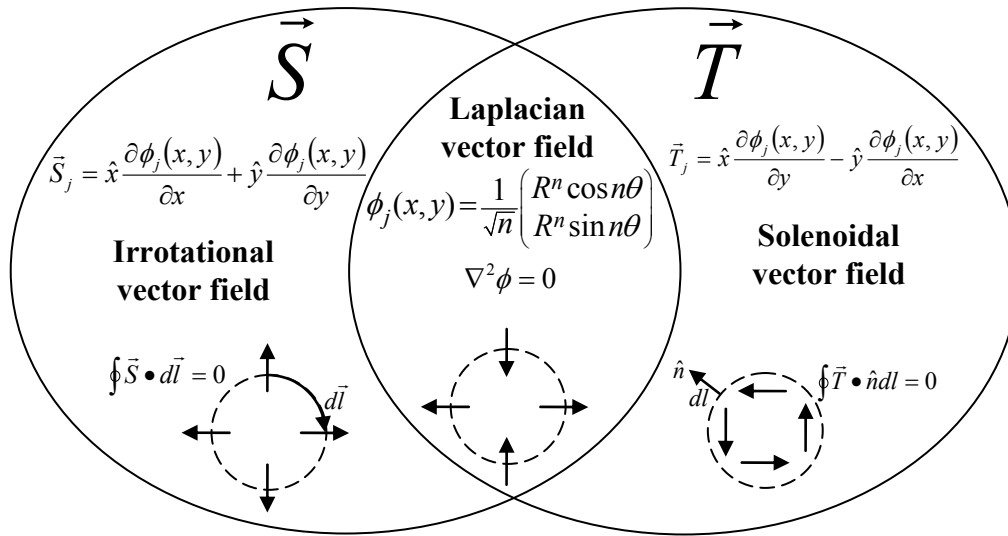


Figure E-1: Relations between the \vec{s} and \vec{t} polynomials. The Laplacian vectors are the overlap between \vec{s} and \vec{t} sets. The dashed circles and associated solid arrows illustrate the local behaviors of the vectors in different sets.

Appendix F

PSD CALIBRATION

The signals outputted by a PSD are a pair of analog voltage signals that are proportional to the location of the centroid of the incident light along each axis of the detector face. This voltage signals must first be converted to lateral motion of the centroid by knowing the properties of the detector and applying a calibration coefficient to the data. This lateral motion is then converted to changes in angle by knowing the radial distance R_i from the steering mirror at the top of the beam to the reference at the bottom, the angular change $\delta\theta_{ij}$ can be calculated from the change in the lateral position of the reference beams' centroid δl_{ij} by using:

$$\delta\theta_{ij} = C_{ij}(\delta l_{ij} / R_i), \quad (6.1)$$

where the subscript i denotes which reference beam ($i = \text{North, South, East, or West}$) and j denotes the detector axis direction ($j = x \text{ or } y$). The term C_{ij} is a constant of proportionality that is used to convert from the voltage output of the PSD system into microns. It has a nominal value of $C_{ij} = \pm 500 \mu\text{m/V}$ for the detectors used, but varies slightly depending on reference orientation and axis. These constants can be determined by using the PSD calibration procedures discussed in this appendix.

To measure the calibration coefficient, the test setup shown in Figure F-1 was used. The PSD was mounted on a set of X-Y stages with micron resolution digital

indicators to measure the lateral motion of the detector. A HeNe laser was bolted fixed to the table to use as a light source.

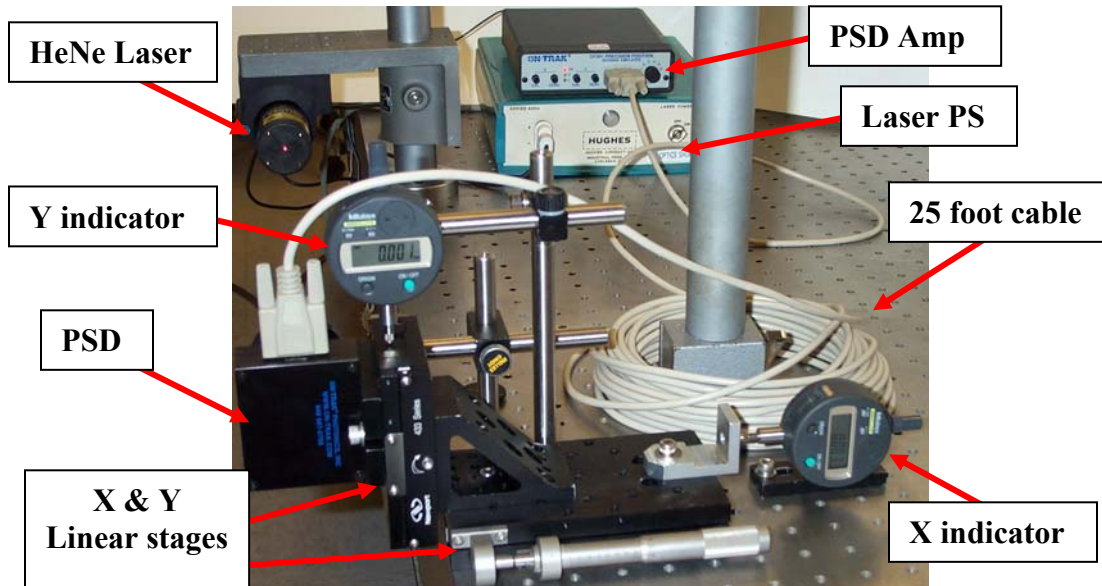


Figure F-1: Bench top setup for calibrating a Position Sensing Detector. The PSD is mounted on a two-axis stage with electronic indicators to measure displacements at the micron level, while a laser spot is incident on the detector face. The change in voltage is compared to the change in position to determine the detector's linearity and calibration coefficients.

The voltage readings from the PSD amplifier were run into the National Instruments Compact FieldPoint interface, discussed in Section B.8, where they could then be read by a data analysis computer. A piece of LABVIEW software developed by Gallagher for interfacing with PSDs was used to read the voltage signals from the Compact FieldPoint [15]. The interface is shown in Figure F-2. The interface has a plot representing the detector face with a live spot showing the X/Y position of the centroid on the detector face. The software is set up to log the PSD values, either continuously, or as a time average.

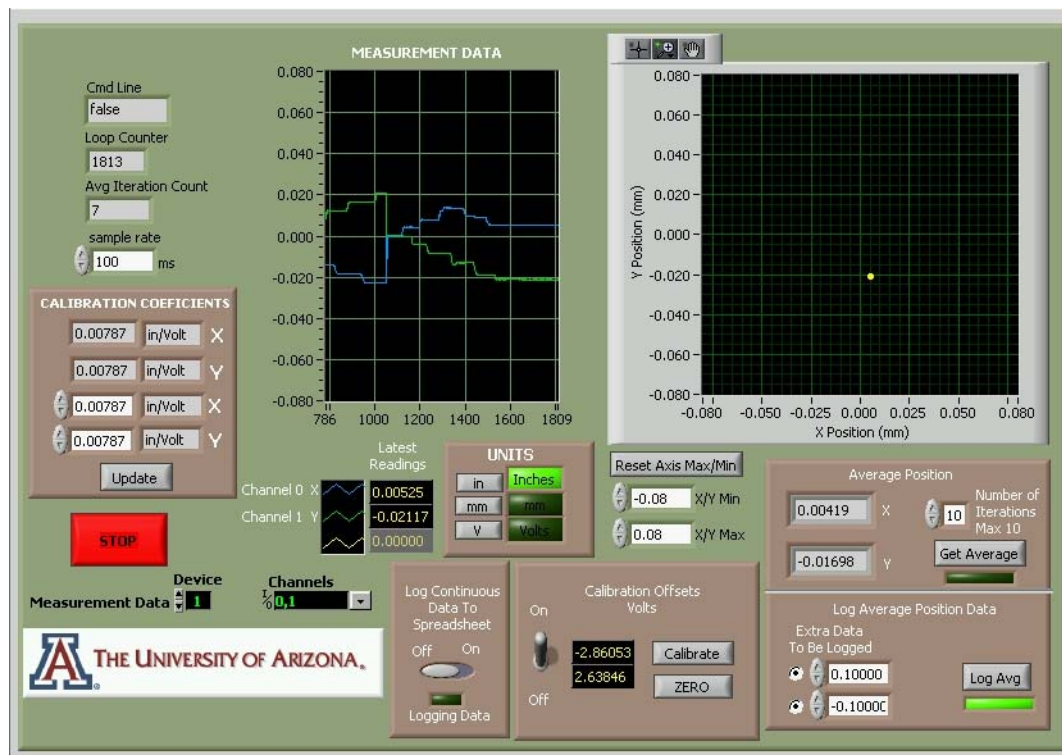


Figure F-2: PSD interface frontend developed in LABVIEW by Gallagher [15].

The software was used to log time averaged measurements of the centroid's position across the detector at discrete measurement positions. A set of scans were made across each axis of the PSD. To record the data the following steps were taken:

1. The beam was put close to the center of the detector in one axis and at the edge of the axis to be scanned,
2. An average of 10 data points were recorded using the "Log Average" button on the software,
3. The micrometer was adjusted in one axis and not the other (100 μm increments),
4. The reading from both micrometers were logged into the extra data field of the software,

5. The micrometer position was adjusted and more data was logged for the next position,
6. This was repeated until the scan was completed across the entire detector face, and
7. The process was repeated for the other axis.

Figure F-3 shows the curves for the X and Y Axis Voltage vs. Position. The chart labeled “Scan in X direction” represents the data that was recorded when the PSD was moved along the X axis with the micrometer and the Y axis was held constant. Similarly, the chart labeled “Scan in Y direction” represents the data where they PSD was moved along the Y axis of the detector and the X axis held constant.

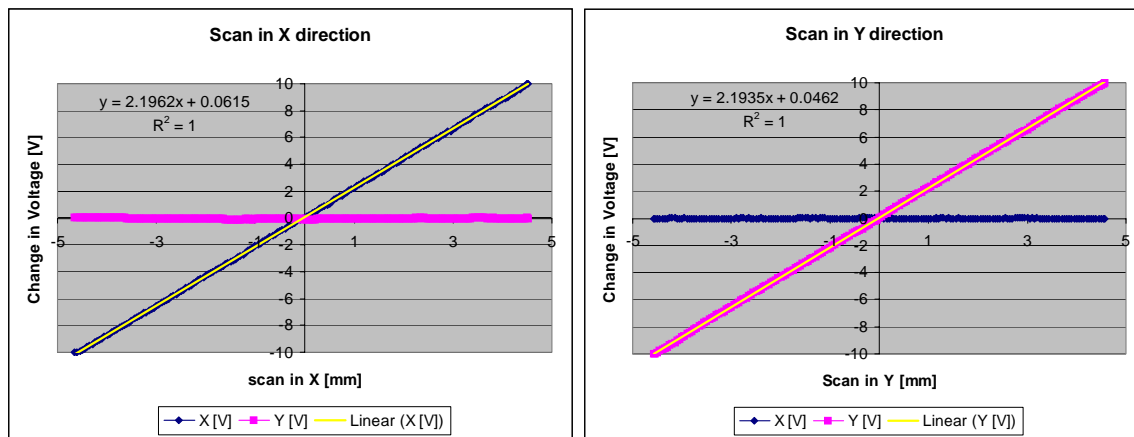


Figure F-3: Resulting plots from the bench top calibration showing the linearity the PSD. From the slope of the lines, the calibration coefficients relating output voltage and displacement can be determined.

The plots show that the PSD is linear in both the X and Y axes. The calibration coefficients for the detector is calculated from the inverse of the slope of the curve in each axis to be $c_x = 0.45533$ mm/V in the X-axis and $c_y = 0.45589$ mm/V in the Y-axis.

Calibration Coefficients C_{ij} for the four PSDs in the external reference system are calculated using

$$C_{ij} = c_x \cos(\varphi_j + \delta\varphi_j) + c_y \sin(\varphi_j + \delta\varphi_j) \quad (\mathbf{F.2})$$

where φ_j is the nominal clocking angle of the detector around the mirror and $\delta\varphi_j$ is the deviation from the nominal. For the four surface references, the nominal values of φ_j are listed in Table F-1. Because the surface references must be removed from the mirror during grinding and added during testing, the clocking angle is not consistent. For this reason, if the PSD correction is to be applied, the error in the clocking angle $\delta\varphi_j$ for each reference must be determined each time.

Table F-1: List of nominal clocking angle of the PSDs for each surface reference.

Surface Reference	Nominal Clocking Angle φ_j
North	0°
South	180°
East	270°
West	90°

For testing GMT, the easiest way to measure φ_j is to use the Primary Mirror Positioner (PMP) to move the mirror in a specific way, and get measurements from the PSDs both before and after. An example is to have all four reference beams aligned, take a measurement of the initial position of the centroids on each PSD, move the PMP 0.5 mm due west, and then take a second measurement. The change in position of the centroid in the detector face in both X and Y can be measure for each detector, then φ_j can be calculated using

$$\varphi_j = \arctan\left(\frac{\Delta x_j}{\Delta y_j}\right), \quad (\mathbf{F.3})$$

where Δx_j is the measured displacement of the centroid in the X-axis of the PSD and Δy_j is the measured displacement of the centroid in the Y-axis of the PSD.

REFERENCES

1. Agilent Technologies, Inc. "Lasers and optics user's manual", P/N 05517-90045 (July 2002).
2. Automated Precision Inc. website: www.apisensor.com.
3. N. Bobroff, "Residual errors in laser interferometry from air turbulence and nonlinearity", *Appl.Opt.*, **26**:2676 (1987).
4. L. B. Brown, J. B. Merry, and D. N. Wells, "Coordinate measurement with a tracking laser interferometer", *Laser & Applications*, Oct.86, pp. 69-71 (1986).
5. J. H. Burge, L. R. Dettmann, and S. C. West, "Null correctors for 6.5-m f/1.25 paraboloidal mirrors", *OSA Trends in Optics and Photonics Vol. 24, Fabrication and Testing of Aspheres*, J. S. Taylor, M. Piscotty, and A. Lindquist eds. (Optical Society of America, Washington DC 1999) pp. 182-186.
6. J. H. Burge, L. B. Kot, H. M. Martin, C. Zhao and R. Zehnder, "Design and analysis for interferometric testing of the GMT primary mirror segments", in *Optomechanical Technologies for Astronomy*, ed. E. Atad-Ettinger, J. Antebi and D. Lemke, Proc. SPIE **6273** (2006).
7. J. H. Burge, L. B. Kot, H. M. Martin, C. Zhao and T. Zobrist, "Alternative surface measurements for GMT primary mirror segments", in *Optomechanical Technologies for Astronomy*, ed. E. Atad-Ettinger, J. Antebi and D. Lemke, Proc. SPIE **6273** (2006).
8. J. H. Burge, P. Su, C. Zhao and T. Zobrist, "Use of a commercial laser tracker for optical alignment", in *Optical System Alignment and Tolerancing*, ed. J. Sasian and M. Ruda, Proc. SPIE **6676** (2007).
9. J. H. Burge, W. Davison, C. Zhao and H. M. Martin, "Development of surface metrology for the Giant Magellan Telescope primary mirror", in *Advanced Optical and Mechanical Technologies in Telescopes and Instrumentation*, ed. E. Atad-Ettinger and D. Lemke, Proc. SPIE **7018** (2008).
10. C. F. Claver, D. Sweeney, J. A. Tyson, B. Althouse, T. Axelrod, T. Axelrod, K. Cook, L. Daggert, J. Kantor, S. Kahn, V. L. Krabbendam, P. Pinto, J. Sebag, C. Stubbs, S. C. Wolff, "Project Status of the 8.4 m LSST", in *Ground-based Telescopes*, ed. J. M. Oschmann Jr., Proc. SPIE **5489** (2004).
11. C. Denker, P. R. Goode, D. Ren, M. A. Saadeghvaziri, A. P. Verdoni, H. Wang, G. Yang, V. Abramenko, W. Cao, R. Coulter, R. Fear, J. Nenow, S. Shoumko, T. J. Spirock, J. R. Varsik, J. Chae, J. R. Kuhn, Y. Moon, Y. D. Park and

- A. Tritschler, "Progress on the 1.6-meter New Solar Telescope at Big Bear Solar Observatory", in *Ground-based and Airborne Telescopes*, ed. L. M. Stepp, Proc. SPIE **6267** (2006).
12. W. T. Estler, "High-accuracy displacement interferometry in air", *Appl. Opt.*, **24**:808 (1985).
 13. Excel Precision Corporation, "The model 1031F receiver user's manual", P/N 1031-0000-9102 REV A (October 1998).
 14. FARO Technologies Inc. website: www.faro.com.
 15. B. B. Gallagher, "Optical Shop Applications for Laser Tracker Metrology Systems", (M.S. Thesis, College of Optical Sciences, University of Arizona, 2003).
 16. G. Gassner and R. Ruland, "Laser tracker calibration: test and angle measurement system", in *15th International Geodätische Woche*, slack-pub-13476 (2009).
 17. GMT Conceptual Design Review, p. 10-57 (February 2006).
 18. H. Goldstein, *Classical Mechanics*, 2nd ed., (Addison-Wesley Publishing Co. Reading, MA, 1980).
 19. A. H. Greenleaf, "Computer-controlled optical surfacing," in *Active Optical Devices and Applications*, ed. W. J. Cuneo, Jr., Proc. SPIE **228** (1980).
 20. A. H. Greenleaf, "Self-calibrating surface measuring machine", *Optical Engineering*, **22**:276 (1983).
 21. B. Hughes, C. Jones, A. Forbes and S. Oldfield, "Study of Measuring an Off-axis 8.4 m Diameter Mirror Surface Using Multilateration", NPL Report DEPC-EM (RES) 008 (September 2005).
 22. Linear Technology Corporation, "LT1013/LT1014 product specification sheet", website: www.linear.com.
 23. ISO/IEC Guide 99-12:2007, *International vocabulary of metrology – basic and general concepts and associated terms*, VIM, third edition, 2007.
 24. M. Johns, "The Giant Magellan Telescope (GMT)", in *Ground-based and Airborne Telescopes*, ed. L. M. Stepp, Proc. SPIE **6267** (2006).
 25. B. A. W. H. Knarren, "Applications of optical fibers in precision heterodyne laser interferometry", (PhD Dissertation, Eindhoven: Technische Universiteit Eindhoven, 2003).

26. O. Kwon, J. C. Wyant, and C. R. Hayslett, "Rough surface interferometry at 10.6 μm ", *Appl. Opt.*, **19**:1862 (1980).
27. Leica Geosystems website: www.leica-geosystems.com/metrology.
28. L. Ma, L. Wang, T. Cao, J. Wang, X. He, and C. Xiong, "A large-scale laser plane calibration system", *Meas. Sci. Technol.*, **18**:1768 (2007).
29. H. M. Martin, R. G. Allen, J. H. Burge, L. R. Dettmann, D. A. Ketelsen, S. M. Miller, and J. M. Sasian, "Fabrication of mirrors for the Magellan Telescopes and the Large Binocular Telescope", in *Large Ground-based Telescopes*, ed. J. M. Oschmann and L. M. Stepp, *Proc. SPIE* **4837** (2003).
30. H. M. Martin, J. H. Burge, B. Cuerden, S. M. Miller, B. Smith, and C. Zhao, "Manufacture of 8.4 m off-axis segments: a 1/5 scale demonstration", in *Optical Fabrication, Metrology, and Material Advancements for Telescopes*, ed. E. Atad-Ettedgui and P. Dierickx, *Proc. SPIE* **5494** (2004).
31. H. M. Martin, J. H. Burge, S. D. Miller, B. K. Smith, R. Zehnder and C. Zhao, "Manufacture of a 1.7-m prototype of the GMT primary mirror segments", in *Optomechanical Technologies for Astronomy*, ed. E. Atad-Ettedgui, J. Antebi and D. Lemke, *Proc. SPIE* **6273** (2006).
32. H. M. Martin, J. H. Burge, B. Cuerden, W. B. Davison, J. S. Kingsley, W. C. Kittrell, R. D. Lutz, S. M. Miller, C. Zhao and T. Zobrist, "Progress in manufacturing the first 8.4 m off-axis segment for the Giant Magellan Telescope", in *Advanced Optical and Mechanical Technologies in Telescopes and Instrumentation*, ed. E. Atad-Ettedgui and D. Lemke, *Proc. SPIE* **7018** (2008).
33. On-Trak Photonics, Inc. "Position Sensing Detectors for Non-Contact Measurements of Position, Motion, Distance, and Vibration." January 2004, <http://www.on-trak.com/position-sensing-detectors.html>.
34. J. F. Ouyang, W. L. Liu, Y. G. Yan, and D. X. Sun, "Angular error calibration of laser tracker system", in *Advanced Laser Technologies*, ed. I. A. Shcherbakov, K. Xu, Q. Wang, A. V. Priezhev, and V. I. Pustovoy, *Proc. SPIE* **6344** (2006).
35. R. E. Ruland, "The Chesapeake laser tracker in industrial metrology", in *International Workshop on Accelerator Alignment*, slack-pub-11423 (1993).
36. T. Schmitz, C. Evans, A. Davies, and W. T. Estler, "Displacement uncertainty in interferometric radius measurements", *Ann. CIRP*, **51**:451 (2002).
37. P. Su, J. Sasian, and J. H. Burge, "Shear test of off-axis surface with axisymmetric parent", in *Optical Manufacturing and Testing VII*, ed. By J. Burge, O. Faehnle, and R. Williamson, *Proc. SPIE* **6671** (2007).

38. P. Su, J. H. Burge, B. Cuerden, and H. M. Martin, "Scanning pentaprism measurements of off-axis aspherics", in *Advanced Optical and Mechanical Technologies in Telescopes and Instrumentation*, ed. E. Atad-Ettinger and D. Lemke, Proc. SPIE **7018** (2008).
39. P. Su, "Absolute measurements of large mirrors", (Ph.D. Dissertation, College of Optical Sciences, University of Arizona, 2008).
40. Thor Labs website: www.thorlabs.com.
41. C. Zhao and J. H. Burge, "Orthonormal vector polynomials in a unit circle, Part I: basis set derived from gradients of Zernike polynomials", *Optics Express*, **15**:18014 (2007).
42. C. Zhao and J. H. Burge, "Orthonormal vector polynomials in a unit circle, Part II: completing the basis set", *Optics Express*, **16**:6586 (2008).
43. H. Zhuang and Z. S. Roth, "Modeling gimbal axis misalignments and mirror center offset in a single-beam laser tracking measurement system", in *International Journal of Robotics Research*, **14**:211 (1995).
44. T. Zobrist, J. H. Burge, W. B. Davison, and H. M. Martin, "Measurements of large optical surfaces with a laser tracker", in *Advanced Optical and Mechanical Technologies in Telescopes and Instrumentation*, ed. E. Atad-Ettinger and D. Lemke, Proc. SPIE **7018** (2008).
45. T. Zobrist, J. H. Burge, and H. M. Martin, "Laser tracker surface measurements of the 8.4 m GMT primary mirror segment", in *Optical Manufacturing and Testing VIII*, ed. J. H. Burge, O. W. Föhnle, and R. Williamson, Proc. SPIE **7426** (2009).

ILLUSTRATION CREDITS

The following images are used with permission from Agilent Technologies, Inc.

- Figure B-1: Agilent 5517B laser head dimensions.
- Figure B-2: Agilent 10705A single beam interferometer (left) and Agilent 10704A retroreflector (right).
- Figure B-3: Agilent 10705A single beam interferometer dimensions.
- Figure B-4: Single beam interferometer reference and measurement laser beam paths.
- Figure B-5: Agilent 10704A retroreflector dimensions.
- Figure B-6: Dimensions of the Agilent 10701A 50% beam splitter (left) and Agilent 10707A beam bender (right).
- Figure B-7: Dimensions of the Agilent 10780F remote receiver with 2 meter fiber optic and remote sensor.

The following image is used with permission from FARO Technologies, Inc.

- Figure 3-1: A laser tracker measures the location of an SMR in three dimensions and tracks the relative motion.